UNIVERSITÀ DEGLI STUDI DI NAPOLI FEDERICO II

FACOLTÀ DI INGEGNERIA
Dipartimento di Ingegneria dei Materiali e della Produzione

Dottorato in Ingegneria dei Materiali e delle Strutture
XXIV Ciclo

INVESTIGATING MECHANICAL BEHAVIOR OF CORD-RUBBER COMPOSITES BY MULTI-SCALE EXPERIMENTAL AND THEORETICAL APPROACH

Ph.D. Thesis

Maria Giovanna Pastore Carbone

Advisor: Prof. Giuseppe Mensitieri

December 2011

Abstract

Cord-rubber composites are the skeleton of pneumatic tires. Due to axial stiffness combined with high flexibility, such composites are the perfect material for carcass construction. The availability of detailed information on their mechanical response is of paramount importance in the design of performing tires; hence, both experimental characterization and computer simulation of cord-rubber composites are of great interest to researchers and engineers involved in tire design. However, a macroscopic approach is mostly adopted and the single cord-rubber lamina is treated as an orthotropic material. This approach neglects the phenomena that arise inside the lamina on a mesoscopic and a microscopic scale that are indeed responsible for failure mechanisms and local tire heating.

This thesis addresses with an innovative investigation of mechanical response of cord-rubber composites, which is based on a multi-scale approach adopted in both experimental investigation and theoretical modeling. In particular, the mechanical response of the cord-rubber composite and of its constituents has been investigated on both a macroscopic and a microscopic scale. The macroscopic response of the lamina has been characterized by tensile test (both static and dynamic) and has been discussed in the light of the well established approaches based on the rule of mixtures. It has been found that mechanical behavior strongly depends on sample length. According to micromechanical models, such a 'finite fiber length effect' is generally ascribed to the efficiency of stress transfer into the uniaxial composite. Actually, it has been theoretically found that this dependence becomes particularly pronounced whether the mismatch between the elastic properties of matrix and reinforcement is considerable, such as for cord-rubber composites. Hence a microscopic investigation has been carried out by micro Raman spectroscopy that has been found to be a very powerful tool for the study of micromechanics of composites. Corded reinforcement has thus been preliminarily examined by investigating molecular deformation processes and evaluating the contributions of single

filaments to the response of the overall structure. In addition, since reinforcement can be actually adopted as a strain or stress sensor embedded into the composite, the micromechanical response of the composite has been investigated. In particular, the effect of sample length upon the parameters that govern stress transfer has been examined in detail, providing information on reinforcing efficiency of cord. Results of the micromechanical investigation have then been correlated to the macroscopical findings.

A three-dimensional finite element model of the cord-rubber lamina has also been developed by adopting a multi-scale hybrid analytical/numerical approach. Cord has been first modeled by an analytical model that accounts for tension-twisting coupling and relates the constitutive behavior to the hierarchical structure of the cord itself. On the basis of this analytical model, a homogenized cylindrical model of the cord has been implemented in the FEM code, incorporating the relevant mechanical features of the aforementioned cord analytical model. Finally, the overall mechanical model for the composite has thus been implemented by embedding the hybrid cord model into a FEM non-linear hyperelastic matrix. Simulation results have highlighted a significant tension-twisting coupling for the composite and comparison with the commonly adopted orthotropic model have been analyzed.

Acknowledgements

Maria Giovanna Pastore Carbone
December 2011

Contents

x

«Να εύχεσαι νάναι μακρύς ο δρόμος»

(*Hope your road is long*)

K. Kavafis, Ithaki (1911)

Chapter 1

Cord-rubber composites:
the skeleton of pneumatic tires

1.1 Introduction

In the last decades, most of modern technologies have been requiring materials whose features can be *ad-hoc* tailored and that can provide peculiar combinations of several properties that cannot be contemporary found in conventional material, such as metals, ceramics and polymers. The idea of coupling different materials in such a way to get a combination whose properties are better than each component is very ancient: in fact, by mixing straw and mud, our forebears used to create a very good material for building. In composite materials, the combination of a matrix and a reinforcement leads to a product whose final chemical-physical properties cannot be found in the separated components and that can be easily tailored according to the requirements of the final product. For many years they have been fitting the requirements of several niche fields (aerospace, ship, automobile, biomedical); nevertheless, nowadays they are commonly adopted also for manufacturing product destined to mainstream market.

Cord-rubber composites are a classic example of composite materials that find application in everyone's quotidian life. In fact they are the main components of pneumatic tire [1].

These elastomeric composites are made up of:

a. a low-modulus rubber matrix, characterized by high extensibility;

b. a twisted reinforcement (the 'cord') characterized by high modulus and strength and low bending stiffness;

c. an adhesive film (termed 'dip') which bonds the reinforcement to the matrix.

Such a combination is really effective when the structure needs a high stiffness in reinforcement direction and also flexibility in the plane perpendicular to cords. These are properties that satisfy exactly tires requirements, such as strength in the cord direction for holding air pressure, but also flexibility in order to provide a comfortable ride and cut down on fatigue from bumpy roads. Furthermore, tire needs to sustain large deformation, with high load carrying capacity and fatigue strength. All of these features make cord-rubber composites the perfect material for tire construction. In particular, the performance features of pneumatic tires are mainly controlled by the anisotropic properties of the cord-rubber composite: the low-modulus, high-elongation rubber contains the air and provides abrasion resistance and road grip; the high-modulus, low-elongation cords carry most of the loads applied to the tire in service [2].

In this Chapter, the nature and the role of cord-rubber composites will be analyzed in detail. Therefore it will be necessary to start with the analysis of a pneumatic tire, in order to get a complete and introductory description of the question.

1.2 Pneumatic tire

A pneumatic tire is a toroidal-like, flexible structure filled with compressed air that guarantees the running gear–ground contact in a vehicle. The main functions that a tire is requested to fulfill are:

· to support the weight of the vehicle;

· to cushion the vehicle over surface irregularities;

· to provide sufficient traction for driving and braking;

· to provide adequate steering control and direction stability [3].

From a geometrical point of view, tire is a surface of double curvature, which is a non-developable surface and yet it must deform to give an area of contact on a plane road surface. Vehicle load causes tires to deflect until the average contact area pressure is balanced by the tires' internal air pressure. All of these external

causes determine a very complex tensional state in the tire structure, making it a very interesting and difficult system to be analyzed.

The structure of a pneumatic tire derives from a compromise of geometric and mechanical requirements: constancy of effective dimensions along with flexibility and stiffness. A certain uniformity is required to achieve a constant angle height and effective rolling radius on smooth roads, and it could be easily obtained by a rigid wheel. On the other hand, flexibility is required for the absorption of road irregularities. Furthermore, a certain stiffness is required in order to sustain the complex stress field due to vehicle load.

These features can be obtained by combining a very compliant material, such as rubber, with a load carrying reinforcement, which is a high performing materials, providing strength and stability.

The structure of a tubeless tire (that is designed for use without a separate, removable inner tube) is mainly made up of three parts: the carcass (or casing), the beads and the tread. The carcass, which is the most important structural element of the tire, is made up of a number of layers (plies) of flexible cords of high modulus of elasticity (i.e. steel, polyester, nylon, rayon) embedded into a matrix of low modulus rubber compounds, as shown in Figure 1.1. The cords are anchored around the beads (made of high tensile strength steel wires), which serve as the 'foundations' for the carcass and provide adequate seating of the tire on the wheel rim [4]. This mechanism makes the carcass demountably fitted on the rim. The tread is the only part of the tire to be directly in contact with the road surface. It performs several functions, such as protecting the carcass (e.g. providing a wear resistant layer), providing frictional contact with the road sufficient to transmit driving, braking and cornering forces, and ensuring an adequate level of frictional adhesion between the tire and the road over a wide range of service conditions. It consists of a special rubber compound that is specially formulated to provide a balance between wear, traction, handling and rolling resistance. A pattern (molded into the tread during vulcanization) is also designed to provide uniform wear, to channel water out of the footprint, and to minimize pattern noise on a variety of road surfaces. Both the tread compound and the tread design must perform effectively in a multitude of driving conditions, including wet, dry or snow covered surfaces, while also meeting customer expectations for acceptable wear resistance, low noise, and good ride quality. For instance, for driving in severe winter conditions, snow tires have been specifically designed with increased tread depth and specially formulated tread compounds (with a lower Tg).
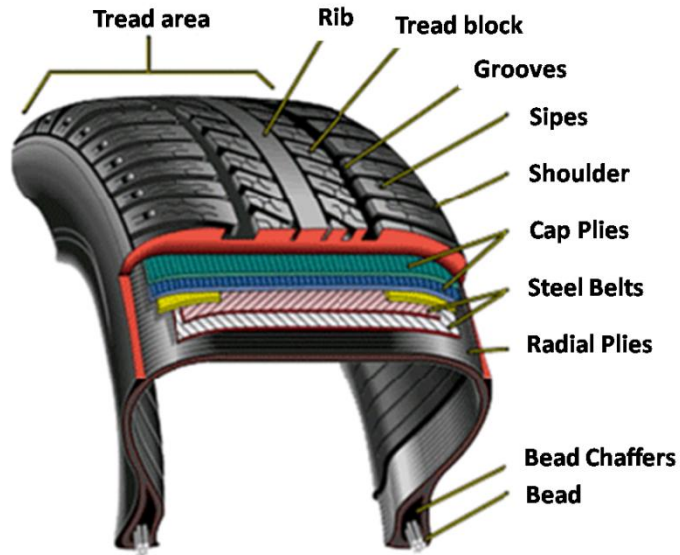
Figure 1.1 Radial tire structure

	BIAS-PLY TIRE	the tread and the sidewall share the same casing plies ↓ sidewall flexing is transmitted to the tread ↓ • rapid wear • reduced traction • high fuel consumption
	RADIAL TIRE	stable crown and larger contact patch ↓ better pressure distribution ↓ • reduced wear • comfort and handling • reduced fuel consumption

Figure 1.2.Bias-ply tire vs. radial tire [1,2]

The mechanical characteristics of tires are the main factors that determine the operating stability of vehicles, and also important characteristics that affect the brake safety and running stability of vehicles [5]. Tire performing features can be broadly modulated by varying the orientation of cord-rubber plies. The crown angle is defined as the angle between the path of the cords into a layer and the circumferential center line of the tire. The bias-ply and the radial tires are the main constructions (Figure 1.2). In the bias-ply tire, the crossed layers of ply cord run diagonally to the tread (i.e. half of the layers have the cords at a positive crown angle and half at a negative angle, and is generally lower than 38°). In the radial tire all of the cord plies lay at 90 degrees to the direction of travel and across the tire from lip to lip. This design avoids having the plies rub against each other as the tire flexes, reducing the rolling friction of the tire. This allows vehicles with radial tires to achieve better fuel economy than vehicles with bias-ply tires. However, in the radial tire several layers of cords fitted on the top of the carcass under the tread (the so-called 'braker'), laying at various angles (~20°), which are essential for the stability of the tire itself. In fact, the breaker provides rigidity to the tread against the distortions in the lateral direction that are set up during cornering, hence reducing tread wear under this condition of use.

1.3 Cord-rubber composites

As mentioned in the previous paragraph, the most important structural element of the tire is the carcass. The layers of flexible cords embedded into the rubbery matrix are a typical example of *flexible matrix composites*, i.e. composite materials made up of an elastomeric matrix and a continuous, unidirectional reinforcement. Flexible matrix composites (FMCs) utilize the high elongation capability of elastomers to withstand large strains in the direction transverse to the fiber reinforcement while retaining strength and stiffness in the longitudinal direction [6]. FMCs are highly anisotropic and can therefore be tailored to achieve distinctive mechanical characteristics that are difficult to obtain using conventional rigid matrix composites. Also, because of the viscoelastic nature of elastomeric matrix materials, FMC materials have higher internal damping than comparable conventional rigid matrix composites. The development of flexible composites has its own origins in car industry but nowadays it finds several applications in a wide variety of fields (V-belt and muscle actuators are typical examples of the application of flexible composites in modern technologies)

[6,7]. Important experimental studies based on the characterization of the static and dynamic response of FMCs have been performed by Krey et al. [8] and by Kuo et al. [9] and Chou (1989) [6], also highlighting the critical aspects of the testing of these materials, mainly due to the coupling of a highly compliant matrix with a more rigid reinforcement. When the flexible matrix consists of rubber compounds and the reinforcement is made up of steel wires or polymer textiles (cords), the FMC is named cord-rubber composite. It is the properties of the anisotropic rubber cord composite that primarily control the overall performance characteristics of a pneumatic tire. The low modulus, high elongation rubber contains the air and provides abrasion resistance and road grip; the high modulus, low elongation cords provide reinforcement for the rubber and carry most of the loads applied to the tire in service [1].

According to Walter [10], the first quantitative study of cord-rubber lamina elastic properties, in tire industry, was published in Germany in 1939 by Martin who analysed bias-ply aircraft tires using thin shell theory to approximate toroidal tire behaviour. However, the most important activity on these materials began 20-25 years later: Clark [11] in the USA, Akasaka [12] in Japan, Gough [4,13] in Great Britain and Biderman [14] in Soviet Union are the pioneers in this specific field. Clark's work represents the apex of the intense experimental and theoretical studies performed in 20th century on cord-rubber composites and on the overall behaviour of the tire.
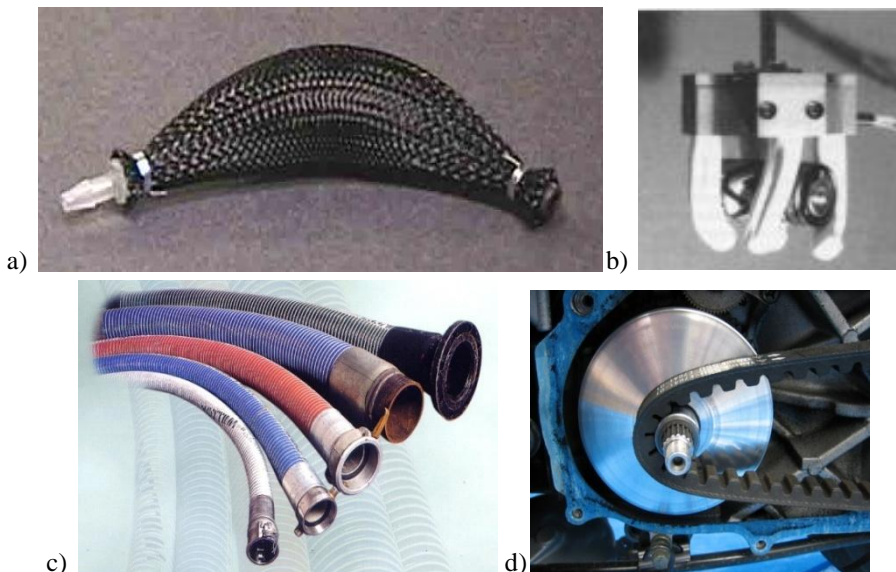
Figure 1.3 Typical applications of flexible matrix composites:
a) muscle actuators, b) robotic finger, c) hose, d) V-belt)

Details on these theoretical approaches adopted to model the mechanical response of cord-rubber composites can be found in Chapter 3.

Cord-rubber composite strongly differ from conventional rigid matrix based composites (e.g. carbon fiber/epoxy composites) [11]. First of all, in rigid composites, reinforcement consists of small filaments (such as graphite or glass) that are well dispersed into the composite or with particular arrangements. In cord-rubber composite, reinforcement has a twisted structure, being responsible of coupling between axial tension and torsion of cross-sectional area. Furthermore, in rubber cord composites, reinforcement volume fractions (10-40%) are relatively low compared to those employed in rigid filamentary composites (more than 50%). This apparently low content arises because a certain amount of rubber insulation is needed between cords in the same ply (interply) and between cords in adjacent plies (interply) to avoid friction between cords and to promote adequate fatigue resistance of the tire in service.

In order to analyze the behavior of cord-rubber composite, it is of paramount importance to have a complete comprehension of the role these materials play as structural part into the tire and of the materials the composite consists of, i.e. matrix and cords.

As will be described in the following section, the reason why rubber cord composites are employed in the construction of tires can be found in the geometrical requirement demanding for the ability to deform from a surface of double curvature to a plane surface, whereas the contact tire/ground arises.

1.4 Why cord-rubber composites: an overview on mechanism of load carrying in tire

The pneumatic tire presents a challenging stress analysis problem. It is a pressurized membrane structure of revolution reinforced by a network of cords that lay at an angle to the circumferential direction. The cords are folded around a rigid hoop of steel wires, which anchors the tire to the rim.

The simplest approach is the static inflated and deflected analysis that is generally performed on the base of membrane structures mechanics. In fact, the problem of the contact tire/ground can be reduced to the case of a toroid in contact with a flat surface [1].

In an undeflected tire, the cords are tensioned by the excess pressure exerted by the inflating gas over the external pressure (atmosphere pressure). The equilibrium shape of the carcass is essentially determined by cord paths and, as

the tire is pressed against a flat roadway, the tread is compressed and consequently the carcass loses its axial symmetry, with the development of a flattened contact patch.

If there is no tread, the carcass would become flat over the contact area with the ground. Therefore, since the cords in this area would lie in a flat plane parallel to the ground plane (i.e. the line of the cord is straight), in this region the tension in the cord bears no relation to the internal inflating pressure. Actually, on the basis of static force resolution laws, a path with an infinite radius of curvature results in zero resultant force opposing the gas pressure. The tension in the cords across the flat part on the contact patch is therefore determined primarily by the cord tension transmitted from the adjacent free wall of the tire, modified by the effect of the transition curvature around the perimeter of the flat contact patch (deradialization). It follows that the contact pressure between the tire carcass and the ground will be equal the inflation pressure, plus an extra contribution due to pressures necessary to develop the bending stresses within the transition zone (non-zero bending stiffness due to the layers of cords).
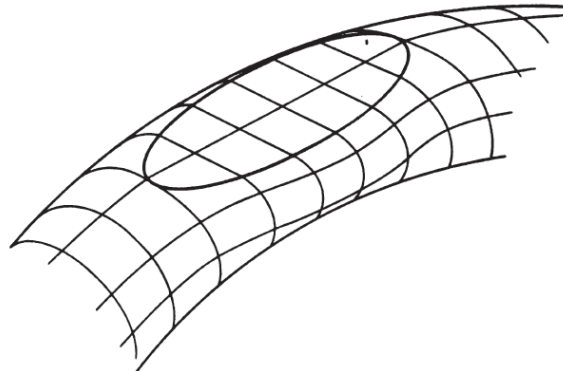
Figure 1.4 Perspective sketch of the contact patch in a toroidal shell [1]
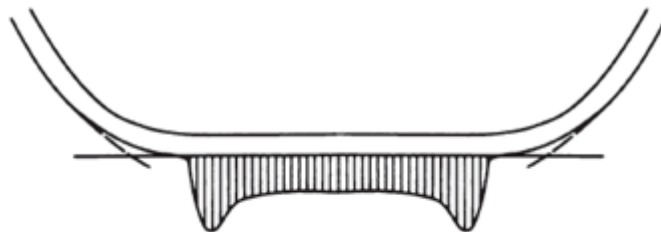
Figure 1.5 Effect of bending stiffness on contact pressure [1]

Also the presence of the tread rubber causes the actual contact pressure to be locally greater than the inflation pressure (and to differ in different parts of the contact patch). For these reasons the actual load that a tire carries is higher than the product of the inflation pressure and the overall contact area. This load must be transmitted to the wheel and this involves not only the transmission of forces between bead and rim but also the transmission through the structure, as shown in Figure 1.6. It is worthy of note to highlight that a similar distortion can be possible only if the structure itself is made up of composite layers made up of high modulus cords, embedded into a low modulus matrix. Some geometrical considerations can be useful in order to understand the way a shell structure of double curvature can deformate by developing a flat surface. In particular, let consider the inverse case, i.e. the mechanism leading to the formation of a surface of double curvature from the initial flat plane. In Figure 1.7 a schematic of a two-ply rubber cord composites is shown. One ply consists of cords lying in the direction *AB* (or, analogously, *CD*) while the cords of the second ply are parallel to *BC* (or, analogously, *DA*). If this two-ply is subjected to biaxial extension (arising from the aforementioned deforming mechanism), since cords are inextensible, in one layer the cord *AB* will move to the new position *a'b'* and, in the other layer, the cord will move from *BC* to *b''d''*. These movements are permitted by the low modulus matrix, which develops shears in order to accommodate the new cord arrangement. Actually, both for bias tires - where two layers of fabric-reinforced rubber are wrapped on a cylinder with the cords lying at opposite angles - and for the breaker (or belt) in radial tires, the cords form small parallelograms with major and minor axes in the circumferential and transverse directions. As the tire is formed into its characteristic shape, the increase in diameter causes the cords to rotate - the parallelograms extend in the circumferential direction and contract in the transverse direction. The local flattening of the surface of double curvature (final tire) involves a procedure that is reverse of the aforementioned, i.e. the problem is analogous the initial tensions are reduced during the process (instead of being increased). It is also clear that, in changing from a surface of double curvature to a plane surface, the high modulus reinforcement must bend. Flexibility is obtained by reducing reinforcement diameter and/or by using multiple strand cord in which separate filaments are thin enough to keep stresses below the permanent set and the fatigue limit.
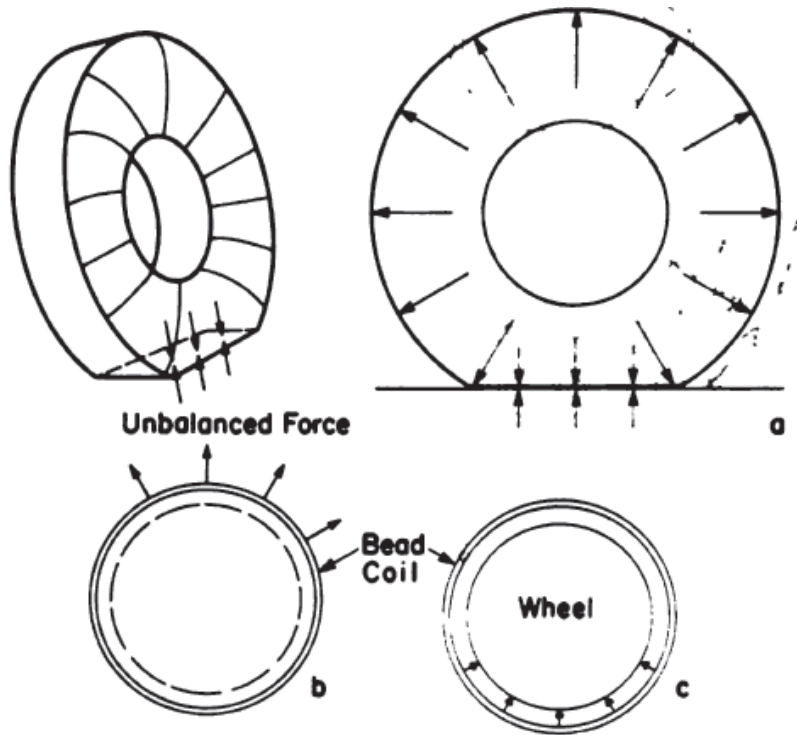
Figure 1.6 Load transfer from the ground to the wheel. (a) In the contact zone with the ground, the inflation pressure forces are transmitted by compression without producing a resultant reaction on the ring. The absence of forces on this part leaves the forces due to inflation pressure on the top sector of the band unresisted by an opposing force on the bottom sector, while at other parts of the tire outward forces have zero resultant. The resultant upward force on the upper half of the ring, causes the sidewall tensions in the upper half to be greater than the lower half (b) and this force pulls the bead coil against the base of the wheel rim above the contact area, thus transmitting the upward force to the wheel (c) [1].
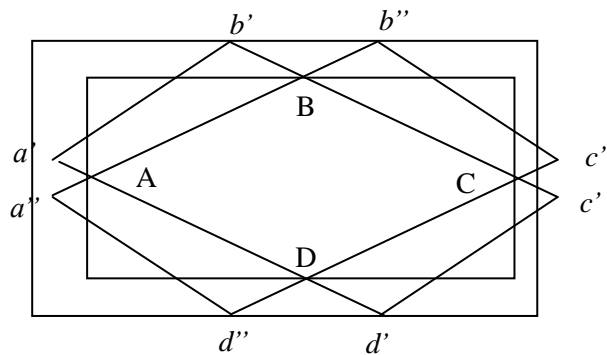
Figure 1.7 Schematic of two-ply cord-rubber composite under biaxial extension

1.5 Aim of this thesis

Historically, pneumatic tires began in Great Britain during the late 1800s as an upgrade from solid rubber tires. They had small cross-sections and high pressures, principally for bicycle applications. Tubeless tires were introduced with improvements in rim design in the early 1950s: belted bias tires became popular in the late 1960s while radial tires, first introduced in Europe, became popular in the USA starting in the early 1970s and now dominate the passenger tire market. This brief historical description infers that tire technology (and, consequently, industry) has got tremendously ahead in the last two centuries. A literature survey clearly reveals that there exists a large number of published works in journals and conference proceedings in the field of structural analysis of pneumatic tires both by computer simulation and experimental characterization [15-22]. In addition, there are also many unpublished papers in this field generated by R&D and technical departments of tire companies. Obviously the analysis of this complicated structure is still of interest to researchers and engineers involved in tire design and optimization. For instance, the response to the complex loading conditions to whom tire is subjected and the overall performance can be *ad-hoc* tailored by varying the properties and the distribution of the constituents materials into the cord-rubber layers (e.g., the different performing properties between radial and bias tires are a simple example of the way macroscopic changes in the structure may affect the final response of the tire). However, since the very complex miscellany of constitutive behaviors, geometries and the variety of loading conditions, this is not straightforward. Actually carcass modeling (and, consequently, design) is generally performed by adopting a streamlined approach, in which the single constituent unit is an orthotropic cord-rubber lamina [16,17]. This macroscopic approach neglects the phenomena that arise inside the lamina on a mesoscopic and a microscopic scale. For example, the warped nature of the reinforcement is commonly neglected although it can be indeed essential for a general understanding of some problems. In fact the mechanism responsible for the interface failure originates on a mesoscopic scale from the stress distribution within the cord and the matrix [23]; for instance, tire carcass failure is usually due either to fatigue failure of rubber close to the cord, caused by high stresses resulting from improper construction or irregular cord spacing, or to cord fatigue from excessive compressive stresses. Also local friction at the interface contributes to local tire heating [24]. Hence, a more realistic prediction is needed for the design of more performing tires. For instance, a multi-scale

investigation of cord-rubber composites may represent an innovative advance in tire technology since it can take into account more likely information about the behavior of the components and, consequently, it can provide more precise information. For this purpose, a multi-scale approach has been adopted in the experimental investigation and in the theoretical modeling of cord-rubber lamina. This activity has been carried out in collaboration with Bridgestone Technical Centre Europe (Rome), professor Costas Galiotis of Institute of Chemical Engineering and High Temperature Processes of Foundation of Research and Technology of Hellas (Patra, Greece) and with professor Massimiliano Fraldi of Department of Structural Engineering of University of Napoli Federico II.

In particular, the mechanical response of cord-rubber composite and of constituents (matrix compound and polymeric cords) has been investigated on both a macroscopic and a microscopic scale. Regarding the experimental characterization, the macroscopic response of the lamina has been investigated by means of tensile test (both static and dynamic) and has been discussed in the light of the well established approaches based on the rule of mixtures [10]. Nevertheless, tensile test do not provide any information on the mechanism by which the two phases contribute to lamina response. Hence a microscopic investigation has been carried out by micro Raman spectroscopy that has been found to be a very powerful tool for the study of micromechanics of composites [25]. First of all, this technique allows for the investigation of molecular deformation processes of polymers [26], leading to a detailed analysis of the structure-property relationships of fiber reinforcement. In particular, corded reinforcement has been closely examined, by evaluating the contributions of single filaments to the response of the overall structure. In addition, micro Raman spectroscopy is a reliable, well-established and nondestructive testing methodology for composite micromechanics since reinforcement can be actually adopted as a strain or stress sensor embedded into the composite. Hence the micromechanical response of the composite has been investigated, by determining several parameters that govern stress transfer (e.g. characteristic transfer lengths).

Besides the experimental characterization, a new multi-scale, three-dimensional finite element model of the cord-rubber lamina, based on a hybrid analytical/numerical approach, has been developed in collaboration with professor Fraldi. Unlike the aforementioned orthotropic approach that are commonly adopted in modeling unidirectional laminae, the capability of this model relies on the possibility of simulating the tension-twisting coupling of the

cord and, in turn, of the overall composite, which determines a peculiar stress state in the interfacial zone. Cord behavior has been first modeled by using Costello's analytical model [27], which accounts for tension-twisting coupling and relates the cord constitutive behavior to the hierarchical structure of the cord itself. On the basis of this analytical model, a homogenized cylindrical model of the cords has been implemented in the FEM code, incorporating the relevant mechanical features of the aforementioned cord analytical model. Finally, the overall mechanical model for the composite has then been implemented by embedding the hybrid cord model in a FEM pad for the rubber matrix. Both the rubber matrix and the polymeric cord have been modelled as non-linear hyperelastic materials. The information collected at experimental stage on the behavior of rubber and cord has been a matter of high importance for modeling. Due to the detailed information obtained on a multi-scale approach, this work hence represents a significant step forward beyond the current state of the art in cord-rubber analysis.
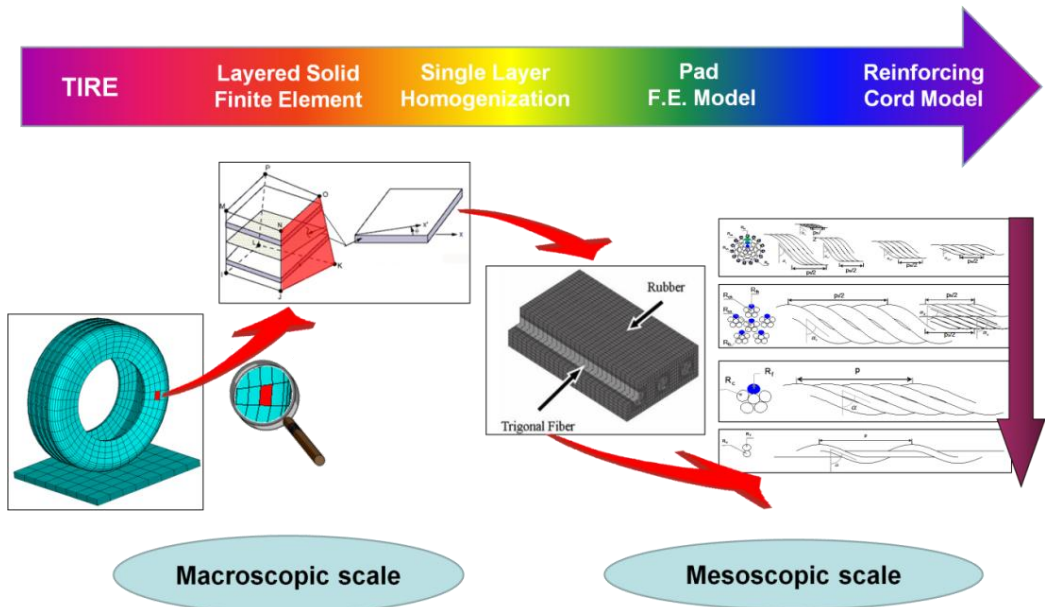
Figure 1.8 Multi-scale approach in tire modeling

An insight into the constituents of cord-rubber composites

2.1 Introduction

Composite materials are engineered or naturally occurring materials made up of two or more constituent phases with significantly different physical or chemical properties which remain separate and distinct at the macroscopic or microscopic scale within the finished structure. The constituents are divided into two categories, namely matrix and reinforcement, and a synergism produces properties unavailable from the individual materials. The matrix surrounds and supports the reinforcement materials by maintaining their relative positions and guarantees the cohesion of the material itself. The reinforcement offers mechanical and physical properties to enhance the matrix properties. In flexible composite, furthermore, matrix and reinforcement must guarantee the flexibility of the final composite. As stated previously, this can be obtained with a rubbery matrix and a corded reinforcement. In this Chapter, a detailed description of the main chemico-physical features of matrix and the reinforcement is given. Furthermore, adhesion and cord-rubber manufacturing process are described.

2.2 Elastomeric matrix: rubber compound

The matrix of cord-rubber composite is a compound mainly made up of vulcanized rubber and particulate filler. The detailed description of the composition, the physical properties and the manufacture process of the matrix are reported in the following.

2.2.1 Compound composition and preparation

The elastomer is the main ingredient of the compound. According to the ASTM Standards Definitions [28], an elastomer is 'a natural or synthetic polymer which at room temperature can be stretched repeatedly to at least twice its original length and which after removal of the tensile load will immediately and forcibly return to approximately its original length'. It is usually made from a mixture of materials (solid or liquid) and in most cases the base polymer is crosslinked by either chemical or physical links [29]. SBR (styrene-butadiene rubber), BR (polybutadiene rubber), NR (natural rubber or 1,4 cis poly-isoprene) are the most used elastomers in tire applications. However, for more than a century, only natural rubber obtained from 'Hevea braxiliensis' was used. Rubber was obtained by the precipitation of rubber latex (i.e. an aqueous suspension of rubber particles - mainly made of $(C_5H_8)_n$ hydrocarbons - with a diameter from 0.1 to 1.0 µm). However, this form was sticky, used to lose elasticity and harden at low temperatures. These negative features were overcome with the vulcanization process, invented by Goodyear in 1839; this process consists in a chemical reaction with sulfurs that leads to the crosslinking of rubber macromolecules [30]. In fact, a key feature of sulfurs is the ability in forming thermodynamically stable chains. The common, thermodynamically stable form of sulfur at ambient conditions is the orthorhombic α-sulfur. As a consequence of the sulfur ability for catenation, rhombic sulfur is made of 8 sulfur atoms in a packed ring structure (Figure 2.1). The main steps in vulcanization reaction are:
- sulfur (in the form α) dissolution into rubber;
- ring splitting, i.e. sulphur is activated for vulcanization (activation occurs thanks to temperature and/or is promoted by bases, mercaptans, metal oxides and accelerators);
- reaction of sulfur with reactive sites present in the elastomer.
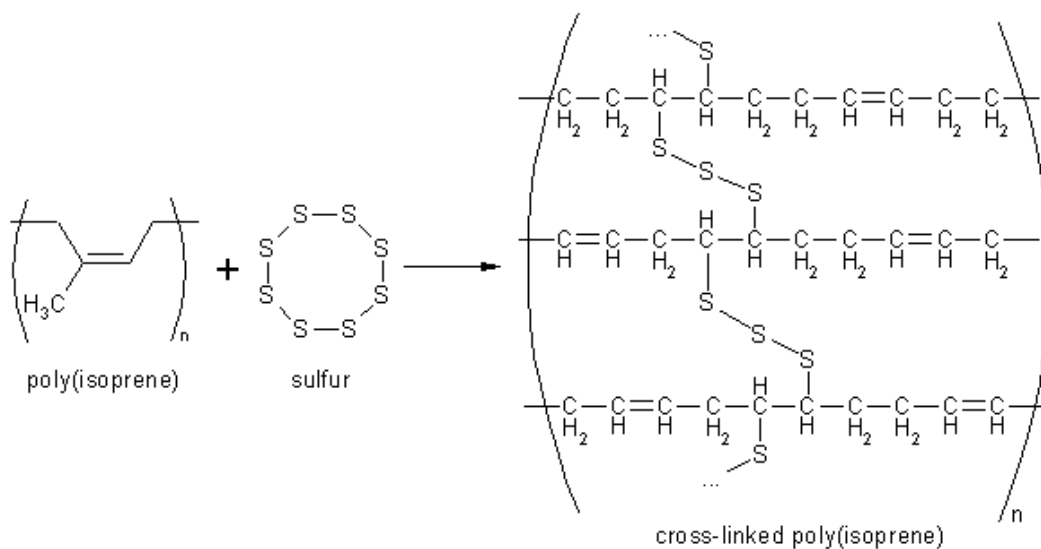
Figure 2.1 Vulcanization of poly(isoprene)

Hence the chemical vulcanization system is another important part of the compound. Sulfur, zinc oxide and vulcanizing accelerators are the main ingredients of this sub-system.

The elastomer is filled with several particles (i.e., carbon black, silica) that create a tridimensional network into the matrix itself, improving mechanical properties and abrasion resistance. The presence of carbon black is responsible of a peculiar non-linear behavior of rubber compounds, under both static and dynamic stimuli, known as Mullins and Payne effects [31-37].

Softeners, plasticizers (oils, resin and waxes) are added to the compound in order to enhance the manufacturing process and chemical protective agents (antioxidants, antiozonants) are used to protect the compound from ambient conditions.

With such a variety of ingredients, the main properties for a given tire compound can be usually obtained from a number of different compositions. For example, modulus and hardness can be tailored by varying the amount, the fineness and the structure of the carbon black, the amount of softener, or the degree of crosslinking. As a practical example, we can consider that in winter tires - that designed to provide improved performance under low temperature conditions - the tread compound is usually softer than that used in tires for summer conditions, thus providing better grip on ice and snow; however it wears more quickly at higher temperatures.

The manufacturing process of a rubber compound is divided into several steps: compounding, mixing, milling.

Compounding is the operation of bringing together all the ingredients required to mix a batch of rubber compound. Each component has a different mix of ingredients according to the properties required for that component.

Mixing is the process of applying mechanical work to the ingredients in order to blend them into a homogeneous substance. Internal mixers are often equipped with two counter-rotating rotors in a large housing that shear the rubber charge along with the additives. The mixing is done in three or four stages to incorporate the ingredients in the desired order. The shearing action generates considerable heat, so both rotors and housing are water-cooled to maintain a temperature low enough to assure that vulcanization does not begin.

After mixing, the rubber charge is dropped onto an open rubber mill batchoff system. A mill consists of twin counter-rotating rolls, one serrated, providing additional mechanical working to the rubber and producing a thick rubber sheet. The sheet is pulled off the rollers in the form of a strip. The strip is cooled, dusted with talc, and laid down into a pallet bin.

The ideal compound at this point would have a highly uniform material dispersion; however in practice there is considerable non-uniformity to the dispersion. This is due to several causes, including hot and cold spots in the mixer housing and rotors, excessive rotor clearance, rotor wear, and poorly circulating flow paths.

The milled, green rubber is so ready for the component preparation (by extrusion, calendering) and, after assembling, it is subjected to the curing process (i.e. applying pressure to the green tire in a mold in order to give it its final shape, and applying heat energy to stimulate the chemical reaction between the rubber and other materials).

2.2.2 Mechanical properties of rubber compounds

The physical properties of any rubber compound depend on the state of cure [38], which is upon how far the vulcanization reaction has been carried. The crosslinked network is very important in defining the final physical properties and is determined, for a given rubber compound, by vulcanization time and temperature.

Vulcanization process is objectively represented by vulcanization curves (Figure 2.2). The curves allow the determination of optimum production-related technical conditions and the exact compounds control. These curves are determined by using the vulcameters, which automatically record the whole

vulcanization curve for each single specimen; this curve represents the dynamic shear modulus of cyclically stressed test specimen during vulcanization.

Initially, there is a sudden increase in torque, as the chamber is closed. Then, as the rubber is heated, viscosity decreases resulting into a torque decrease. As the vulcanization proceeds, rubber becomes an elastic solid, and the torque rises. If the torque reaches the plateau, the curve indicates that curing is completed and a stable network has been formed. If chain scission and/or crosslink breakage is dominant, the torque starts decreases ('reversion').

The nature of the crosslinks is technically important because they cannot be too numerous, or flexibility of the network will suffer, but their number must be adequate to suppress plastic flow. The effect of cure on the physical properties of a rubber compound is generally evaluated by vulcanizing a series of sheets for different times at the same temperature; this procedure can be then repeated also at several temperatures in order to have a more complete description of the dependence from the two operating variables. From these sheets, dumbbell-shaped specimens are cut and static tensile tests are performed, according to international standards [39]. As shown in Figure 2.3, a stress-strain curve of a vulcanized rubber is highly non-linear: in particular, it is concave toward the strain axis at low strains and concave toward the stress axis for higher strains (strain hardening). The concavity is accentuated by the occurrence of stress-induced crystallization at higher elongations. There is no yield point before failure. Volume changes are negligible [40] and the Poisson's ratio is assumed to be 0.5. It is well known that the elastic modulus of polymeric materials falls down with temperature; however, rubber shows an inverse trend. In fact, in the transition range from glassy to the rubber state, modulus falls rapidly with increasing temperature but further temperature increase results in a slowly rising modulus. This rise was first observed by Gough in 1805, as a contraction of stretched rubber specimens when they were heated. Lord Kelvin gave a thermodynamic interpretation of the so-called 'thermoelastic inversion', explained on the bases of the entropic origin of rubber elasticity [30]. Further details of this phenomenon will be given in the following paragraph.
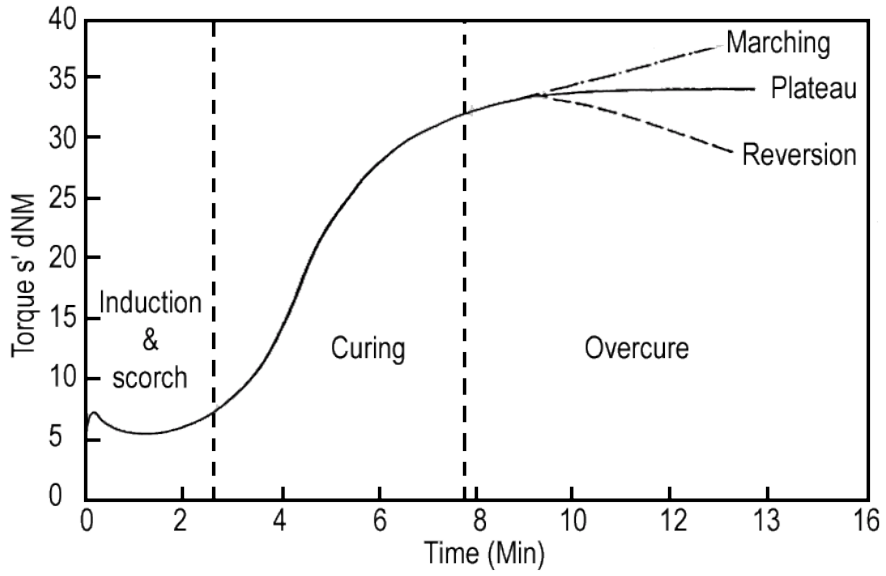
Figure 2.2 A typical example of vulcanization curve
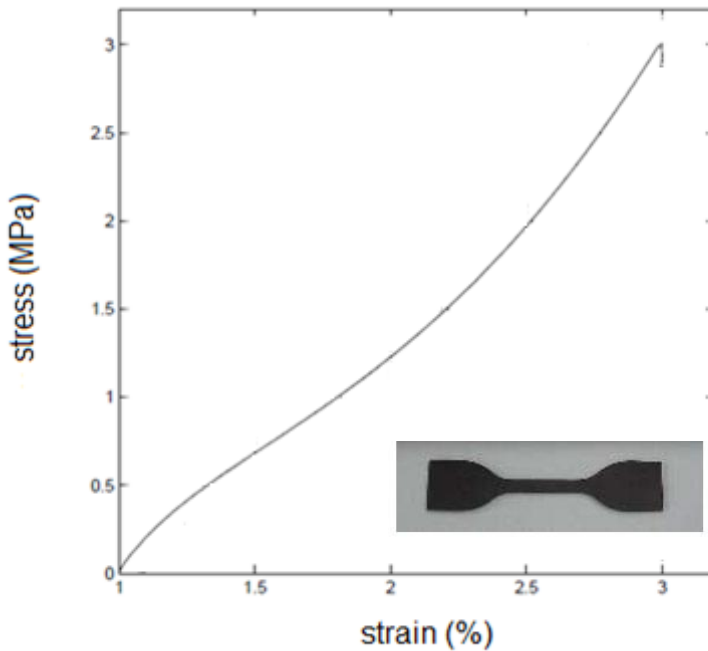
Figure 2.3 Stress-strain curve obtained from tensile test on a dumbbell specimen (in the inset)

2.2.3 Rubber elasticity

The high extensibility and the low Young modulus (order of a few MPa), coupled with the thermoelastic behavior, could not be explained on the basis of molecular cohesion. Only macromolecular science could provide for the understanding of these phenomena, and rubber behavior could be interpreted on the basis of the ideal chain statistics, phenomenological approaches and of continuum mechanics.

The basic features of the stress-strain behavior have been initially modeled by statistical mechanics approaches of rubber elasticity, as well described by Treloar in an excellent review [30].

Let's consider a structure of randomly-oriented long molecular chains; in the Gaussian approach, the distribution of the end-to-end length, *r*, of a chain is given by *P(r)*:

$$P(r) = 4\pi \left(\frac{3}{2\pi n l^2}\right)^{3/2} r^2 exp\left(\frac{3r^2}{2nl^2}\right) \tag{2.1}$$

where n and l are the number and the length of links.

The average initial length, termed L_o, is given by:

$$L_o = (\overline{r^2})^{1/2} = (nl^2)^{\frac{1}{2}} = \sqrt{n}\, l \tag{2.2}$$

The application of a deformation induces the stretching of the chain structure and a entropy decrease. If the assembly of N chains is deformed by a principal stretch state $(\lambda_1, \lambda_2, \lambda_3)$, without approaching the fully extended length *nl*, the elastic strain energy function *W* can be derived directly from the change in configurational entropy:

$$W = \frac{1}{2}NkT(\lambda_1^2 + \lambda_2^2 + \lambda_3^2 - 3) = \frac{1}{2}G(\lambda_1^2 + \lambda_2^2 + \lambda_3^2 - 3) \tag{2.3}$$

where k is Boltzmann's constant and T is absolute temperature. G is the modulus of rigidity which depends on chain molecular weight through the relation

$$G = NkT = \rho RT/M_c \tag{2.4}$$

where ρ is the density of the rubber and M_c is the number-average network chain molecular weight.

In this approach, the deformation is assumed not to be accompanied by any change in internal energy and the work of deformation is simply equal to $-T\Delta S$. In case of simply extension, a single extension ratio λ, with equal contractions in the transverse dimensions, can be used. The condition for constancy of volume requires that

$$\lambda_1 = \lambda \text{ and } \lambda_2 = \lambda_3 = \lambda^{-1/2} \qquad (2.5)$$

Hence the elastic strain energy function becomes

$$W = \frac{1}{2} NkT(\lambda^2 + \frac{2}{\lambda} - 3) \qquad (2.6)$$

If we assume that the specimen - in the unstrained state - has the shape of a cube with a unit edge length, we can calculate the force per unit unstrained cross-sectional area (engineered stress) as

$$\sigma = NkT\left(\lambda - \frac{1}{\lambda^2}\right) = G\left(\lambda - \frac{1}{\lambda^2}\right) \qquad (2.7)$$

This equation predicts that, at small strains, stress is linearly proportional to strain (Hookean). At higher strains, however, the behavior becomes non-linear (commonly referred as neo-Hookean behavior).

In particular, in the light of this first approach for rubber elasticity, it is possible to elucidate the aforementioned phenomenon termed thermoelastic inversion (Figure 2.4). In fact, the thermodynamics treatment demonstrates that the force necessary to elongate a sample of rubber at a constant length is proportional to the absolute temperature[1]. According to Treloar, [30] several experimental showed that this conclusion holds approximately for natural rubber at fairly high extensions. At low extensions, however, the tension rises less rapidly with

---

[1] According to the first and second laws of thermodynamics, the deformation of an elastic system involves changes in both internal energy and entropy which are related by:

$$\left(\frac{\partial U}{\partial L}\right)_T = F + T\left(\frac{\partial S}{\partial L}\right)_T = F - T\left(\frac{\partial F}{\partial T}\right)_L$$

The derivative $(\partial U/\partial L)_T$ vanishes for ideal elastic systems, which, in the case of rubberlike materials, means that the polymer chains can rotate freely and its internal energy U does not change with conformation, analogously to the case of an ideal gas, where the absence of molecular forces implies that its internal energy does not change with volume.
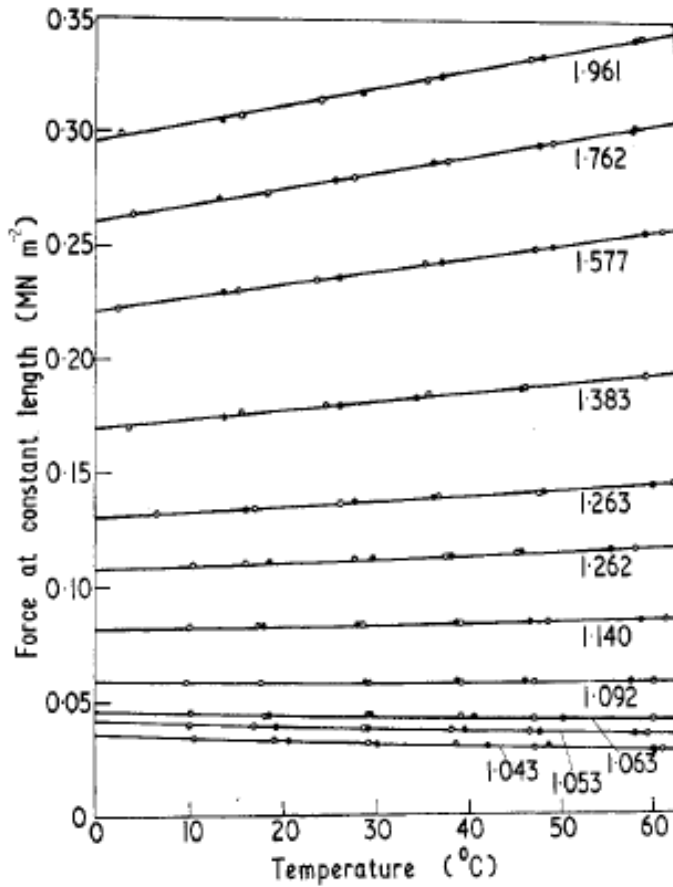
Figure 2.4 Thermoelastic inversion [30]

increase in temperature, and for extensions of less than 10% it actually decreases. Actually, this phenomenon arises from the small variations of volume which accompany a change of temperature or the application of a force. On a thermodynamic scale, those variations are very significant. For instance, it is straightforward to demonstrate that an increase of temperature, by increasing the volume (and hence the unstrained length of the sample), will reduce the strain at constant length. This can lead to a reduction of stress, although the modulus (*NkT*) increases. Accordingly, the Eq. (2.7) can be expressed for small strains as by

$$\sigma = NkT\varepsilon \qquad\qquad (2.7a)$$

where ε is the strain defined as $\lambda - 1$ and that can be also expressed as

23

$$\varepsilon = \varepsilon_o - \frac{\beta}{3}(T - T_o) \qquad (2.8)$$

where ε_o is the strain at an arbitrary reference temperature T_o and β is volume expansivity. By substituting (2.7a) into (2.8), the strain at which the inversion appears (corresponding to changes in sign of temperature coefficient of the stress $(\partial F/\partial T)_L$) is found to be

$$(\varepsilon_o)_{invers} = \frac{\beta}{3}(2T - T_o) \qquad (2.8a)$$

Insertion of typical values, for example, $\beta = 6.6 \times 10^{-4}$, $T_o = 293$ K and T = 343 K, Eq. (2.8a) gives $(\varepsilon_o)_{invers} = 0.088$, or 8.8%, which is sufficiently close to the observed value.

Because rubber is highly extensible, small-strain elasticity theory is inadequate to describe the response to large strains because, as the chain extension approaches this limiting value, the Gaussian distribution model becomes increasingly inaccurate. Hence, at deformations where r begins to approach nl, the non-Gaussian nature of the chain stretch must be taken into account. It is possible to derive a relation between the force f on a single chain and the distance r between its ends which is valid over the whole range of extension and that is based on the Langevin chain statistics [41-43].The resulting non-Gaussian force-extension relationship for a chain is given by

$$f = \frac{kT}{l}\mathcal{L}^{-1}(\frac{r}{nl}) \qquad (2.9)$$

in which $\mathcal{L}^{-1}$ is the inverse Langevin function, defined as follows:

$$\frac{r}{nl} = coth\beta - \frac{1}{\beta} = \mathcal{L}(\beta)$$

$$\beta = \mathcal{L}^{-1}(\frac{r}{nl}) \qquad (2.10)$$
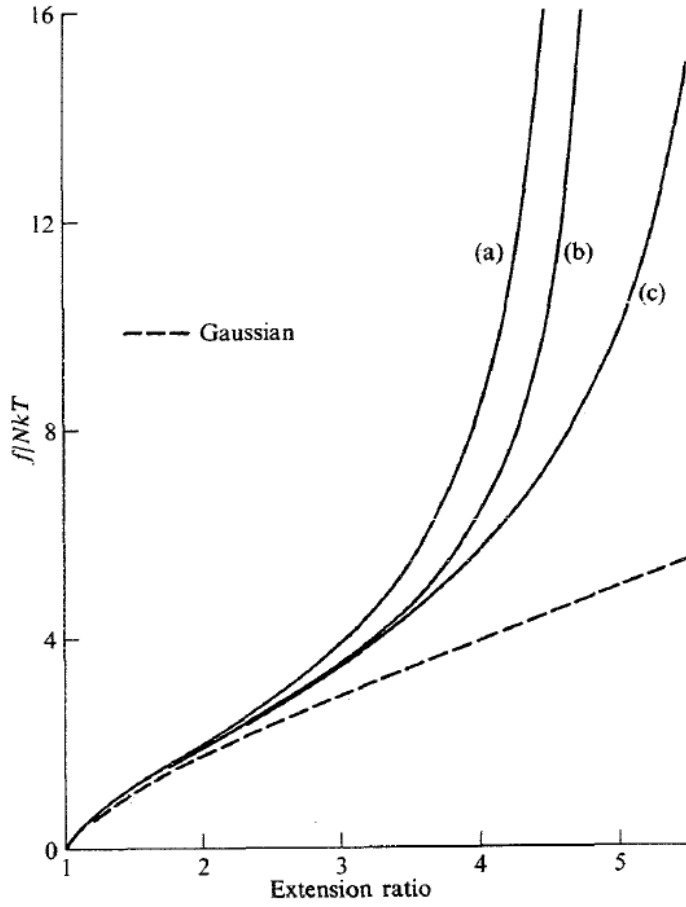
Figure 2.5 Comparison between force-extension curves:
gaussian form (broken curve), non-gaussian models (A-B-C) [30]

Another important approach in describing rubber elasticity is the invariant-based continuum mechanics treatment, mainly developed by Mooney [44] and Rivlin [45]. For an isotropic, hyperelastic material, the strain energy density depends on stretch via one or more of the three invariants, I_i, of the stretch tensor:

$$I_1 = \lambda_1^2 + \lambda_2^2 + \lambda_3^2$$
$$I_2 = \lambda_1^2 \lambda_2^2 + \lambda_2^2 \lambda_3^2 + \lambda_1^2 \lambda_3^2 \qquad (2.11)$$
$$I_3 = \lambda_1^2 \lambda_2^2 \lambda_3^2$$

Because rubber is virtually incompressible, the product $\lambda_1\lambda_2\lambda_3 = 1$ and I_3 does not contribute to the strain energy. Rivlin proposed a general expression for W, as

$$W = \sum_{i,j=0}^{\infty} C_{ij} \, (I_1 - 3)^i (I_2 - 3)^j \tag{2.12}$$

where C_{ij} are material parameters. The simplest form we can derive is

$$W = C_{10}(I_1 - 3) \tag{2.13}$$

that is the neo-Hookean model.
If also the second term is kept, the Mooney-Rivlin model is obtained:

$$W = C_{10}(I_1 - 3) + C_{01}(I_2 - 3) \tag{2.14}$$

The discussed models, both based on the statistical mechanics of the chain and on the invariant-based continuum mechanics, are the simplest approaches in treating rubber elasticity. Then a variety of models have been implemented in the last 60 years, providing several constitutive laws that model elastic behavior of rubber more accurately than the simple neo-Hookean, by taking into account other phenomena, such as the stiffening observed at high strains [46-50].

2.2.4 Rubber viscoelasticity

The time dependent behavior of rubber compounds, the so-called viscoelastic behavior, is very important for tire performance. In fact, tire deflections occur so rapidly that equilibrium conditions are not approached for rubber deformations in tires. For instance, the frequencies that the tread can experience in service are of the order of magnitude of some MHz [2]. In general, rubber viscoelasticity becomes evident in a dependence of mechanical properties on rate of deformation, on time-deformation history and on temperature. For a tire in service, typical processes that dominated by viscoelastic properties are tensile and tear strength mechanisms and abrasion. Many studies have been performed on the viscoelastic properties of rubber compounds: creep and stress relaxation tests have been performed under several ambient conditions (e.g different

temperatures) [51,52]. Figure 2.6a shows a diagram illustrating the delayed response of a rubber in a creep test, where a sample is loaded with a constant weight: the response starts with an initial rapid deformation, followed by a slow and gradual approach to the equilibrium deformation. Figure 2.6b shows a stress relaxation curve for and SBR tread type compound, where a specimen is subjected to a constant compression; in particular, it has been found that stress relaxation at moderate temperature is largely a physical phenomenon while at elevate temperatures it is usually associated with chemical changes such as oxidation and degradation.
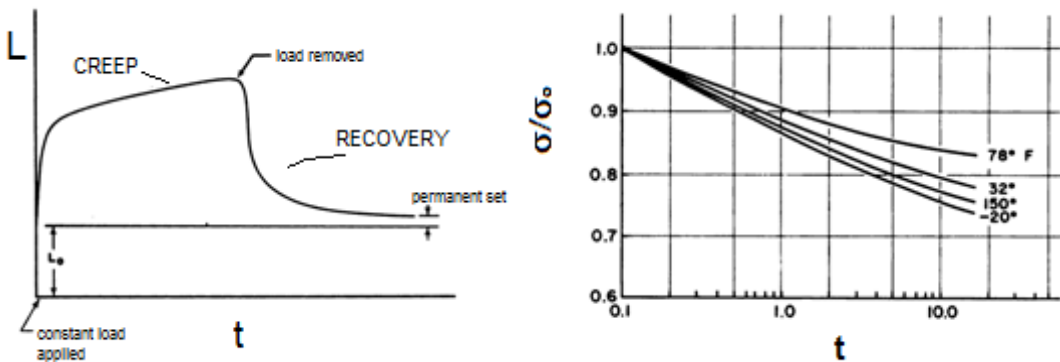
Figure 2.6 Creep (a) and compressive stress relaxation for SBR tread compound [1]

The molecular basis for rubber viscoelasticity lies in viscous forces acting on the segments of a chain molecule as they move in response to an applied stress. Each segment is essentially drawn through a very viscous medium consisting of its neighbors, so that its motion is retarded and an appreciable time is required to adjust to a stress. Semiquantitative calculations based on such a molecular picture show that it is essentially correct [53]. However, the mathematical theory of linear viscoelasticity can be presented by a simple analysis of ideal spring-dashpots models that represent, respectively, the elastic and the viscous components of the response of the material to stress. These models are well-established for transient tests: for stress relaxation, which is a decay of stress at a constant applied strain, it is convenient to model the material with a large number of Maxwell elements in parallel; while for the description of creep, Voigt-Kelvin elements in series are advantageous (Figure 2.7)

Figure 2.7 Maxwell (left) and Voigt-Kelvin (right) models

If the material does not display a linear viscoelastic behavior, such models cannot be expected to cover a wide range of behavior. In particular, the adoption of a number of elements may be then used to describe the system (e.g. the Maxwell–Wiechert model), giving rise to a distribution of relaxation times. When the mathematical approach described above is carried to the limit for a continuous distribution of relaxation times, the distribution function is known as the relaxation spectrum of the material.

Creep and stress relaxation are fundamental test adopted for the investigation of viscoelasticity and are convenient for studying material response at long times (minutes to days), but less accurate at shorter times (seconds and less). Dynamic tests, in which the stress (or strain) resulting from a sinusoidal strain (or stress) is measured, are often well-suited for filling out the 'short-time' range of polymer response. In particular, in the specific case of a tire in service, the system is subjected to a cyclic deformation, since the solicitation occurs in a cyclic manner [2].

When a viscoelastic material is subjected to a sinusoidal stress, a steady state will eventually be reached in which the resulting strain is also sinusoidal, having the same angular frequency but retarded in phase by an angle δ; this is analogous to the delayed strain observed in creep experiments. The strain lags the stress by the phase angle δ (Figure 2.8). If the origin along the time axis is selected to coincide with a time at which the strain passes through its maximum, the strain and stress functions can be written as:

$$\varepsilon = \varepsilon_o \cos \omega t \tag{2.15}$$

$$\sigma = \sigma_o \cos(\omega t + \delta) \tag{2.16}$$

It is convenient to write the stress function as a complex quantity σ^* whose real part is in phase with the strain and whose imaginary part is 90° out of phase with it:

$$\sigma^* = \sigma'_o \cos \omega t + i\, \sigma''_o \sin \omega t \tag{2.17}$$

It is hence useful the introduction of the 'rotating vector' (ω is the frequency) for the representation of stress and strain in the complex plane (inset Figure 2.8). This vector permits to develop the relations between the various parameters in harmonic relations:

$$\tan\delta = \sigma''_o / \sigma'_o \tag{2.18}$$

$$|\sigma^*| = \sqrt{(\sigma'_0)^2 + (\sigma''_0)^2} \tag{2.19}$$

$$\sigma'_o = \sigma_o \cos \delta \tag{2.20}$$

$$\sigma''_o = \sigma_o \sin \delta \tag{2.21}$$

By using this complex form of the stress function to define two different dynamic moduli, both being ratios of stress to strain as usual but having very different molecular interpretations and macroscopic consequences. The 'real' or 'storage' modulus is defined as the ratio of the in-phase stress to the strain:

$$E' = \sigma'_o / \varepsilon_o \tag{2.22}$$

The other is the 'imaginary' or 'loss' modulus, defined as the ratio of the out-of-phase stress to the strain:
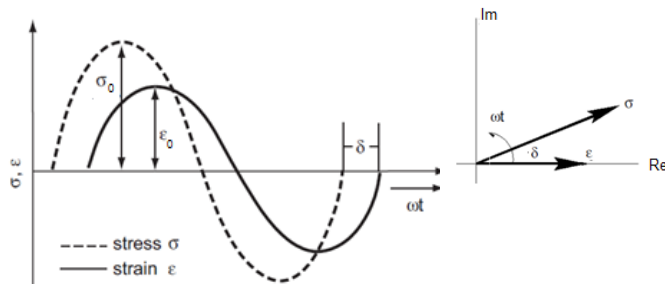
$$E'' = \sigma''_o / \varepsilon_o \tag{2.23}$$

Figure 2.8 Sinusoidal oscillation and response of a linear viscoelastic material. Inset: rotating vector

2.2.5 Reinforcement of rubber with carbon black – Inelastic behavior

In order to get better physical and processing properties, several additives are added to rubber. Particulate fillers, for instance, can increase the strength of an amorphous rubber more than 10-fold. However, in order to cause a significant reinforcement, filler must possess a high specific surface area. Structure and surface chemistry also play important roles in reinforcement mechanism. The most effective reinforcing fillers for rubber are carbon black and silica, produced with a primary particle size of 100 Å. These types of particles also aggregate into irregular structures that are characterized by a large amount of void volume (within the pervaded space), in which rubber macromolecules can be 'occluded'. The overall combination of occluded rubber and filler aggregate is a reinforcing entity, resulting into an increase of the effective volume fraction of filler. Rubber and carbon black also become chemically linked, by shear mixing. In fact, if the filled and yet uncrosslinked compound is tried to be dissolved into a good solvent, only a portion of rubber dissolves, leaving a 'carbon gel'. This gel consists of carbon black and of 'bound rubber', which is the remainder of the rubber which is strongly bound to the filler itself [54] (Figure 2.9).

The use of fillers induces an increasing of modulus, of strength and of abrasion resistance. Furthermore, besides enhancing these properties, carbon black also improves processability by reducing melt elasticity. This means that shaping operations, such as extrusion and calendaring, occur with less shrinkage and melt distortion. However, highly-filled rubber compounds are seriously inelastic, in a peculiar way. In fact, they are softened by straining, and softened more the greater the pre-strain is, as shown schematically in Figure 2.10a. Thus, the original stress-strain relation is not reproducible unless the sample is allowed to recover by resting for several months, or annealed by heating for an hour or so at temperatures of 100°C or higher. This large effect of strain history on the mechanical behavior is named the 'Mullins' effect [31-33] and seems to be due to slipping of rubber molecules over energy barriers on the surface of filler particles or becoming detached from the filler surface.
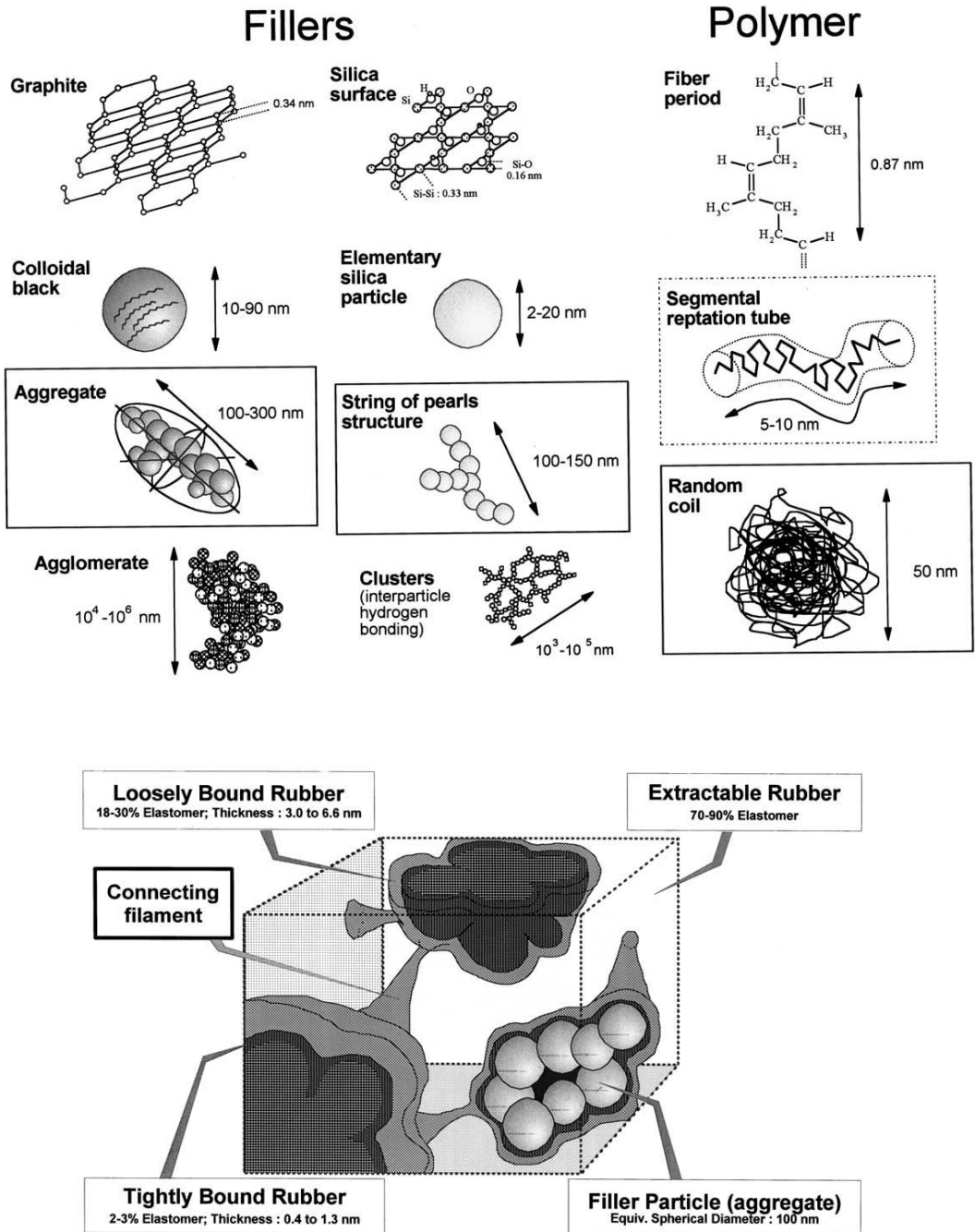
Figure 2.9 Schematic description of the morphology of fillers, rubber and of carbon black filled rubber compound [54]

A similar effect can be observed when filled rubber undergoes quite small cyclic strains, generally in the range 0.1-10%. Storage modulus is then found to decrease dramatically over this range of dynamic strain amplitude (DSA), as shown in Figure 2.10b. Again, although partial recovery occurs almost immediately on returning to small deformation amplitudes, complete recovery takes months of rest unless the sample is heated to accelerate the recovery. This softening phenomenon was observed in 1950 by Warring [34] and later it was studied by Payne after whom the effect is named the 'Payne' effect [35,37]. It was found that this effect is exponentially increased by increasing filler loading. The Payne effect is mainly related to the filler network created in the polymer matrix. In fact, in the early analysis, Payne attributed the softening to 'the structure of the carbon black, and may be visualized as filler-filler linkages of physical nature which are broken down by straining' [36]. This structure was further clarified by Medalia as the 'interaggregate association by physical forces, not the structure or aggregate bulkiness' as generally termed in the rubber industry [55]. Basically, the rubber trapped in the filler network or agglomerates loses its identity as an elastomer and behaves as filler in terms of mechanical properties. Therefore, the effective volume of the polymer bearing the overall stress is reduced by filler networking, resulting in increased modulus which is governed primarily by the filler concentration. The increasing strain amplitude induces the breakdown of the filler network, resulting in the release of the 'trapped' rubber so that the effective filler volume fraction and hence the modulus would decrease [56].

Both the Mullins and the Payne effects significantly overlap and they cannot be easily separated; they render modeling of the mechanical response of typical tire compounds extremely difficult since they cannot be described successfully by any elastic constitutive law. However, several attempts have been made to model the overall behavior of filled rubbers and, among all the molecular, FEM and continuous mechanics approaches, the efforts of Lion [57], Bergstrom and Boyce [48], Gauthier et al. [58], Lorenz and Kluppel [59] are worthy of note. Instead, the tire designer must accept quite approximate representations of the elastic properties of present-day tire compounds, recognizing that they are subjected to complex strains and strain histories that have major, and unfortunately ill-defined, effects on the corresponding stresses.
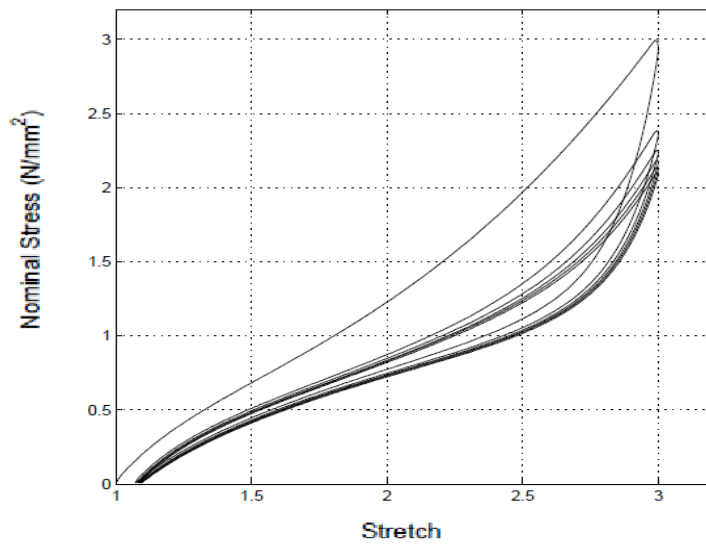
(a)
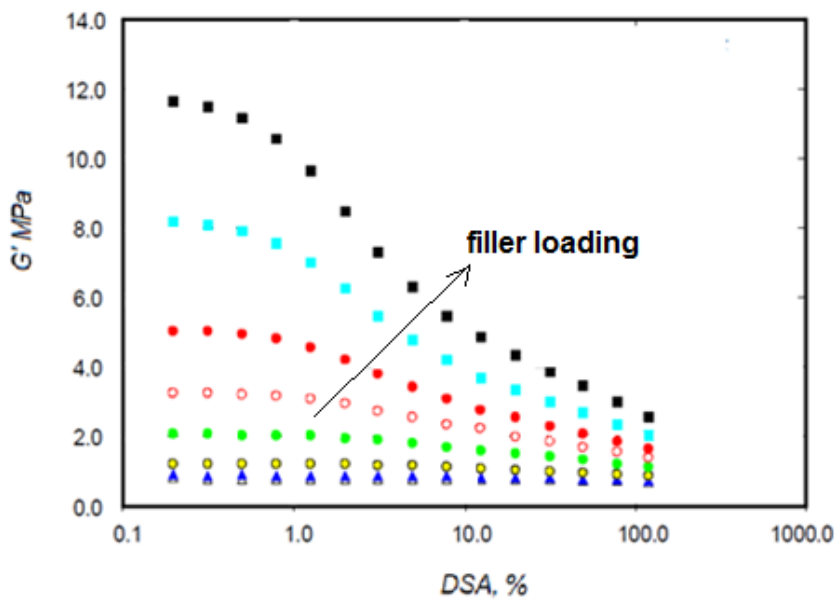
(b)

Figure 2.10 Compound non-linearities: (a) Hysteresis in stress-strain curve or 'Mullins effect'; (b) Payne effect

2.3 Corded reinforcement: textile 'cord'

The main features of pneumatic tires, such as the high specific mechanical properties, flexibility, dimensional and shape stabilities, are achieved through the typical reinforcement of cord-rubber composites [1,2]. Tire cords are the strength members of a tire. Furthermore, they must define the tire shape, support the inertial loads and contain the inflation gas. They must ensure dimensional stability for uniformity, handling and ride and provide axial and lateral rigidity necessary during acceleration, braking and cornering. In order to guarantee durability, they must also provide bruise, fatigue and resistance to separation.

In order to provide all of these functions, cords have to satisfy the following requirements:

- large length to diameter ratio;
- high axial orientation for axial stiffness and strength;
- high flexibility due to low bending stiffness;
- hierarchical twisted structure to allow filaments to exert axial strength along with other filaments in the bundle.

However, tire design must prevent cord from operating in compression.

Both steel and polymeric cords are used in tire carcass. Generally steel cord are used as reinforcement in the belt package while polymeric cords are used in body plies (cf. Figure 1.1). The description will be nevertheless limited to polymeric (or textile) cords.

Textile corded reinforcement are complex structures made of hundreds filaments twisted and organized into substructures [60]. Filaments from a production spinneret are first gathered together, slightly twisted in yarns; yarns are then cabled together in helicoidal structures (on several levels) termed cords (cf. Figure 2.11). The filaments are generally twisted 'Z' into yarns and the yarns are back-twisted 'S' to form the cord.

Thanks to the hierarchical and twisted structure, cords exhibit high specific properties (e.g. axial stiffness and tensile strength) combined with low bending stiffness. This is achieved through the high number of continuous filaments that cooperate in the overall structure. In particular, unlike the each filament that generally shows a transversally isotropic behavior, the twist of filaments leads to a peculiar mechanical behavior that is characterized by a trigonal behavior. Actually, when such a structure undergoes an axial load, filaments are both stretched and rotated transversally to cord axis, leading to an axial tension-twisting coupling. Several pieces of literature [27,61-64] deal with the mechanical behavior of corded structures and define a constitutive equation

Figure 2.11 Hemp rope illustrating cord construction levels [2]

providing for this coupling as a function of filament material and structure construction (twist level, twist angle, cord, yarn and filament radii). However, these models often adopt extremely complex formulations. Costello's model is worthy of note, thanks to its simple formulation and completeness in phenomena description [27]. Details of this analytical model are given in Chapter 3.

The terminology of corded structures comes from textile industry. The size of a tire filament, yarn, or cord is measured by its weight per unit length - linear density or 'denier' (denier is the weight in grams of 9000 meters) or 'decitex' (weight in grams of 1 km). Textile cords are identified by their yarn denier and their construction. Thus a 940/2 8x8 nylon cord is formed from two 940-decitex yarns twisted separately at 8 turns per inch and then back-twisted together at 8 turns per inch to form the cord. For a given material, use of higher denier yarns or more yarns per cord result in a higher breaking strength of the cord.

2.3.1 Reinforcement materials

Five materials are currently used in tire textile: rayon, nylon, polyester, aramid and steel. Tire fabrics have changed in response to the constant demand for better tire performance. The early pneumatic tires developed in the 1880s for bicycles by J.B. Dunlop and applied to automobiles in the 1890s used expensive Irish flax. Cotton soon replaced flax and remained the major tire textile until

World War II and it has been phased out since the mid-1950s. Continuous filament viscose rayon and steel cord were introduced in the late 1930s. Nylon became generally available for tires in the late 1940s and has met the needs of heavy-duty tires in large truck, earthmover, and aircraft tires. However, rayon held sway in passenger tires, particularly for new cars, because of poor ride characteristics with nylon due to its lower dimensional stability. Finally, polyester cords were introduced by Goodyear in the early 1960s to provide better strength than rayon and better dimensional stability than nylon. Polyester has gone through several technical improvements to surmount early shortcomings and nowadays has become the dominant textile for passenger and light truck radial carcasses in North America and has increasing use worldwide. Aramid fiber was introduced in 1974 by DuPont and, since then, it has shown slow but steady growth, particularly in radial tire belts, but its high cost is a limit. The high modulus of steel and aramid find their major use in radial belts and in single-ply carcasses for large radial tires. Rayon is used in both carcass and belt of passenger radial tires but lacks strength for durable heavy-duty tires. Modern polyester cord is an excellent carcass textile for use with steel belts in passenger and light truck tires and is becoming dominant worldwide. However, it lacks the toughness and heat resistance required for large tires where nylon is the textile of choice in large bias truck, earthmover and aircraft tires but nylon and polyester do not have the high stiffness necessary for good performance in radial belts. Yarn and textile producers are making continuing improvements in their products; therefore these data are for a general comparison only. In particular, modifications in the last twenty years have resulted in significant improvements in the dimensional stability of polyester and the tensile strength of steel. Also, aramid modifications have improved its compression fatigue properties [2].

The following table summarizes typical physical properties of some commonly used cord sizes of organic textile fabrics [2]. Data are for untreated yarn bundles lightly twisted at 0.2 to 0.3 turns per inch.

	Rayon	Nylon 6	Nylon 66	Polyester	Aramid	Steel
Tenacity [cN/tex]	50	80	85	80	190	35
Elongation at break[%]	6	19	16	13	4	2.5
Initial modulus [cN/tex]	800	300	500	850	4000	1500
Shrinkage [% at 150°C]	<0.1	6	5	2	<0.1	<0.1
Moisture regain [% at RT]	13	4.5	4.5	0.5	<2	<0.1
Specific gravity	1.52	1.14	1.14	1.38	1.44	7.85
Melting temperature [°C]	>210	225	250	250	>500	--
Glass transition temperature [°C]	-	55	55	80	-	-
Heat resistance [°C]	150	180	180	180	250	-

Table 2.I Filament properties of major tire textiles [2]

	Rayon	Nylon 66	Polyester	Aramid
Linear density [dtex]	**1840**	**940**	**1100**	**1500**
n. of filaments	**1000**	**140**	**210**	**1000**
Breaking force [N]	96	80	94	325
Breaking tenacity [mN/tex]	510	840	848	2030
Elongation at break[%]	12.8	18	11.2	4.8
Shrinkage [% at 180°C]	-	5.1	7.6	-

Table 2.II Physical properties of commercial tire cords [2]

In the following the main features of the materials used for tire reinforcement are reported.

Polyester. It is the general name given to the polyethylene terephthalate fibers, the product of condensation polymerization of ethylene glycol and terephthalic acid. Polyester must be used with carefully designed rubber adhesion systems and carcass rubber compounds in order to prevent cord deterioration in use. Polyester cord is not recommended for use in high-load/high-speed/high-temperature applications, as in truck, aircraft and racing tires, because of the rapid loss in properties at temperatures above 120°C. However, increased molecular weight and revised processing have lead to newer modifications: the so-called DSP-PET (dimensionally stable PET) is characterized by a 50% increased modulus and 50% reduced shrinkage, bringing it close to rayon for dimensional stability. It has become relatively inexpensive making it a good choice for passenger and small light truck tires.

Rayon. Rayon is a man-made fiber, based on regenerated cellulose. Tire cord strength has been improved 300% by improved coagulation and heat treatment.

The low-shrink, high-modulus, good-adhesion properties of rayon make it an excellent choice for use in passenger tires. However, rayon has lost market share to polyester due to higher cost. Rayon is used for racing tires and has gained renewed interest in the development of an extended-mobility self-supporting passenger tire.

Nylon. It is the generic name for the linear aliphatic polyamides. Chemically, they are related to the naturally occurring proteins, including silk and wool. The major difference between the natural products and the synthetics lies in the relative position of the amide groups. Nylon 6 (polycaprolactam) and Nylon 66 (product of condensation between adipic acid and hexamethylene diamine) are the two types used in tire cords. Nylon tire cord strength has been improved 25-50% from early versions by processing modifications. Its low modulus and low glass transition temperature make it unacceptable as a belt material or for passenger tires. Nylon is preferred in uses requiring carcass toughness, bruise and impact resistance, high strength, and low heat generation, e.g., in tires for medium and heavy-duty trucks, off-road equipment, and aircraft. In these applications nylon can be used in the bias-ply tire carcass or in radial tire carcasses with steel or aramid belts.

Aramid. Although the aromatic polyamides are closely related to the nylons (the aliphatic polyamides), the substitution of the aliphatic carbon backbone by aromatic groups brings about considerable changes in the properties of the resultant fibers. The most common commercial material is poly(p-phenylene terephthalamide), known as Kevlar™ or Twaron™. Aramid cords have very high strength, high modulus, and low elongation. The relatively high cost has slowed adoption as a general radial belt material. It is particularly suited where weight is important, such as in the belts of radial aircraft tires or in overlay plies for premium high-speed tires. As with steel cords, aramid can be used as multiple plies in flat belts. In a multiply carcass construction, aramid's low elongation will prevent the outer ply from adjusting to the average curvature, thus placing the inner plies into compression. This reduces the contribution of the inner plies to the total strength, but, more seriously, early failures of the inner ply are encountered due to the poor dynamic fatigue resistance of aramid in compression [65].
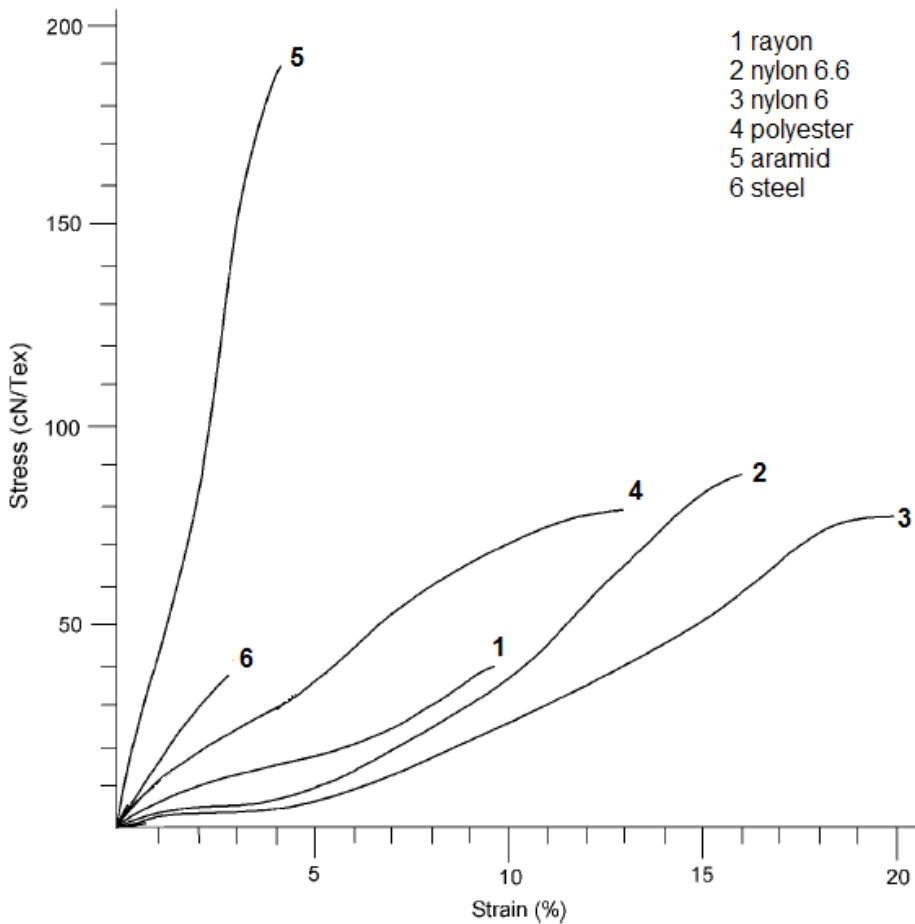
Figure 2.12 Typical stress-strain curve for major textiles filaments

2.3.2 Physical properties of textile cords

Construction and linear density, along with monofilament properties, are the main factor in determining the final performance of a cord. Various efforts have been made to investigate the effects of these parameters on the tire cord performance. Frisch had investigated rayon, PET, and Polyethylene Naphthalate (PEN) tire reinforcement materials with different twisting conditions [66]. Hockenberger and Koral had investigated the effect of twist on the cord performance of PEN, dimensionally stable polyester and high tenacity polyester cords [67]. Effect of combined twist with linear density has been investigated by A. Aytaç et al. on nylon 6.6 cords [68].

Twist is the distinguishing feature of corded reinforcement and plays a very important role in determining the tensile response of such a structure. In fact,

because fibers are not isotropic, the fiber orientation has a determining effect on the system properties. In particular, as twist increases, the helix angle (between cord axis and filament axis) increases, thus resulting into a reduction of initial modulus and of strength, along with an increasing of elongation at break. Higher twists permit a cord to behave like a spring which will not open up under compression (that is a very important requirement for tire construction), without losing flexibility; lower twists instead allow cord to behave as a rod, maximizing the strength.

Generally, twist level of tire cord is kept in a certain range since it has been found that, when the twist is applied to any textile yarn, the breaking strength and fatigue resistance initially increase up to an optimum twist level, and then decrease because of a further increase in twist level that would put extra stress on the yarn and cause a dangerous fiber-to-fiber friction. As twist increases the tenacity decreases, fatigue in compression improves (the main reason for higher twists), the cord cost per tire increases (because cords become shorter as they are twisted), and shrinkage during processing and cure increases.

Regarding linear density, it has been found that the increasing of this parameter (other construction features being equal) induces an improvement of tensile behavior, i.e. initial modulus, strength, elongation at break and breaking energy increase.

Strength and fatigue resistance are essential parameters for achieving tire durability; breaking energy indeed provides greater resistance to impacts from road hazards such as rocks, curbs, debris or potholes.

Uniform cord distribution in the finished tire is essential for tire uniformity and performance. For this reason, cords are also woven into a coherent sheet using a very light pick fabric as the weft at a very low fill count. The function of the pick is to maintain a uniform warp cord spacing during the downstream operations, such as, shipping, adhesive dipping and heat treating, calendering, tire building and lifting.
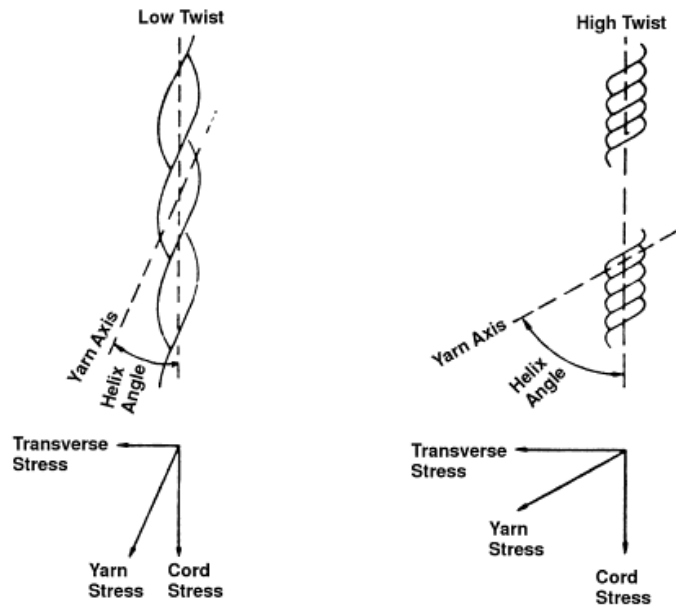
Figure 2.13 Dependence of stress field on cord twist

2.3.3 Textile cord manufacture

The processes for producing continuous textile filaments are melt spinning (for nylon and polyester) and solution spinning (for rayon and aramid).

In the melt spinning process molten polymer is filtered and pumped through a spinneret containing a large number of very fine holes. The extruded semi-molten polymer is then stretched to about 25 times its original length while solidifying in a cool air stream. The solidified and lubricated bundle is cold-drawn over a series of take-up rolls. Since the drawing process elongates the filaments by several hundred percent while the polymer is still above its glass transition temperature, it increases the strength and modulus, and reduces the breaking elongation, by increasing the polymer crystallinity and molecular orientation. The final structure of drawn, crystalline thermoplastic polymers contains crystalline fibrils, highly aligned polymer molecules and unoriented molecules. Finally, the filament bundles are gathered, lightly twisted, and stored on 'beams' to be transferred for further processing and cord manufacture.

Rayon and aramids must be dissolved for filaments manufacture since they have no defined melting temperature. A concentrated solution is pumped through the spinneret into a coagulating bath of non-solvent (wet spinning) or air-dried to

41

evaporate the solvent (dry spinning). During drying, filaments are subjected to tension; however, they are not extensively drawn since crystallinity and orientation are already high. Spin finish is applied and the filament bundles are 'beamed' for downstream processing. After these processes, filament has to be assembled into a cord. Cords are formed by cable twisting when two or more yarn plies are back twisted in the 'S' direction to form a greige (untreated) cord. Tire cords are generally balanced with equal twist levels in yarns and cords.

2.4 Cord-rubber adhesion

The performance of tires strongly depends on the efficiency of the combination of rubber and cord, and on the level of adhesion between the two phases. In order to get a certain level of adhesion, an adhesive ('dip') is applied between them. In particular, the adhesion of cord to rubber differs greatly from that in any other fields. In fact, the properties required for cord-to-rubber adhesives are summarized as follows:

· there are significant differences in molecular polarities and reactivities for rubber and cord material. In order to achieve a good level of adhesion of cord to rubber, it is desirable to have an intermediate modulus and two-faceted properties in terms of molecular polarity and reactivity;

· cord-rubber composites require flexibility and to meet this requirement, it is necessary for the adhesive to be flexible, too;

· heat and fatigue resistance are required. It is then necessary for the adhesive to have a three-dimensional network structure, to be non-fluid under high temperature and stress, and to have a high tenacity;

· water-based adhesive are required for operational reasons;

· resin ingredients are fluid in the baking process and must change to an insoluble polymer when cured.

Hence, rubber blended with polar and reactive resin is widely used in practice. Conventional resorcinol-formaldehyde-latex (RFL) adhesion systems provide required adhesion for nylon cords whereas polyester cords require the use of reactive chemicals [69]. Resorcinol and formaldehyde react in the dip to give a strong polar polymer with good adhesion the polar tire cord, while the rubber component of the latex provides good bonding to the rubber. In particular, RFL formulation also depends on to compound type to be used in tire and can be changed according to the customer requests. The adhesion of rayon, nylon, polyester, and aramids has been reviewed extensively [70-72] and several

studies have shown that the structure of the cured RFL consists of a continuous resin phase and dispersed latex particles [73, 74] as shown in the in Figure 2.14. The adhesion between rubber and dip coated synthetic fiber is achieved through mainly three mechanisms which are considered as general rules for all adhering surfaces. The first one is the mechanical interlocking which is related to the roughness of the surfaces. The second one is the physico-chemical bonding due to the hydrogen bonding between the functional groups of substrates. The third one is the chemical bonding between the polar functional groups of the substrates [75].
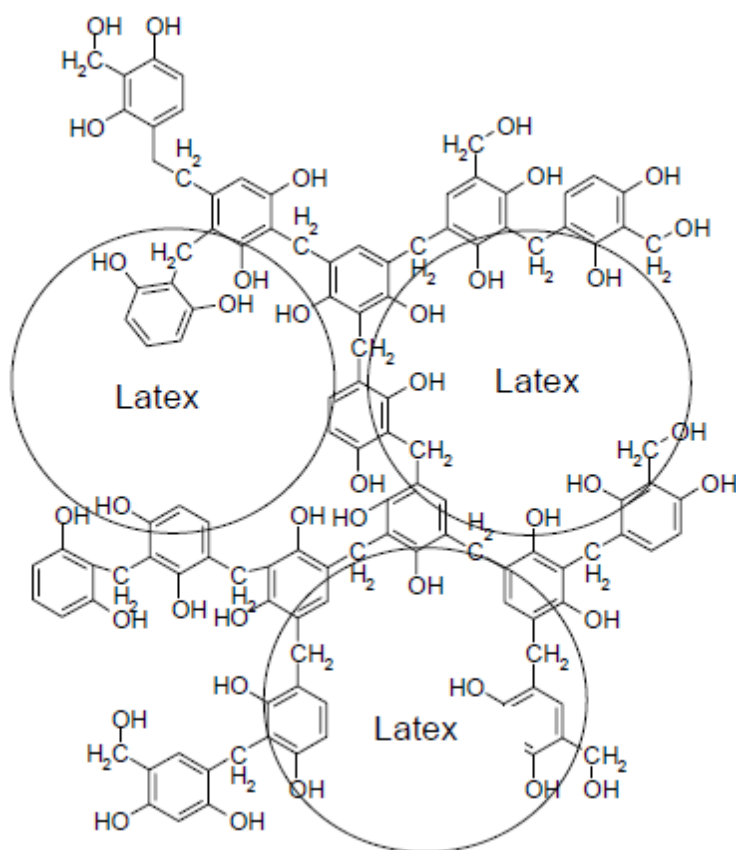
Figure 2.14 Morphology of the RFL system

Failure mechanism is of paramount importance for durability of tires and, for instance, tire carcass failures were often attributed to failure at the adhesive interface. In fact, it is well known that cords in the tire in service are continuously flexed, extended and compressed. Therefore, the reinforcing

43

materials must withstand to a large number of fatigue cycles without losing the initial properties [76]. Good adhesive durability is achieved by minimizing the abrupt change in modulus at the cord-rubber interface by introducing an adhesive layer of intermediate modulus. In particular, it is generally accepted that the adhesive provides both chemical bonding between the rubber and the cord surface and by mechanical interlocking as the rubber penetrates within the cord interstices. Accordingly, the adhesive must accommodate the large differences in moduli of the two materials.

During tire cord dipping process, the adhesive is applied to the reinforcement while it is treated under controlled condition of temperature and tension. Actually, dipping process and heat-setting (thermo-mechanical treatment necessary to adjust the final properties of the cords, for instance reduction of shrinkage) are concurrently performed in a treatment unit (Figure 2.15). Hence, dipping and baking of the adhesive is intimately tied in with cord stretching and relaxation procedures. Furthermore, by using proper dipping procedures it is possible to achieve the prime goal of the cord adhesive that is to avoid separation at the cord-adhesive interface, at the rubber-adhesive interface, or within the adhesive itself (Figure 2.16).

RFL is used for rayon and nylon exclusively and as the outer dip for polyester and aramid cords. Typically, resorcinol and formaldehyde are mixed and 'matured' for up to 24 hours; then, the latex is blended and the cord is dipped before tensioning. Dip formulations contain 2.5% total solids and dip pickup (that is a measure of penetration depth) is controlled to be about 6 - 8%. The cord is then tensioned and treated at high temperature in order to permit resin cure. Complete total wetting of the cord is necessary to prevent spotty adhesion. Good dip penetration is important for good adhesion and cord compaction and the optimal level of dip penetration is defined by two or three filament layers. However, polyester and aramid polymers are much less reactive to standard RFL and must be pretreated to obtain good adhesion, as schematically reported in Figure 2.16. A common practice is to employ a multistage dipping process that consists in pre-dipping the cord in an aqueous solution of a reactive chemical, such as an epoxide or a blocked isocyanate, along with a small amount of wetting agent to give uniform dip pickup. After tensioning and heating, the cord is dipped again in a standard RFL for final process. Typical times through each of the steps are generally 30-60 seconds.

The dip formulation, amount of dip pickup and the curing conditions can all affect adhesion and must be optimized. Strict quality control must be implemented once optimum conditions are established. Problems that must be

avoided are: inadequate wetting of the cord, inadequate dip pickup, excessive dip pickup (which can result in flaking off of the adhesive) or overheating during treatment. Any of these conditions can reduce adhesion.
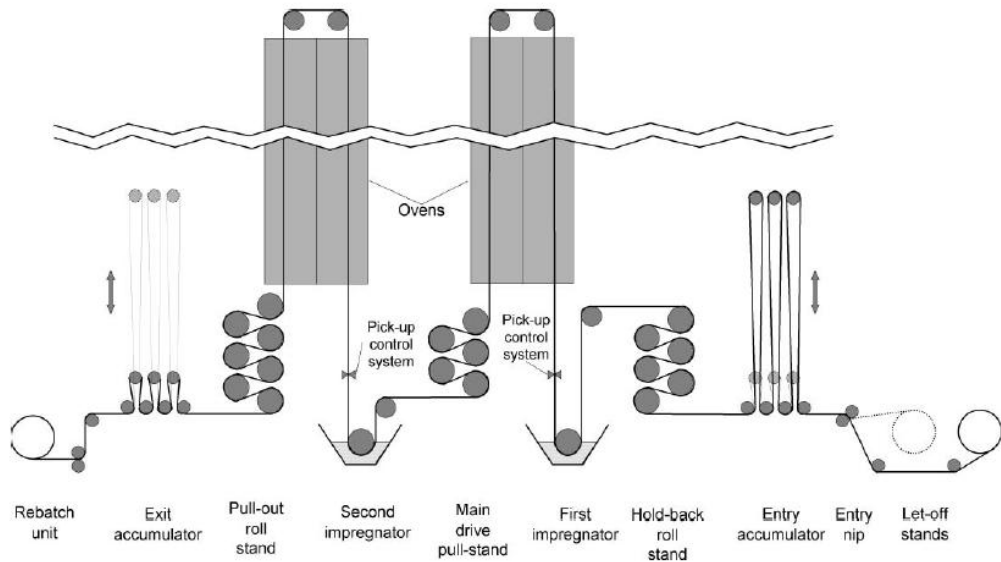

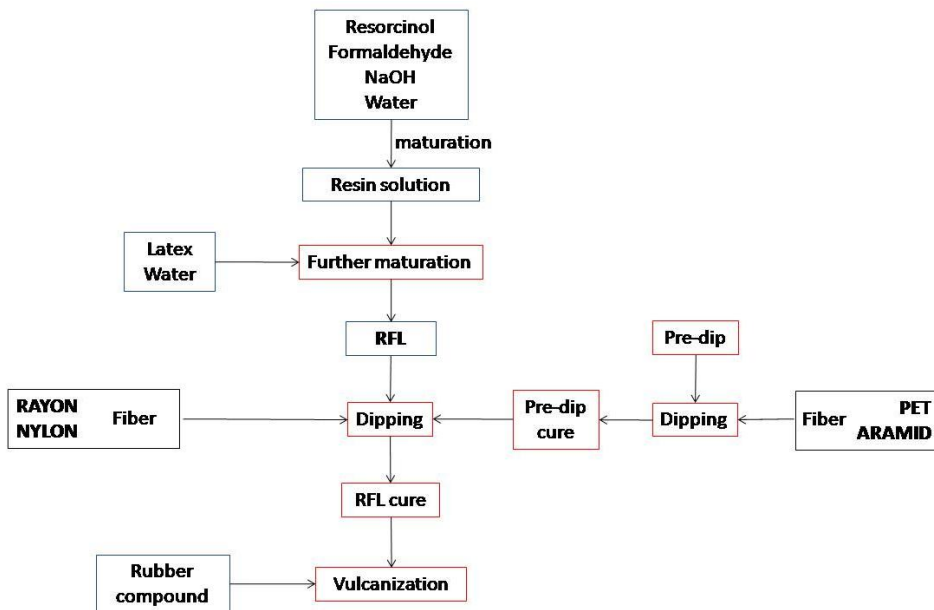Figure 2.15 Cords treatment unit

Figure 2.16 Cords treatment unit Schematic representation of various fiber dipping processes
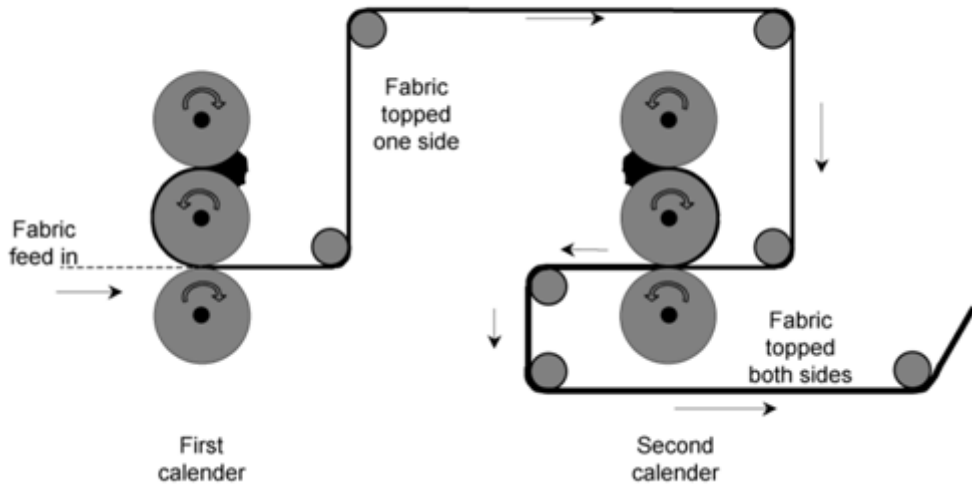
2.5 Cord-rubber composite assembly

The most important process used to combine textiles and rubber is calendering [77]. The basic principle of this technique is shown in Figure 2.17, where a simple three-bowl calender is illustrated (a). Basically, rubber compound is pre-warmed and then fed to the top nip, in order to get a smooth sheet of rubber running around the bowl. Then the coherent sheet of cords is fed into the lower nip, which presses it into intimate contact with the rubber sheet running from the top bowl. Rayon and, occasionally, nylon cords are previously dried, by treating them over a set of heated rollers, at temperatures around 100-110 °C. There are two modes for calendering process, namely frictioning and topping. In frictioning, the centre bowl runs at a higher speed than the top and bottom bowls and, when the two materials meet at the lower nip, the speed differential between the centre bowl with the rubber, and the lower bowl and fabric forces the rubber to penetrate the sheet of cords. Furthermore, the process is characterized by a higher heat build-up achieved in the rolling bank of rubber and also, consequently, a smoother, softer and thinner layer of rubber running round the bowl. For topping, all the rolls of the calender run at the same speed and, when the rubber sheet meets the cords, it is pressed on the top of them without penetrating the sheet of cords; hence this treatment needs a previous frictioning at least for one face of the fabric. Generally, rubber compound is topped onto both faces of cord sheet by passing twice on a simple three-bowl calender, or by passing it in two such calenders arranged in tandem. The latter requires a complicated lacing path for the fabric, in order to present the opposite face of the fabric to the second calender, as illustrated in Figure 2.17b. It is possible to top both sides of the cord sheet in one step by using 4-bowl calendering set-ups, as illustrated in Figure 2.17c.

Several parameters must be controlled in order to obtain the optimum result during calendaring. First of all, the behavior of the compound; in fact, it is necessary to ensure that the scorch and plasticity of the compound are satisfactory for such processing. Then, the feed of the compound from the warm-up feed mills that must equal the rate at which the compound is being applied to the cords; too high a feed rate would lead to an increasing rolling bank at the calender nip while too low a feed rate would give poor calendering, with potential uncovered areas, uneven thickness and surface blemishes. Secondly, the calender bowl temperatures that must be controlled to give uniform coverage and surface smoothness. Furthermore, the tension of cords at the calendar nip must be set correctly (generally set at around 2-3% of the

a) BASIC THREE-BOWL CALENDERING
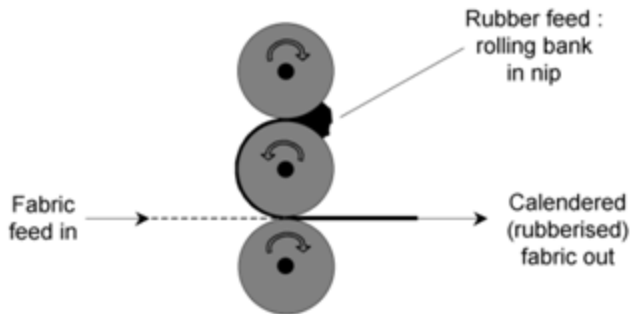
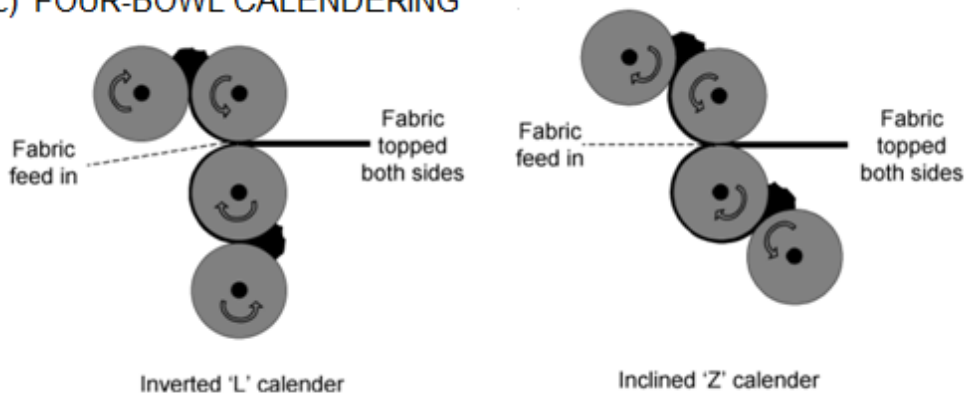## b) TANDEM THREE-BOWL CALENDERS

c) FOUR-BOWL CALENDERING

Figure 2.17 Cord-rubber composite calendering

ultimate strength of the fabric); lower tension leads to folding or creasing of the fabric, which in turn can lead to crushing and damage on passing through the nip; higher tensions lead indeed to uneven coverage, or excessively tight edges may lead to poor control of the line of the fabric or to sagging and creasing in the centre of the cord sheet. The final and most critical parameter to control is the thickness of rubber. On passing the rubber through the nip, high pressures are generated (up to at least 1 ton per centimeter width of bowl), and these pressures will cause the bowls to deflect. Whereas the bowls are set parallel when unloaded, under the pressures of operation this deflection will give a rubber sheet, which is thicker in the middle. This deflection will depend on the plasticity of the compound, the width being processed and the design of the calender. To minimize this problem and to obtain as a uniform sheet as possible, most calender bowls are 'profiled' to correct this, i.e., they are ground with a convex contour.

Chapter 3

Overview on modeling of macro- and micro-mechanics of cord-rubber composites

3.1 Macromechanics of cord-rubber composites

Common composite materials for structural applications are those with either continuous or chopped fibers embedded in a softer matrix. Particulate composites made up of particles dispersed in a matrix are also commonly used. Different materials can also be combined on a microscopic or nano-scale to form a composite, or two-phase material, such as carbon-black filled rubber compounds. The resulting rubber compound is macroscopically *homogeneous*, since the material properties do not vary with position on a macro level whereas fibrous composites are macroscopically *heterogeneous* since the material properties do depend on position on the macro level, i.e. on the different properties of the fiber and the matrix. Since cord-rubber composites are unidirectional composites, the scope of this discussion is limited to the mechanics of continuous fiber composites.

The mechanical response of a cord-rubber composite significantly differs from the behaviour of an orthotropic lamina. This is primarily due to the peculiar tension-twisting coupling of the corded reinforcement, which consequently leads to a 'trigonal' behaviour of the composite itself. Furthermore, the majority of conventional composites are characterized by a rigid matrix, which sustain only

small strain. Cord-rubber composites undergo instead very large strains and non-linearities play an important role in the overall response of the material.

The first quantitative study of elastic properties of cord-rubber composites for tire application was published in Germany in 1939 by Martin [78] who analysed bias-ply aircraft tires using thin shell theory to approximate toroidal tire behavior. Martin's analysis of the orthotropic composite elastic constants assumes that fibers are inextensible and the matrix stiffness is negligible small; this approach has been referred as the classical netting analysis. Gough [13] and Tangorra [79] developed expressions for the elastic constants of a single unidirectional ply based on the method of analysing plywood; they neglected the flexural stiffness of the cords and treated them as unidirectional load carrying bodies, with no transverse properties. Then Akasaka and Hirano [12] simplified Gough-Tangorra equations noticing that there is a huge difference in moduli between cord and rubber and that, in most applications, cord volume fraction is very small (cf. following paragraphs for details).

Since '60s Clark performed an extensive analysis of cord-rubber composites [1,11,80-84]. He underlined the differences between rigid composites and cord-rubber composites, considering that they are basically due to reinforcement structure. In fact the reinforcement is twisted (in order to improve bending properties, cf. Chapter 1 for details) and this configuration couples tension in strand to strand twist, so that the orthotropy is lost, in practice. This means that lamina itself is coupled between tension in the cord direction and twist of the 1-2 plane. Clark still considers the lamina as an orthotropic material but he introduced the bimodular assumption to consider, in a simple manner, the effect due to cord structure. In the bimodular simplification, cord behaviour can be idealized into two linear regions: the first characterized by the rearrangement of individual filaments in the cord; a second one, in which filaments are fully effective in enhancing stiffness.

One of the first attempts in modelling non-linearities of rubber cord composites was made by Kuo et al. [9], introducing the concept of the waviness of the fibres: this geometrical assumption is representative of reinforcement reorientation under a tensile load. In particular, the gradual straightening of the wavy fibres under external loading, in fact, results in enhanced stiffness with increase in deformation.

All of these approaches are valid attempts in modeling mechanical behavior of cord-rubber composites and provide good predictions when compared to experimental results. However, none of them is able to provide the actual composite response, with the peculiar tension-twisting coupling. A very

interesting approach, in this respect, is the model developed by Shield and Costello [85,86], derived on the basis of Kirchhoff's theory of plates and using a new constitutive equation for corded structures that accounts for the aforementioned coupling [27].

Finally, Finite Elements Method (FEM) represents the most powerful technique for the prediction of mechanical behavior of complex structures. Finite element methods that allow the cord and rubber properties to be specified separately, rather than smeared into composite coefficients, can provide a very powerful method to represent the non-linear response of cord-rubber composites and to gain detailed information on the response of the composite, whereas the complex analytical model do not even provide. Pidaparti's contribution to FEM modeling of cord-rubber composites is worthy of note: in a first analysis, he treated lamina as an orthotropic material [87] and introduced non-linearities [88]. Afterwards he has introduced new FEM approach to take into account cord tension-twisting coupling by using warping elements [23]. In the following, three modeling approaches will be discussed: the one based the classical lamination theory, the bimodular approach and Costello's model.

3.1.1 Orthotropic behavior assumption

First attempts in studying rubber cord composites were made neglecting the actual mechanics of cords (due to their hierarchical twisted structure), that is treating the reinforcement as simple cylinders; hence cord-rubber lamina is seen as an orthotropic material. Once the elastic constants are known, for a single ply, the constants for a series of ply at arbitrary orientations in a laminate can be determined using classical lamination theory. Therefore the mechanical behavior of continuous cord reinforced rubber can be approximately described by the linear composite theory developed for more rigid composites such as glass fiber reinforced epoxy [1,90]. However, the flexibility of cord-rubber composites allows for large deformations, which requires a more complex analysis [91]. However, linear composite analysis combined with non-linear finite element analysis can give a reasonable description of the material response for most applications.

Most rigid composite structures are composed of filamentary reinforcement (such as glass or graphite) in a matrix proportioned in such a way that the diameter of an individual filament is very much smaller than the thickness of the part in question. Reinforcement volume loadings are quite high and in many

ways it is reasonable to assume that material stiffness and elastic properties are averaged over the thickness, giving rise to a composite material property. Most structural uses are based on a series of filaments being laid parallel to one another, as to form a highly isotropic solid having three principal material directions, these being the direction of the reinforcement ('1') and the two mutually perpendicular directions to filament's one ('2' and '3') (Figure 3.1). Each lamina is defined specially orthotropic and treated as a two-dimensional load carrying element in the 1-2 plane, those effects in the 3rd direction being given a secondary role (plain stress conditions).
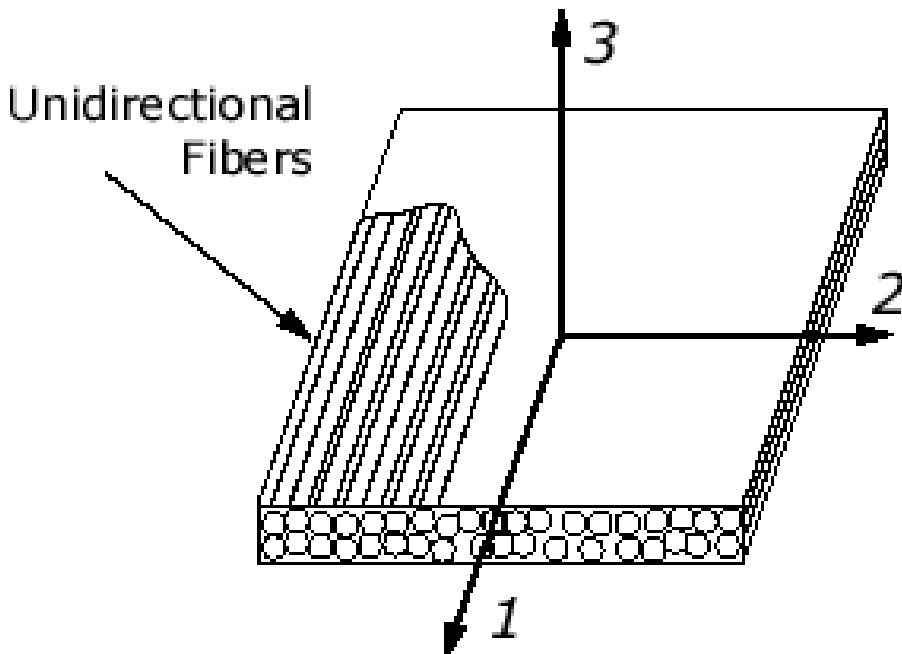

Figure 3.1 Schematic f an orthotropic lamina

In these conditions, for linear elastic materials, the Hooke's law assumes the following form:

$$\begin{bmatrix} \sigma_1 \\ \sigma_2 \\ \tau_{12} \end{bmatrix} = \begin{bmatrix} C_{11} & C_{12} & 0 \\ C_{21} & C_{22} & 0 \\ 0 & 0 & C_{33} \end{bmatrix} \begin{bmatrix} \epsilon_1 \\ \epsilon_2 \\ \gamma_{12} \end{bmatrix} \tag{3.1}$$

where:

$$C_{11} = \frac{E_1}{1 - \nu_{12}\nu_{21}} \qquad C_{12} = \frac{\nu_{12}E_2}{1 - \nu_{12}\nu_{21}} = \frac{\nu_{21}E_1}{1 - \nu_{12}\nu_{21}}$$

$$C_{33} = G_{12}$$

$$C_{22} = \frac{E_2}{1 - \nu_{12}\nu_{21}} \qquad \frac{\nu_{12}}{\nu_{21}} = \frac{E_1}{E_2}$$

$$(3.2)$$

Hence, five elastic constants are needed to define the 'effective' mechanical response of unidirectional lamina; four are independent. These constants can be experimentally determined by means of measurements performed on the lamina (macroscopical approach) or can be computed since mechanical properties of matrix and reinforcement are known (micromechanical approach). Being known the four independent constants, the 'off-axis' response – that is lamina behavior in a reference system different from the principal one – is obtained using a transformation matrix.

The principal directions of material orthotropy (1,2) do not always coincide with the reference directions used for the structure (*x, y*). An example is the angled belts of a radial tire, where the direction of the belt wires is at an angle (e.g., 20 degrees) to the tire axes *x-y-z*. The circumferential (*x*) and lateral (*y*) stiffnesses of the belt are desired for tire design and analysis. When this occurs, a method of transforming the stress-strain relations from one coordinate system to another is needed. Such a system is termed 'generally orthotropic' and its response to load is more complicated than that of a unidirectional specially orthotropic since an applied tensile stress now produces shearing strain as well as the expected normal strain.

The stress-strain relations governing the off-axis response of a lamina in the plane stress state are the following:

$$\varepsilon_x = \sigma_x/E_x - \nu_{yx}\,\sigma_y/E_y - \lambda_x\,\tau_{xy}$$
$$\varepsilon_y = \sigma_y/E_y - \nu_{xy}\,\sigma_x/E_x - \lambda_y\,\tau_{xy} \qquad (3.3)$$
$$\gamma_{xy} = \tau_{xy}/G_{xy} - \lambda_x\,\sigma_x - \lambda_y\,\sigma_y$$

where θ is the angle between load direction and direction '1' (Figure 3.2).
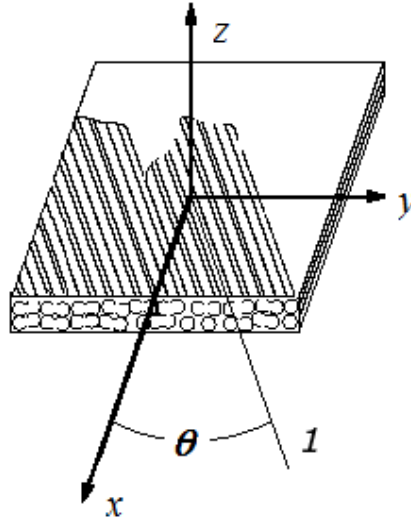
Figure 3.2 Schematic for a general orthotropic lamina

Properties in off-axis directions (denoted by subscripts '*x*' and '*y*') are linked to principal axes by means of the following expressions:

$$1/E_x = cos^4\theta/E_1 + (1/G_{12} - 2\ v_{12}/\ E_1)sin^2\ \theta\ cos^2\theta + sin^4\theta/E_2 \qquad (3.4)$$

$$1/E_y = sin^4\theta/E_1 + (1/G_{12} - 2\ v_{12}/\ E_1)sin^2\ \theta\ cos^2\theta + cos^4\theta/E_2 \qquad (3.5)$$

$$1/G_{xy} = cos^2 2\theta/G_{12} + [(1 + v_{12})/\ E_1 + (1 + v_{21})/\ E_2]\ sin^2 2\theta \qquad (3.6)$$

$$v_{xy}/E_x = v_{yx}/E_y \qquad (3.7)$$

$$\lambda_x = sin\ 2\theta[sin^2\theta\ /\ E_2 - cos^{\ 2}\ \theta/\ E_2 + 1/2(1/G_{12} - 2\ v_{12}/\ E_1)cos\ 2\theta] \qquad (3.8)$$

$$\lambda_y = sin\ 2\theta[cos^{\ 2}\theta\ /\ E_2 - sin^2\ \theta/\ E_2 - 1/2(1/G_{12} - 2\ v_{12}/\ E_1)cos\ 2\theta] \qquad (3.9)$$

The coefficients λ_x and λ_y, which couple normal stresses with shearing strain (and shearing stress with normal strains), vanish in case of special orthotropy. Also in this case, the elastic constants are functions of the mechanical properties of the constituents, e.g., the cord and the rubber modulus.

The most important method used for the calculation of elastic constants of an orthotropic lamina are known as 'micromechanical' since the expressions are determined by recognizing the inhomogeneous nature of the lamina and by utilizing the properties and the concentrations of reinforcement and matrix. Micromechanics of cord-rubber composites [92,93] will be described in the following.
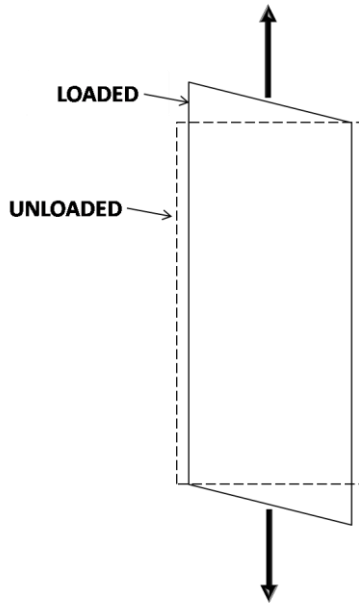
Figure 3.3 Tension-shear coupling for a special orthotropic lamina

3.1.2 Clark's bimodular analysis

Between 1960 and 1989 Clark performed an general analysis of rubber-cord laminate, extending classic lamination theory to rubber cord composites [1,11,80-84,94]. First of all, Clark reasserts the way rubber cord composites differ from conventional, rigid composites. In rigid composites, reinforcement consists of small filaments (such as graphite or glass) that are well dispersed into the composite or with particular arrangements. In cord-rubber composite, reinforcement has a twisted structure; this twist is responsible of coupling between tension and torsion, hence *transverse isotropy of reinforcement is lost*. Also they are characterized by peculiar effects due to internal filament slip into a twisted structure [11].

Then, the very low modulus matrix which provides a very little lateral reinforcement against cord buckling and, since the internal section of most strands of filaments is not fully penetrated by the dip, they are supported laterally only by adjacent filaments. Due to twist, the initial shape of individual filament is curved, and the filament straightens under tension and becomes stiffer. All these effects combine to result into the stress-strain curves of lamina in the direction '1' to be strongly non-linear. The transition region can occur at

different levels of cord strain $\varepsilon_1{}^*$, depending on the reinforcing cord material and structure. This peculiar behavior has been discussed in literature as bimodular response. A typical stress strain curve is showed in Figure 3.4.

Clark had the innovative idea to adopt the concept of bimodular material in the classical orthotropic treatment. The stress strain curve of the unidirectional lamina is idealized to be divided into two linear regions, I and II. Region I is the low cord modulus region, in which filaments contribute a little to lamina stiffness because twisted filaments are only rearranged under tension. Region II is characterized by higher modulus because filaments are fully effective in enhancing stiffness. The intersection of these two linearized regions expresses a material property, the cord characteristic strain $\varepsilon_1{}^*$. So, to fully characterize the mechanical behavior of lamina, by keeping the orthotropic-like approach, eleven elastic constants are needed: 5 for both region I and region II, and $\varepsilon_1{}^*$. Adopting this simplistic approach, Clark studied the static and dynamic behavior of cord-rubber composite (mainly cylindrical structures and not only plates), evaluating in both the cases materials constants. Furthermore, he analyzed the effect of cord orientation on lamina response and validated the bimodular approach, in the contest of the classical lamination theory.
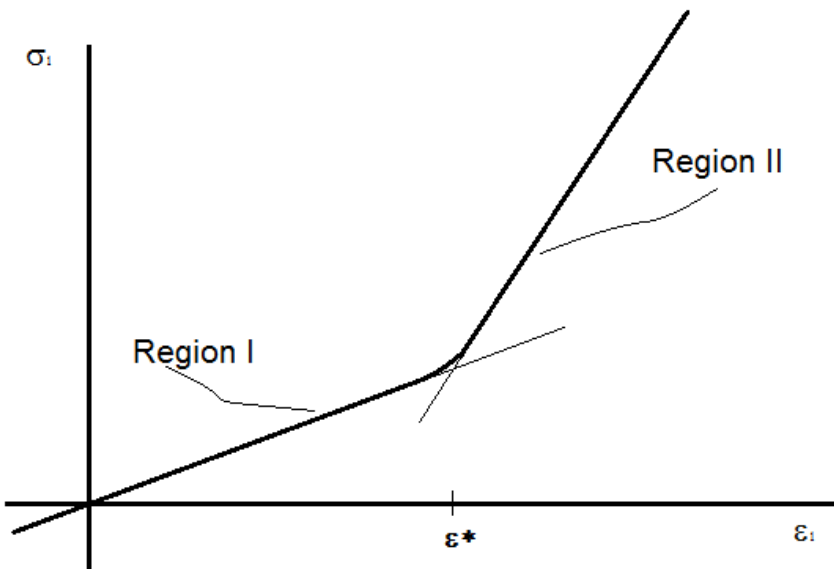

Figure 3.4 Stress-strain curve for a bimodular material

3.1.3 Costello's model

The first attempt including the actual constitutive behavior of the cord in the model of cord-rubber composites can be found in the work of Shield and Costello [85,86]. This model takes into account the extension-twisting coupling of the cord (and, consequently, of the lamina) as well as the exact location of the cord within the composite plate. Shield and Costello adopted two different approaches for developing this model, an energetic and an equilibrium one, leading to the same final results and based on the use of the same constitutive equation for the cord, derived by Costello in 'The Theory of Wire Rope' [27].
By virtue of the importance of this model, it is worthy to digress with a discussion on the development of the constitutive equation of corded structures.

a.   Tension-twisting coupling of corded structures

A simple straight strand is the basic corded structure; it is made up of a straight centre wire surrounded by several helical wires (Figure 3.5). In order to study the problem of such a structure subjected to an external solicitation (axial and/or twisting), it is important to analyze the static problem coupled with geometric requirements.

Equilibrium equations. Figure 3.6 shows the principal torsion-flexural coordinate system $\{x,y,z\}$ adopted for the representation of the wire; the z axes is tangent to wire centerline and centered on it. In the most general case of loading of a wire, three components of force and three couples act on a given cross-section. N and N' are the components of shear force in x and y directions, respectively, T is the axial tension in the wire, G and G' are the components of bending moment in x and y directions, respectively, H is the twisting moment in the wire. In addition to these forces and moments, there may be also distributed forces, such as contact forces, and distributed moments that act on the outer surface of the wire.   These distributed forces and moments are X, Y, and Z (defined as components of external load per centerline wire unit length in the x, y, and z directions, respectively) and K, K', and Θ (defined as the components of external moment per centerline wire unit length in the $x,$ y and z directions, respectively).
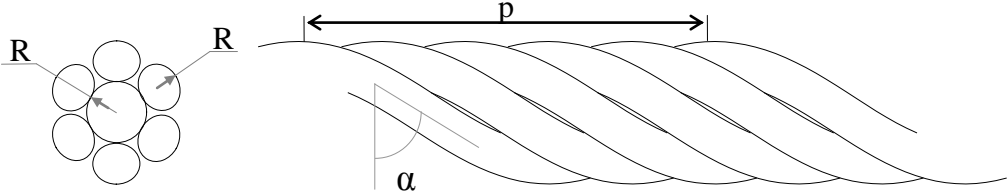
Figure 3.5 Cross section and front of a straight strand with 6 external filament.
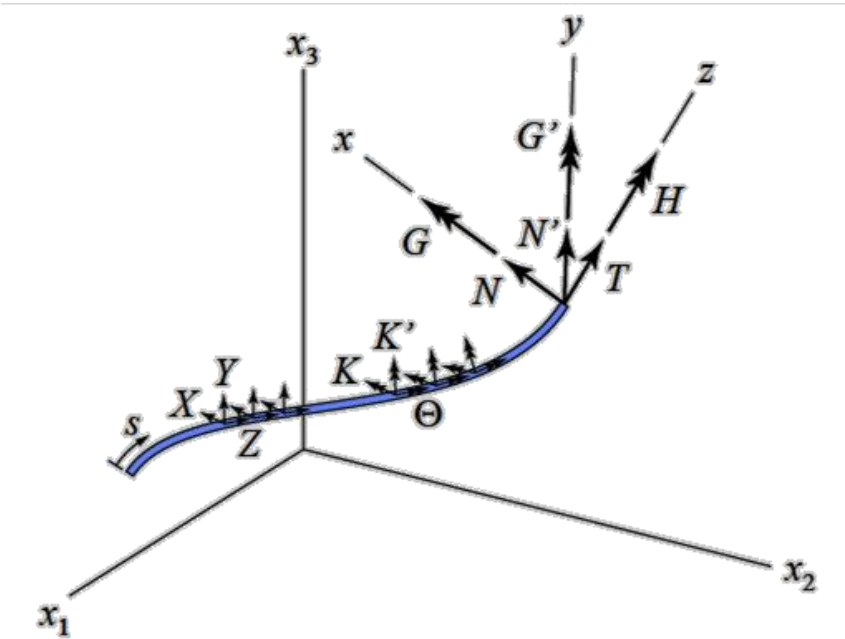

Figure 3.6 Principal torsion-flexural coordinate system and forces acting on a wire.

The equations of equilibrium of the wire in $\{x,y,z\}$ coordinate system are defined as follows:

$$\frac{dN}{ds} - N'\tau + T\kappa' + X = 0 \tag{3.10}$$

$$\frac{dN'}{ds} - T\kappa + N\tau + Y = 0 \tag{3.11}$$

$$\frac{dT}{ds} - N\kappa' + N'\kappa + Z = 0 \tag{3.12}$$

$$\frac{dG}{ds} - G'\tau + H\kappa' - N + K = 0 \tag{3.13}$$

$$\frac{dG'}{ds} - H\kappa + G\tau + N + K' = 0 \tag{3.14}$$

$$\frac{dH}{ds} - G\kappa' + G'\kappa + \Theta = 0 \tag{3.15}$$

where s is the arc length along centreline of a generic external wire, κ and κ' are the components of curvature in, respectively, the x and y directions and τ is the twist per unit length of the wire.

Such relations define a set of non linear equations that are valid for large deflections.

Besides the equations of equilibrium, the constitutive relations, linking between the generalized forces and the components of curvature, twist, and elongation, are necessary to solve the problems:

$$T = AE\xi_f \tag{3.16}$$

$$H = C(\tau - \tau_0) \tag{3.17}$$

$$G = EI_x(\kappa - \kappa_o) \tag{3.18}$$

$$G' = EI_y(\kappa' - \kappa'_o) \tag{3.19}$$

where E is elasticity modulus of the material, C is the torsional rigidity, I_x and I_y cross sectional moment of inertia around the x and y axes, respectively, A is wire cross sectional area and ξ_f axial wire strain. For a wire with a circular cross section of radius R, the constitutive relations are written as follows:

$$T = \pi R^2 E \xi_f \tag{3.16a}$$

$$H = \frac{\pi R^4 E}{4(1 + v)}(\tau - \tau_0) \tag{3.17a}$$

$$G = \frac{\pi R^4 E}{4}(\kappa - \kappa_o) \tag{3.18a}$$

$$G' = \frac{\pi R^4 E}{4}(\kappa' - \kappa'_o) \tag{3.19a}$$

Geometry. In order to get a simple straight strand, a central filament of radius R_c must be surrounded by m helical wires of same radius R_f, twisted at a helix angle α. Accordingly, the radius of the helix defined by the external filaments path is defined as:

$$r_h = R_c + R_f \tag{3.20}$$

e and pitch of this helix is related to r_h and to helix angle α as by:

$$P = 2\,r_h\,\pi\tan\alpha \tag{3.21}$$

The parameter defining geometry of filaments (i.e., radii, number, helix angle) determine whether the surrounding filaments are in contact with core filament or not. The geometrical condition for core touching is given by:

$$R_f\sqrt{1 + \frac{\tan^2\left(\dfrac{\pi}{2} - \dfrac{\pi}{m}\right)}{\sin^2(\alpha)}} < R_c + R_f \tag{3.22}$$

Axial response of a single helical filament. In case of a single helical wire subjected to an axial load, the axial tension T is assumed to be constant along the length of the wire, with no bending moment acting, that is $K = K' = 0$. Hence, equilibrium equations assume the form:

$$N'\tau + T\kappa' + X = 0 \tag{3.10a}$$

$$Y = 0 \tag{3.11a}$$

$$Z = 0 \tag{3.12a}$$

$$-G'\tau + H\kappa' - N = 0 \tag{3.13a}$$

$$N = 0 \tag{3.14a}$$

$$\Theta = 0 \tag{3.15a}$$

In case of small variations of helix filament angle as $|\Delta\alpha| < 1$, the following solutions are obtained for the deformed helix configuration:

$$\frac{G'}{ER^3_f} = \frac{\pi}{4} R_f \Delta\kappa' \tag{3.23}$$

$$\frac{N'}{ER^2_f} = \frac{H}{ER^2_f} \frac{\cos^2(\alpha)}{r_h} - \frac{G'}{ER^2_f} \frac{\sin(\alpha)\cos(\alpha)}{r_h} \tag{3.24}$$

$$\frac{H}{ER^3_f} = \frac{\pi}{4(1+\nu)} R_f \Delta\tau \tag{3.25}$$

$$\frac{T}{ER^2_f} = \pi\xi_f \tag{3.26}$$

$$\frac{X}{ER_f} = \frac{N'}{ER_f} \frac{\sin(\alpha)\cos(\alpha)}{r_h} - \frac{T}{ER_f} \frac{\cos^2(\alpha)}{r_h} \tag{3.27}$$

By constitutive remarks, it is possible to link strand deformations to effective deformations in the wires in terms of curvature, twist increment and strand axis elongation. According to the general thin theory of Love [95], the kinematics of a rod and, for this particular case of a generic wire, are fully defined by the following four parameters:

$$\Delta \kappa' = -\frac{2\sin(\alpha)\cos(\alpha)}{r_h}\Delta\alpha + \nu\frac{R_c\xi_c + R_f\xi_f}{r_h}\frac{\cos^2(\alpha)}{r_h} \tag{3.28}$$

$$\Delta \tau = \frac{1 - 2\sin^2(\alpha)}{r_h}\Delta\alpha + \nu\frac{R_c\xi_c + R_f\xi_f}{r_h}\frac{\sin(\alpha)\cos(\alpha)}{r_h} \tag{3.29}$$

$$\xi_f = \xi_c - \frac{\Delta\alpha}{\tan(\alpha)} = \varepsilon - \frac{\Delta\alpha}{\tan(\alpha)} \tag{3.30}$$

$$\tau = \frac{\xi_f}{r_h\tan(\alpha)} - \frac{\Delta\alpha}{r_h} + \nu\frac{R_c\xi_c + R_f\xi_f}{r^2_h} \tag{3.31}$$

ξ_f is wire deformation along its axis; $\Delta\kappa$ is the component of curvature variation in the wire related to x direction in the local wire coordinate system; $\Delta\kappa$' is the component of curvature variation in the wire related to y direction in the local wire coordinate system and τ is the filament angle twist per unit length in the strand. ε is the strand axial deformation.

Projecting wire forces on strand axial directions, both axial force and moment can be computed as:

$$F = T\sin(\alpha) + N'\cos(\alpha) \tag{3.32}$$

$$M = H\sin(\alpha) + G'\cos(\alpha) + Tr_2\cos(\alpha) - N'r_2\sin(\alpha) \tag{3.33}$$

Hence for an helical filament in a straight strand, equations above allow to correlate loads to strand deformations in terms of ε and τ, starting from the initial configuration. The constitutive equation that highlights the axial tension-twisting coupling can be expressed into the following matrix form:

$$\begin{bmatrix} F \\ M \end{bmatrix} = \begin{bmatrix} C_1 & C_2 \\ C_3 & C_4 \end{bmatrix} \begin{bmatrix} \varepsilon \\ \beta \end{bmatrix} \tag{3.33a}$$

where C_i represents model parameters, depending on cord geometry (yarn radii, twist angle) and filament Poisson ratio (Figure 3.5) and β is the rotational strain of the strand defined as:

$$\beta = \left(R_c + R_f \right) \tau \qquad (3.35)$$

Load deformation laws are based on initial configuration of the strand, defined through R_c, R_f and α, and assumed stress free.

b. Tension-twisting coupling of cord-rubber composite

The elastic approach is based on the equilibrium of a plate element that is considered as the results consist of a contribution for the matrix plus a contribution from the cord. Since the model is based on the Kirchhoff-Love plate theory, the following assumptions are made:

· straight lines normal to the mid-surface remain straight after deformation;
· straight lines normal to the mid-surface remain normal to the mid-surface after deformation;
· the thickness of the plate does not change during a deformation.

Furthermore, these other assumptions are added:

· linear elastic behavior for the matrix;
· reinforcement treated as one-dimensional line element, geometrically
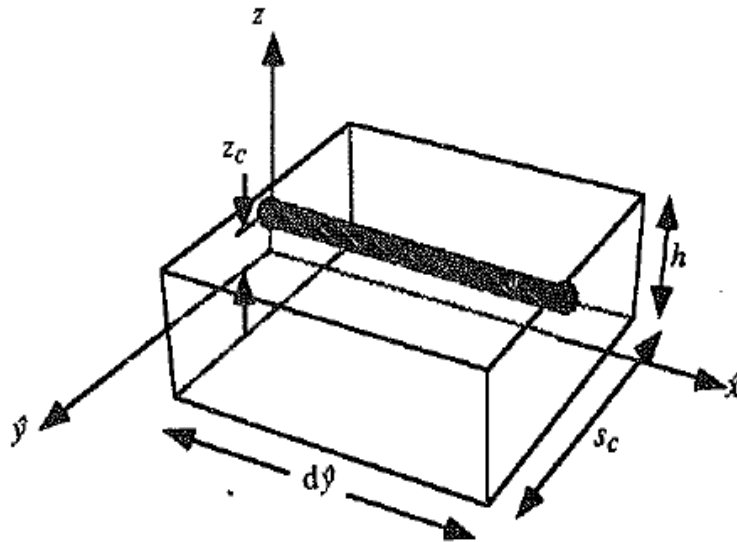· unimodular cords: same response in tension and compression.

Figure 3.7 Plate and cord geometrical features [85]

The formulation is based on the equilibrium of a small element of the plate (Figure 3.7); the usual equilibrium equations are:

$$\frac{\partial N_x}{\partial x} + \frac{\partial N_{yx}}{\partial y} + p_x = 0 \qquad (3.36)$$

$$\frac{\partial N_{xy}}{\partial x} + \frac{\partial N_y}{\partial y} + p_y = 0 \qquad (3.37)$$

$$N_{xy} = N_{yx} \qquad (3.38)$$

$$\frac{\partial Q_x}{\partial x} + \frac{\partial NQ_y}{\partial y} + p_z = 0 \qquad (3.39)$$

$$\frac{\partial M_x}{\partial x} + \frac{\partial M_{yx}}{\partial y} - Q_x = 0 \qquad (3.40)$$

$$\frac{\partial M_{xy}}{\partial x} + \frac{\partial M_y}{\partial y} - Q_y = 0 \qquad (3.41)$$

According to Kirchhoff theory, the displacements along x and y-directions are assumed to be linear functions of z coordinate and the transverse displacement is assumed to be constant through the thickness of the plate:

$$u(x, y, z) = U(x, y) - z\frac{\partial W}{\partial x}$$
$$v(x, y, z) = V(x, y) - z\frac{\partial W}{\partial y} \qquad (3.42)$$
$$w(x, y, z) = W(x, y)$$

where U, V and W are the displacement of a point (x,y) on the middle surface.

In solving the problem, Shield and Costello adopt the constitutive equation for cord introduced in the previous section, Eq. (3.33).

In the case of uniaxial tension, the solution of model equation leads to the following expression for composite E_1:

$$E_1 = E_m + c_1 E_c f_c \left[1 - \frac{6c_2 c_3 f_c (1+\nu_m)}{c_1 (\overline{Ah}^2 \overline{E} + 6c_4 f_c (1+\nu_m))} \right] \qquad (3.43)$$

It is straightforward to notice that this relationship is a peculiar form of the rule of mixtures, where a new term – accounting for the tension-twisting coupling - is introduced. Actually, the term in the brackets represents the reduction of stiffness due to non-zero transverse rotation. An interesting result of this model is the possibility to predict lamina twisting, as a function of cord and matrix properties: very compliant matrices allow cord twisting, thus resulting in a significant twisting of the overall lamina; stiffer matrices, instead, limit cord movement and reduce this effect (Figure 3.8).
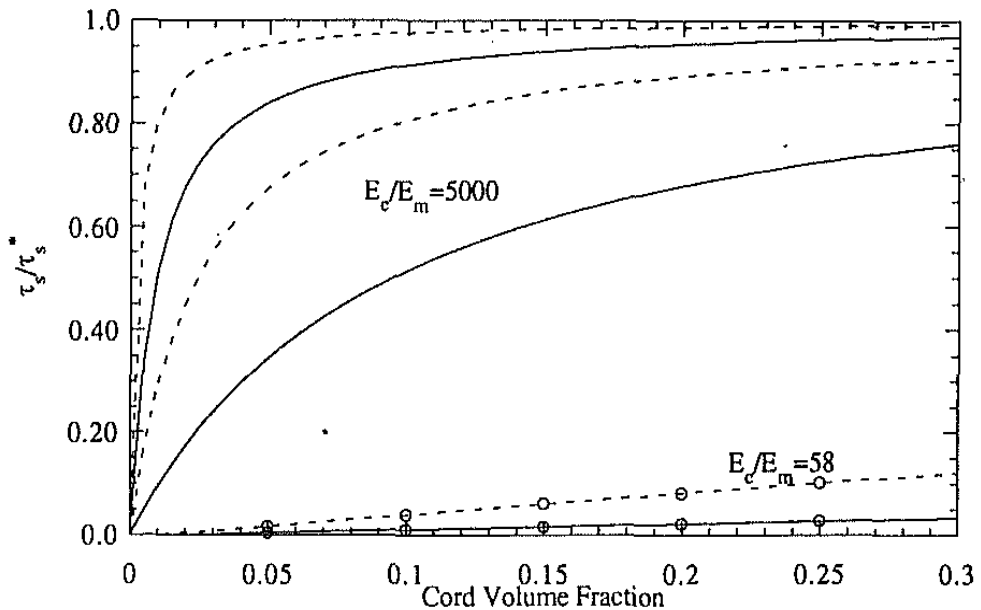

Figure 3.8 Prediction of lamina twist as a function of cord volume fraction and matrix modulus [85]

65

3.2 Micromechanics of composites

In the macromechanical study of composites, the material is assumed to be homogeneous. The properties of the composite are determined by experiments on the composite. The effects of the individual constituent material are only accounted for by its influence on the average properties of the composite.

A different approach is to predict the properties of the composite based on the properties of the constituents. This is called micromechanics theory and it examines the interaction of the constituent materials and determines the role of each phase on the effective properties of the composites. Some of these theories are discussed in the following. This representation is more complex than the macromechanics approach, however simplified tools exist for the calculation of the effective composite properties.

3.2.1 Constituent contribution to cord-rubber lamina properties

The following sections present the most widely used equations for calculating the elastic constants of a single orthotropic lamina.

a. Halpin-Tsai equations

The following equations are used for the calculation of elastic constants [92]:

$$E_1 = E_c V_c + E_r(1 - V_c) \tag{3.44}$$

$$E_2 = E_r [E_c(1 + \zeta_1 V_c) + \zeta_1 E_r(1 - V_c)] / [E_c((1 - V_c) + \zeta_1 E_r(1 + V_c/\zeta_1)] \tag{3.45}$$

$$G_{12} = G_r [G_c(1 + \zeta_2 V_c) + \zeta_2 G_r(1 - V_c)] / [G_c (1 - V_c) + \zeta_2 G_r(1 + V_c/\zeta_2)] \tag{3.46}$$

$$v_{12} = v_c v_c + v_r(1 - V_c) \tag{3.47}$$

$$v_{21} = v_{12} E_2/E_1 \tag{3.48}$$

where
ζ_1, ζ_2 = parameters depending on reinforcement geometry and spacing
E_c, E_r = Young modulus of cord and rubber
G_c, G_r = shear modulus of cord and rubber
v_c, v_r = Poisson's ratios of cord and rubber
V_c = cord volumetric fraction
For cord with circular section and for $E_c \gg E_r$, $\zeta_1 = 2$ e $\zeta_2 = 1$; hence, (3.45) and (3.46) become [93]:

$$E_2 = E_r(1 + 2V_c)/(1 - V_c) \qquad (3.45a)$$

$$G_{12} = \{G_r[G_c + G_r + (G_c - G_r)V_c]\}/[G_c + G_r - (G_c - G_r)V_c] \qquad (3.46a)$$

The relationship for longitudinal modulus and the major Poisson ratio are known as the *rule of mixtures*; the expression for secondary Poisson ratio follows the symmetrical nature of stress-strain law for orthotropic laminae; the relations for the transverse and shear moduli are semi-empirical in nature.

The derivation of the rule of mixtures is very simple. Longitudinal modulus can be derived for cord and rubber acting in parallel as hookean springs ('Voigt model') and subjected to the same strain ($\varepsilon_1^m = \varepsilon_1^f = \varepsilon$). While the expression of transverse modulus can be obtained by considering that cord and rubber act as spring in series, when a uniaxial load is applied to the composite perpendicular to the direction of the cords [90].
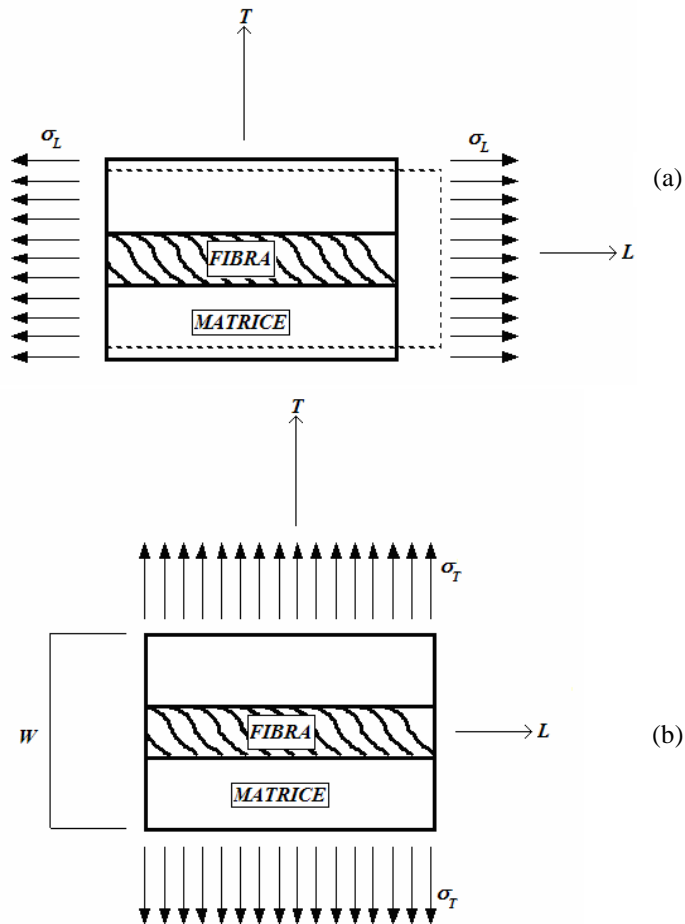

Figure 3.9 Voigt (a) and Reuss (b) models for composite

67

b. Gough-Tangorra equations

Goungh and Tangorra developed the following expressions for a cord-rubber lamina [13,79]:

$$E_1 = E_cV_c + E_r(1 - V_c) \tag{3.44b}$$

$$E_2 = \{4E_r\,(1 - V_c)\,[E_cV_c + E_r(1 - V_c)]\}/[3E_cV_c + 4E_r(1 - V_c)] \tag{3.45b}$$

$$G_{12} = G_r/(1 - V_c) \tag{3.46b}$$

$$v_{12} = 0.5 \tag{3.47b}$$

$$v_{21} = v_{12}E_2/E_1 \tag{3.48b}$$

Matrix is incompressible and transverse properties of cords are neglected. It follows that elastic constants are independent on cord shear modulus and Poisson ratio.

c. Akasaka-Hirano equations

In 1972 Akasaka and Hirano [12] derived the following equations from Gough-Tangorra, by noting cord Young modulus is higher than rubber's one and cord content is small compared to unity:

$$E_1 = E_cV_c \tag{3.44c}$$

$$E_2 = 4E_r/3 \tag{3.45c}$$

$$G_{12} = G_r \tag{3.46c}$$

$$v_{12} = 0.5 \tag{3.47c}$$

$$v_{21} = 0 \tag{3.48c}$$

In these three formulations, the transverse and the shear moduli of the ply are dominated by rubber properties while longitudinal modulus is dominated by cord properties.

It is remarkable noting that, when a unidirectional cord-rubber sheet is subjected to simple tension, an interesting deformation behavior occurs, which is not observed in rigid composites. In fact, generally orthotropic materials are characterized by the coupling between stretching and shear. Using Akasaka-Hirano relationships for the determination of elastic constants, the following

result is obtained:

$$\gamma_{xy} = S_{16} \approx \frac{-2sin\theta cos^3\theta}{E_2}(2 - tan^2\theta)\sigma_x \qquad (3.49)$$

Thus, the stretching-shear coupling vanishes at $\theta \approx 54.7°$, while $\gamma_{xy} < 0$ for $\theta <$ 54.7° and $\gamma_{xy} > 0$ for $\theta >$54.7°.

d. Clark's equations

In this approach [94], an energy method is used to formulate expressions for the lamina elastic constants without requiring detailed cord properties such as shear modulus and Poisson's ratio. The theory uses a stiffening parameter φ indicating the degree of stiffening imposed by the cord structure.

$$E_1 = E_c V_c + 12G_r/(1 - V_c) \qquad (3.44d)$$

$$E_2 = G_r \{4-[4/(2+\varphi)+(4+2\varphi)/(2+\varphi)^2]\}/(1-V_c) \qquad (3.45d)$$

$$G_{12} = G_r /(1 - V_c) \qquad (3.46d)$$

$$v_{12} = 0.5 \qquad (3.47d)$$

$$v_{21} = v_{12}E_2/E_1 \qquad (3.48d)$$

Lamination theory has surely provided an efficient mean for the analysis of rubber-cord laminae but it is worthy to note that it has several limits:

·   in tire under operating conditions, cords can be subjected to large strains and non-linearity cannot be neglected;
·   this theory, based on the plane stress state, neglects interlaminar deformations;
·   viscoelasticity is neglected;
·   dip effect is neglected because perfect adhesion between matrix and cords is assumed.

3.2.2 Shear Lag models

The 'effective' properties that can be obtained through the approaches discussed in the previous sections assume a condition of infinitely long cylinders. Actually, reinforcement has a finite length and, under this condition, one would expect that the reinforcing properties of the fibers would be 'degraded'. In this section, with the introduction of stress transfer analysis, a quantification of this effect is discussed. However, it is restrict to the case of a dilute condition, in which no interaction between fibers is considered.

The most widely used model describing the effect of loading a unidirectional composite are the shear lag (SL) models, originally proposed by Cox [96] and subsequently developed by others [97-99], which center on the transfer of tensile stress from matrix to fiber by means of interfacial shear stresses.

The base of the calculations is shown schematically in the diagram depicted in Figure 3.10 [100]. Imaginary reference lines, drawn on a fiber and the surrounding matrix, are useful for the understanding of the problem. In the initial configuration these reference lines are straight and normal to the fiber axis (Figure 3.10a) and, as an external loading is applied only to the matrix (in the parallel direction to the fiber axis), they distort in such a manner as shown in Figure 3.10b. The shear distortions of the matrix close to the fiber are schematically depicted in Figure 3.10c, where a fiber element is enlarged. This last schematic is fundamental for the evaluation of shear stress. In particular, the model assumes the shear stresses to rise in the matrix and at the interface (not in the fiber).

The radial variation of shear stress in the matrix, τ, at a given axial distance x from the fiber mid-point, can be easily calculated by equating the shear forces on neighboring annuli (r_1, r_2 being the radii, dx being the length)

$$2\pi r_1 \tau_1 dx = 2\pi r_2 \tau_2 dx \qquad (3.50)$$

leading to

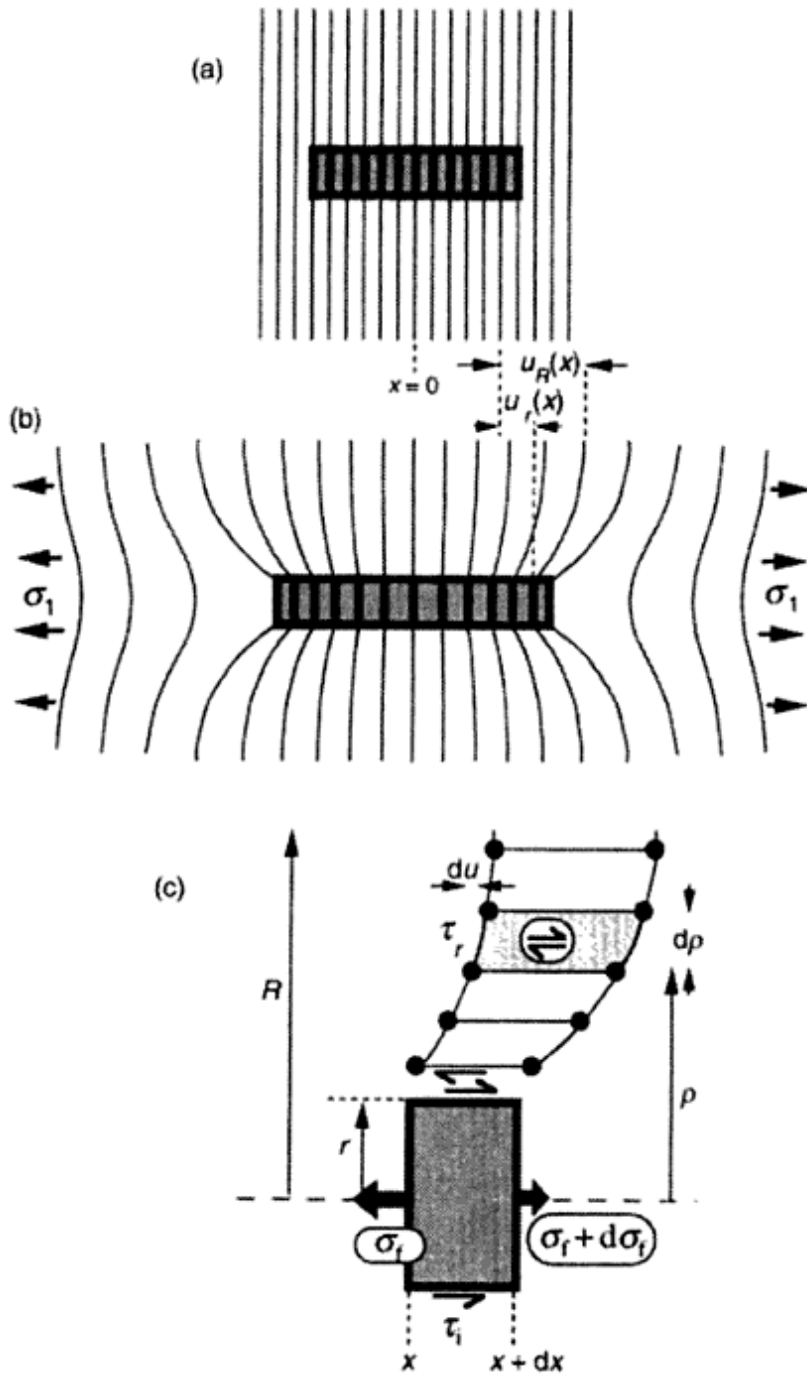$$\frac{\tau_1}{\tau_2} = \frac{r_2}{r_1} \qquad (3.51)$$

Figure 3.10 Schematic illustration of the basis of the shear lag model, showing: (a) the unstressed system, (b) axial displacements u introduced on applying tension parallel to the fiber and (c) the variation with radial location of the shear stress and strain in the matrix [100].

Therefore the shear stress τ in the matrix at any radius ρ can be related to τ_i, shear stress at the fiber/matrix interface, as by

$$\tau = \tau_i \left(\frac{r}{\rho}\right) \tag{3.52}$$

r being the fiber radius.

The strain field around the fiber can thus be defined in terms of the displacement u of the matrix in the x-direction, relative to the initial position (original configuration). The increment of this displacement, du, on moving out from the fiber axis by $d\rho$, is connected to the shear strain γ, and hence to shear stress by the shear modulus G_m

$$\frac{du}{d\rho} = \gamma = \frac{\tau}{G_m} = \frac{\tau_i}{G_m}\left(\frac{r}{\rho}\right) \tag{3.53}$$

For any given value of x, the difference between u_R, the axial displacement of the matrix at a radius R and the displacement of the interface (radius r) is given by the following integration

$$u_R - u_r = \int_{u_r}^{u_R} du = \frac{\tau_i r}{G_m} \int_r^R \frac{d\rho}{\rho} = \frac{\tau_i r}{G_m} \ln(R/r) \tag{3.54}$$

The matrix strain is assumed to be uniform, far from the immediate vicinity of the fiber. The radius R represents a far-field location where this condition becomes operative. Whereas the composite is made up of an array of fibers, the appropriate value of R/r is related to the proximity of neighboring fibers and hence to the fiber volume fraction, V_f. In particular, the exact relationship between R/r and V_f depends on the way the fibers are arranged; however, because R/r appears in a logarithmic term, the final result is very slightly depending on the details of the fiber arrangement.

The build-up of tensile stress in the fiber σ_f is determined from the distribution of interfacial shear stress. Referring to Figure 3.10c, the basic force balance acting on an element of the fiber is

$$2\pi r \tau_i dx = -\pi r^2 d\sigma_f \qquad (3.55)$$

$$\frac{d\sigma_f}{dx} = -\frac{2\tau_i}{r} \qquad (3.56)$$

The variation of τ_i with x is unknown *a priori*, but the equation (3.56) can be used to relate it to displacements and hence to axial strains. It is assumed that there is no shear strain in the fiber and that the interfacial adhesion is perfect ($u_r = u_f$, where u_f is the displacement of the fiber surface). By using the common relationship that relates the shear modulus to the Young modulus for a homogeneous and isotropic material,

$$G_m = \frac{E_m}{2(1 + v_m)} \qquad (3.57)$$

and its substitution in (II) leads to

$$\frac{d\sigma_f}{dx} = -\frac{2E_m(u_R - u_r)}{(1 + v_m)r^2 \ln(\frac{1}{V_f})} \qquad (3.58)$$

The displacements are unknown, but their differentials are related to identifiable strains. For the fiber we have

$$\frac{du_r}{dx} = \epsilon_f = \frac{\sigma_f}{E_f} \qquad (3.59)$$

The corresponding expression for the matrix is less well defined. The differential of u_R will approximate to the far-field matrix strain,

$$\frac{du_R}{dx} = \epsilon_m \qquad (3.60)$$

Considering the definitions of ϵ_m and ϵ_f, we have

$$\frac{d^2\sigma_f}{dx^2} = -\frac{2E_m}{(1+\nu_m)r^2\ln\left(\frac{1}{V_f}\right)}\left(\frac{du_R}{dx} - \frac{du_r}{dx}\right)$$

$$= -\frac{2E_m}{(1+\nu_m)r^2\ln\left(\frac{1}{V_f}\right)}(\epsilon_m - \frac{\sigma_f}{E_f})$$

(3.61)

that can be rearranged in the following form

$$\frac{d^2\sigma_f}{dx^2} - \frac{2E_m}{E_f(1+\nu_m)r^2\ln\left(\frac{1}{V_f}\right)}\sigma_f = -\frac{2E_m}{(1+\nu_m)r^2\ln\left(\frac{1}{V_f}\right)}\epsilon_m$$

(3.62)

Introducing the shear lag parameter, β, defined as by[2]

$$\beta = \frac{2E_m}{E_f(1+\nu_m)\ln\left(\frac{1}{V_f}\right)}$$

(3.63)

the differential equation can be written as

$$\frac{d^2\sigma_f}{dx^2} - \left(\frac{\beta}{r}\right)^2\sigma_f = -\left(\frac{\beta}{r}\right)^2\epsilon_m$$

(3.64)

Assuming that there is no stress at the ends of the fiber (the load is applied only to the matrix, as stated before), the solution to this differential equation is given by

---

[2] Several definitions are available for β. For example, McCartney [98] and Nairn [99] define the shear lag parameter as:

$$\beta_{Nairn,McCartney} = \frac{1}{R_f}\sqrt{\frac{2}{E_f E_m}\left[\frac{E_f V_f + E_m V_m}{\frac{V_m}{4G_f} + \frac{1}{2G_m}(\frac{1}{V_m}\ln\frac{1}{V_f} - 1 - \frac{V_m}{2})}\right]}$$

$$\sigma_f(x) = E_f \epsilon_m \left[1 - \frac{\cosh(\frac{\beta x}{r})}{\cosh(\frac{\beta L}{r})} \right] \qquad (3.65)$$
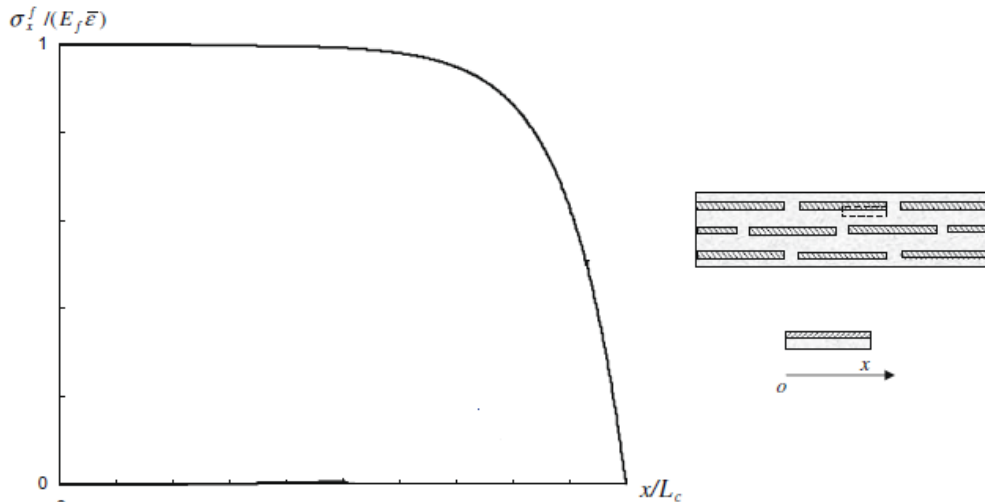
with L being fiber length.

Figure 3.11 Typical example of axial stress in the fiber predicted by shear lag model

This model predicts that tensile stress is zero at the fiber ends and shows a maximum in the centre (Figure 3.11). Conversely, the interfacial shear stress is zero in the center and maximum at the ends. If the fiber has a high aspect ratio, it means that is long enough for the tensile stress to build up until the fiber has a strain equal to that of the matrix and the composite. This gives rise to the 'positively affected length' (PAL), a plateau region of the fiber stress curve and zero interfacial shear stress. The region of the fiber near the ends (the 'transfer' or ineffective' length) - that is out of the PAL - is less heavily stressed than this central plateau region, so that the average fiber stress is lower than in long-fiber composite subjected to the same external load. The reinforcing efficiency decreases as the fiber length is reduced, since this increases the proportion of the total fiber length which is not fully loaded.

In the positively affected length the strain in the fiber builds up to the plateau (matrix) value. Provided that the system remains fully elastic and there is no interfacial sliding, this value depends only on the elastic constants of fiber and matrix (for instance, in case of a stiffer matrix, such as a metal, the stress

transfer length will be shorter, as a result of higher interfacial shear stresses). For short fibers, the stress does not build up to a plateau value. Such fibers do not provide a very efficient reinforcement because they carry much less stress than longer fibers would in the same system.

The equation for the stress in the fiber, together with the assumption of an average tensile strain in the matrix equal to that imposed on the composite, can be used to evaluate the composite stiffness. This leads to:

$$\sigma_1 = \epsilon_1 \left[V_f E_f \left(1 - \frac{tanh\frac{\beta L}{2r}}{\frac{\beta L}{2r}} \right) + (1 - V_f)E_m \right] \tag{3.66}$$

Hence the elastic modulus of the composite, with the respect to the fiber direction, is given by

$$E_1 = V_f E_f \left(1 - \frac{tanh\frac{\beta L}{2r}}{\frac{\beta L}{2r}} \right) + (1 - V_f)E_m \tag{3.67}$$
,

This is a particular form of rule of mixtures that takes into account for the fiber modulus reduction owing to the lack of ideality due to the stress transfer conditions.

Many attempts have been made to model the micromechanics of composites under several conditions; in particular, the work of McCartney [98] is worthy of note for the rigorous formulation of the elastic problem and for the analysis of several conditions (matrix crack in a perfectly bonded composite, fiber crack in a perfectly bonded composite, matrix crack with a frictional slip at the interface). Remarkable models have also been developed for single and multi-fiber pull-out tests [101], for fragmentation test [102] and for viscoelastic matrix [103] and elastoplastic matrix composites [104].

3.2.3 Stress transfer in cord-rubber composites

Paris [105] has developed the solution to stress transfer problem for the case of cord-rubber composites. This approach is based on the classical shear lag model in which the constitutive equation for the cord developed by Costello [27] is introduced to take into account the tension-twisting coupling.
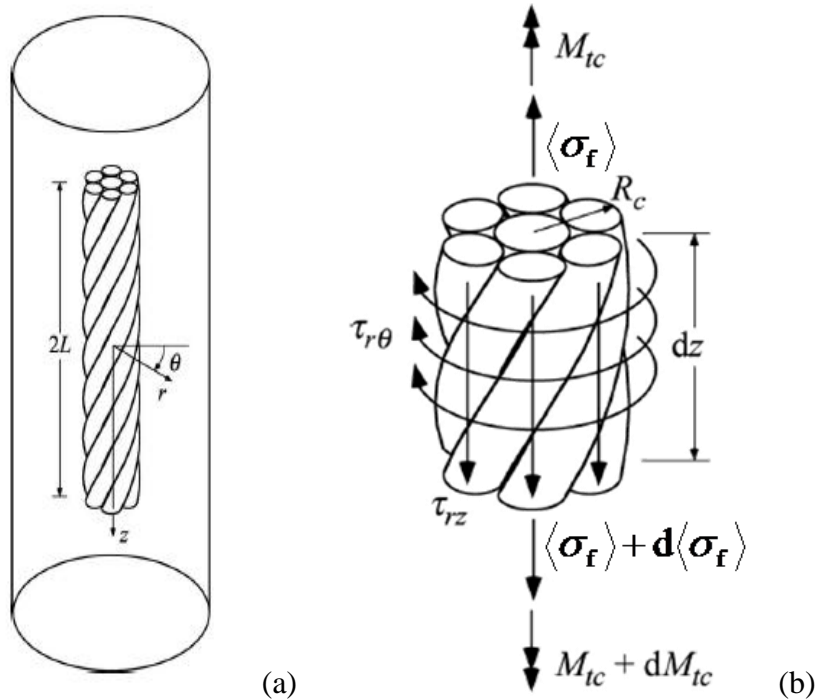

Figure 3.12 Schematic for Paris formulation: a) cord-rubber model; b) an element of the cord

The cord-rubber composite and the cord element with the details of the symbolism adopted in this model are shown in Figure 3.12.
The equilibrium equations (written in cylindrical coordinates) for the cord element yield

$$\frac{\partial \langle \sigma_f \rangle}{\partial z} = -\frac{2\tau_{rzi}}{R_c} \tag{3.68}$$

and

$$\frac{\partial M_t}{\partial z} + 2\pi R_c^2 \tau_{r\theta i} = 0 \tag{3.69}$$

77

For the matrix, the equilibrium equations in cylindrical coordinates yield

$$\frac{\partial \sigma_r}{\partial r} + \frac{1}{r}\frac{\partial \tau_{r\theta}}{\partial \theta} + \frac{\partial \tau_{rz}}{\partial z} + \frac{\sigma_r - \sigma_\theta}{r} + f_r = 0 \tag{3.70}$$

$$\frac{\partial \tau_{r\theta}}{\partial r} + \frac{1}{r}\frac{\partial \sigma_\theta}{\partial \theta} + \frac{\partial \tau_{\theta z}}{\partial z} + \frac{2\tau_{r\theta}}{r} + f_\theta = 0 \tag{3.71}$$

$$\frac{\partial \tau_{rz}}{\partial r} + \frac{1}{r}\frac{\partial \tau_{\theta z}}{\partial \theta} + \frac{\partial \sigma_z}{\partial z} + \frac{\tau_{rz}}{r} + f_z = 0 \tag{3.72}$$

Assuming that load transfer occurs between cords and matrix through shear stresses at the interface and that cord ends are stress-free, axial stress and twisting moment in the cord are given by the following expressions

$$\left\langle \sigma_f \right\rangle \propto \sum_{i=1}^{2} d_i \cosh(\lambda_i z) + \sum_{j=1}^{2} d_j \sinh(\lambda_j z) \tag{3.73}$$

$$M_t \propto \sum_{i=1}^{2} k_i d_i \cosh(\lambda_i z) + \sum_{j=1}^{2} k_j d_j \sinh(\lambda_j z) \tag{3.74}$$

where $d_{i,j}$, $k_{i,j}$ and $\lambda_{i,j}$ are parameters depending on cord elastic constants (C_k) (consequently dependent on cord geometry) and on matrix shear modulus.

An example of cord axial force and shear stress at the interface (calculated by Paris for the case study of steel cord-rubber composite) is shown in Figure 3.13. The cord axial force is zero at the ends of the cord. The rate of change of the cord axial force is larger near the cord ends and decreases to zero at the center of the cord. The maximum cord axial force occurs at the center of the cord and is significantly greater for long cords than for short ones, and the maximum axial shear stress at the cord/matrix interface occurs at the ends of the cord and is greater for long cords than it is for short ones. As the length of the cord increases, the value of the cord axial force approaches the value of the axial force of a cord subjected to the composite average axial strain and rate of twist. Also, the cord axial twisting moment is zero at the ends of the cord. The circumferential shear stress and the rate of change of the cord axial twisting moment are greatest near the ends of the cord and decrease to zero at the center of the cord. The maximum cord axial twisting moment occurs at the center of the cord and is significantly greater for long cords than for short ones, and the circumferential shear stress at the interface occurs at the ends of the cord and is greater for long cords than it is for short ones. As the length of the cord

increases, the value of the cord axial twisting moment approaches the value of the twisting moment of a cord subjected to the composite average axial strain and rate of twist. This model hence underlines the effect of embedded cord length on the final response of the composite and leads to the final dependence of the modulus of the embedded cord on the shape factor (defined as the ratio of cord length to cord diameter), as shown in Figure 3.14.
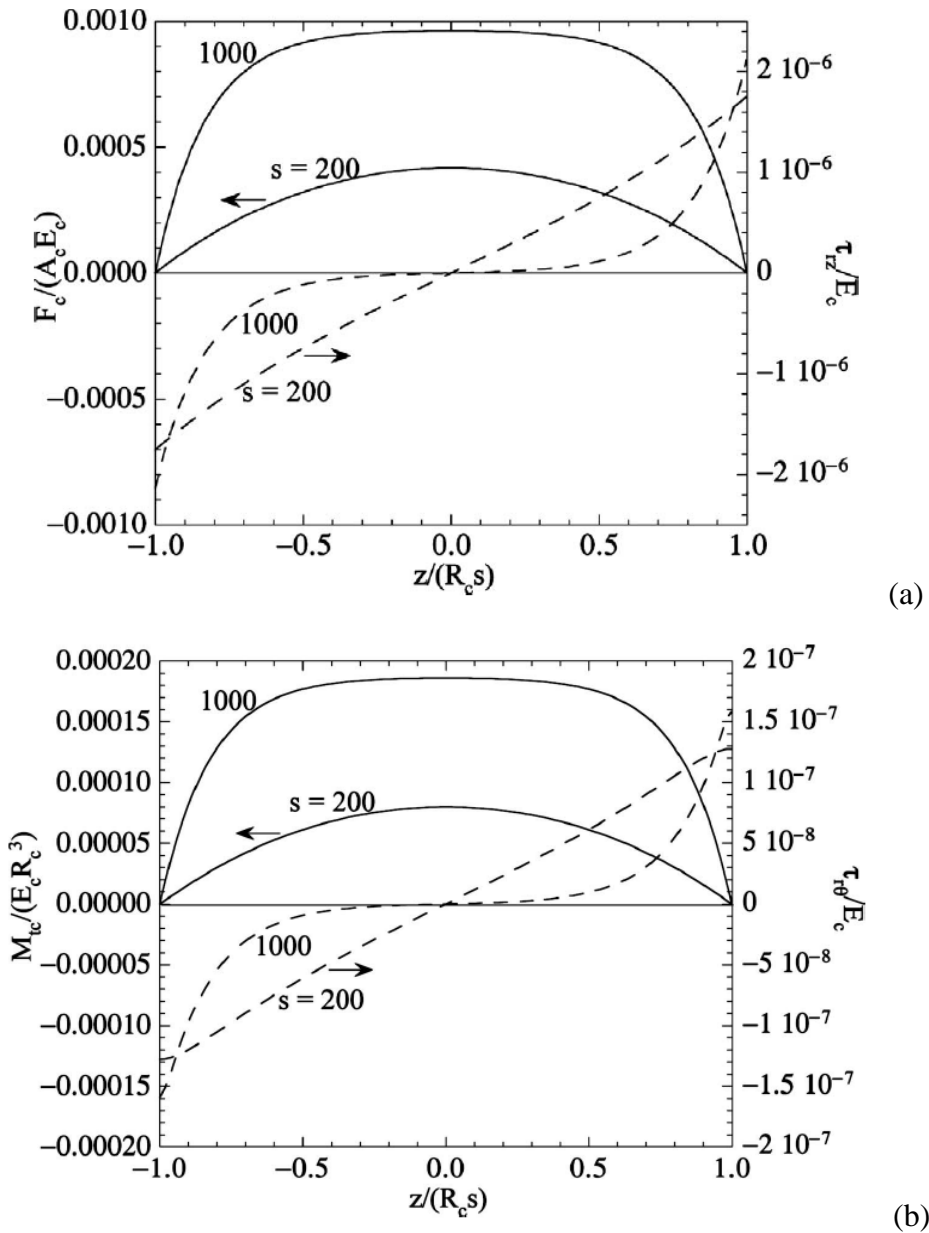

(a)

(b)

Figure 3.13 Cord axial force and shear stress at the interface (a) and cord twisting moment and circumferential shear stress at the interface (b) [105]
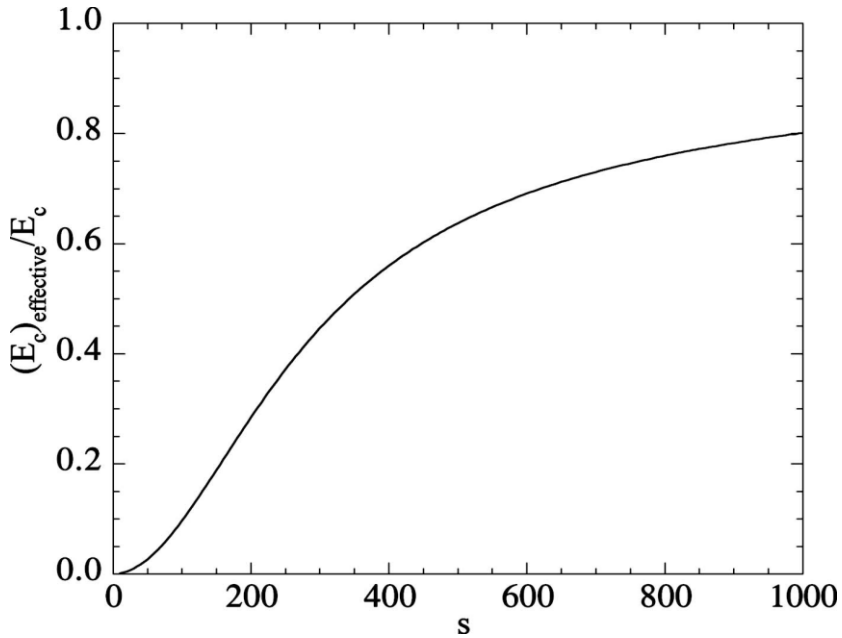
Figure 3.14 Embedded cord modulus as a function of the shape factor [105]

These results, however, apply only in to the dilute suspension case. In the nondilute case, the degrading effect of a finite *L/2r* value would probably be less severe, but still qualitatively the same as that discussed in this section.

Chapter 4

Experimental investigation of macromechanics of cord-rubber composites

4.1 General considerations

The experimental characterization of materials is a question of paramount importance in applied science and engineering because it provides basic features about the behavior of a material when it is exposed to several conditions. For instance, the response of a material to an external mechanical solicitation gives a lot of information that are extremely useful in the design of products and structures. Constitutive behavior, stiffness and elongation at break are elementary examples of mechanical properties that are evaluated in the choice of a material for a specific structural application. Mechanical testing of materials has been one of the major and critical research areas in material science, since the era of industrial revolution. At the macro-scale, many standardized techniques have been developed to measure reliable values of elastic modulus, yield strength, fatigue strength, fracture toughness and other properties such as adhesion and residual stress that represent characteristic and universally recognized features for a given material [106].

The choice of a material is finally performed on the base of the combination of all its properties (e.g., thermal, transport and electric) that are pondered according to the requirements of the final product. In particular, in the last

decades, most of modern technologies have been requiring materials that offer peculiar combinations of several properties that cannot be found - at the same time - in conventional materials. In composite materials, the combination of a matrix and a reinforcement leads to final chemical-physical properties which cannot be found in the separated components and that can be easily tailored; hence they have been fitting the requirements of several niche fields (aerospace, building, ship, automobile, biomedical). However, the heterogeneous nature of the composite materials entails a more complex (anisotropic) behavior. Hence, all the more reason for the characterization of composite materials to require a larger number of information for a detailed and complete investigation.

Cord-rubber composites adopted in tire carcass are a typical example of complex composite materials. As discussed in Chapter 2, matrix is an elastomeric compound that is heterogeneous on a micro-scale and that shows a highly non-linear viscoelastic behavior. Also polymeric cords are structures made up of thousands of viscoelastic filaments that are twisted together in a cohesive, hierarchical structure. The twisted nature of cords leads to a peculiar axial tension-twisting coupling, as stated in Chapter 3. The lamina hence consists of two phases that significantly differ one from the other and has an overall trigonal behavior that represents a very intricate challenge from both experimental and theoretical perspectives. Despite this complex nature, the knowledge of the response of a cord-rubber lamina and of the two individual phases is a crucial element in tire design and production.

An intensive and detailed experimental characterization of the macroscopic behavior of cord-rubber unidirectional lamina and of the constituent phases has been carried out. In particular, in the light of a multi-scale analysis of this material, the experimental characterization of the macromechanics of cord-rubber composite represents the first step towards a general understanding of the main phenomenology of this material due to non-linearities, anisotropy, time-dependent behavior. Furthermore, the macroscopic investigation of the behavior of the individual phases is also essential to get the information necessary for the implementation of both analytical and numerical models able to predict both the micro- and the macromechanics of the overall composite material.

This chapter addresses the experimental characterization of macromechanics of cord-rubber composites, with particular emphasis on both elastic and viscoelastic aspects. Furthermore, for the aforementioned reasons, the behavior of the individual constituents has been investigated on a macro-scale in order to get an overview on mechanical behavior, glassy transition, volumetric behavior and relaxation times of both phases.

4.2 Materials

Two main systems have been characterized:

- model composite
- real composite

Both the composite materials, at this stage of the research activity, rubber and the different adopted cords were gently supplied by Bridgestone Technical Centre Europe (TCE), Rome (Italy).

The model composite is made up of rubber compound reinforced with PET dipped cords, whose features are given as follows. The adopted cord is made up of 2 yarns, whose linear density corresponds to 1670 dtex; cord construction is characterized by a twist level of 270x390 and a twist angle of 29.98°. The term 'model' refers to the non-practical nature of these model systems, characterized by a very low cord fraction (dilute system, with no cord-cord interaction), therefore they are not actually used in tire production. The nominal cord volume fraction was 5.5% (as evaluated on the basis of geometrical considerations). Model pads were been prepared by compression molding in the laboratories of Bridgestone TCE.

Also ten different cord-rubber 'real' pads characterized, whose features are shown in table 4.I. They were prepared by calendering, according to the industrial manufacturing process. All of these laminae are made up of the same rubber compound; nevertheless, reinforcement changes, for construction as well as filament material (PET and rayon). It is useful to attribute an identification code to each real pad; for this purpose, cord end count (i.e. the number of cords in a 10 cm-wide lamina) has been adopted to identify each real pad under examination. In particular, pads 60, 90, 114, 120, 136 and 140 are built with the same cord and differ mainly for cord end count. Furthermore, pad 120 has been produced with three different thicknesses.

Figure 4.1 Schematic of a 'model' and of a 'real' cord-rubber lamina

PET CORD-RUBBER COMPOSITES								
cord end count	60	90	100	111	114	120	136	140
cord construction [dtex]	1100/2	1100/2	2200/2	1670/2	1100/2	1100/2	1100/2	1100/2
twist level	470x470	470x470	340x340	270x390	470x470	470x470	470x470	470x470
cord nominal diameter [mm]	0.56	0.56	0.78	0.68	0.56	0.56	0.56	0.56
pad nominal thickness [mm]	0.66	0.67	1.26	1.2	1.10	0.71 / 1.18 / 1.80	0.89	0.8
cord fraction [%]	23	33	38	35	25	38.8 / 23.8 / 15.6	36	41

Table 4.I Features of PET cord composites

RAYON CORD-RUBBER COMPOSITES		
cord end count	98	116
cord construction [dtex]	1840/3	1840/2
twist level	402x402	472x472
cord diameter [mm]	0.84	0.71
cord fraction [%]	40	41
pad thickness [mm]	1.27	1.08

Table 4.II Features of rayon cord composites

4.3 Experimental characterization

The mechanical behavior (both elastic and viscoelastic) of cord-rubber composites has been characterized by tensile test and dynamic-mechanical analysis (DMA). First, preliminary tests were performed on rubber and on cord to obtain a theoretical reference frame for the composite. In particular, information on glassy transition and on relaxation times of both phases were provided through DMA and stress relaxation test; also dilatometric measurements were conducted in order to gain information on the volumetric behavior (and, consequently, on the bulk modulus) of both rubber and cord material. Tensile tests also provided information on the elastic behavior and failure of the two phases. In fact, both the analytical models mentioned in Chapter 2 and the model developed at finite elements (whose details will be given in Chapter 6) require the availability of specific information on the two separated phases.

4.3.1 Stress relaxation

The viscoelastic behavior of matrix and reinforcement has been characterized through stress relaxation. Test on cord have been performed at room temperature by using the dynamic-mechanical thermal analyzed TA Q800 (TA Instruments, New Castle, DE, USA). Custom-made clamps were adopted to fix the sample (with knots at the ends to further prevent the slippage). Under a preload of 2 N, a constant tensile strain of 0.1% is applied while the instrument records the force necessary to keep it. Tests on rubber compound have been performed at room temperature by using the universal testing machine INSTRON mod. 5566 (Norwood, MA, USA). Tests have been performed at several strain levels (1, 5, 10, 20, 50 and 100%), applied at a constant strain rate (8.5 mm/s).

4.3.2 Dilatometry

The dilatometric behavior of a material is representative of the response of the materials itself, in terms of volume changes, to the imposed changes in pressure and/or temperature. The dilatometer is also used to measure bulk properties such as the specific volume as a function of pressure and temperature, the bulk creep compliance and thermal (equilibrium) expansion coefficient. The bulk

compliance may be thus inverted to yield the bulk modulus. The measurements of all the these properties are performed by monitoring the volume change of the specimen which results from the imposed changes in pressure and/or temperature, by measuring the change in specimen length, L(t, T, P), with the aid of a built-in linearly variable differential transformer (LVDT). In order to get information on the compressibility of the rubber and of the PET cord, pressure-Volume-Temperature (PVT) tests have been performed. The dilatometric behavior has been investigated using an high pressure Gnomix dilatometer (GNOMIX Inc. Boulder, CO USA) that permits the determination of specific volume of polymer solids and melts in the range of temperature from room temperature to 400°C and from pressure between atmospheric and 200 MPa. A schematic of the apparatus is shown in Figure 4.2. The sample is enclosed in a piezometer cell: this is a rigid sample cell, one of which is closed off by a flexible metal bellows. The space in the cell is filled with a confining fluid under vacuum (mercury). A hydrostatic pressure of silicone oil is produced in the pressure vessel surrounding the cell by a motorized pump. This pressure is transmitted to the contents of the sample cell by a flexible bellows. The deflection of the bellows is a measure for the volume change of the sample; the length change of the bellows is measured by a linear variable differential transducer (LVDT). Temperature is reached through an electrical heater surrounding the vessel.

Rubber sample, consisting of small slices collected into a nickel-cup, has been subjected to isothermal compressions ('ITS steps') from room temperature to 180°C, at pressures up to 200 MPa. Concerning PET cord, a compact, bundle-like sample has been created. Initially yarn was obtained by untwisting cord, previously subjected to a procedure for dip elimination (as suggested by Bridgestone TCE). A loom press was used to reduce fiber waviness (deriving from cord twisted structure) and then, finally, yarn was cut in 2 cm-long pieces. These pieces were collected in a bundle and placed in the nickel-cup. ITS were performed on PET sample at pressures up to 200 MPa, from room temperature to 270°C (above melting point), followed by cooling until room temperature.
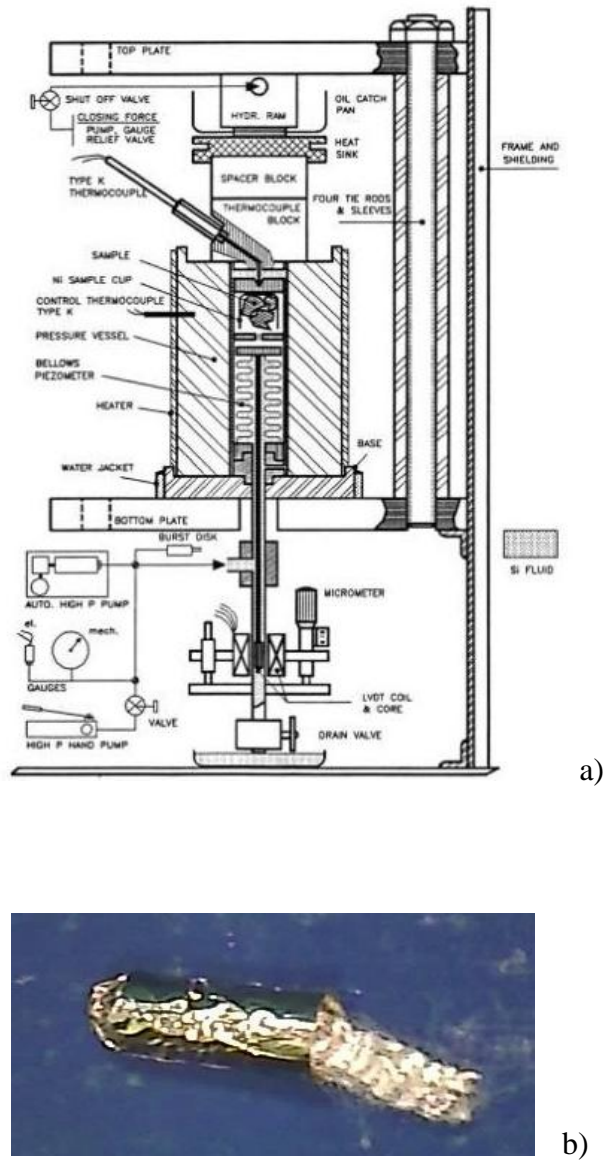
a)

b)

Figure 4.2 Details on dilatometry: a) schematic of GNOMIX pVT apparatus; b) bundle of PET fiber into the Ni-cup

4.3.3 Dynamic-mechanical analysis (DMA)

Dynamic mechanical analysis (DMA) yields information about the mechanical properties of a specimen as a function of time and temperature by subjecting it to a small, usually sinusoidal, oscillating force. Viscoelastic characterization of the model composite and of the constitutive phases has been carried out mostly by using a dynamic-mechanical thermal analyzer (Q800, TA Instruments, New Castle, DE, USA). Tests of rubber and of composite have been performed with a tension-film clamping system, allowing for the testing of maximum 25mm-long, 6.5mm-wide and 2mm-thick samples. For cords, special clamps were used to ensure no slip during test. Uniaxial samples were created by cutting the original pad with a scalpel into a small rectangle, the dimension being the aforementioned ones. Also off-axis specimens with cord at different orientation ($\theta = 0°$, 30°, 60°, 90°) were investigated. Furthermore, a new clamping system has been designed, created and tested for the improvement of composite testing. These new custom-made grips have been designed to act as a sort of 'appendices' that both grip sample ends and block cords, in order to improve mechanical response of the uniaxial lamina. This system consists of steel clamps that are complementary to instrument clamping fixtures. Specimens were prepared with cords coming out from the ends (Figure 4.3). Dynamic temperature scan measurements were performed over the temperature range of -45°C to 180°C, with a heating rate of 5 °C/min, under a dynamic strain with amplitude of 0.025% of the pre-strained sample length and at a constant frequency of 10 Hz. In fact the use of tensioning clamps prescribes the application of a preload, which is a static force keeping the sample taut, whose value is determined in the linear zone of a predetermined load-extension curve.
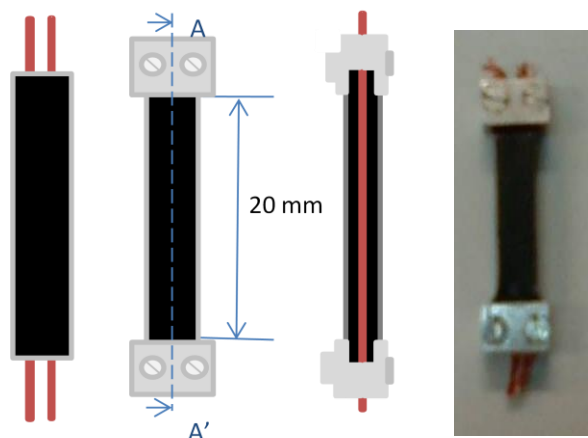

Figure 4.3 Custom-made clamping system (schematic representation and photo)

4.3.4 Tensile test

Mechanical properties of materials such as elastic or Young modulus, tensile strength, yielding point are generally determined by tensile tests. In its simplest form (uniaxial tension), tensile test is conducted by gripping opposite ends of a specimen within the load frame of a test machine. A stretching deformation is applied by the machine, and the load cell measures the force necessary to generate that elongation. During the process, force-extension data, are monitored and recorded and, by knowing the initial geometry of the specimen (i.e., cross area and length), they are set off in stress and strain data.

The mechanical response of rubber compound, all the cords and the cord-rubber composites was investigated by using a universal machine (INSTRON mod. 5566, (Norwood, MA, USA) equipped with a load cell of 10 kN. Generally, the elongation has been measured by monitoring crosshead position; nevertheless, in composite testing also an optical method has been adopted, based on the use of two high resolution CCD micro-cameras mounted on a movable stage and able to recognize, follow and record the displacement of white markers drawn on the sample (Figure 4.4a).

Dumbbell rubber compound specimens have been tested according to the international standard ASTM D412-98a. Cords were tested according to the standard procedure ASTM D885-07, by using particular grips (Figure 4.4b) that are specially designed to overcome the slipping and breaking problems associated with these samples. Tests on both materials were performed at strain rates as recommended by the aforementioned ASTM standards. Regarding the ideal composite, rectangular specimens with a nominal width of 10 mm and several nominal lengths (50 – 60 - 90 - 100 – 140 - 150 - 180 - 200 mm) have been cut from the original pad using a scalpel. Rectangular specimens have been cut also from real composite pads; however, only four gauge lengths were chosen (50 – 100 – 150 – 200 mm).

Composites have been tested at both quasi-static conditions (i.e. 1%/min) and at 120%/min. For each set (material, test condition), tests were repeated ten times and results were averaged.

a)

b)

Figure 4.4 Special set-ups for tensile test : a) CCD cameras coupled to the
dynamometer INSTRON and b) grips for rope testing

4.4 Results and discussion

4.4.1 Stress relaxation

Results of stress relaxation test on dipped cord and on rubber composite are shown in Figure 4.5 and 4.6, respectively. Marked relaxation reveals that cord has a strong viscoelastic behavior and the initial fall of stress provides information on the relaxation time, found of the order of 300 s. The results of stress relaxation tests performed on rubber reveal that the relaxation time is around 100 s and that the equilibrium value of stress is clearly proportional to the applied strain. The effect of raise time on relaxation processes has also been investigated, revealing a strong dependence of material response on this parameter (Figure 4.6b).
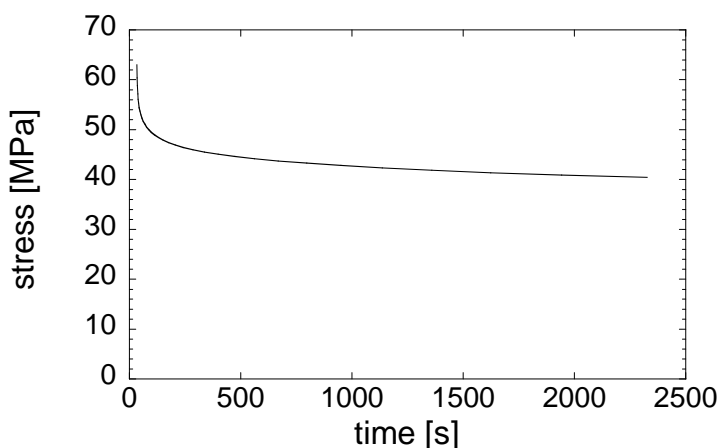
Figure 4.5 Stress relaxation of dipped cord
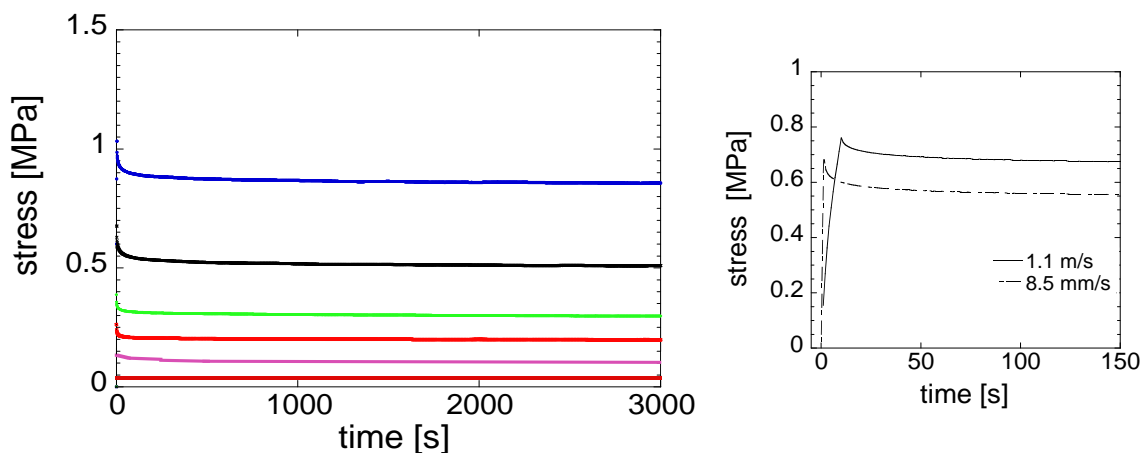
Figure 4.6 Tensile stress relaxation on rubber at different strain : 1% (orange), 5% (pink), 10% (red), 20% (green), 50% (black), 100% (blue). Inset: effect of strain rate

4.4.2 Dilatometry

pVT tests performed on rubber and on cord have provided information on the volumetric behavior of the two materials, in terms of volume changes as a function of pressure and temperature. Results are shown in Figures 4.7 and 4.8. Since the dilatometer GNOMIX measures volume changes (Δv) evaluated with respect to a reference volume, it is necessary to correct the raw data with a constant value. The calculation of the so-called 'additive volume' is performed on the basis of the specific volume of the sample material as measured in controlled conditions of pressure and temperature (generally ambient conditions). A literature value has been used for PET fiber (found to be equal to 0.741 cm^3/g [107]); concerning rubber, the room temperature specific volume of 0.887 cm^3/g has been provided from Bridgestone TCE. Furthermore, since measurement have been performed in the pressure range 10-200 MPa, the ambient pressure data have been extrapolated by using the Tait equation [108].

The specific volume decreases with the application of the increasing hydrostatic compression and increases by heating. In particular, the presence of discontinuity among the ITS curves, at a certain temperature, provides information on an eventual melting transition. The test performed on PET shows the presence of a melting transition (starting at 235°C ca.) in the investigated region.

pVT measurement also gives information on the bulk modulus of a materials, defined as

$$K = -\hat{V}\frac{\partial P}{\partial \hat{V}}$$

(4.1)

From isothermal compression, it is straightforward the evaluation of $\dfrac{\partial P}{\partial \hat{V}}$. Thus, bulk modulus of rubber has been found to be 2.67 GPa, in line with values that can be found in literature [40]. Regarding the measurement performed on PET cord, at low pressures it is possible that the confining fluid does not completely fill voids in the bound-like sample; in this case, for the determination of bulk modulus, high pressure data have been elaborated to be sure that all the material in the Ni-cup was surrounded by mercury. According to this procedure, and supposing that cord behaves like fibers to hydrostatic compression, the measured value of bulk modulus has been found to be equal to 5.79 GPa.
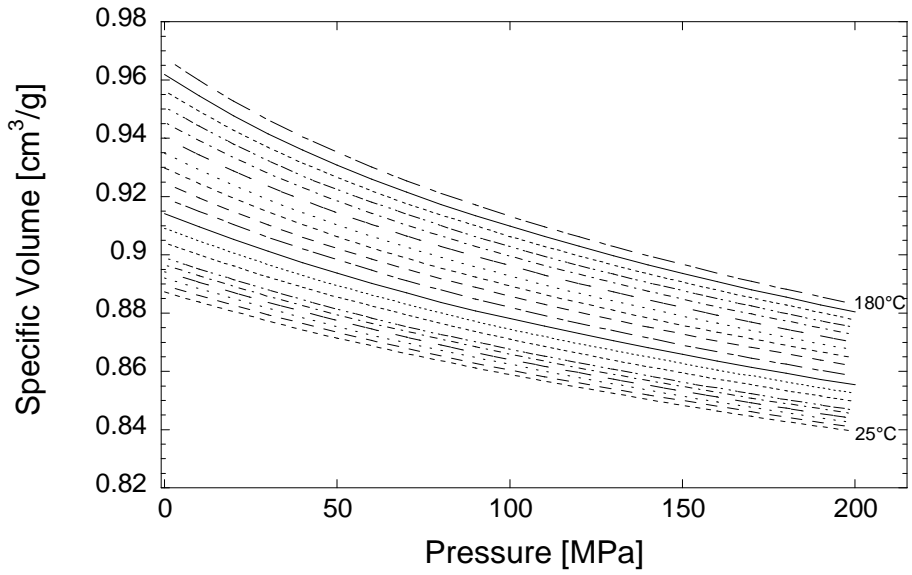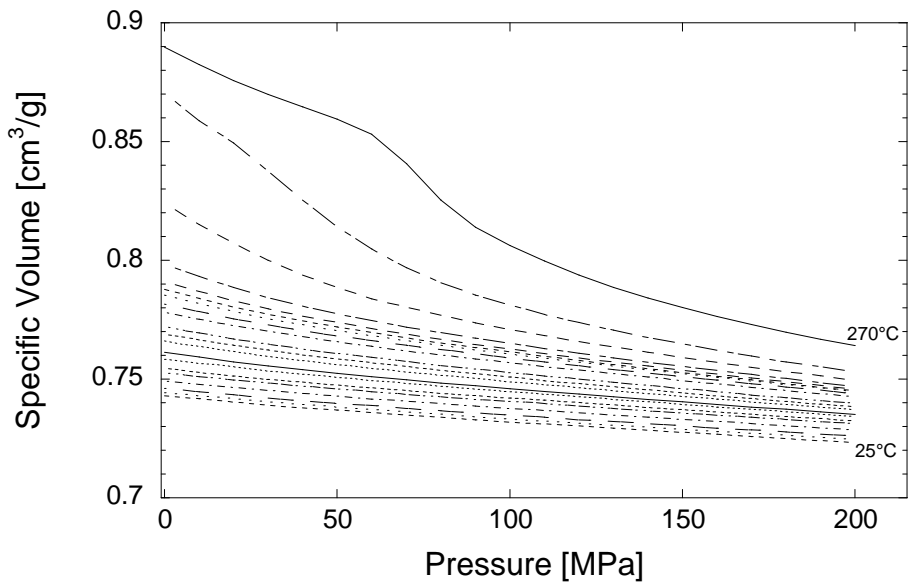
Figure 4.7 Isothermal compression on rubber

Figure 4.8 Isothermal compression on PET cord.

4.4.3 Dynamic-mechanical analysis

Temperature scan tests have been performed on rubber compound and on PET dipped cord; results are shown in Figure 4.9, showing E' and tanδ as a function of temperature. The presence of a fall in E', along with a peak in tanδ curve, reveals the glassy transitions for rubber (found to be -20 °C ca.) and for PET dipped cord (ca. 135 °C). Results of temperature scan test performed on model composite, for different values of angle θ, are shown in Figure 4.10. The response of composite lamina, in terms of E' and tanδ, is strongly influenced by cord orientation: the behavior of the uniaxial lamina ($\theta = 0°$) is governed by cord response while transverse properties (represented by lamina with $\theta = 90°$) are matrix-dominated. All the other orientations show an intermediate behavior.

a)

b)
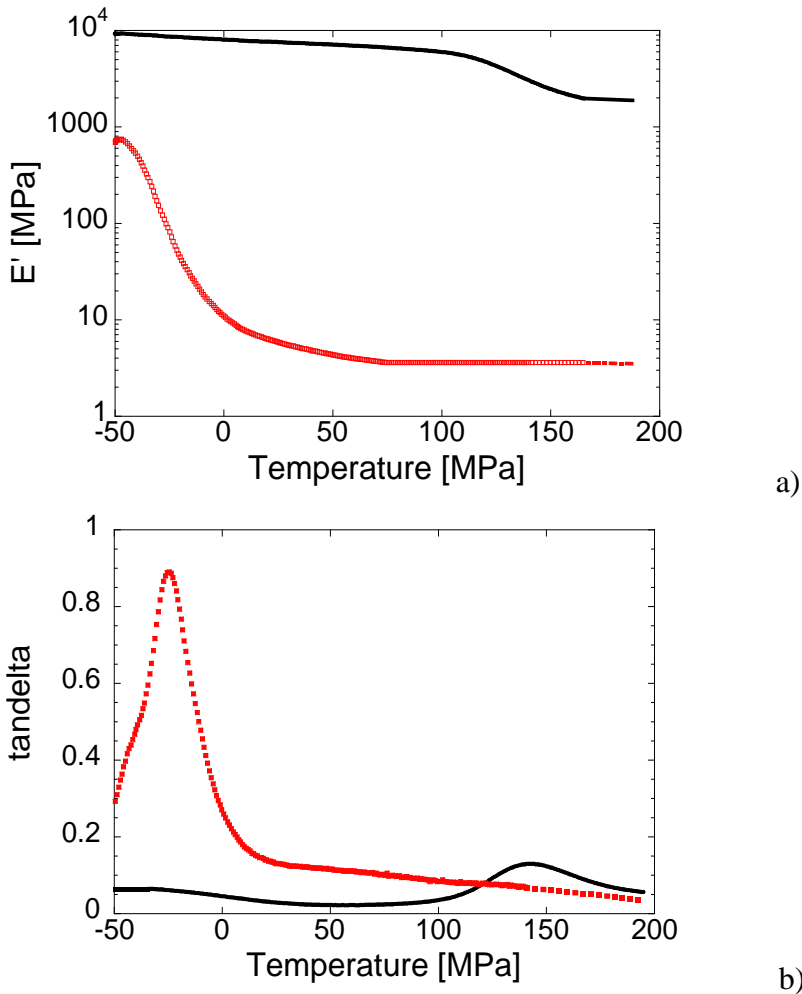
Figure 4.9 Temperature scans for rubber (red) and PET dipped cord (black): storage modulus (a) and tanδ (b)

The sharp fall of E' is representative of a transition, which is also shown by a peak of tanδ. So, we notice that all composite show glassy transition of rubber; while glassy transition of cords is only shown by the uniaxial composite, although it is not well-defined.
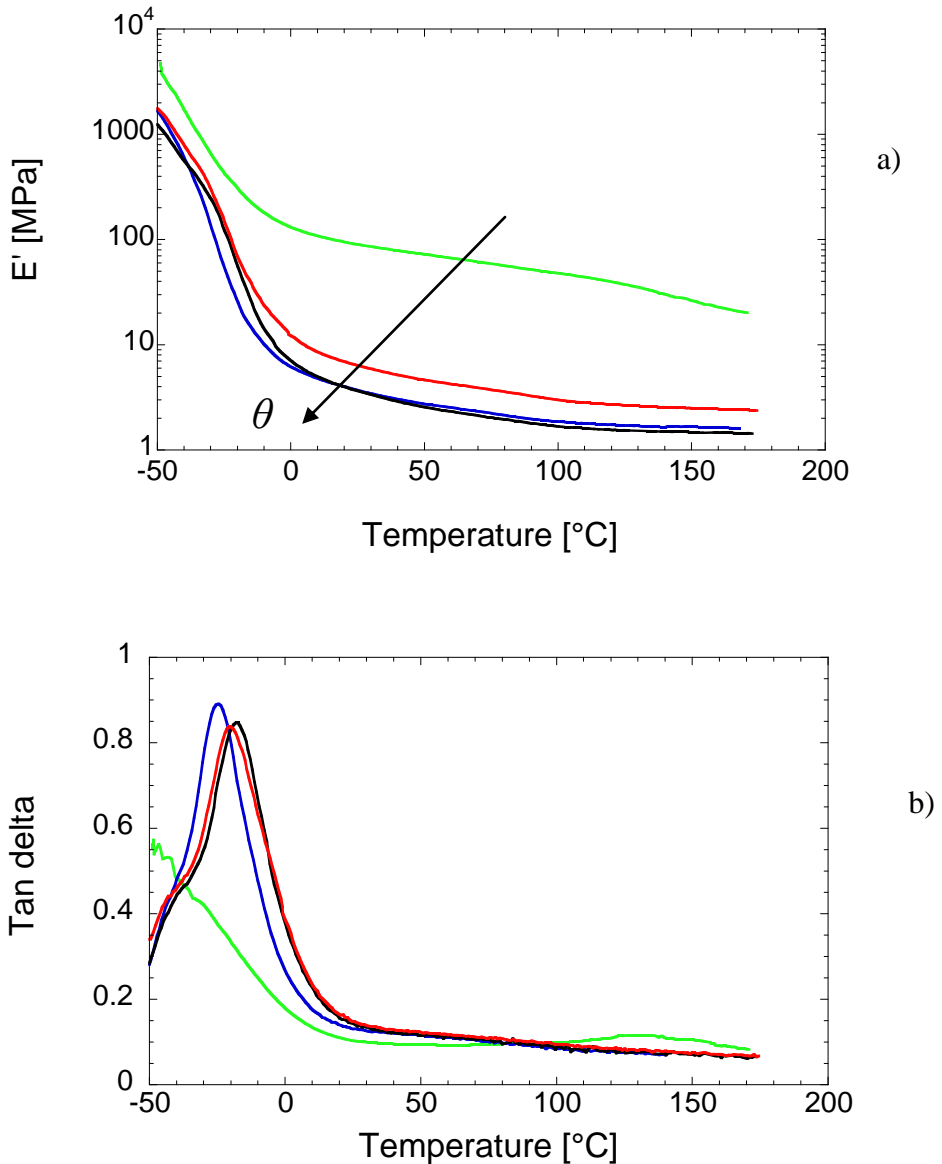

Figure 4.10 Effect of angle θ on E' (a) and tanδ (b) for model composites: 0°(green), 30° (red), 60° (black) and 90° (blue)

In order to get a reference frame for the quality of composite testing, the values of $E'(T)$ measured for rubber and dipped cord can be used to estimate a theoretical storage modulus for the uniaxial composite. The Correspondence Principle states that the linear elastostatic analysis can be converted to dynamic linear viscoelastic analysis by replacing elastic moduli or compliances with complex moduli and compliances, respectively [109]. Hence it allows for the extension of the rule of mixtures from the elastic to the viscoelastic behavior. Accordingly, the storage modulus of the composite evaluated in cord direction (E'_1) can be written as:

$$E'_1 = V_r E'_r + V_c E'_c \qquad (4.2)$$

where V is the volumetric fraction of the constituent and the subscripts r and c refer, respectively, to rubber and cord. The comparison between theoretical and measured E' for the model composite is shown in Figure 4.11 in which a significant difference in values and shape of E' is highlighted. This difference can be ascribed to a critical aspect of the testing of flexible composites: it is well-known that is to achieve a good clamping, in order to transfer load from matrix to cord inside the composite [110]. The extremely compliant matrix cannot transmit the total force from the fixtures to the cords and, to obtain a good test, cords should be engaged by clamping.
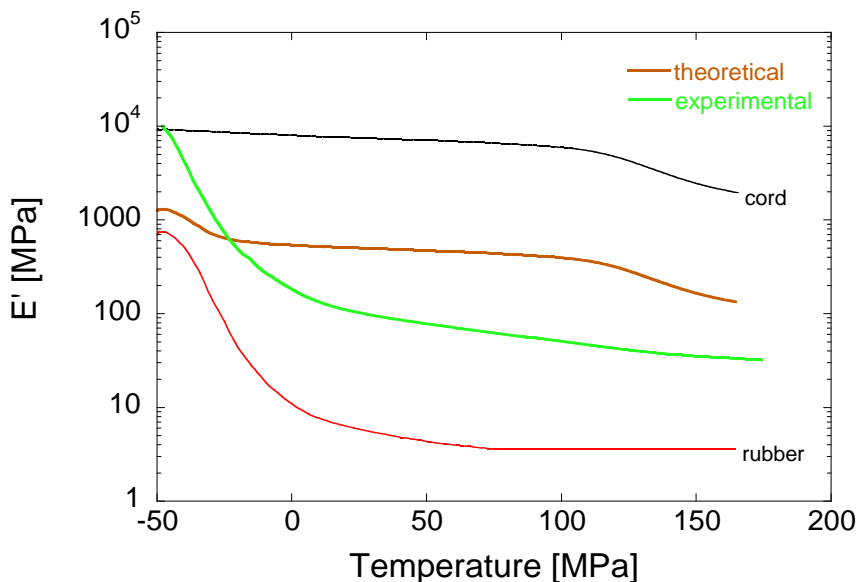

Figure 4.11 Comparison between theoretical and measured E' for the uniaxial model composite

Effect of clamping torque. In order to analyze the aforementioned critical aspect, the effect of clamping pressure on *E'* of uniaxial samples has been investigated. Sample has been clamped with a controlled clamping torque by means of a torque wrench. Since the clamped area is determined only by grip geometry, the correlation between clamping torque and clamping pressure is straightforward. The response of uniaxial samples, in terms of *E'*, is thus shown in Figure 4.12. Response seems to be proportional to clamping torque. An increase of 50 % ca. for E' has been estimated for an increase of clamping torque from 0.34 to 1.02 Nm.

The effect of clamping torque has been investigated also for the case of off-axis samples. Typical results of this investigation are shown in Figure 4.13 (for samples with $\theta = 30°$). Off-axis samples do not feel the mismatch matrix/cord as much as uniaxial lamina since, with the increase of angle θ, composite behavior is progressively closer to the only matrix. Consequently, the effect of clamping torque decreases with angle θ, until it vanishes for transverse lamina (cf. Figure 4.14a, results evaluated at room temperature). This effect can be explained by considering that, as hold is increased, clamp tips penetrate the sample; hence soft matrix deformates and cords are much more involved in load carrying (Figure 4.14b).
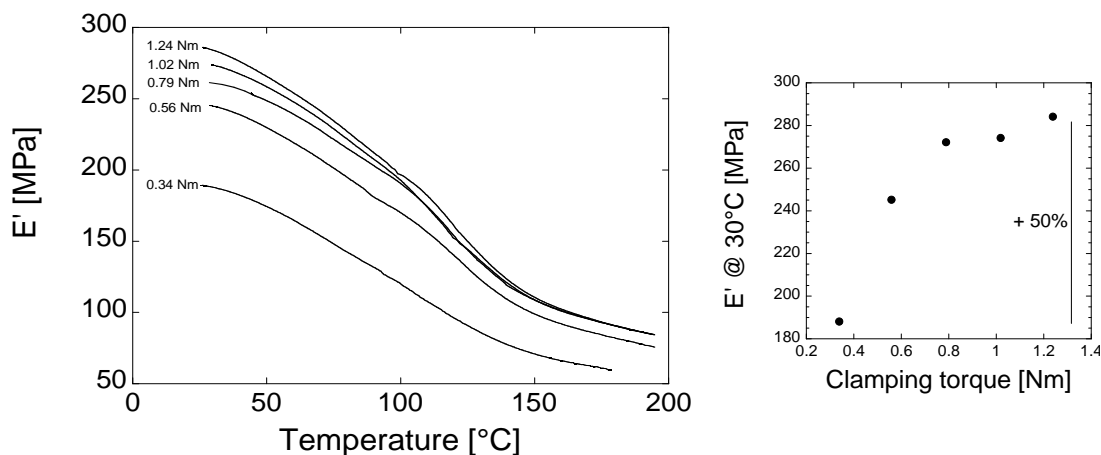

Figure 4.12 Effect of clamping torque on E' for uniaxial model lamina:
Temperature scan measurements (left) and E' at 30°C as function of applied clamping torque (right)
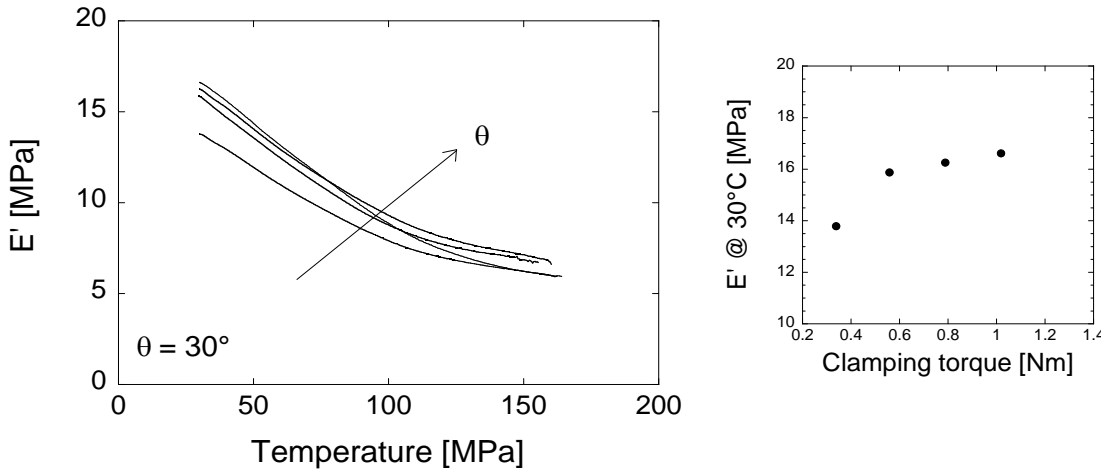
Figure 4.13 Effect of clamping torque on lamina with θ=30°: temperature scans (left) and E' vs clamping torque (right)

(a)

(b)

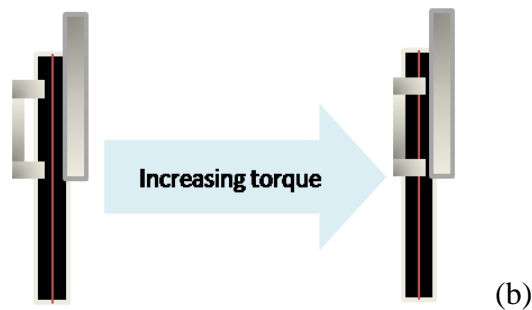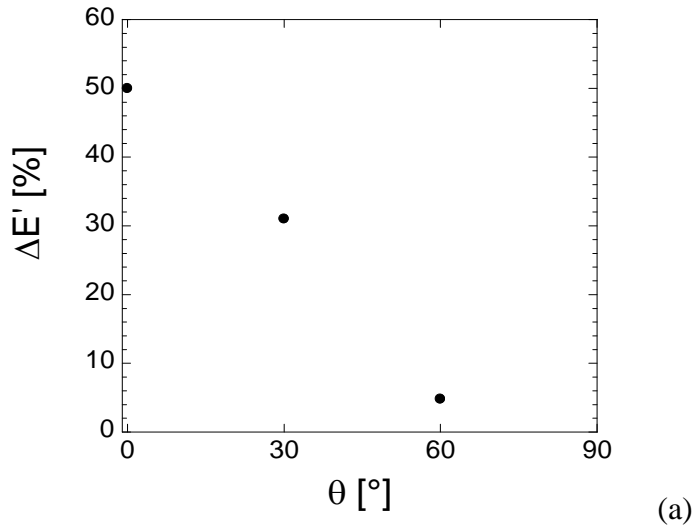Figure 4.14 Dependence of the effect of clamping torque on angle θ (ΔE' has been evaluated from 0.34 to 1.02 Nm) (a) and schematic of the mechanism responsible for the effect of clamping torque (b)

Custom-made clamping system for uniaxial composite. In order to improve the response of uniaxial lamina, a particular clamping system has been designed (Figure 4.3). First of all, the reliability of this modified clamping system has been verified by performing temperature scan tests on rubber and on cord, separately. Comparison of these results with test performed using the DMA standard clamps show that the modified clamping system does not compromise the response of the investigated sample (Figure 4.15). Deviation lies within the experimental error.
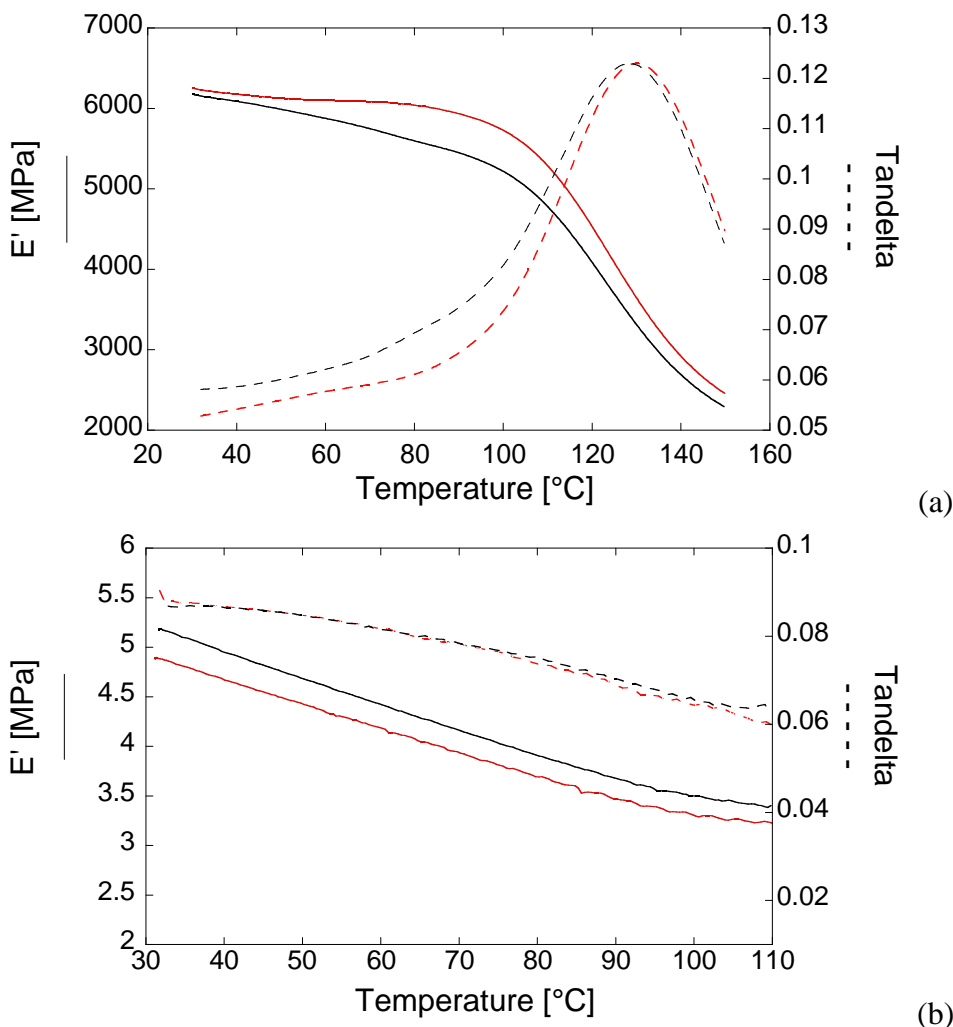

(a)

(b)

Figure 4.15 Verification of modified clamping system reliability. Comparison between standard (red line) and modified clamps (black line): temperature scan for cord (a) and for rubber (b)

Temperature scan test was then performed on model composite. Measurements were repeated ten times and the results are shown in Figure 4.16a. In order to discuss reproducibility of these measurements (independently of material), the experimental E' has been normalized to the cord fraction, V_c, for each sample (actually, it was found to vary from 4.88 to 6.22%). The normalized E' for each sample (gray lines) and the average normalized E' (black line) are shown in Figure 4.16b. In the light of these measurements, this proposed procedure was found to be reproducible within 2.9%.
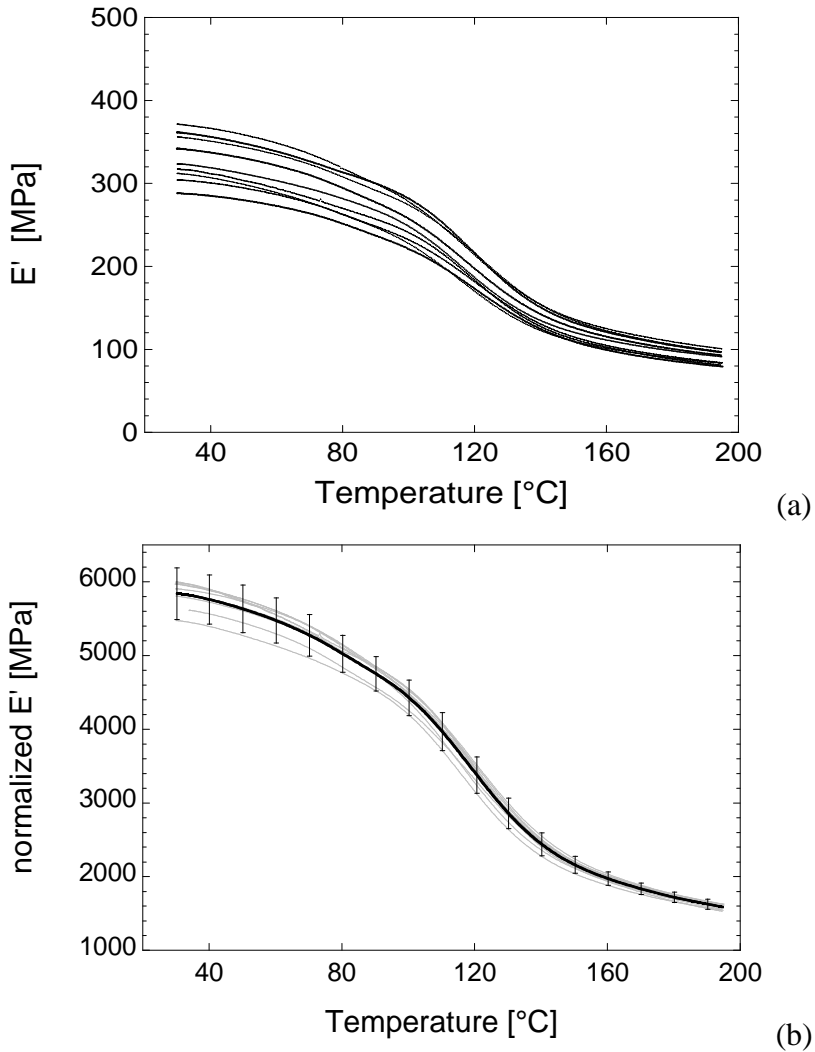
(a)

(b)

Figure 4.16 Verification of modified clamping system reproducibility
a) E' vs. temperature; b) normalized E' vs. temperature

Finally, Figure 4.17 shows the comparison among the values of the storage modulus of model composite in cord direction as estimated by using the standard DMA clamp (at the highest clamping torque, 1.02 Nm) and the custom-made clamping system and the theoretical prediction as obtained with the rule of mixture. The comparison has been performed in terms of E' normalized to the cord volume fraction of the composite, in order to get information about the technique, independently of the investigated sample.

It has been calculated that, at a reference temperature (for instance 30°C), *E'* deviates from predicted value of around -40% for standard clamp and -9% for the custom-made clamps. This result confirms the efficiency of the designed clamping system. Nevertheless, it is worth noting that this system cannot be used for testing off-axis samples.
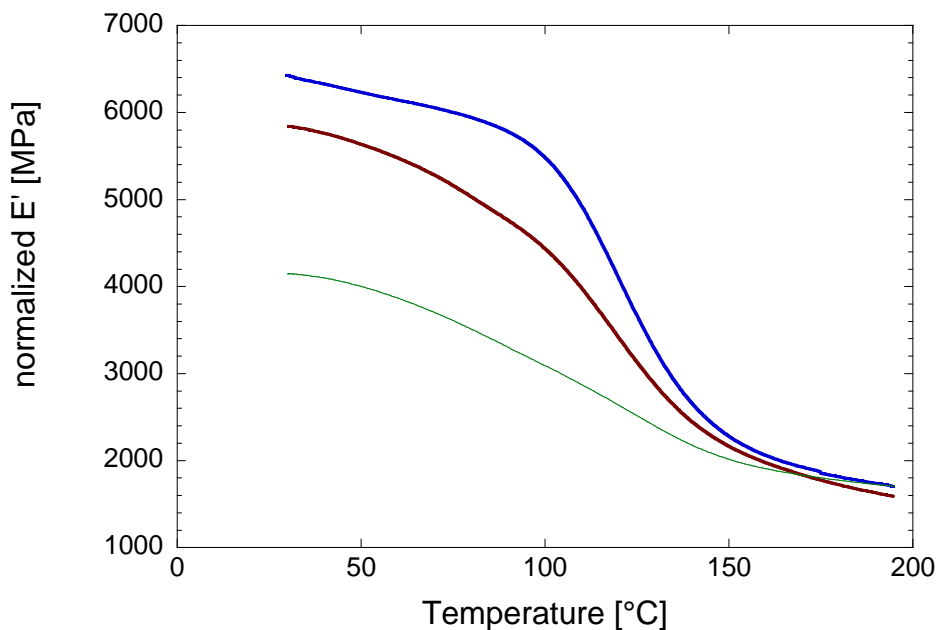

Figure 4.17 Temperature scan for uniaxial lamina for standard (brown) and custom-made (red) clamps , compared to prediction (blue)

Cord-rubber composite as general orthotropic material: the angular dependence of E'. Results of temperature scan measurement performed on samples with different cord orientation, in terms of *E'*, can be discussed in the light of the classical lamination theory (extended to viscoelasticity by means of the Correspondence Principle [109]). Figure 4.18 shows the value of *E'* evaluated at a reference temperature (30 °C) as a function of cord orientation in the composite. Experimental results are compared to the prediction as evaluated by using the following equation (cf. 3.1.1 for details)

$$\frac{1}{E'_x} = \frac{1}{E'_1} cos^4\theta + \left(\frac{1}{G'_{12}} - 2\frac{v'_{12}}{E'_1}\right) sin^2\theta \, cos^2\theta + \frac{1}{E'_2} sin^4\theta \qquad (3.4b)$$

where the parameters E_1, E_2, v_{12} and G_{12} have been evaluated according to Akasaka-Hirano relationship (cfr. Chapter 3), starting from the mechanical properties of rubber and cord. This finding is in accordance with the results of Clark [11], revealing that the relations derived from the classical lamination theory can be adopted to interpret the response of cord-rubber composites, provided that the properties are converted according to the Correspondence Principle [109].
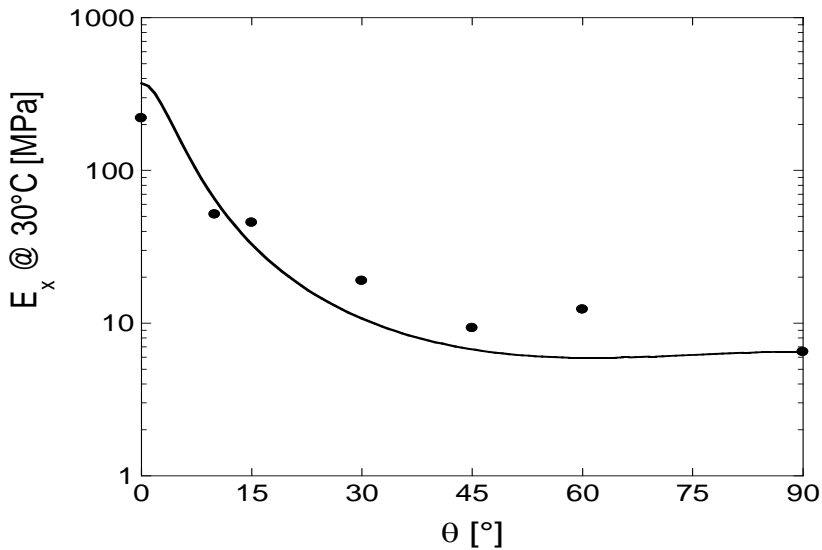

Figure 4.18 Angular dependence of E': experimental data vs. lamination theory prediction

4.4.4 Tensile test

Mechanical behavior of rubber and cords. Tensile tests have revealed the mechanical response of rubber and cords. Results of this characterization are shown, respectively, in Figure 4.19 and 4.20. Stress-strain curve of rubber compound is highly non-linear and failure occurs at around 570% strain. In particular, after an initial region characterized by significant non-linearity for strains up to 100%, a strain-hardening zone is found and that is related to the stretching of macromolecules leading to oriented domains [1]. Stress-strain curves of PET (Figure 4.20a) and rayon (Figure 4.20b) dipped cords show three main regions: a very initial low-modulus region characterized by fiber rearrangement in the twisted structure, then an elastic region in which filaments start becoming effective in the overall response of the cord and that also includes yielding, and a final strain-hardening region until failure. The response of rayon cords is clearly lower than polyester cords and the difference between the elastic and the train-hardening regions appears much more pronounced. This result is mainly ascribed to the different properties of the monofilaments, as shown in Figure 2.12, where typical stress-strain curves for the most used fibers used in tire cords are reported. In particular, the three types of PET cords adopted in composite preparation are characterized by both different linear density and twist (on both cord and yarn levels). Until yielding, PET cords behave indistinguishably; in the strain-hardening zone the behavior differs indeed. In particular, the cord with the higher linear density (2200/2 – 340x340) shows higher elastic modulus and strength; the unbalanced cord with the intermediate linear density (1670/2 – 270x390) shows an intermediate response while the cord with the lower density and the higher twist level shows the worse response (1100/2 – 470x470). Regarding failure, cord with the higher twist level shows an increasing of elongation at break. Accordingly, rayon cord with higher linear density and lower twist (1840/3 – 403x402) shows improved mechanical features (modulus and strength) as compared to the 1840/2 – 472x472 that, furthermore, shows a larger elongation at break, due to higher twist. The response of rayon cord at small strain differs instead for the two cords, probably due to the significant difference in construction: the cord made up of three yarns appear stiffer than the two-yarn cord. The main mechanical features of the analyzed materials are reported in the tables 4.III and 4.IV. Cords Young moduli have been calculated in the elastic region (after initial rearrangement) and in the strain-hardening region.
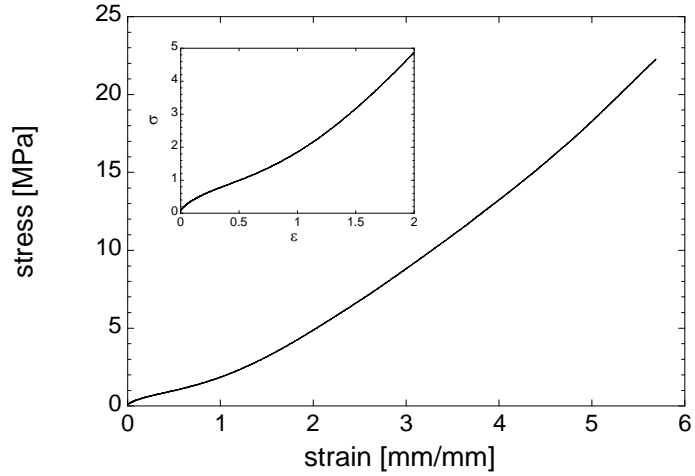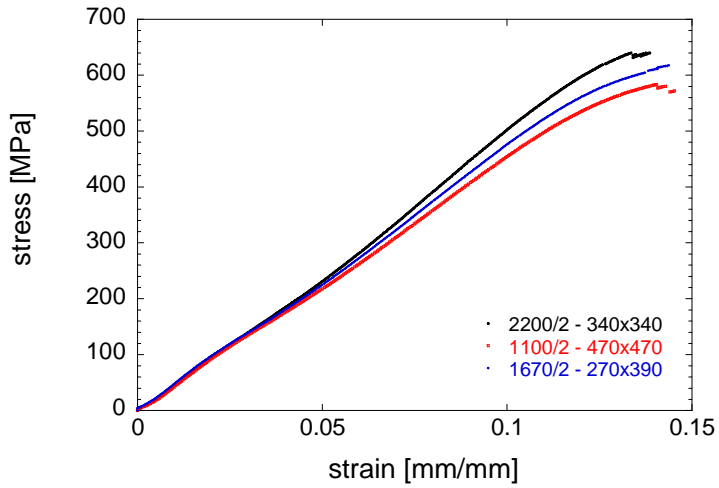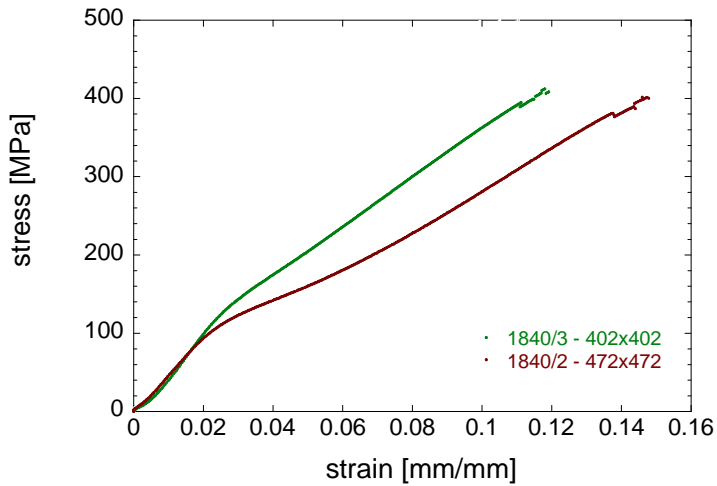
Figure 4.19 Stress-strain curve for rubber compound. Inset: zoom on the first region

(a)

(b)

Figure 4.20 Stress-strain curve of the cords used in the real composites: PET (a) and rayon (b)

104

	E @ ε = 1% [MPa]	Tensile strenght [MPa]	Elongation at break [%]
Rubber	4.62	22.2	567

Table 4.III Mechanical properties of rubber compound

	E @ ε = 1% [MPa]	E @ ε = 7% [MPa]	Tensile strenght [MPa]	Elongation at break [%]
PET 1100/2 – 470x470	4950	4723	586	14.3
PET 2200/2 – 340x340	5173	5438	642	13.8
PET 1670/2 – 270x390	5120	5038	617	14.3
RY 1840/3 - 402x402	5518	3157	412	11.8
RY 1840/2 - 472x472	5051	2489	401	14.8

Table 4.IV Mechanical properties of cords

Mechanical behavior of model composite. The effect of sample length on the mechanical response of uniaxial lamina has been investigated with quasi-static test. Tests have been performed on sample with different gauge lengths and two examples of stress-strain curves, obtained by testing 100 mm and 200 mm-long samples, are shown in Figure 4.21a. The stress-strain curve is non-linear and, like cord, three zones can be clearly distinguished); furthermore, the behavior changes significantly with sample length. In this investigation, composite failure will not be discussed because failure never appeared in gauge length. The Young modulus (evaluated at 1% strain) is found to increase with sample length, as exhibited in Figure 4.21b. The improvement of mechanical response with sample length is generally attributed to a 'finite fiber length effect', due to the reinforcing efficiency of the fiber that increases with length. Longitudinal Young modulus has actually been found to exhibit maximum reinforcement and greatest sensitivity to the fiber geometry [111]. Load is transmitted continuously along the entire length of the fiber through shear stresses acting on interface; the axial stress hence increases to a maximum in the midpoint. Micromechanical models describe stress transfer mechanisms (cf. Chapter 3) and derive that the fiber needs to achieve a critical length in order to get full reinforcing efficiency. Thus it is interesting to define a macroscopic efficiency, which is a parameter that permits to compare quantitatively the response of the composite as measured by tensile test and the ideal behavior of an infinitely long composite. Accordingly, this parameter can be defined as the ratio of the measured Young modulus to the theoretical one as calculated by using the rule of mixture, as

written in the form of Akasaka-Hirano (Eq. 3.44c). Figure 4.22a shows the dependence of the macroscopic efficiency on gauge length. It is obvious that this parameter increases with sample length and that only the mechanical response of long samples approaches the ideal behavior. This straightforwardly means that the Young modulus increases until it asymptotically tends to 80% of the predicted value.

In particular, it is worth noting that the rule of mixture was derived for infinitely long composite, hence the ideal behavior is referred to matrix and fiber working in isostrain condition. The micromechanics reveals that the strain in the fiber may not build up to the maximum value indeed and the theoretical prediction for longitudinal modulus of a composite should take into account the dependence on fiber length. At this stage it is interesting to interpret this result in the light of Shear-Lag models [96-99]. According to micromechanical models, in fact, it is possible to define two characteristic lengths, namely the transfer length and the positively affected length or PAL (cf. Chapter 3). The SL model predicts that the PAL increases with sample total length (Figure 4.22b) and, as length increases, its contribution to the overall response of the sample grows as well as the transfer length ('ineffective' zones) gradually loses its influence. Basically, in the positively affected length, composite response can be predicted by means of the rule of mixtures since the isostrain condition is achieved. Hence, as sample length increases, the difference between the measured and the predicted values of modulus becomes smaller and smaller because the effective length assumes an increasing weight on the overall sample length. For the investigated lengths, the material reaches the 80% ca. of theoretical stiffness, in agreement with the predicted results (for 200mm-long samples, $L_{effective}$ is 80% ca. of the total length). Furthermore, data shown in Figure 4.22 have been fitted with the Eq. (3.67) and the shear lag parameter β has been found (0.0478).

These first results obtained on a macroscopic scale have trot out the mechanism of stress transfer that has just qualitatively been discussed. However, a detailed experimental analysis of the micromechanics of cord-rubber composites will be developed in Chapter 5.
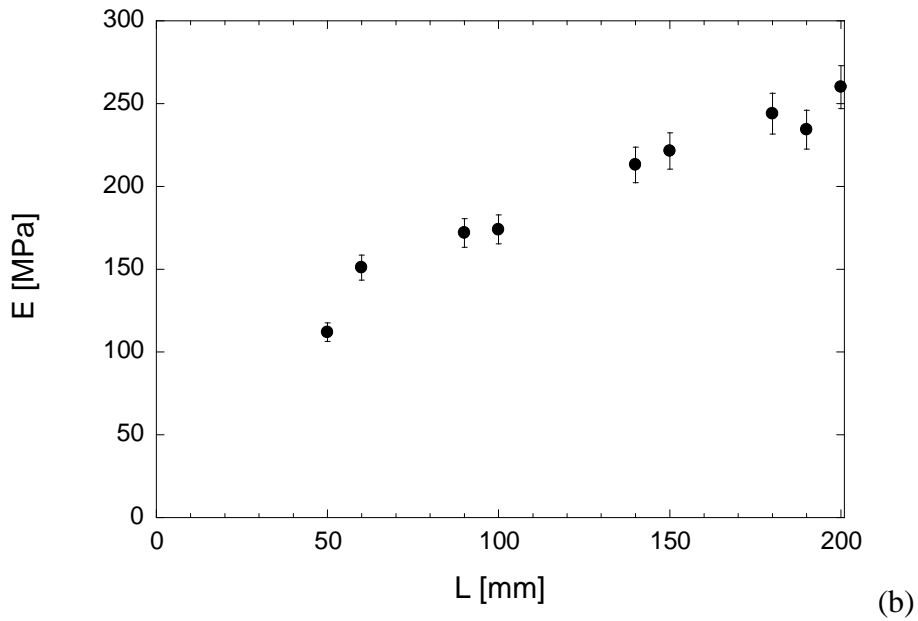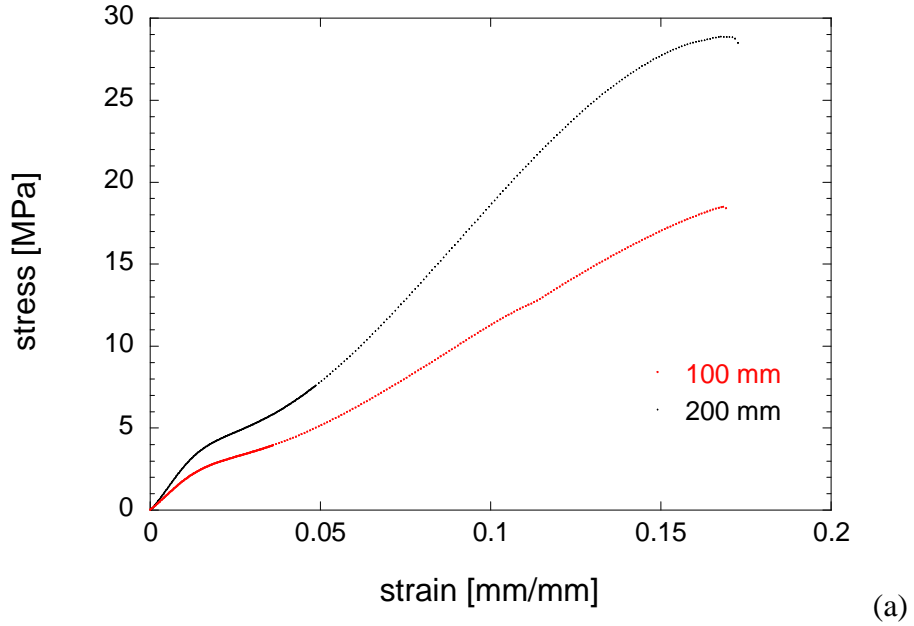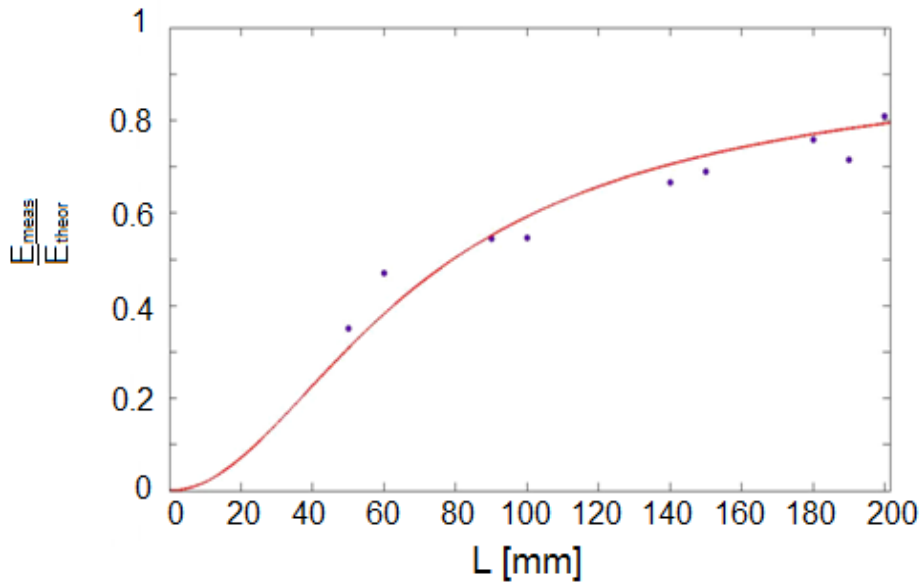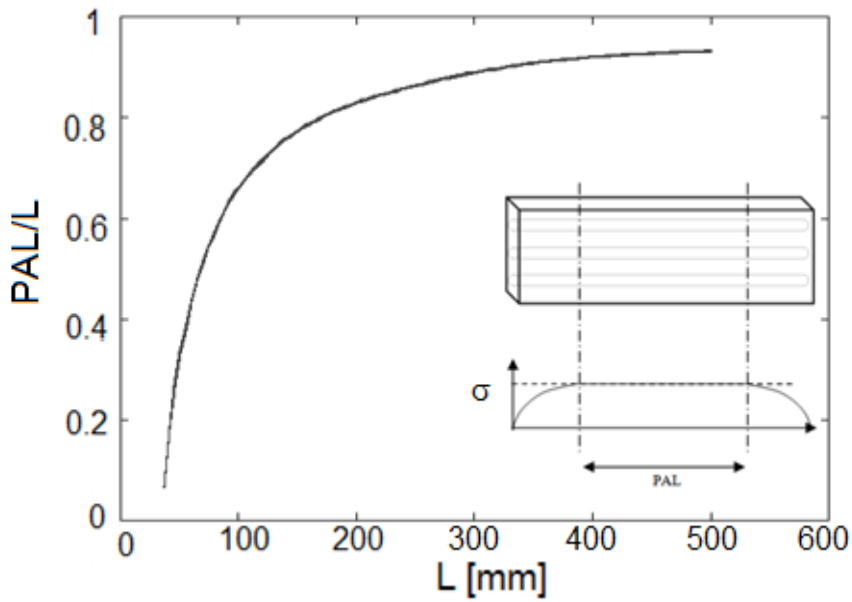
(a)

(b)

Figure 4.21. Effect of sample length on mechanical response of uniaxial model composite: a) comparison between stress strain curves obtained at two gauge lengths; b) Young modulus as a function of gauge length

(a)

(b)

Figure 4.22. a) Macroscopic efficiency of model uniaxial composites as a function of gauge length. b) Positively affected length (normalized to gauge length) as a function of sample length, from SL model prediction. Inset: schematic of theoretical axial stress distribution in the reinforcement

Mechanical response of model composite in the 'positively affected length'. In order to verify the behavior of the composite in the PAL, quasi-static tensile tests have been also performed by measuring the strain in the central zone of the sample by using an optic system. In the light of the preliminary investigation, 200 mm-long samples have been chosen. The optical measurement has been carried out by following the displacement of two white markers, placed at 50 mm from sample centre, defining the bounds of a tentative PAL, as shown in Figure 4.23a. This means that the tentative PAL has been supposed to be at least 100 mm (50% of the whole gauge length). By comparing the tentative PAL and the prediction shown in Figure 4.22b, it is straightforward to note that the experimental choice has been made by underestimating (of 100% ca.) the predicted result. The stress-strain curve obtained by evaluating the strain in the tentative PAL is shown in Figure 4.23b as well as the stress-strain curve obtained by measuring strain on the whole sample by using crosshead position. Tests have been performed in the elastic region, at strains up to 2.2%.The difference between the two curves implies that the mechanical response evidently improves in the tentative PAL. Tests performed by increasing this characteristic length until the predicted PAL confirm the result. In particular, in order to quantify the different behavior for the whole sample length and the PAL, the modulus evaluated from the initial slope of the σ-ε curve as obtained by measuring displacement from crosshead position (E_L) has been normalized to the modulus related to the σ-ε curve whose strain has been measured in the PAL by means of CCD cameras (E_{PAL}). It has been found that ratio E_L/E_{PAL} is equal to 0.86 that means, basically, that the response of the whole sample (including both PAL and ineffective lengths) just reaches the 86% of the response of the composite in the positively affected length, whereas the reinforcement is fully effective. In fact, the ineffective length negatively contributes to the average behavior of the composite and, consequently, a worsen response is observed due to the lack of reinforcing efficiency.
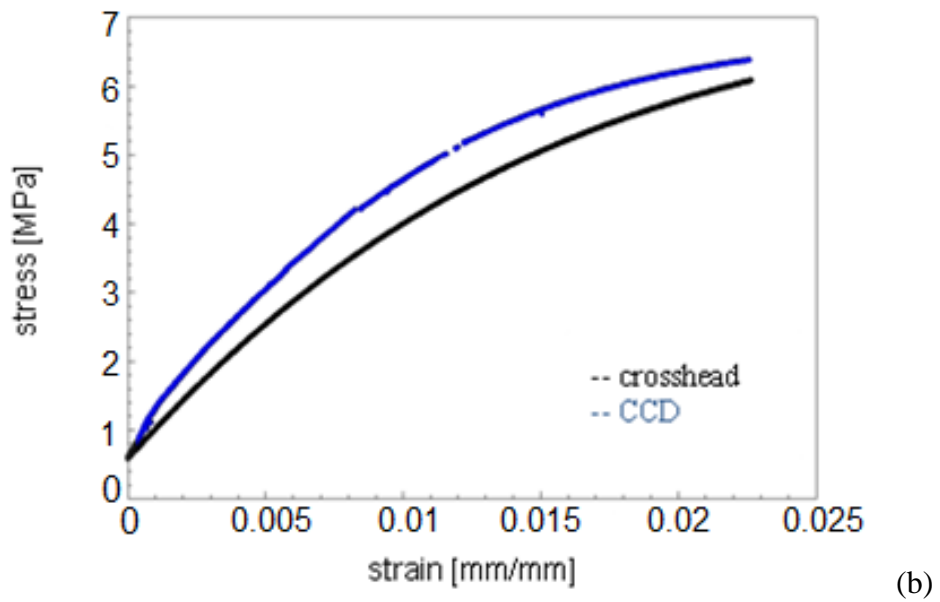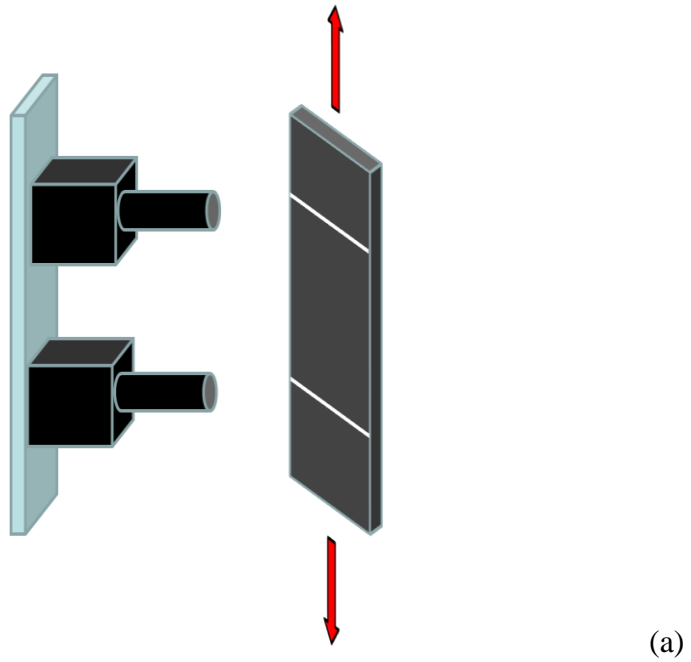
(a)

(b)

Figure 4.23 Investigating the PAL: a) schematic of measurement; b) comparison of stress strain curves for unidirectional ideal composite

Mechanical behavior of real composites. Figure 4.24a shows the comparison between the stress-strain curves of pad 111 as measured by tensile test performed at 1%/min on sample with different gauge lengths. Like model composites, the non-linear behavior and a strong 'finite fiber length effect' can be highlighted. In particular, the measured value of Young is shown to increase with sample length until it reaches an asymptotical value for lengths longer than 150 mm. The investigation has been carried out also at a higher strain rate (i.e. 100%/min), revealing the same behavior noticed in quasi-static test (Figure 4.24b).
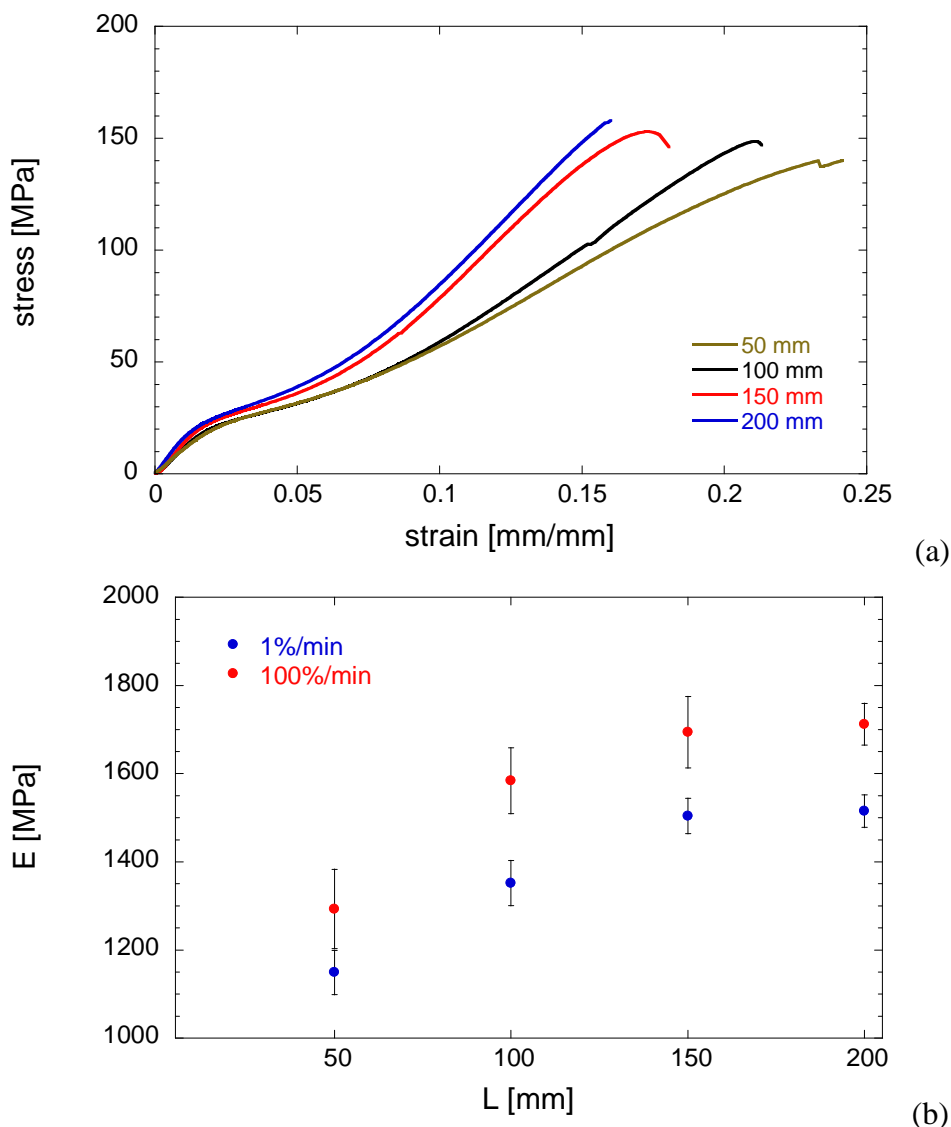

(a)

(b)

Figure 4.24 Effect of sample length for pad 111: stress-strain curve (a) and Young modulus vs. sample length (b)

In fact, since the pronounced viscoelastic nature of the material, samples that have been tested at higher strain rate show higher values of E, compared to the results of the quasi-static test. All of the other real laminae show the same behavior. As expected on the basis of shear lag models, Young modulus increases with sample length, until it reaches an asymptotical value when the sample is long enough for the effective length to exceed transfer length (less effective). The minimum requested lengths that ensure a good response (compared to rule of mixtures prediction) have been determined on the basis of this characterization and are shown in table 4.V.

Pad	L_{min} [mm]
111	150
100	150
114	100
136	200
98	200
116	150

Table 4.V Minimum length for pads under investigation

Effect of clamping pressure. Tests on pad 111 have also been performed by applying several levels of clamping torque. Samples with three characteristic gauge lengths (50 – 150 – 190 mm) have been subjected to quasi-static test, clamped with a torque wrench (USAG, Italy) at 10, 20, 30, 40 Nm. A clamping area of 250 mm^2 has been adopted. Results are shown in Fig. 4.25. In contrast with results of dynamic-mechanical analysis performed on short samples, no evident clamping effect can be noticed. On 150 mm-long samples, the increasing of clamping torque seems to worsen material response, inducing a decrease in Young modulus, contrary to the expectations. Actually, according to shear lag models, the effect of clamping torque should be significant for short samples, because as clamping pressure increases, cords are more involved in load carrying. For very long sample (L > PAL), clamping torque should not play any importance on mechanical response because stress transfer should be good, regardless of clamping conditions. Figure 4.26 shows the ratio of the shear-lag simulated modulus of a matrix-embedded cord and the predicted modulus as a function of composite length. Shear lag models contemplate two boundary conditions:

1. load is applied to matrix edges (i.e., reinforcement ends are stress-free);
2. load is applied only to reinforcement ends (i.e., matrix ends are stress-free).

In the real testing, clamping involves both the matrix and the reinforcement, unless special specimens are prepared. Hence, cases 1 (depicted in red) and 2 (depicted in black) represent, respectively, the lower and the upper bound for modulus prediction. The actual response is an intermediate state and should feel the effect of clamping pressure as a function of sample length.
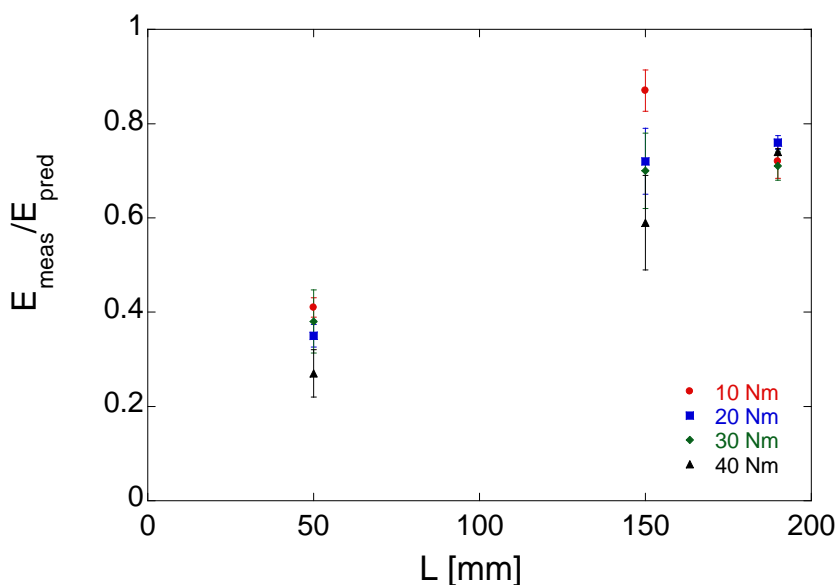

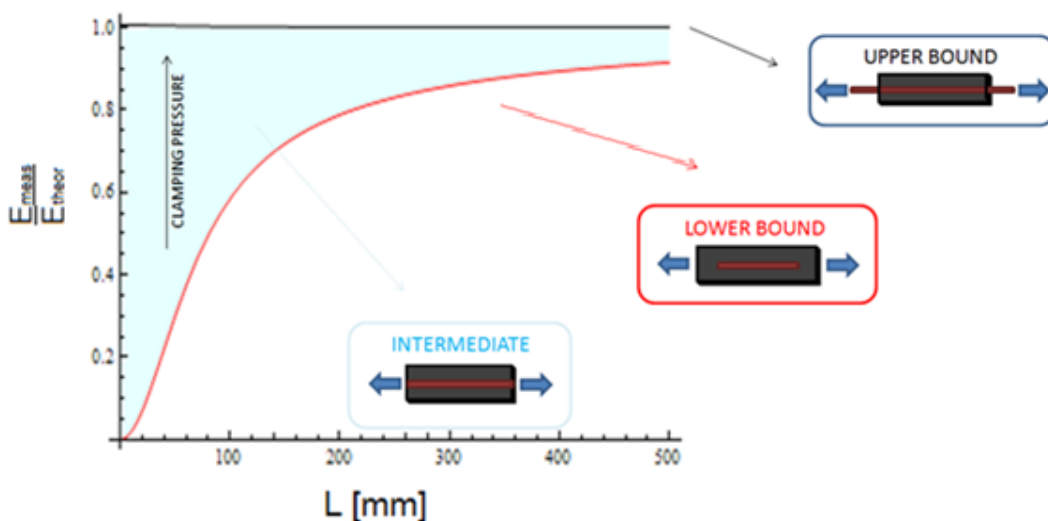Fig. 4.25 Effect of clamping torque on samples with several lengths

Figure 4.26 Expected trend for clamping effect combined to 'finite length fiber effect'

Effect of cord volume fraction and of cord spacing. In the light of the 'finite fiber length effect' observed for all the pads, tensile tests have been performed on 200 mm-long samples cut from pads 60, 90, 114, 120, 134 and 140. These laminae are made up of the same PET cord (1100/2 – 470x470) and differ for cord end count (and, consequently, for cord spacing) and for thickness. In particular, pad 120 has been produced with three different thicknesses (low, 'LT', medium, 'MT', and high, 'HT') resulting into three different cord content (cord spacing being equal). Results of tensile test performed on pad 120 are shown in Figure 4.27 in terms of Young modulus (evaluated at 1% strain). Young modulus is found to increase linearly with cord volume fraction, in accordance with the rule of mixtures. Furthermore, whereas the matrix contribution to the composite response is neglected (e.g. in the Akasaka-Hirano approach), the slope of the fitting line represents cord modulus and it is found to be consistent with the measured value reported in Table 4.IV.

Figure 4.28 shows the results of the investigation performed on all of the aforementioned pad, cord type being equal. Young modulus is reported as a function of cord end count (a) and of cord volume fraction (b).

Cord end count defines the number of cords that can be found in a 100 mm-wide pad. Cord type and pad thickness being equal, pads with different values of cord end count are characterized by different values of reinforcement volume fraction, resulting in a different mechanical response. Also in this case, obviously, elastic modulus is a linear function of cord volume fraction and the slope of the fitting line is consistent with the measured cord modulus.

Aside from the stiffening due to the increasing of reinforcement content, the variation of cord end count may induce a modification in composite response due to a different level of 'interaction' between consecutive cords. Actually, this effect could be induced by to a sort of matrix hardening, due to a confinement of the matrix itself in the interphase region between two consecutive cords. This confinement can lead to a significant hardening for the matrix [112,113], whose response becomes intermediate between the two phases and differs significantly from the bulk (Figure 4.29). For pad with high cord end count, cord spacing decreases and the contribution of interphase increases on the overall amount of matrix, hence enhancing pad stiffness.
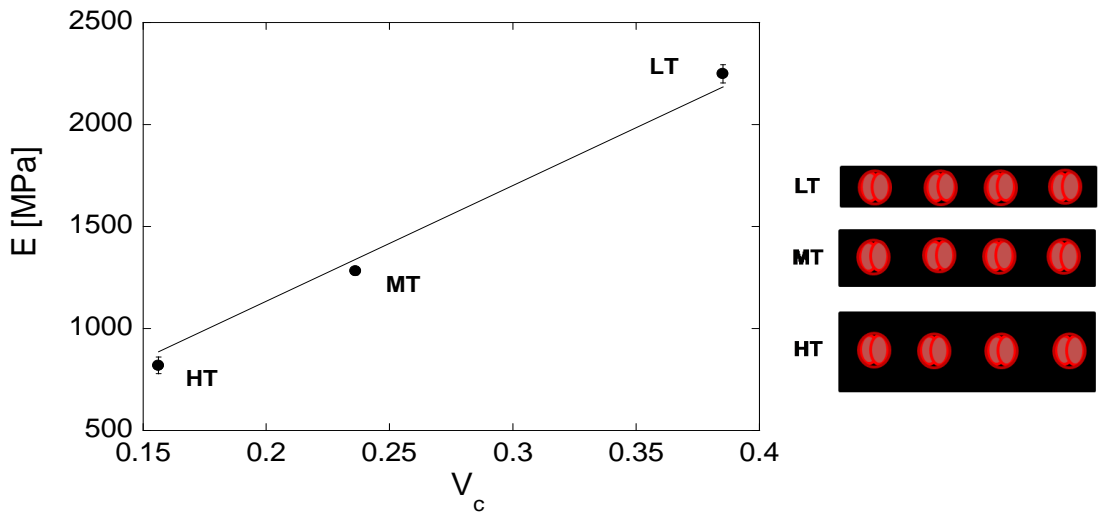
Figure 4.27 Effect of cord volume fraction: varying pad thickness
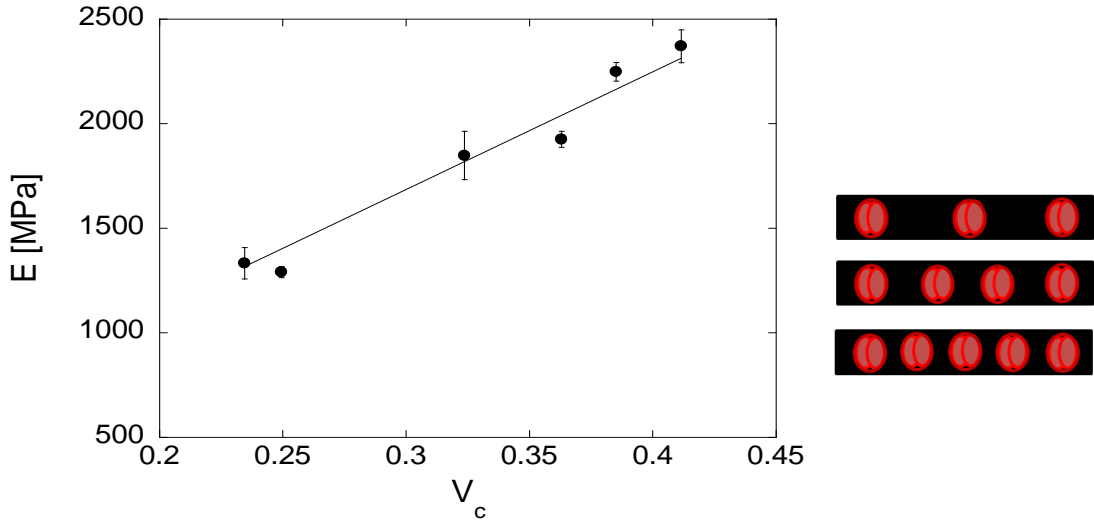

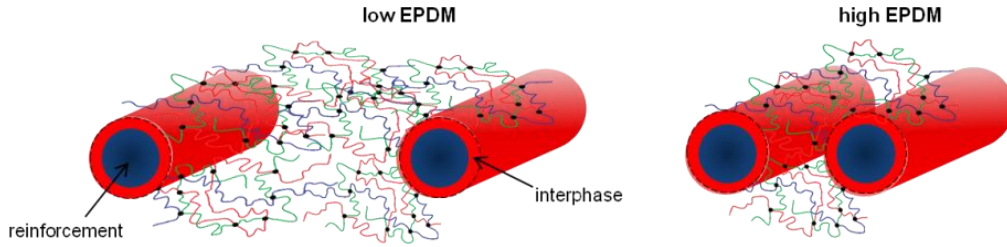Figure 4.28 Effect of cord volume fraction: varying cord end count

Figure 4.29 Role of interphase in the effect of cord spacing

Owing to lack of pads characterized by different cord end count but with a fixed cord volume fraction (since the difficulties in controlling exactly pad thickness during material preparation), a simple trick has been adopted in data elaboration for the investigation of such effect. Elastic modulus has been simply normalized to the nominal cord volume fraction and shown as function of cord spacing, as calculated from cord end count and nominal cord radius (Figure 4.30). Results of tensile test do not show any difference among the several pads, in terms of normalized modulus. Hence it seems that an increasing interaction does not lead to any noticeable increasing of composite response. Nevertheless, it is worthy of note considering that it may be difficult to investigate such an effect because of the limited sensitivity of the experimental technique. Further investigation with more powerful techniques is then required in order to find eventual interaction among cords.
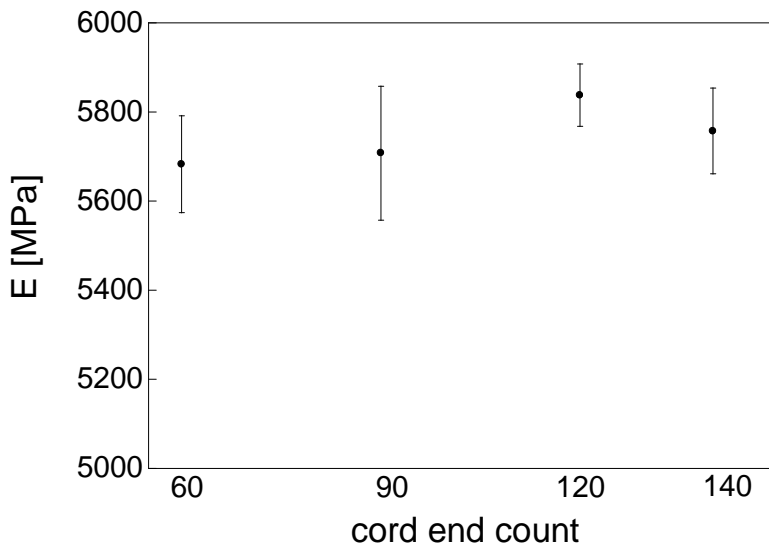

Figure 4.30 Effect of cord end count as effect of cord spacing

Chapter 5

Experimental investigation of micromechanics of cord-rubber composites

5.1 From macro- to micromechanical investigation

Macromechanical characterization of cord-rubber composites has revealed that the macroscopical response is strongly affected by specimen length. According to micromechanical models (cf. Par. 3.2), in fact, such a 'finite fiber length effect' can be ascribed to the efficiency of stress transfer into the uniaxial composite. In particular, a macroscopical efficiency has been defined and has been adopted for the comparison of the actual response of the composite with the ideal behavior as determined through the rule of mixtures. However, it is known that this relation was derived for matrix and fiber working in isostrain condition [90]. Actually, this condition is not always verified because the strain in the fiber may not build up to the maximum value. In fact relative strain occurs between the fiber and the matrix thus creating a shear stress at the interface. According to the micromechanical approaches, the high shear stress developed near discontinuities (e.g. the fiber ends) must be accommodated in order to take advantage of the properties of high-strength fibers. Hence, there is a critical value of fiber length required for achieving the reinforcing effectiveness. If the fiber is long enough for the tensile stress to build up, the isostrain condition is achieved among the two phases. This gives rise to the 'positively affected

length' (PAL), a plateau region of the fiber stress curve and zero interfacial shear stress. The region of the fiber near the ends (the 'transfer' or 'ineffective' length) - that is out of the PAL - is less heavily stressed than this central plateau region, so that the average fiber stress is lower than in long-fiber composite subjected to the same external load. The reinforcing efficiency decreases as the fiber length is reduced, since this increases the proportion of the total fiber length which is not fully loaded. Provided that the system remains fully elastic and there is no interfacial sliding, the two characteristic lengths depend only on the elastic constants of fiber and matrix (for instance, in case of a stiffer matrix, such as a metal, the stress transfer length will be shorter, as a result of higher interfacial shear stresses). At the light of these considerations, micromechanical models do reveal that the modulus of a uniaxial lamina is proportional to the length of the reinforcement. Obviously, this dependence becomes particularly pronounced whether the mismatch between the elastic properties of matrix and reinforcement is considerable, such as for cord-rubber composites. In such conditions, the application of the rule of mixtures may induce an error in the prediction of the behavior of the composite, since it does not account for the aforementioned dependence [96-100,105].

A micromechanical investigation based on micro Raman spectroscopy (μRS) has been carried out in order to gain information about the quality of stress transfer into cord-rubber composites and to discuss the macroscopical ascertainment. In the last decades, μRS has been drawn increasing attention as a tool for the investigation of deformational processes in polymer fibers and of composites micromechanics. Several works have shown that several fibers (such aramid [114] or carbon [115,116]) can be used as remote strain (or stress) sensors in the composite material they actually reinforce. This technique is based on the fact that the frequencies or wavenumbers of the Raman bands of many high-performance fibers shift under the application of a macroscopical strain (or, analogously, stress). Thus, the availability of a *calibration curve* meant as Raman wavenumber versus strain (or stress) provides a tool that can convert the Raman characteristics of a matrix-embedded fiber into the values of axial strain (or stress).

This technique has been adopted to determine the efficiency of stress transfer into a model cord-rubber composite, whose matrix was prepared with a peculiar formulation in order to ease Raman spectra acquisition from the embedded PET cord. The effect of specimen length has been examined in detail on both continuous and discontinuous composites. Finally, the results of this

investigation, in terms of reinforcing efficiency, have been used to assess the macroscopical response of continuous cord-rubber composites.

5.2 Monitoring deformation processes using micro Raman spectroscopy

Raman spectroscopy is an inelastic scattering technique that probes the vibrational modes of chemical bond into materials [117]. For quite a long time this technique was mainly devoted to fundamental research, but instrumental progress (laser miniaturization, CCD detection, notch filters and data processing software) have rendered it a general characterization method. In the last decades it has been drawing particular attention since its versatility in providing a fingerprint of molecules over several ambient conditions and the applications nowadays range over several fields, especially in solid state physics and in materials science. It provides basic phase identification and also subtle spectra variations that can be used to assess nano-scale structural changes and characterize micromechanical behavior. In particular, such applications require often a high spatial resolution that can be achieved by focusing monochromatic light with standard optical microscopy techniques. The so-called micro Raman spectroscopy (µRS) is characterized by a spatial resolution that typically ranges between 1 and 5 µm, and is limited by the quality of the optical components and the optical arrangement used to focus the beam. This high spatial resolution makes µRS the best tool to map phase and strain distributions in many materials. Furthermore, it provides a unique insight into the relationship between macroscopic deformation and the processes that occur at the molecular or microstructural level and has now revolutionized common understanding of the micromechanics of fiber deformation.

It has been found that the frequencies or wavenumbers of the Raman bands of many high-performance fibers shift on the application of stress to the fibers. The phenomenon was first reported for the deformation of polydiacetylene single crystal fibres [118] and subsequently confirmed by others [119-122]. This behavior has been ascribed to the macroscopic deformation being transformed directly into stressing of the covalent bonds and changes in the bond angles [119]. In fact the vibrational frequencies in a molecule are proportional to the 'spring constant', or interatomic force, between the atoms. As a consequence of the anharmonicity of atomic bond, when a material is strained, the interatomic

distance changes resulting in a change of the interatomic force, and thus in a change in the vibrational frequency (or, analogously, in wavenumber).

Several materials have been then characterized (e.g Kevlar, carbon fiber, polyamides) and a large amount of works has been produced [117]. In fact, knowledge obtained from the technique is of both academic and industrial interest to study relationships between microstructure and macroscopic physical properties in polymers. Furthermore, it has paved the way for a powerful technique for the micromechanical studies at the fiber/matrix interface [123]. Details of the technique are given in the following.

5.2.1 Fundamentals of Raman spectroscopy

Vibrations in Crystalline Solids. The collective vibrations that occur in a crystal can be represented by the superposition of plane waves that virtually propagate to infinity [124], called normal modes of vibration. These plane waves are commonly modeled by quasi-particles called *phonons*. A normal coordinate of the form $Q=Q_0cos(2\pi v_{vib}t)$, which is actually a linear combination of bond lengths and bond angles, is associated with each normal mode. Depending on the dominant term in the normal coordinate, modes can be classified as either stretching (v), bending (δ), torsional (τ) or librational (R'/T' pseudo-rotations/translations) and lattice modes (the latter include the relative displacement of the unit cells).

There are modes with in-phase oscillations of neighboring atoms and modes with out of phase oscillations. The former are called acoustic vibrations and the latter are called optical vibrations. On the other hand, phonons are referred to as being longitudinal or transversal depending on whether the atoms move parallel or perpendicular to the direction of wave propagation given by their wavevectors, $\vec{k}$. Figure 5.1 illustrates the concept of phonons in crystals showing the transverse vibrations in a one-dimensional lattice.

The Raman effect. As a group of atoms vibrates, the electron cloud, and thus the polarizability, changes instantaneously. The interaction of the periodic change in the charge distribution with an imposed electromagnetic field is the origin of several types of light scattering phenomena including infrared (IR) and Raman effects (Figure 5.2). First observed by C. V. Raman in 1928 [125], Raman scattering can be described as the inelastic energy scattering of incident light, which has interacted with the polarizability of chemical bonds in a molecule.
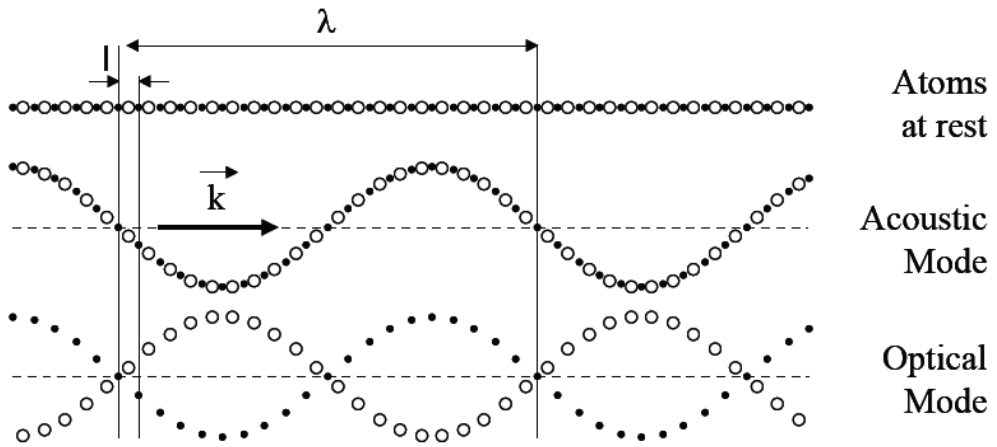
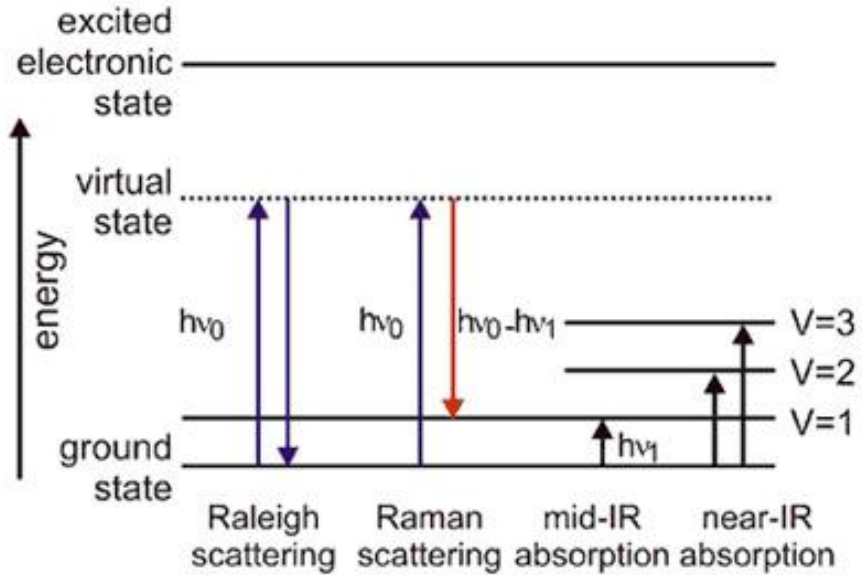Figure 5.1 The transverse phonons in a linear solid

Figure 5.2 Energy level diagram of various vibrational spectroscopic transitions

In particular, the polarization $\vec{P}$ of the dipoles excited in a solid when a laser (of amplitude E_0 and frequency v_{las}) interacts with phonons (of frequency v_{vib}) depends on the polarizability tensor $\bar{\bar{\alpha}}$:

$$\vec{P} = \bar{\bar{\alpha}} \times \vec{E_0} \, cos(2\pi v_{las} t) \qquad (5.1)$$

Since the terms of $\bar{\bar{\alpha}}$ can be individually described as functions of the normal vibration coordinates Q by using a Taylor approximation

$$\alpha_{ij} = \alpha_{ij}^0 + \left(\frac{\partial \alpha_{ij}}{\partial Q}\right)_{Q=Q_0} \times Q \quad (i, j = x, y \text{ or } z) \qquad (5.2)$$

the polarization can be expressed as

$$P_i = \sum_j \alpha_{ij} \times E_j = \sum_j \alpha_{ij}^0 E_{0j} \, cos(2\pi v_{las} t) + \qquad (5.3)$$
$$\frac{E_{0j} Q_0}{2} \left(\frac{\partial \alpha_{ij}}{\partial Q}\right)_{Q=Q_0} \times [cos(2\pi(v_{las} - v_{vib})t) + cos(2\pi(v_{las} + v_{vib})t)] + \cdots$$

Equation 5.3 predicts the two components of scattered light, the quasi-elastic ($v \sim v_{las}$) and inelastic ($v = v_{las} \pm v_{vib}$) one. The former is called the Rayleigh scattering and the latter, which occurs only if vibrations change polarizability ($\frac{\partial \alpha_{ij}}{\partial Q} \neq 0$), is the Raman scattering [126,127]. The condition for a vibrational mode to be Raman active requires that its molecular polarizability should be neither maximum nor minimum when the atoms are at their equilibrium positions.

Furthermore Eq. 5.3 reveals the dual sensitivity of Raman spectroscopy to the electrical (α_{ij}) and mechanical (v_{vib}) properties of the investigated materials. Hence two kinds of parameters influence spectra:

- parameters acting on the 'mechanics' like atomic mass, bond strength or the system geometry (interatomic distances, atomic substitutions) that will set the peaks positions (the eigenfrequencies of matter vibrations);
- parameters acting on the 'charge transfer' (iono-covalency, band structure, electronic insertion) that will set intensity, on the basis of the vibration-induced charge variations occurring at the very bond scale.

It is commonly used to refer to vibration modes by their wavenumber (expressed in cm^{-1} unit):

$$\bar{\nu}_{vib} = \nu/c \tag{5.4}$$

where c is the speed of light. By using this notation, the classical electromagnetic theory of radiations from an oscillating dipole hence demonstrates that Raman peaks have a Lorentzian shape:

$$I(\bar{\nu}) = I_0 \times \int \frac{d^3\vec{k}}{\left[\bar{\nu} - \bar{\nu}(\vec{k})\right]^2 + \left(\frac{\Gamma_0}{2}\right)^2} \tag{5.5}$$

where $\bar{\nu}(\vec{k})$ represents the dispersion branch to which the mode belongs and Γ_0 is the half-width for the ordered reference structure.

5.2.2 Deformational mechanism in polymer fibers

In the assumption that each stretching mode is specific to one given chemical bond, the so-called harmonic model can be adopted to interpret it. As long as elongation is limited, the bond can be modeled by a spring of length l_b, reduced mass μ and constant stiffness k_b. In this model, the interatomic potential is expressed as by

$$V(l_b) = \frac{k_b}{2}(l_b - l_0)^2 \tag{5.6}$$

and

$$\bar{\nu}_{vib} = \frac{1}{2\pi c}\sqrt{\frac{k_b}{\mu}} \tag{5.7}$$

$$k_b = \frac{\partial^2 V}{\partial l_b^2} \tag{5.8}$$

There is no dependence on l_b for k_b and the harmonic potential does not show any stress sensitivity for Raman bands.

Nevertheless, the interaction potential should not be limited to a quadratic term and all real bonds are somewhat anharmonic (Figure 5.3) and include attractive and repulsive contributions.

An example of anharmonicity is given by the Morse potential,

$$V(l) = D_e(1 - e^{-a(l-l_b)})^2 \qquad (5.9)$$

where l is the distance between atoms, D_e is the well depth (defined relative to the dissociated atoms), and a controls the 'width' of the potential (the smaller a the larger the width).
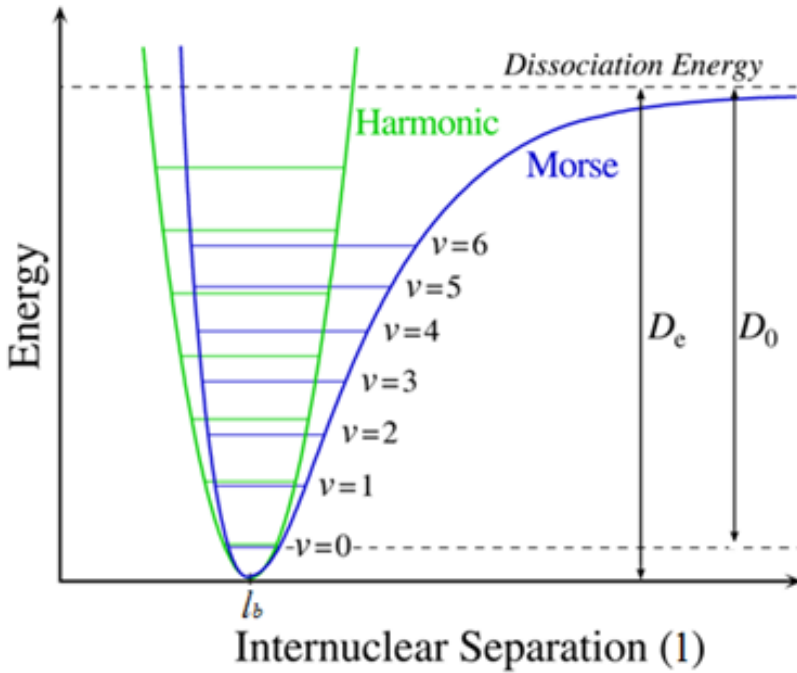

Figure 5.3 Comparison between realistic and harmonic bond potentials

Despite the very significant influence on the physical behavior of materials, anharmonicity is often considered as a simple perturbation. In what is referred to as the 'quasi-harmonic' approximation, the expressions 5.7 and 5.8 are applicable to real potentials. This means that stiffness constant $\left(\frac{\partial^2 V}{\partial l_b^2}\right)$ increases under compression and decreases under tension.

In particular, it is straightforward to determine that there is a direct proportionality factor (S_b^ε) between the bond deformation and the proportionality shift:

124

$$\bar{\nu}_{vib} = \bar{\nu}_0 + S_b^{\varepsilon} \times \varepsilon_{l_b}^{\%} \tag{5.10}$$

where $\varepsilon_{l_b}^{\%}$ is the bond deformation (the superscript '%' indicates that deformation is given as a percentage). From a macroscopic point of view, a tensile (or compressive) stress is expected to decrease (or increase) $\bar{\nu}$.

Raman Spectroscopy of Single Crystals under General Stress. If a deformation is applied to a single crystal, vibrational mode independence is lost and phonon-phonon couplings occur [128]. The fundamental equation of Dynamics then becomes:

$$\mu \frac{\partial^2 r_i}{\partial t^2} = -\sum_{jlm} \frac{\partial k_{ij}}{\partial \varepsilon_{lm}} \varepsilon_{lm} r_j = -= -\sum_{jlm} K_{ijlm} \; r_j = -\left[k_{ii} \times r_i + \sum_{\substack{jlm \\ j \neq i}} K_{ijlm} \; r_j \right] \tag{5.11}$$

$i, j, l, m = x, y \; or \; z$

r_i = component of normal coordinate r in direction i

μ = reduced mass

The wavenumber shifts can then be directly linked to any macroscopic stress/strain via the elastic compliance tensor and the K_{ijlm} coefficients that describe the strain-induced deformation of the bonding potentials. Few of these coefficients are independent in high-symmetry crystals. The mathematical expressions for the stress dependency of optical modes in cubic crystals can be found for given crystallographic directions [128] and planes [129].

The Case of Non-crystalline Materials. A statistical approach is adopted for polycrystalline or amorphous materials since the stress directions are unknown and the tensorial formalism is irrelevant. Let θ_b be the initial angle between a bond and the solicitation axis in a material that is macroscopically strained to $\Delta\varepsilon_M^{\%}$. The considered bond is deformed by an amount of $\Delta\varepsilon_b^{\%} = \Delta\varepsilon_M^{\%} cos\theta_b$ in the simplest assumption. The resultant shift is an integration of Eq. (43) over all bonds:

$$\Delta\bar{\nu}_{vib} \approx S_b^{\varepsilon} \times \int_{\theta=0}^{\theta=\pi/2} \left[p(\theta) \times \Delta\varepsilon_M^{\%} \cos(\theta) \right] d\theta \tag{5.12}$$

where $p(\theta)$ represents the probability for θ_b to be exactly θ. If the material is isotropic, then $p(\theta)$ is a constant and:

$$\Delta\bar{\nu}_{vib} \sim S^\varepsilon \times \Delta\varepsilon_M^\%$$

(5.13)

Therefore, a proportionality factor S^ε, expressed in cm^{-1}/%, links the wavenumber shift to the macroscopic strain in isotropic materials. Besides, if Hooke's law applies over the full strain exploration, then:

$$\Delta\bar{\nu} \sim S^\varepsilon \times \frac{100 \times \Delta\sigma}{E} = S^\sigma \times \Delta\sigma$$

(5.14)

The applied stress $\Delta\sigma$ and Young's modulus E are expressed in GPa and S^σ is the Raman Mechanical Coefficient (RMC). $S^{\varepsilon/\sigma 3}$ is usually negative: wavenumbers decrease under tension and conversely.

Young's modulus is indeed the result, at the macroscopic scale, of the force constant of the various chemical bonds. Consequently, it has been established [130] that

$$S^\varepsilon = k'E^{-1/2}$$

(5.15)

5.2.3 Composite micromechanics by micro Raman spectroscopy

Very few experimental techniques lend themselves to micromechanical characterization of heterogeneous materials since most of them are not specific, rich of limitations and often inapplicable [123]. First, X-rays and neutron diffractions only work on crystallized samples. Ultrasound analysis gives a dynamical view of cracking rather than stress measurements, photoelastometry supposes perfect transparency and SEM observations of resin grids only give an indirect measure of the surface deformations. Other specific methods exist like instrumented (micro-nano)-indentation, fragmentation, 'pull-out', 'push-out' and 'microdroplet' tests but the validity of the models used for data interpretation is questionable due to the large number of parameters.

Nevertheless, in the last decades Raman spectroscopy has been gained ground among all of the experimental techniques for micromechanical investigation of

---

[3] The symbol $S^{\varepsilon/\sigma}$ is generally adopted whenever comments apply to both S^σ and S^ε.

composites. In fact, the finding of a shift of Raman peak induced by a macroscopical solicitation has paved the way for a new branch of μRS, the so-called 'micro Raman extensometry' (μRE) [131]. Based on this approach, Galiotis used for the first time composite reinforcement as a 'mechanical probe' for a polydiacetylene/epoxy composite [25]. In fact, after calibrating the Raman peak shift in these fibers by loading them individually, matrix-embedded fibers act as internal stress/strain sensors of the composite materials they reinforce, provided that the matrix is reasonably transparent (or, almost, does not infer with the Raman spectrum) and that the reinforcement possesses a high cristallinity. Basically, it consists in monitoring *in situ* the Raman vibrational frequencies shift with applied stress or strain for the matrix-embedded fiber and to compare this dependence with the reference fiber (tested in air). Figure 5.4 summarizes the main steps leading to the reference fiber calibration curve. First, the fiber sample is subjected to a step-wise axial deformation into a tensile jig positioned on the microscope stage: at each step, Raman spectrum is acquired in the midpoint (box 1 in Figure 5.4). This allows for the evaluation of Raman peak position as a function of the applied strain (box 2). The mechanical behavior of the reinforcement is then, independently, determined by means of tensile test performed by imposing an effective strain rate equivalent to the one adopted in the Raman test (box 3). Having compared the Raman peak position vs. strain curve with the relation stress-strain, it is straightforward to calculate the dependence of Raman peak position on stress (box 4).

However, by using a tensile tester equipped with a load cell or a remote Raman microprobe, it is to possible to evaluate the calibration curve shown in box 4 in a single and more reliable experiment. However, details on the instrumental set-ups are given in the following. Having the calibration curve, test can be finally performed on the composite. Basically, the measurement is analogous to the one performed on the reinforcement: the composite is deformed and the Raman spectrum is acquired by focusing the laser beam on the embedded reinforcement. At each step, the acquisition can be performed by focusing on the midpoint of the embedded fiber or all along the reinforcement length. Through the calibration curve, the spectral characteristics acquired from the embedded fiber are converted into axial stress.
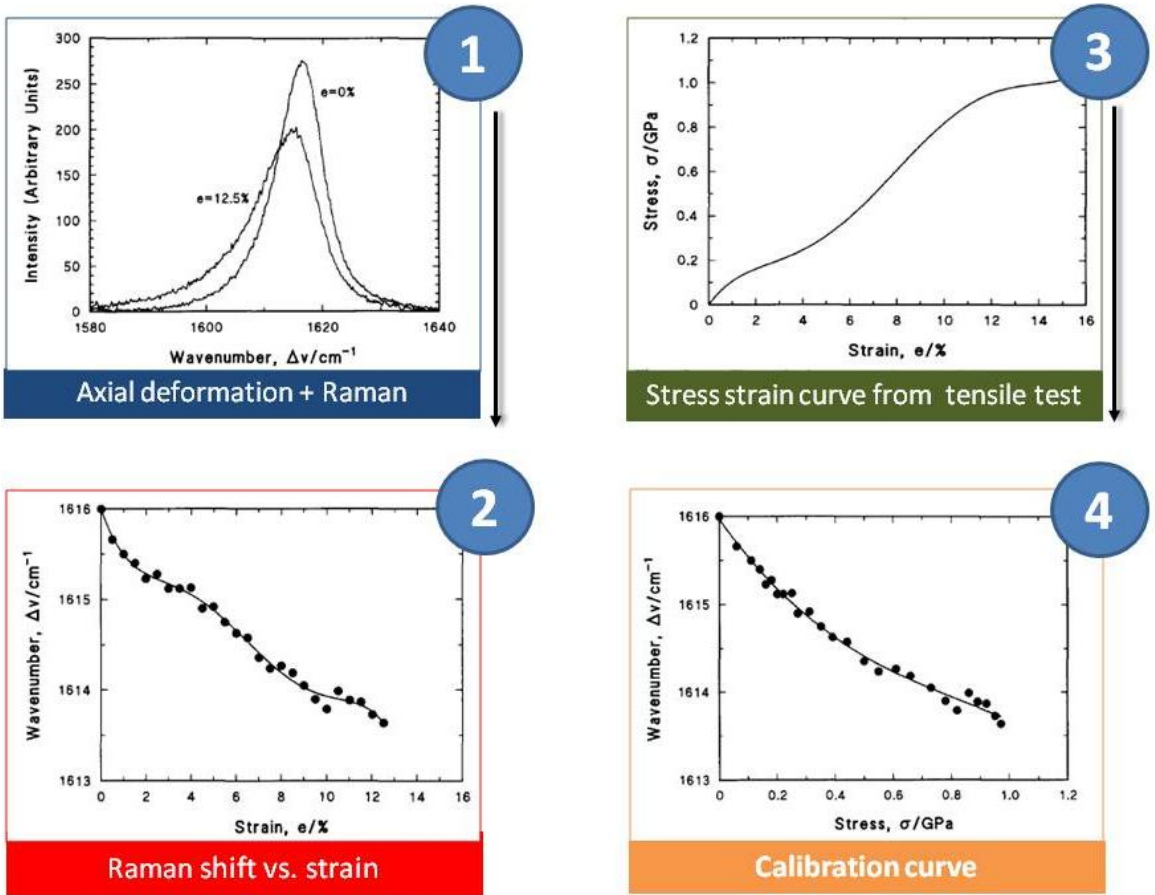
Figure 5.4 Fundamentals step of micro Raman extensometry

In particular, the point-to-point mapping provides for the stress-transfer profiles that can be straightforwardly converted into interfacial shear stress profiles along the length of the fiber by means of a simple balance of forces:

$$\tau_{rx} = -\frac{r}{2}\left(\frac{d\sigma_f}{dx}\right) \tag{5.16}$$

Besides the stress-transfer profiles, the S^ε calibrations and *in-situ* measurement of Raman spectra can be used to derive strain profiles along the fiber, residual strains [123], stress concentration factors, ineffective lengths [132], the interfacial fracture energy G_i [133] or the Coulombian friction coefficient [134].
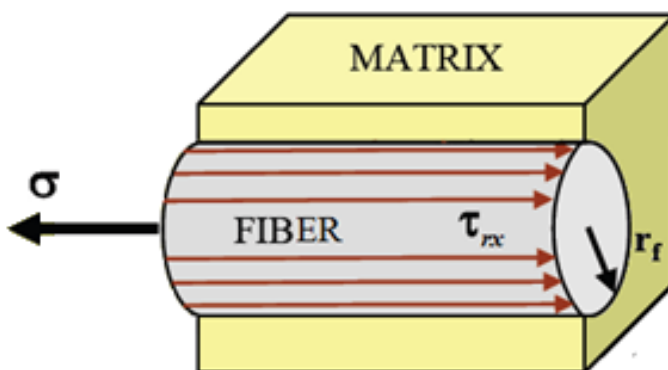
128

Figure 5.5 Schematic illustrations of forces acting on composite element

Two systems are commonly adopted in this technique (Figure 5.6): the conventional Raman microprobe set-up and the remote Raman microprobe (ReRam) [132]. In the conventional microprobe set-up, the laser beam is directed to a microscope that focus it, through a micrometric spot, on the sample mounted on a tensile jig. The scattered beam is then collected by the microscope, sent to the spectrometer and finally directed to a charged coupled device (CCD). The ReRam apparatus utilizes fiber-optic cables for laser delivery and collection; as previously, the laser is first focused on the sample, sent to the spectrometer and then collected by the CCD. However, the use of a flexible fiber optic permits operation of the microprobe in horizontal, vertical and multi-angle position, thus allowing investigation of specimens of different size and shape, mounted on common universal testing machine, and under different environmental conditions.
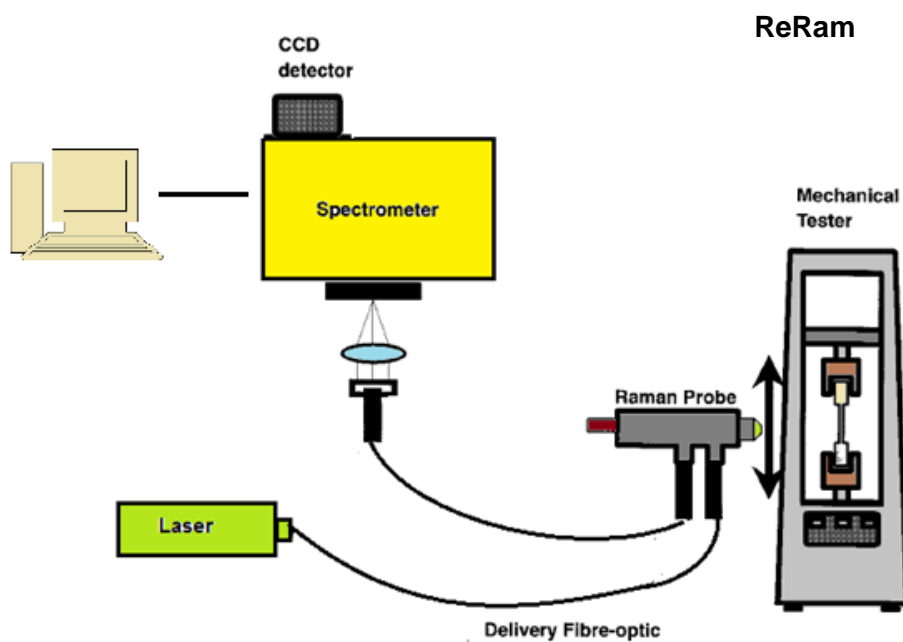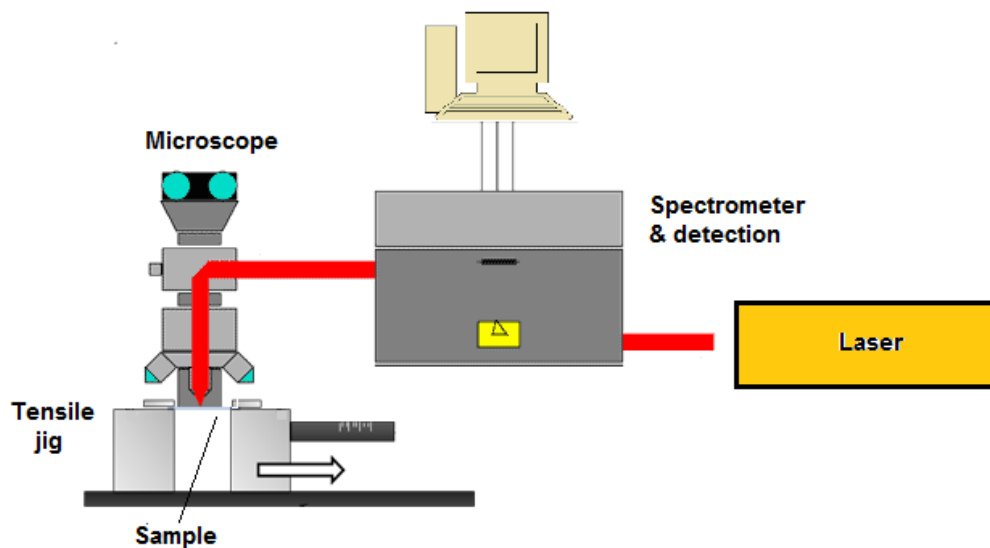
conventional Raman microprobe

Figure 5.6 Schematic of the µRS experimental set-ups

5.3 Experimental

5.3.1 Materials preparation

The material system consisted of PET cord embedded into a matrix of rubber compound. All of the ingredients (rubber compound system and cords) were gently supplied by Bridgestone TCE. Also composite preparation was performed in the laboratories of Bridgestone TCE.

In the following, preparation of the single constituents and of the composite material is described.

PET cords. In this investigation, PET cords made of two twisted yarns were adopted (Figure 5.7a). The characteristic parameter of the cords are reported in table 5.I. In order to achieve a good adhesion with rubber in the composite system, PET cords were coated with a Resorcynhol-Formaldheyde-Latex (RFL) dip. Dipping process consists in a thermomechanical treatment in which cords are concurrently stretched and immersed in the dipping solution, followed by a thermal treatment at 235°C in the oven for the complete cure to occur. In particular, dipping process was preceded by a pre-dipping. Two types of PET cords were prepared, with and without the dip solution; however, since the overall dipping treatment can induce any change into the degree of cristallinity of PET, the two cords were subjected to the same thermomechanical history. The supplied cords were used as received. Furthermore, PET monofilaments were extracted from cord without dip by using tweezers (Figure 5.7b).
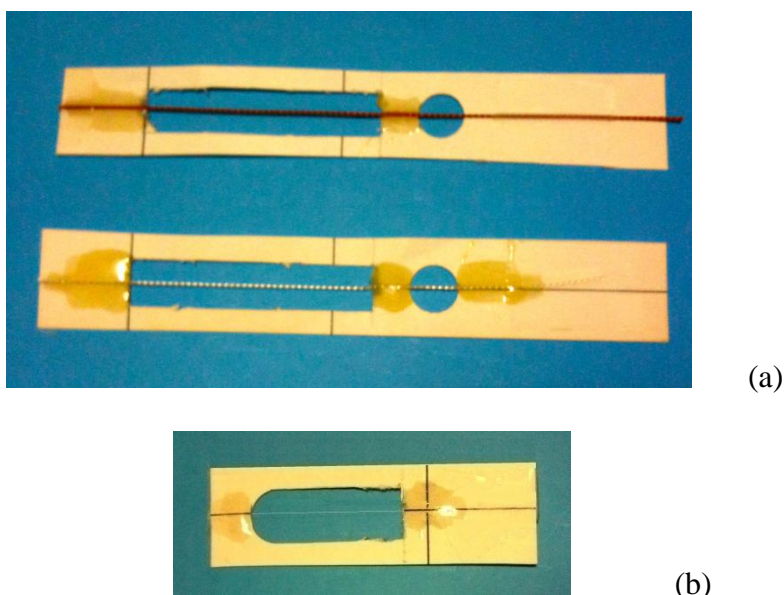

(a)

(b)

Figure 5.7 PET cord (a) and filament (b) samples mounted on the paper frame

These filaments, whose nominal diameter is 20 μm, have been used for a preliminary of study of Raman spectral characteristics (as PET 'precursor') and, consequently, for the investigation of deformational processes by micro Raman spectroscopy.

cord construction [dtex]	1670/2
twist level	270x390
nominal diameter [mm]	0.68

Table 5.I PET cord features

Rubber compound preparation. An *ad-hoc* composition has been prepared for rubber matrix in order to ease spectrum acquisition and to reduce fluorescence. Carbon black and other ingredients (such as antioxidants and antiozonants), which are typically used in rubber compound for tire application, have been thus avoided at this stage. Compound was prepared by mixing natural rubber (NR), sulfur, zinc oxide, fatty acid, N-tert-butylbenzoithiazole-2-sulphenamide (vulcanization accelerant) into a Haake Rheomix series 600/610 batch mixer (Thermo Scientific, Germany). Compounding was performed by mixing all the ingredients for 12 minutes at 30 RPM. Temperature was ensured not to be over 110 °C in order to avoid curing. Composition details are reported in table 5.II.

The obtained rubber compound has been then processed in the mill (preheated at 80 °C ca.) in order to obtain pads of unvulcanized material with a thickness of 1 mm ca.. Optimal vulcanization conditions were determined on the basis of a vulcanization curve, obtained though the rubber Process Analyzer RPA 2000 (Alpha Technologies, Akron, OH, USA) as shown in Figure 5.8. The pad of rubber has been prepared by vulcanizing a milled sheet of compound in a mechanical press at a temperature of 160°C, for 10 minutes, under the pressure of 1.37 MPa.

	Weight percentage
NR	94.08
sulfur	1.22
accelerator	0.94
fatty acid	0.94
ZnO	2.82

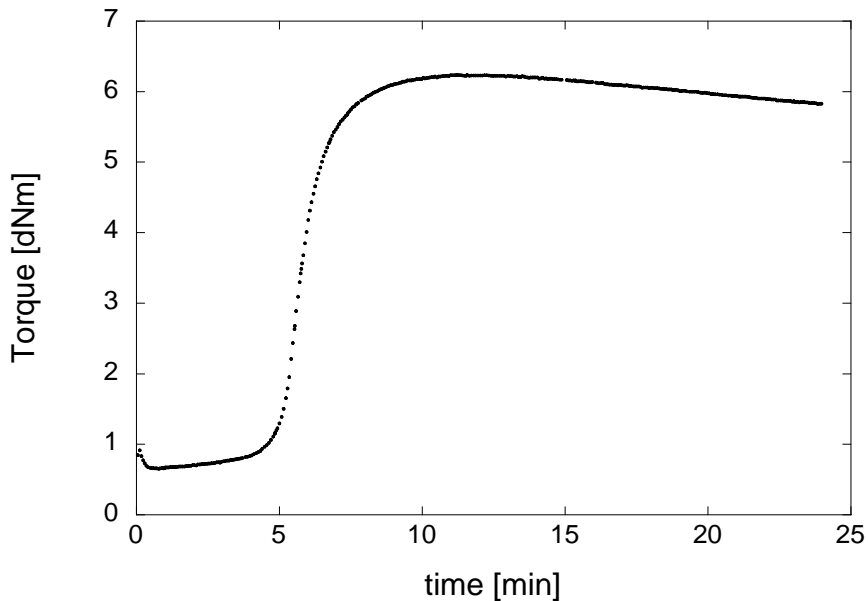Table 5.II Compound composition

Figure 5.8 Vulcanization curve at 160°C

Rubber cord composite. Rubber cord composite pads have been prepared by compression molding. In particular, micro Raman extensometry requires a reasonably transparent matrix. In this case, since rubber compound was not transparent, cords were embedded in the matrix in such a way to be very close to the outer surface of the pad and to be easily visible. Such a solution has been already adopted by one of the authors [132]. Accordingly, a thin rubber layer has to cover the cords and this can be achieved through a peculiar protocol that exploits the initial flowing of rubber before vulcanization starts. Practically, a pad of unvulcanized rubber was put into a mold and, through a comb engraved in the frame of the mold itself, an array of aligned cords was created onto this pad. The system was then subjected to compression for 10 minutes, at 160°C and at the pressure of 1.37 MPa. Due to high temperature, before vulcanization starts, rubber flows (as represented by the initial decrease of torque in the first minute of treatment, as shown in Figure 5.8) and slightly covers the array of cords. The composite was then cooled down naturally at room temperature. The coverage induced by the upper layer of rubber was found to be of the order of 100 μm. Rectangular samples were cut from the composite pad by using a scalpel. In particular, two typologies of specimen have been prepared (Figure 5.9 and Figure 5.10):

- discontinuous composite, in which the cord is embedded only in the gauge length of the sample, i.e. the gripped ends of the specimen consist of only rubber;
- continuous composite: the cord completely crosses the specimen over the full length (gauge length and clamped edges).
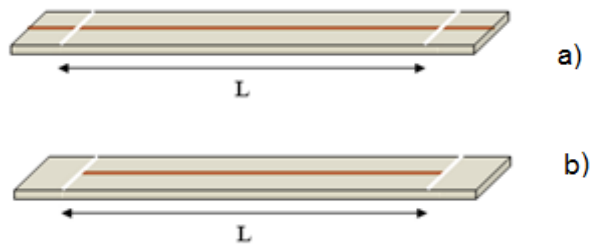

Figure 5.9 Photograph of a cord-rubber pad

Figure 5.10 Geometries of continuous (a) and discontinuous (b) composites. Gauge length 'L' is defined in the schematic

Specimens with a nominal width of 10 mm and with several gauge lengths (10 - 50 – 100 – 150 – 180) were prepared. One embedded cord was essentially used in this investigation. A nominal cord fraction of 1.7% was obtained by adopting this geometry. Nevertheless, sample with different cord contents were prepared by both reducing the width of the 1-cord sample (nominal cord fraction equal to 3%) and varying cord spacing in the cord array arranged in the mold before vulcanization (2 or 3-cords sample, with a nominal cord fraction of 4.7%).

5.3.2 Tensile test

Mechanical characterization of rubber compound, PET monofilament, cords and composite was carried out through tensile test. All specimens were tested using a universal mechanical testing machine INSTRON mod. 5566 (Instron Corp. Norwood, MA, USA). Vulcanized rubber compound was tested following the recommendations given in ASTM D412 [39]. Monofilament and cords were mounted on a cardboard window using a commercial epoxy resin (Araldite[®] Precision, Huntsman Advanced Materials) and a minimum of 48 h was allowed for the adhesive to set completely at room temperature prior to testing, in order to minimize slippage errors. Pre-determined gauge lengths of 30 mm for the monofilament and of 50 mm for the cord were adopted and test were started after carefully cutting both sides of the cardboard window. The cross-sectional areas of both filament and cords were measured by using an optical microscope. In order to investigate the mechanical response of continuous composites, tensile tests have been performed by using rectangular specimens cut from composite pad, with several dimensions as discussed in the previous section. All the tests were performed at a constant rate of 8.77×10^{-4} %/s. A full scale load of 10 N was found to be adequate for monofilament samples and of 10 kN for the cord and the composite. Test were repeated ten times for each material.

5.3.3 Micro Raman Spectroscopy

The Raman microprobe set-up employed here is shown in Figure 5.11. Raman spectra were obtained using the He–Ne laser (632.8 nm). The laser beam, polarized along the fiber axis, was directed through a series of mirrors to a modified Nikon microscope, which was used to focus it to a micrometric spot on the sample via a suitable objective lens (x10, x50 and x100 for, respectively, composite, cord and filament). The power of illumination ranged between 2 mW (for monofilament) and 5 mW (for cord and composite). The 180° back-scattered beam was collected by the same microscope objective and focused on the entrance slit of a SPEX 1877 triple monochromator (Spex, Jobin-Yvon-Horiba Company), where it was analyzed through a grating system. Finally, the spectrometer dispersed light was directed to a Wright instruments CCD detector, which was used as a photon detecting system and the Raman spectra were recorded on a PC. Spectra of undeformed samples were first acquired. Samples were stretched by using a custom-made tensile jig that could be housed on the

microscope platform. It consisted of a fixed clamp and a movable clamp, and strain-controlled steps could be manually performed by means of a micrometer screw. A motorized stage (Nanomotion II, Melles Griot, Albuquerque, NM, USA) allowed translation of the specimen along all three axes with an accuracy of the order of magnitude of the micron, providing for a precise mapping of the sample and giving the possibility of focusing onto a precise point of the sample. Raman spectra of individual PET monofilament extracted from cord and of the whole cords were first collected. Fibers and cords were fixed on a paper frame by using the commercial epoxy resin Araldite® Precision, that was cut at the beginning of the experiment. A gauge length of 30 mm was adopted for filaments and of 50 mm for cords. A minimum of 48 h was allowed for the adhesive to cure at room temperature prior to testing. Samples were stretched in steps of the order of 0.5% strain and, during each step, Raman spectra were acquired in the midpoint of the sample for three times. Each step required a total time of 570 seconds (deforming and focusing required 30 s ca. while spectrum acquisition was performed in 3x60s); an effective strain rate of 8.77×10^{-4}%/s was thus applied during the stretching of the fiber. Continuous and discontinuous composite samples with several gauge lengths (10 - 50 – 100 – 150 – 180 mm) were also stretched in steps of the order of 0.5% and, at each step, Raman spectra were acquired in the midpoint of the embedded cord.
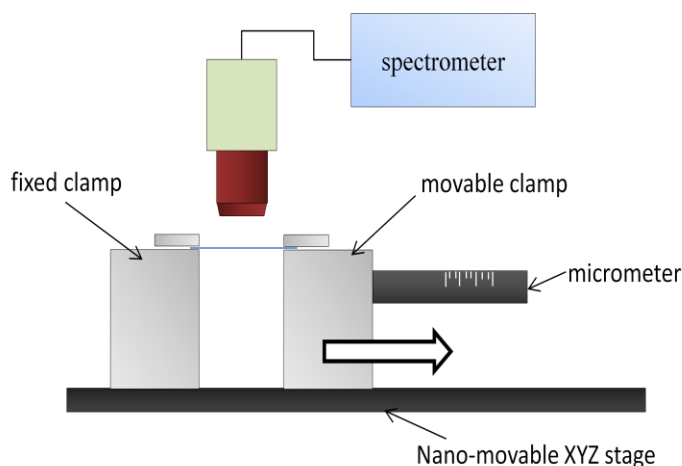

Figure 5.11 Fixed Raman microprobe with a custom-made tensile jig

5.4 Results and discussion

5.4.1 Tensile test

Stress-strain curves provide important information about the mechanical properties of rubber, PET monofilaments and cords. Stress-strain curve of rubber compound is shown in Figure 5.12. As already observed in the investigation of the 'canonic' compound for tire application described in Par. 4.4.4, the stress-strain curve of the special compound is highly non-linear. The stress-strain curve of monofilaments, dipped cord and treated cord (without dip) are shown in Figure 5.13 and Figure 5.14. The stress-strain curve of the monofilament is non-linear; hence it is possible to divide it into three regions: a starting linear region until 1%, followed by initial softening and, finally, a slope increase until failure. The Young modulus, defined as the first derivative of the stress-strain curves, gives more detailed information about the tensile behavior of single fibers [135,136]. Figure 5.13 also shows the modulus-strain curve for PET monofilament: this curve exhibits a modulus maximum at very low strains (0.5%), as already observed by Heuvel et al. [136], that has been ascribed to the breakdown of the entanglement network [135], and a second maximum at 6% strain that has been related to the breaking of the taut tie molecules.

In the stress-strain curves of cords (with dip and without dip) three regions can be clearly distinguished, as already highlighted in the previous Chapter. The first region (strain up to 0.05%) is characterized by a very low slope: it is the low cord modulus zone, in which filaments contribute a little to stiffness because twisted filaments are only rearranged under tension. The second region is characterized by a higher slope or, analogously, a higher modulus because filaments are fully effective in enhancing stiffness after the initial rearrangement. The third wide region, until failure at 13% ca., exhibits softening. The presence of the external dip does not induce no significant variation. However, a slight improvement of mechanical response can be found for dipped cord; it can be simply ascribed to the presence of a another reinforcing phase (the dip) that mainly contributes to a superior cohesion of the corded structure, because of a partially penetration within the outer layers of filaments.

The tensile properties of fiber and cords are listed in Table 5.III. The reported values of the modulus were determined from the initial slopes of the stress-strain curves ($\varepsilon \sim 1\%$).
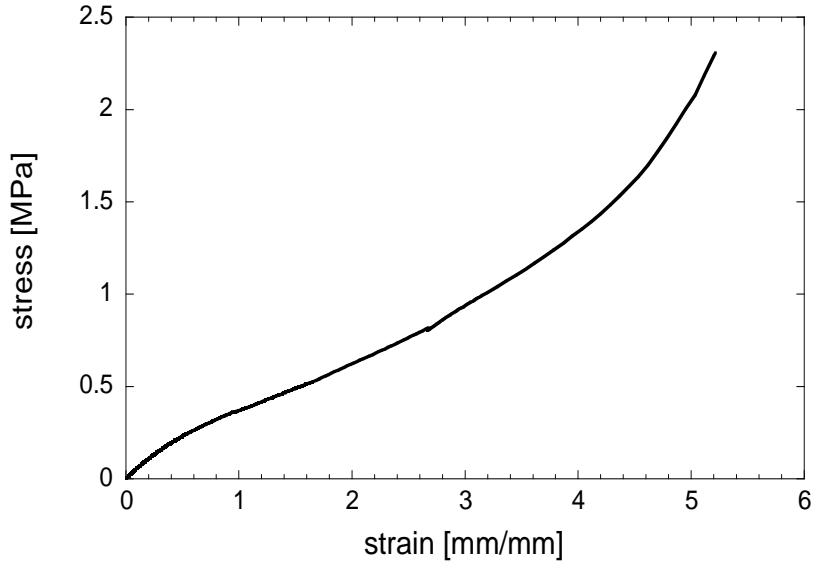
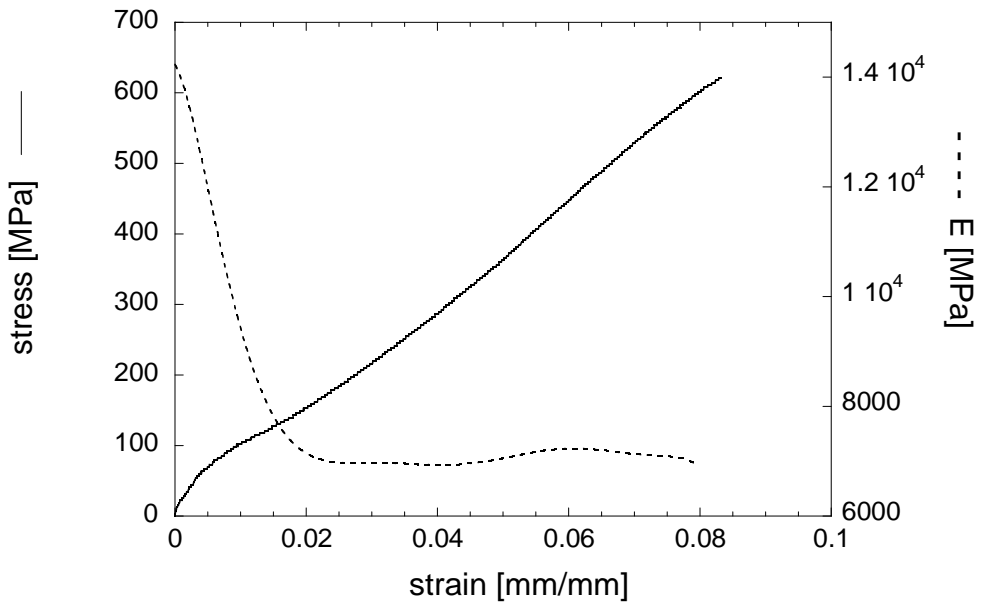Figure 5.12 Stress strain curve for rubber compound

Figure 5.13 Stress-strain curve (solid line) and modulus-strain curve (dotted line) for PET monofilament
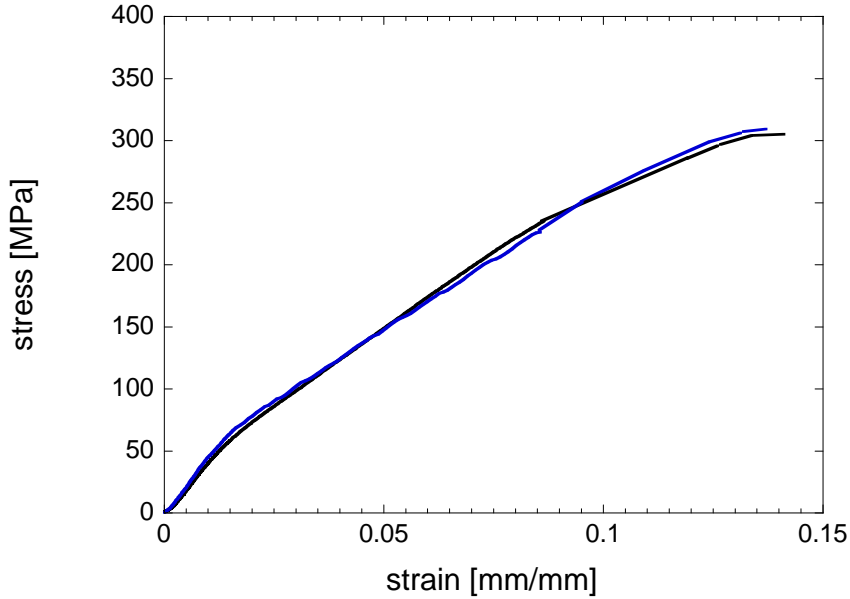
Figure 5.14 Stress strain curve for PET dipped (blue) and undipped (black) cords

Sample	E@ ε =1% [MPa]	Tensile strenght [MPa]	Elongation at break [%]
Rubber compound	0.6	2.3	520
PET monofilament	9450	623	8.3
PET cord without dip	4158	235	12.6
PET dipped cord	4890	230	12.5

Table 5.III Tensile properties of PET monofilament and cords

Figure 5.15 shows the stress-strain curves for continuous composites with two different cord fraction (namely, 1.7 and 3%). The mechanical response evaluated in the longitudinal direction reflects the behavior of the reinforcement and exhibits a clear dependence on sample length. The elastic response of the composite, in terms of Young modulus, is improved as reinforcement length increases, as already observed in the macroscopical investigation discussed in Chapter 4. This pronounced dependence can be ascribed to a 'finite fiber length effect' [111,137]. In particular, Figure 5.16 shows the Young modulus (calculated for ε ~1%) as a function of sample gauge length (L). The theoretical modulus predicted by using the rule of mixtures (2.44c) is shown as a continuous line. The longitudinal Young modulus of the composite is found to

increase significantly with sample length and seems to approach asymptotically the theoretical modulus. As already observed for composite investigated in the previous chapter, a very pronounced 'finite fiber length effect' can be noticed.
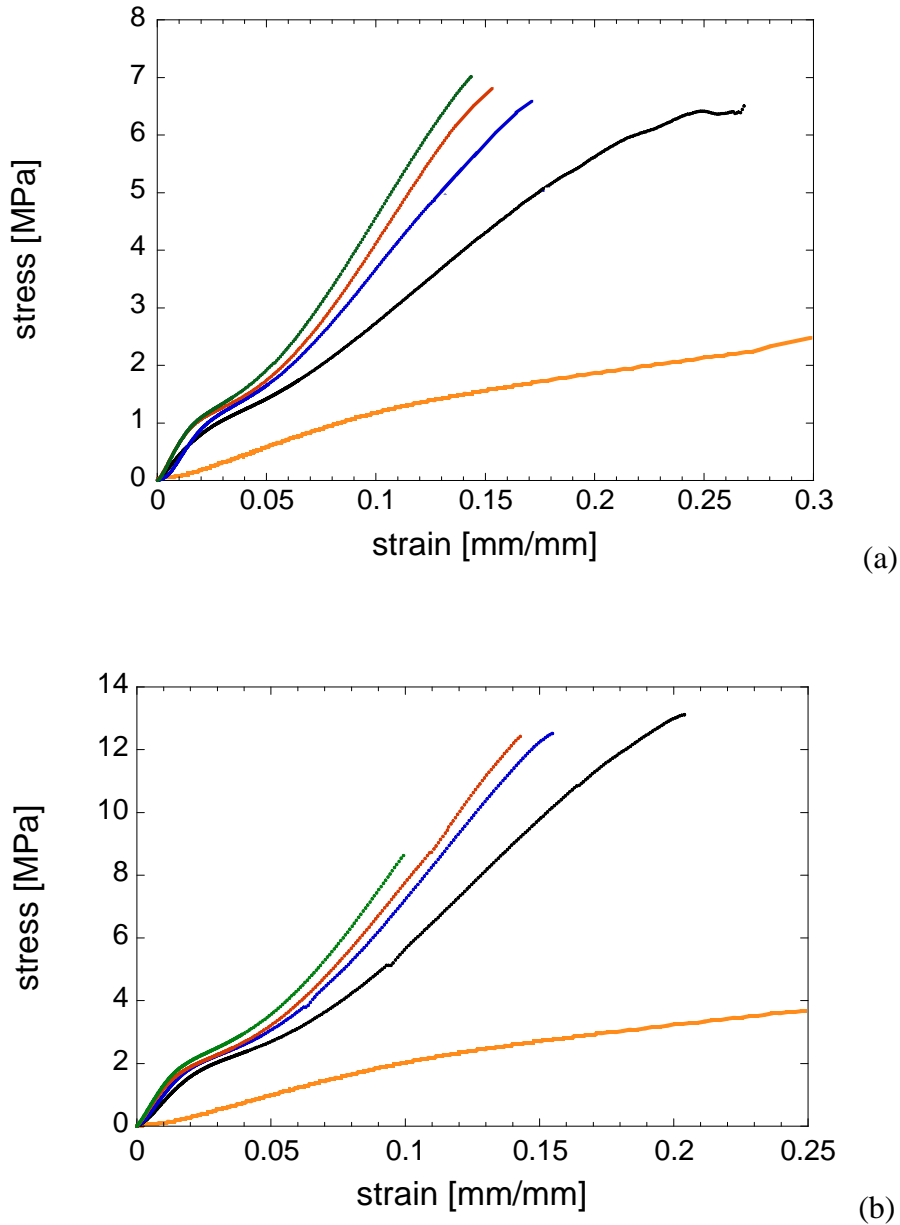

(a)

(b)

Figure 5.15 Stress strain curve for continuous composites at two cord fraction: a) Vc = 1.7%; b) Vc= 3%. Test have been performed at several gauge lengths: 10 mm (orange), 50mm (black), 100mm (blue), 150 mm (red) and 180 mm (green)
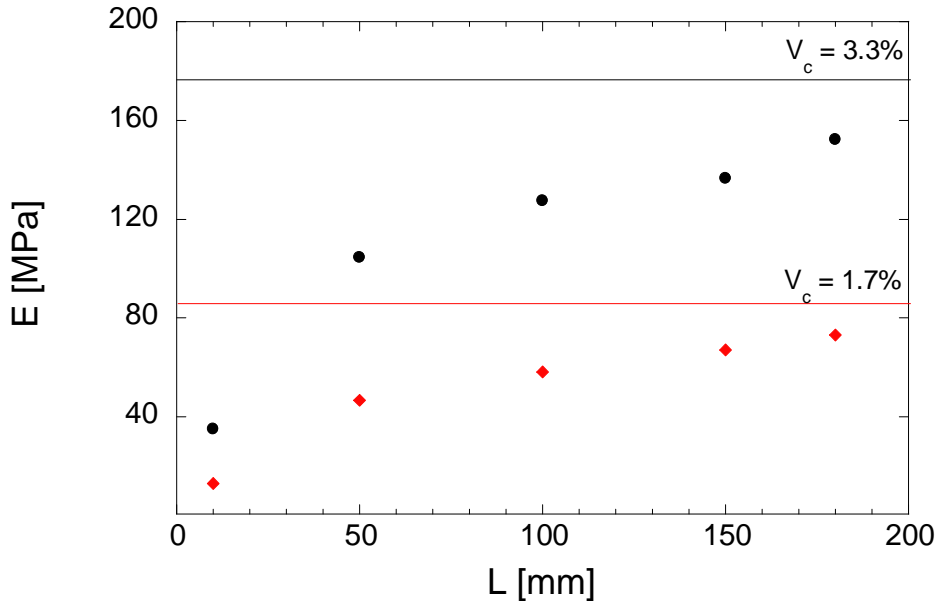
Figure 5.16 Dependence of continuous composite Young modulus on gauge length. Red circles refer to composite with 1.7% cord while black circle to 3%. Lines indicate modulus predictions.

5.4.2 Micro Raman Spectroscopy

Raman spectroscopy of the undeformed reinforcement. Raman spectrum of the monofilament of PET in the range 1400 to 1850 cm^{-1} is shown in Figure 5.17. In this region, two peaks can be found at around 1616 and 1730 cm^{-1}; the former is assigned to C-C stretching in the phenyl group and the latter to carbonyl stretching [138,139]. Both the peaks were found to show strain-induced shift [140], as also highlighted in Figure 5.18, where a schematic of atomic displacement in PET chain is depicted. In particular, in the light of the micromechanical investigation, the discussion will be centered around the observation of the benzene C-C (p-phenylene) stretching band, since it was found that the 1730 cm^{-1} band exhibits a smaller peak shift [141,142]. As already observed [142], the shape of the p-phenylene ring stretching peak is clearly asymmetric. Figure 5.19 shows the comparison between the peak fitting performed by using a single Lorentzian and two Lorentzian functions. The single symmetric function does not give a very good fit for the band. The fitting with two functions better matches peak shape but a higher dispersion is introduced in the measurement since no information is available on the spectral

characteristics of the Lorentzian positioned at lower wavenumbers. Peak position is found to be at 1614.7±0.1 cm^{-1} according to the one-Lorentzian fitting and at 1615.6±0.3 cm^{-1} for the procedure based on the use of two Lorentzian functions. In both the procedures, the band under investigation is found at lower wavenumber that those reported in literature; this discrepancy can be ascribed to the particular thermomechanical history that the material has experienced during dipping and heat-setting process. Several investigations [141,142] adopt the approach based on the peak fitting with one Lorentzian in the investigation of deformational processes of PET fibers.
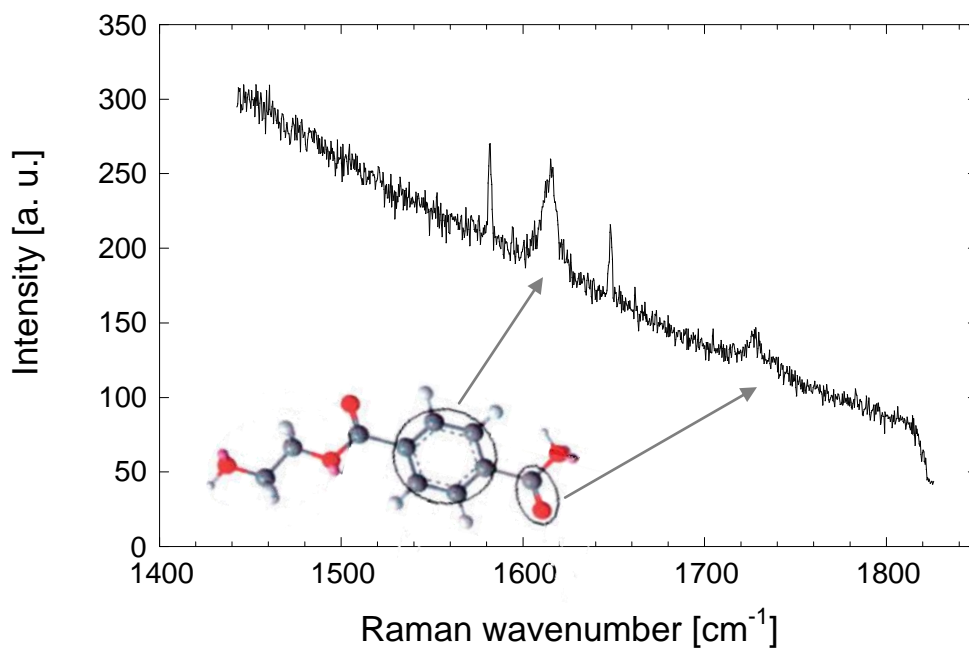

Figure 5.17 PET monofilament Raman spectrum with a schematic of the bonds of PET molecule associated to the main peaks
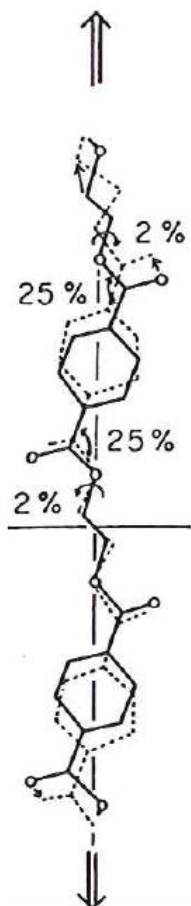
Figure 5.18 Atomic displacement and potential energy distribution theoretically calculated for a planar-zigzag PET chain subjected to a tensile strain of 10% [130]
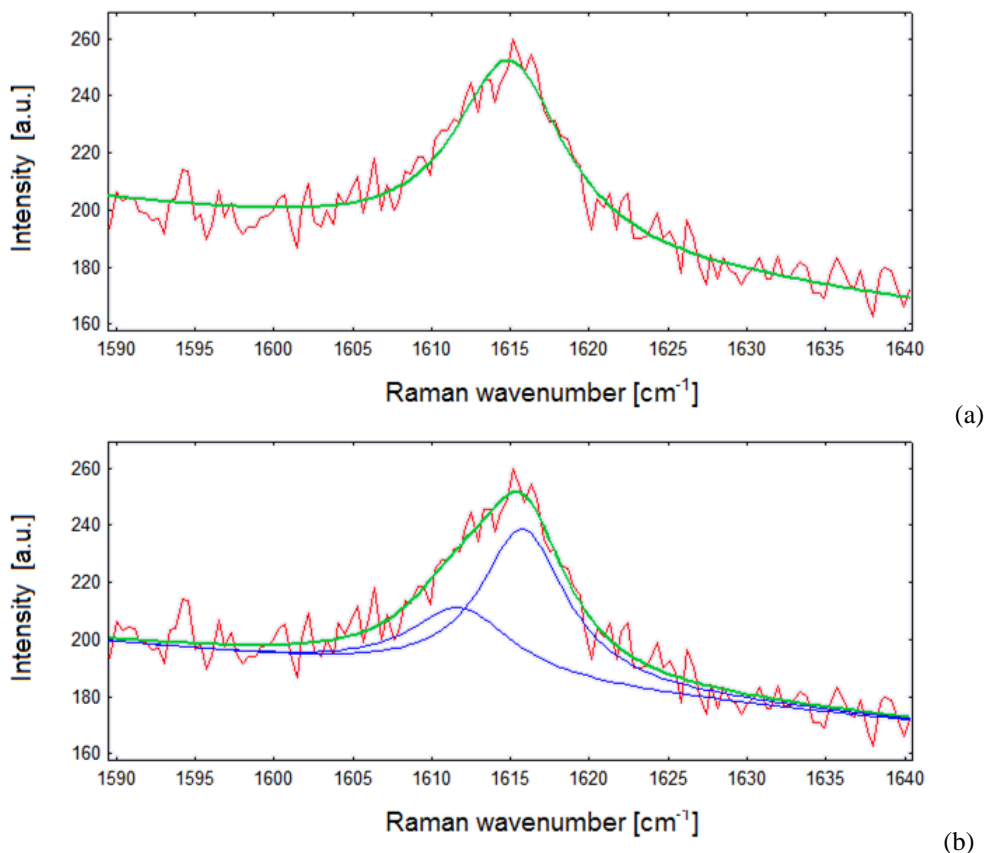
(a)

(b)

Figure 5.19 Comparison between one-Lorentzian (a) and two-Lorentzian (b) fittings of peak related to p-phenylene ring stretching

Plasma lines that can be found in the proximity of the peak under investigation are useful to get information on instrument resolution.

Raman spectrum of cord without dip has been acquired in the range 1400 to 1850 cm^{-1} and is shown in Figure 5.20. The characteristic peaks that were found in the spectrum of PET monofilament are well defined. The p-phenylene stretching peak is also asymmetric and, in the light of the previous analysis, a one-Lorentzian fitting has been adopted to determine the spectral characteristics. Also in this case, plasma lines are present. Unlike the monofilament, cord is a hierarchical structure, in which thousands of filament are twisted with different orientations; hence it is important to perform a preliminary morphological investigation in order to assess any change in peak position and/or of full width at half maximum (FWHM) due to any variation in the focused point, that can be characterized by a different filament orientation to the respect of the polarization

144

direction (parallel to cord axis). In this respect, spectra have been recorded by focusing onto single filaments of the cord structure by means of a long working distance objective at high magnification (x50). Images of investigated area were also recorded and the evaluation of the angle between filament and cord axis (θ_f) has been performed by means of a the open-source software ImageJ [143].

Figure 5.21 shows the peak position and the FWHM as functions of θ_f : it is clear that no trend can be identified since all the data fall within the experimental error (evaluated on the base of 10 measurements performed on the undeformed fiber). This result implies that this experimental setup is unable to provide a reliable tool for the separate investigation of the behavior of the material (i.e. filament) and the one of the structure (i.e. behavior of the filaments into the cord).

The position of the p-phenylene stretching band has been found at 1614.5±0.2 cm^{-1} while the mean value of FWHM is 9.7±0.2 cm^{-1}.
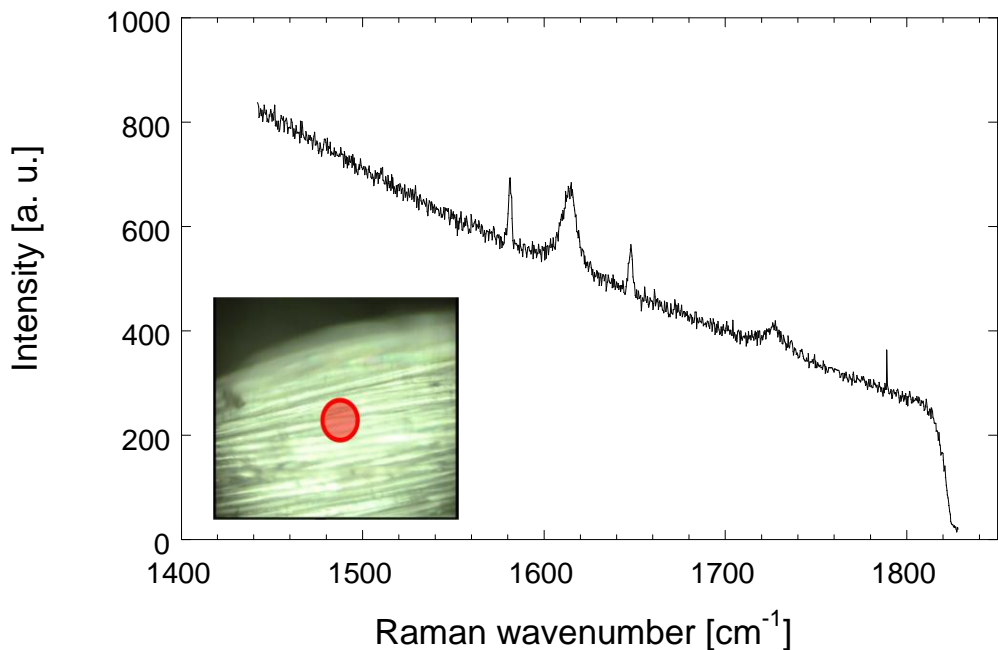

Figure 5.20 PET cord spectrum. Inset: photograph of the investigated cord
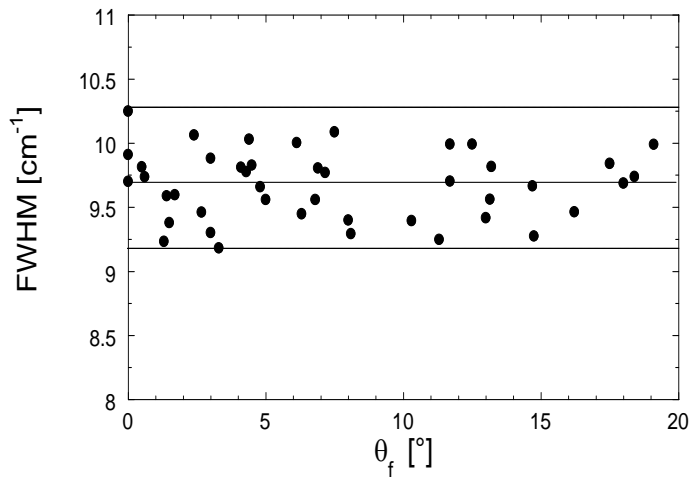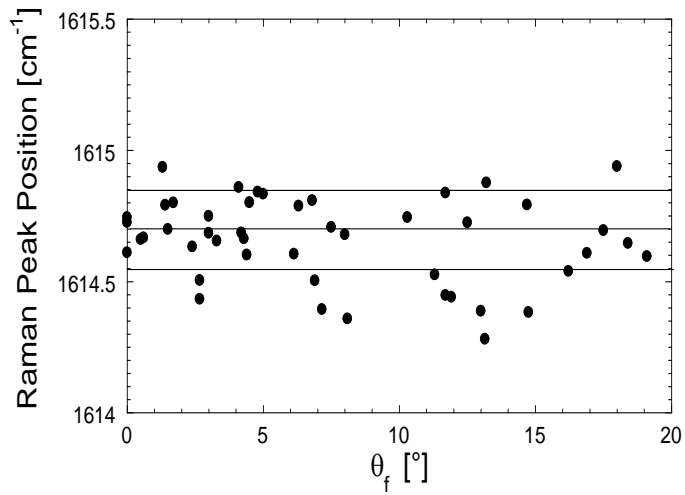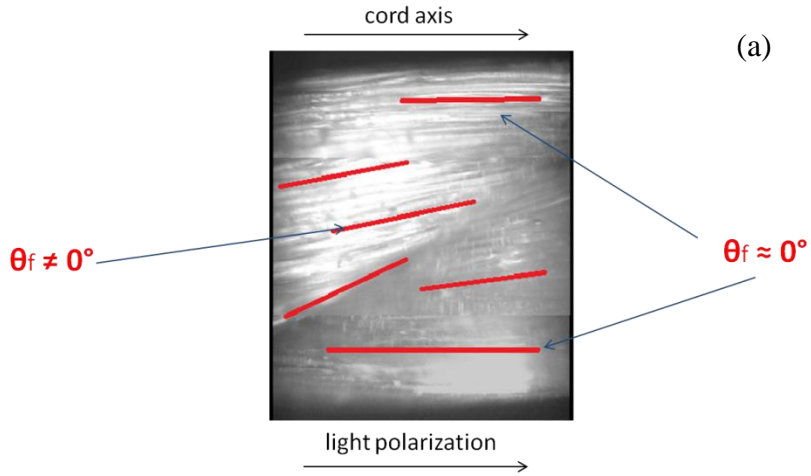
Figure 5.21 Investigation of cord morphology: a) schematic of cord structure; b) Raman peak position as a function of angle θ_f; c) full width at half maximum vs. angle θ_f

Figure 5.22 shows the Raman spectrum acquired from PET dipped cord. Despite the presence of the external dark red layer (RFL dip), the two characteristic bands are clearly detectable. Spectrum thus presents higher fluorescence and the evaluation of the position of the p-phenylene stretching band is characterized by a higher error (1614.4±03 cm^{-1}).
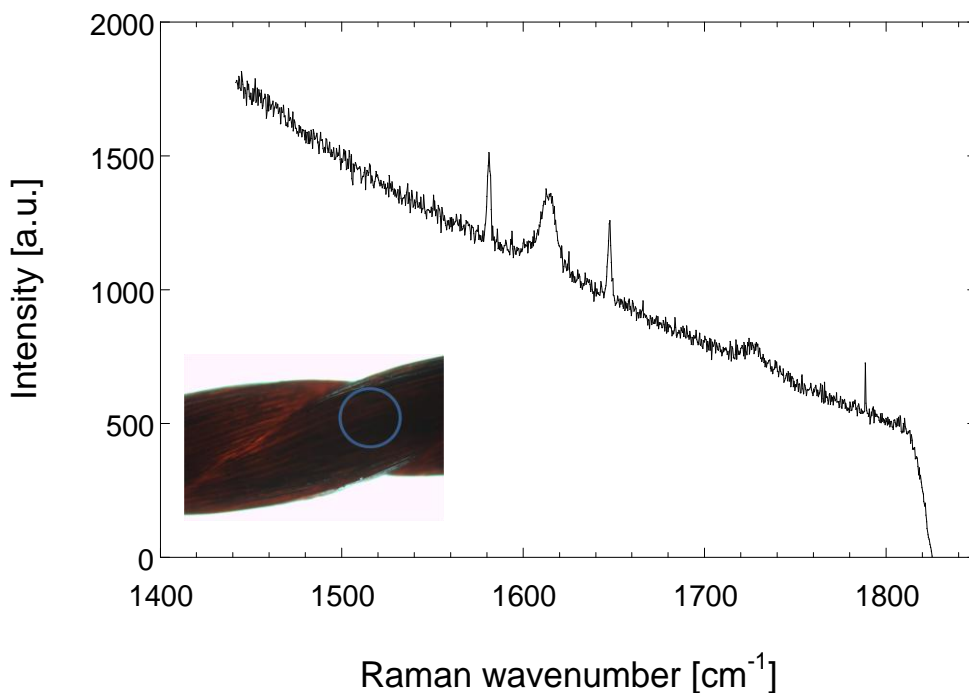

Figure 5.22 Raman spectrum of PET dipped cord. Inset: photograph of the investigated cord

It is important to underline that, within the error bar, the position of the investigated band does not show any changes for the three systems.

Deformational mechanism of the PET fiber. The p-phenylene ring stretching band has been found to shift to lower wavenumber and to broaden with the tensile deformation (Figure 5.23). The variation of the position of this Raman peak with strain, determined by using Lorentzian curve fitting (one function, as stated before) is shown in Figure 5.23a. Peak position may be considered a nearly linear function of applied strain until 5.5%. In this region, it has been found that the rate of peak shift is 0.195 cm^{-1}/% (defined for unit strain). For higher strains, the peak seems to stabilize at a constant position. Full width at half maximum increases for strains up to 6.5% (i.e. the peak broadens) and then remains constant until sample failure.
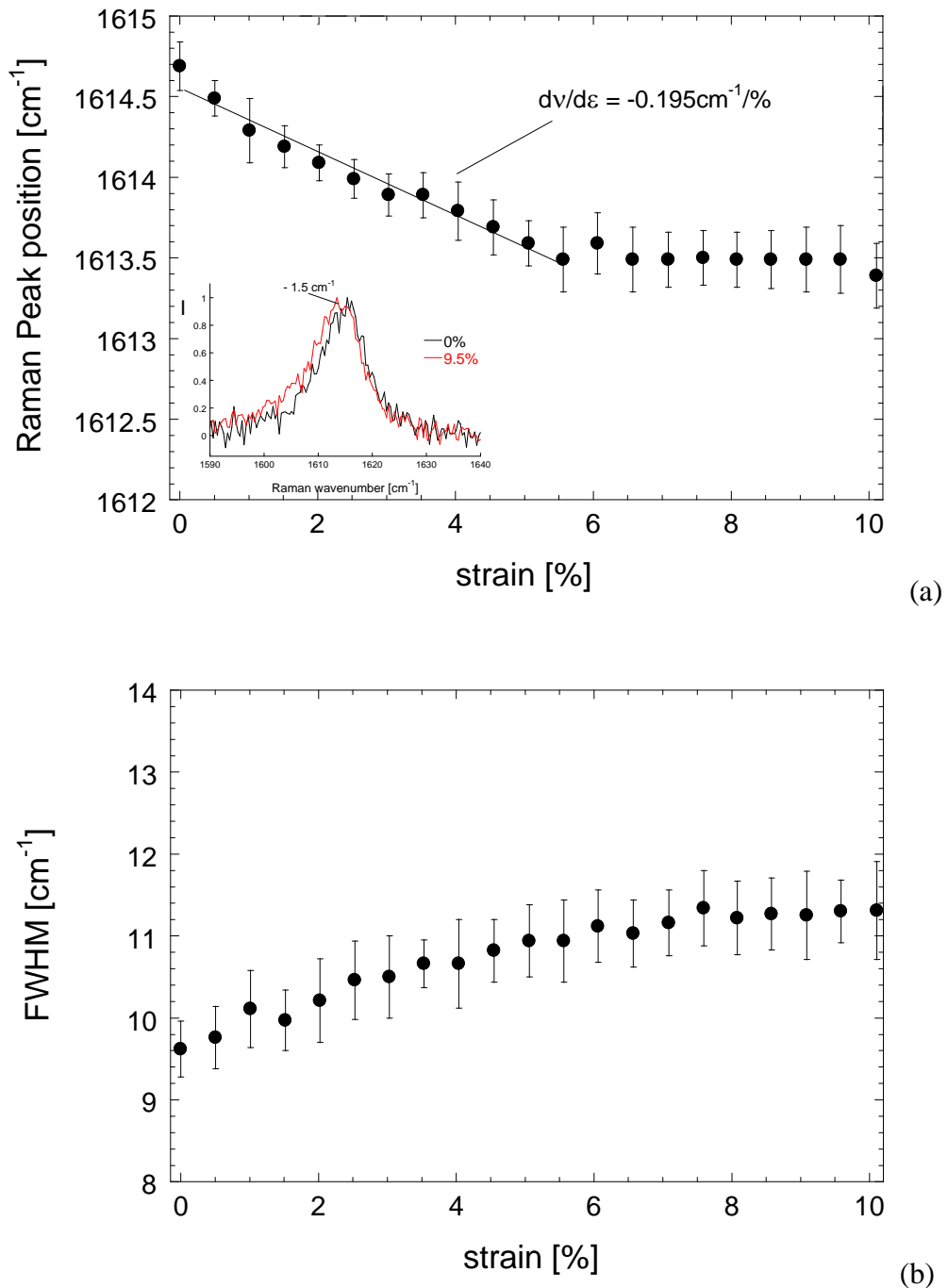
147

(a)

(b)

Figure 5.23 Variation of PET monofilament spectrum during tensile deformation: a) Raman peak position as a function of applied strain; b) Full width at half maximum as a function of applied strain. Inset: detail of Raman spectrum

It is interesting to discuss the results of µRS in the light of mechanical behavior as determined by tensile test. Figure 5.24 shows this comparison that can be useful to correlate the information about the deformational mechanism as investigated on a microscopic and a macroscopic scale. As proposed by Young et al. on the basis of the aggregate model [135,136,144-146], the deformational process of PET fiber can be divided into three stages. The aggregate model envisages that the crystalline domains alternate with highly oriented amorphous regions along the fibrils (Figure 2.24b). It is important to underline that the deformation of the oriented macromolecules in both the regions contributes to the Raman peak shift. In the first stage, the molecule tend to align along the stretching direction in both the crystalline and amorphous domains. In the second stage, the molecules between the crystals and the amorphous domains and some molecules of the amorphous regions are overstressed (as a result of the macroscopic deformation of fibers being translated into the direct stretching of bonds). In the final stage, the macromolecules of the amorphous domains start to break. This more detailed analysis reveals that the curve mirrors the stress-strain curve, already observed by Young et al. [141], suggesting that the shift observed for p-phenylene Raman band is related to stress rather than fiber strain. In fact, according this molecular model, the strain cannot be considered uniform because of the alternation of high-modulus crystals and low-modulus amorphous chains. By combining both the data of tensile test and µRS, it is possible to derive the dependence of the Raman peak position on stress, shown in Figure 5.25. The derived curve provides information on the rate of stress-induces Raman band shift that has been found equal to 2.88 cm^{-1}/GPa, for stress up to 400 MPa.
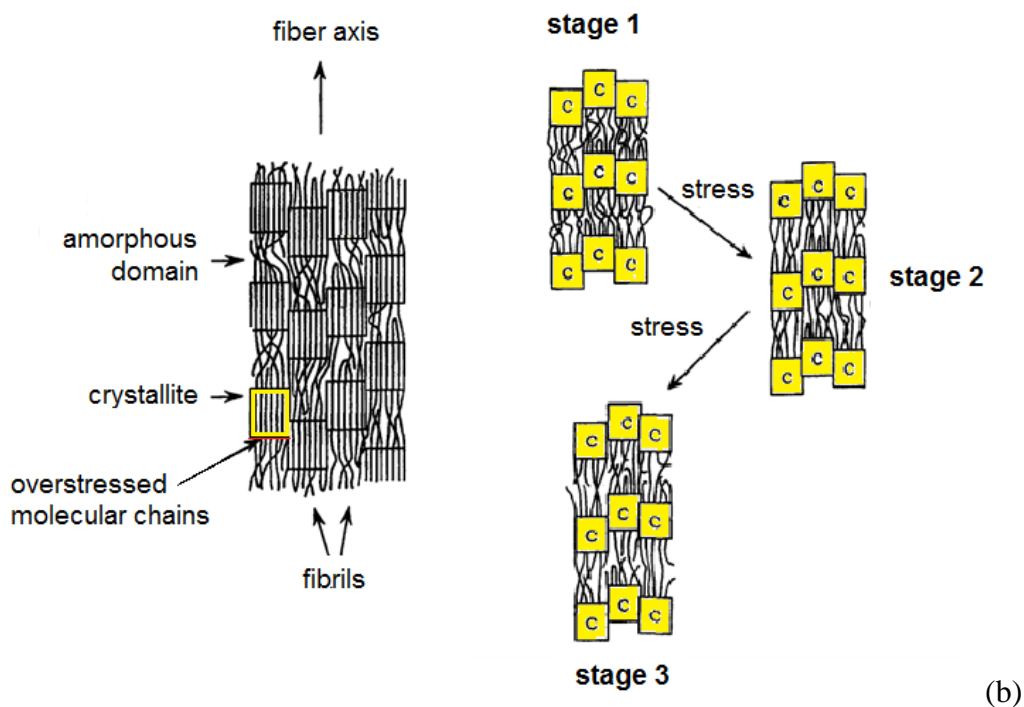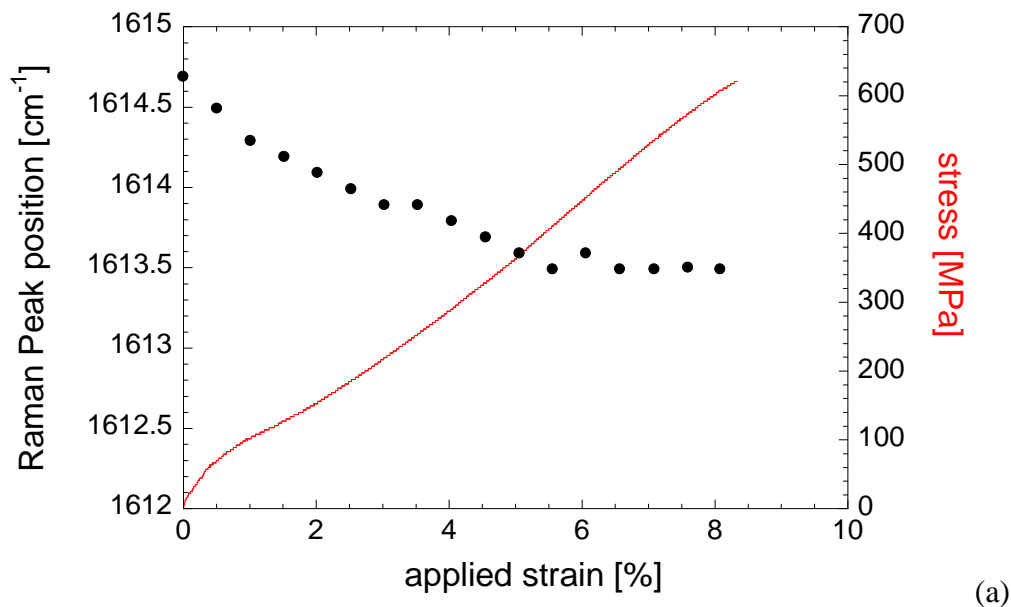
(a)

(b)

Figure 5.24 Deformational process of PET fiber: a) comparison between stress-strain curve and strain-induced Raman shift; b) schematic of molecular model related to tensile deformation of PET fiber
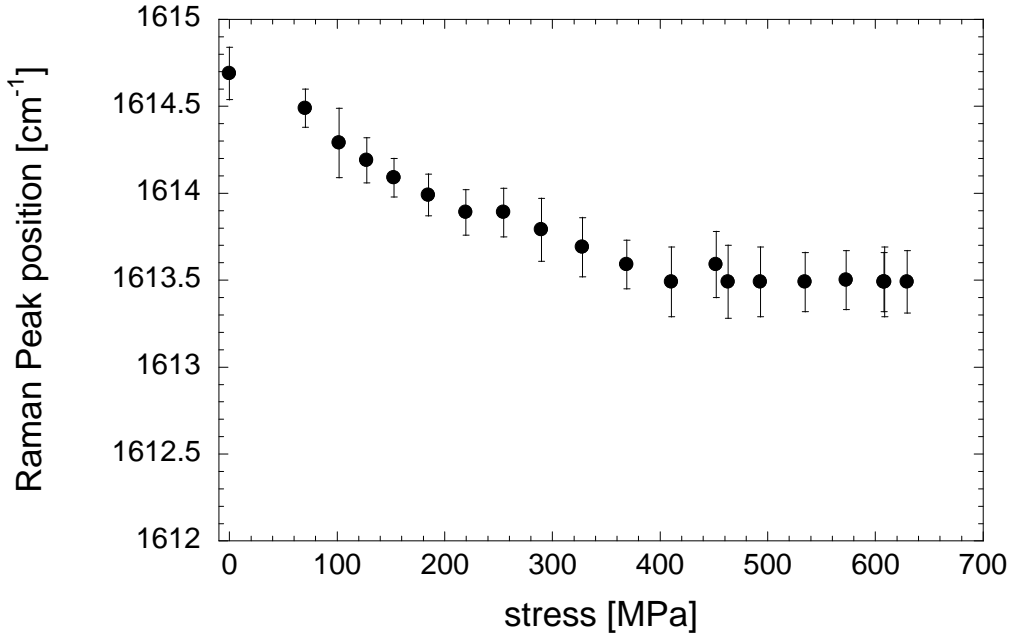
Figure 5.25 Raman peak position as a function of stress for PET monofilament

Finally, it is important to note that the presence of plasma lines has given indication on reproducibility of the measurement and that the dispersion of the experimental data can be mainly ascribed to two factors:

· fitting quality
· heterogeneities of the material.

Deformational mechanism of the PET cord. On the basis of results of cord morphology investigation, spectra have been acquired by focusing onto the sample with a lower magnification objective (10x). For both cords (with and without dip) the p-phenylene ring stretching band has been found to shift to lower wavenumber and to broaden with the tensile deformation. Measurements have been performed by stretching cord up to 10%. Results of the measurements (in terms of strain-induced peak position and FWHM) are illustrated in Figure 5.26 for cord without dip and in Figure 5.27 for cord with dip. Analogously to the case of monofilament, peak position may be considered a nearly linear function of applied strain until 5.5%, in first approximation, and in this region, it has been found that the peak shifts with a rate of 0.1867 cm^{-1}/% for cord without dip and of 0.1717 cm^{-1}/% for dipped cord. For higher strains, the peak seems to stabilize at a constant position. Peak broadens for strains up to 6.5% until remains constant.

.

(a)

(b)

Figure 5.26 Variation of Raman spectrum for PET cord without dip subjected to tensile deformation: a) Raman peak position as a function of applied strain; b) Full width at half maximum as a function of applied strain.
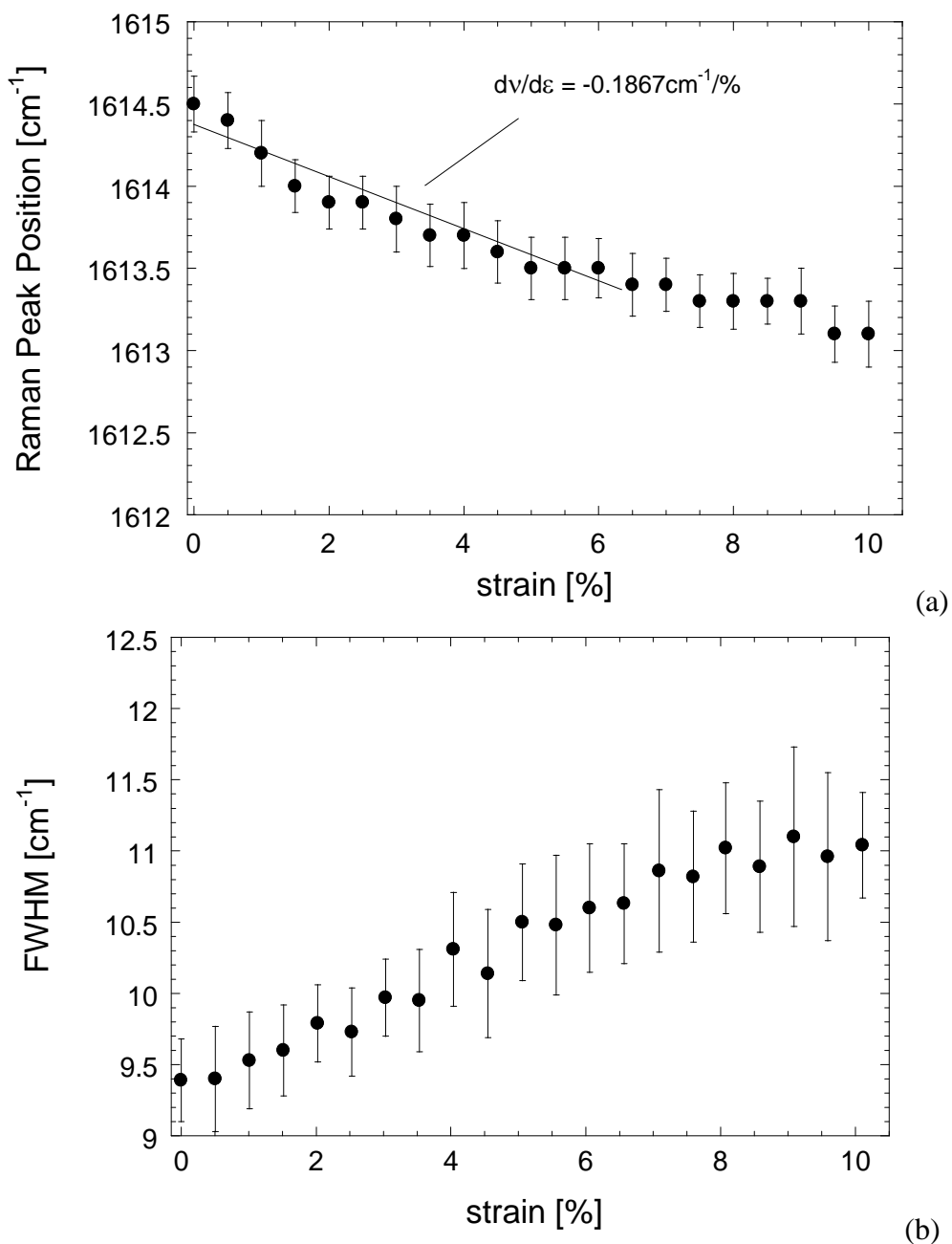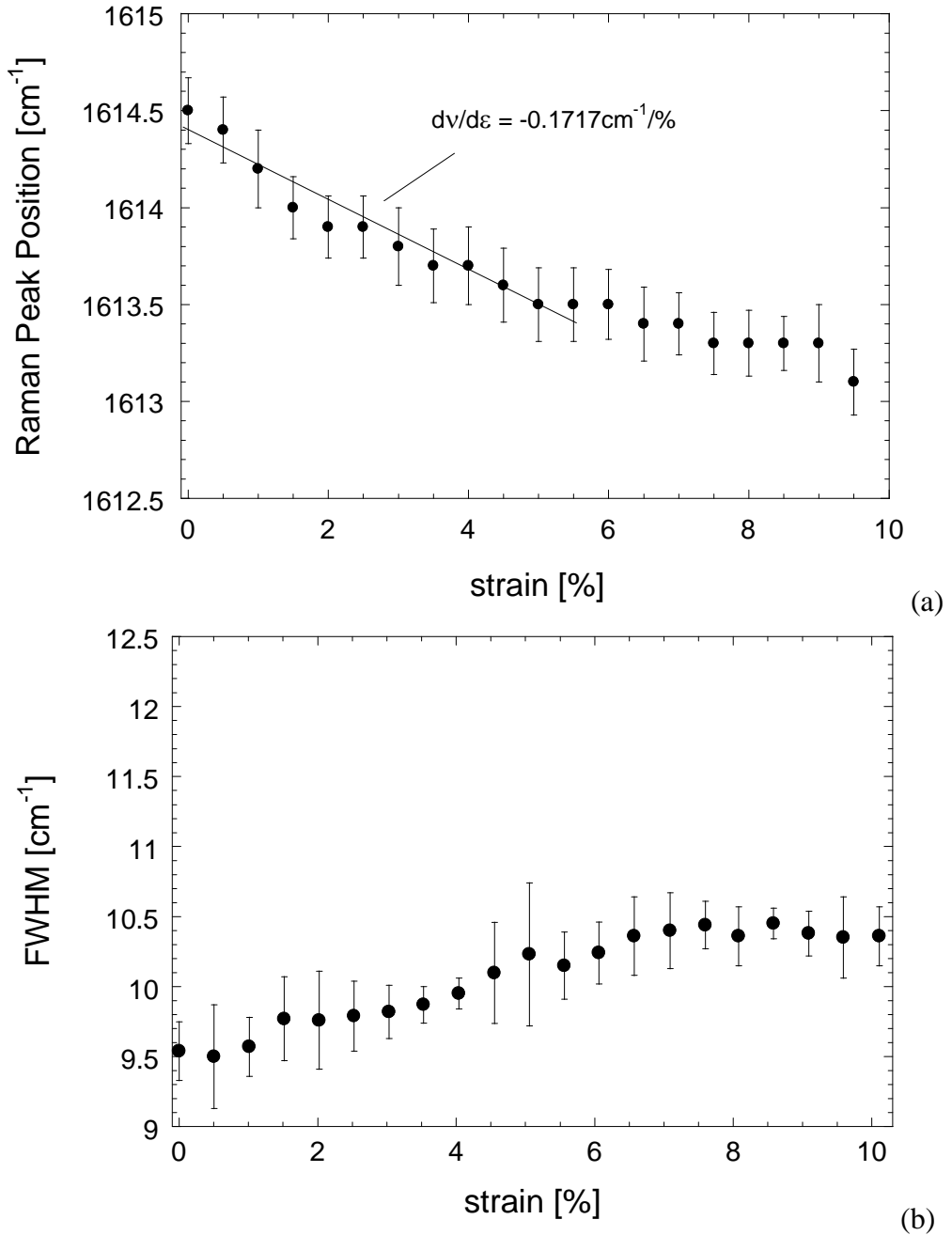
Figure 5.27 Variation of Raman spectrum for PET dipped cord subjected to tensile deformation:
a) Raman peak position as a function of applied strain; b) Full width at half maximum as a
function of applied strain.

Figure 5.28 shows the comparison between the three investigates systems and it is clear that, within the error bar, there is no difference between the filament, the undipped and the dipped cord. As stated before, the starting idea of separating the behavior of the material (from filament investigation) and structure behavior (filament reorientation due to rotation) cannot be realized. The behavior of the cords, in terms of strain-induced peak shift, is equivalent to the behavior of the filament, within the experimental error range, as already expected on the basis of the investigation of cord morphology. Accordingly, when the cord undergoes the axial strain, the final rearrangement of the cord structure at a microscopic scale due to the stretching and the rotation of the filaments [11,27] cannot be investigated. At that stage, the strain-induced Raman peak shift can be thus supposed to be dominated by material behavior. In the light of this result, cord can be directly used as the sensor for probing composite micromechanics and, for the purposes of the investigation of composite micromechanics, there is no need to follow the deformations of the monofilament during cord stretching.
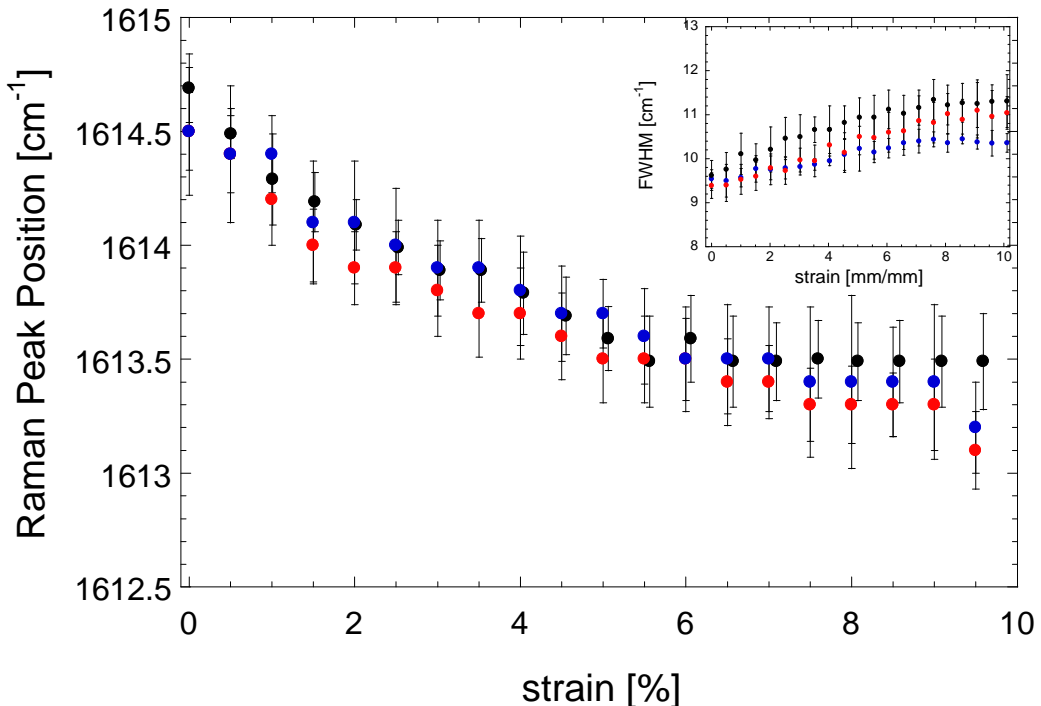
Figure 5.28 Comparison between strain-induced Raman shift for PET monofilament (black), cord without dip (red) and dipped cord (blue). Inset: FWHM

Besides the capability of investigating the deformational mechanism of fibers on a microscopic scale, micro Raman spectroscopy provides a tool for the investigation of micromechanics of composites, by adopting the reinforcement as internal (stress or strain) sensor, as stated in Par. 5.2.3. The curve shown in Figure 5.27a represents a calibration curve for the dipped cord as a strain sensor. In order to adopt cord as a stress-sensor, indeed, it is important to derive the calibration curve in terms of stress-induced Raman shift, as explained schematically in Figure 5.4. By combining the data concerning strain-induced Raman peak position of dipped cord shown in Figure 5.27a with the stress-strain curve of the material (blue line in Figure 5.14), it is possible to obtain the calibration curve shown in Figure 5.29. The derived curve shows a linear behavior for stress up to 150 MPa and provides a rate of stress-induces Raman band shift equal to 5.3 cm^{-1}/GPa.

Figure 5.29 PET dipped cord calibration curve: derived stress-induces Raman band position

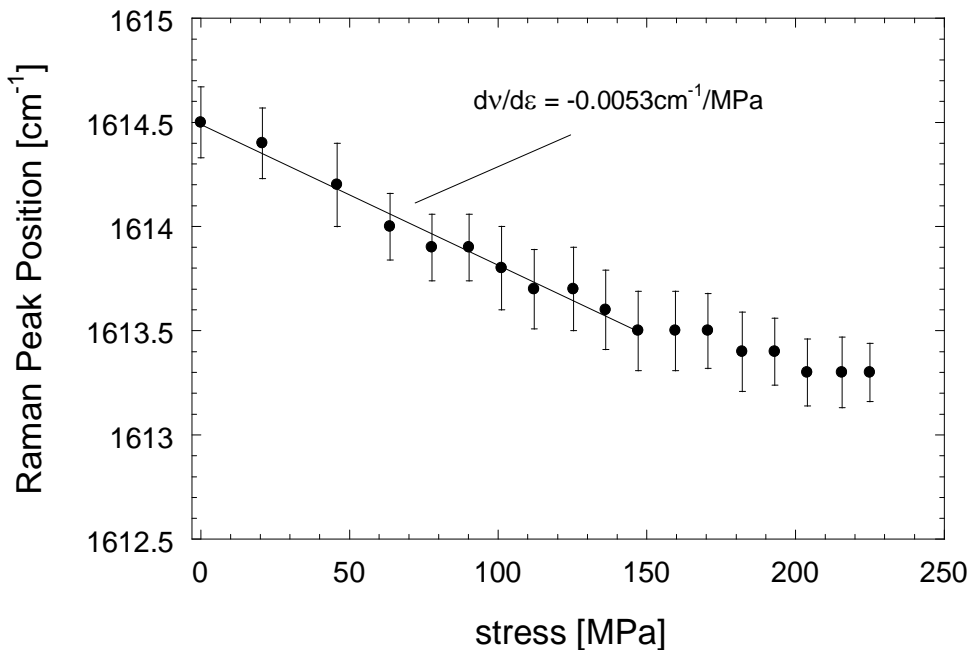*Micro Raman extensometry applied to cord-rubber composites.* Raman spectrum was acquired on the rubber-embedded cord, in the midpoint of the specimen. Specimens with different gauge lengths were analyzed in order to investigate the efficiency of stress transfer that represents the basis of the 'finite fiber length effect' observed in the macromechanical investigation. Experiments were performed on both continuous and discontinuous samples with five gauge lengths (10, 50, 100, 150 and 180 mm). The sample was stretched (strain steps of the order of 0.5%) and Raman spectrum was acquired by focusing on the midpoint of the matrix-embedded cord. The results of the investigation performed on both discontinuous and continuous composites are shown, respectively, in Figure 5.30 and in Figure 5.31 that report the position of the analyzed Raman band as a function of the applied strain. In particular, results are shown for the two sample typologies (one cord embedded into matrix) characterized by two cord volume fraction, namely 1.7 and 3%.

For all the samples, the position of the p-phenylene band of the rubber-embedded cord decreases with the applied strain (as measured by clamp displacement). Peak position may be considered a nearly linear function of applied strain and the slope that is the rate of strain-induced shift increases with sample length for both the continuous and discontinuous samples. Plots shown in Figure 5.32 show the strain-induced shift of composites (for each cord content) as a function of gauge length and highlight that it increases until a plateau is reached. At a certain gauge length, the rate of peak shift increases with cord volume fraction. This trend can be found for both the composites, i.e. continuous and discontinuous. In particular, continuous composites show a higher rate of shift than discontinuous samples. Furthermore, testing of long discontinuous composites has been difficult and vain: in particular, tests performed on 180-mm long specimens have been characterized by interfacial failure near cord ends (noticed by a pull out), resulting in an unsuccessful and unreliable result (obviously, such results are not shown). It is thus useful to compare the rate of strain-induced shift determined for each composite with the rate of peak shift observed for the single dipped cord (represented by the blue line in Figure 5.32). It is evident that only the 180mm-long continuous composite at the highest cord fraction reaches the behavior of the single dipped cord. The results of this analysis are shown in Table 5.IV in terms of ratio of transmitted strain (η^ε) as defined as the ratio of the rate of peak shift for rubber-embedded cord to the rate of peak shift for cord.
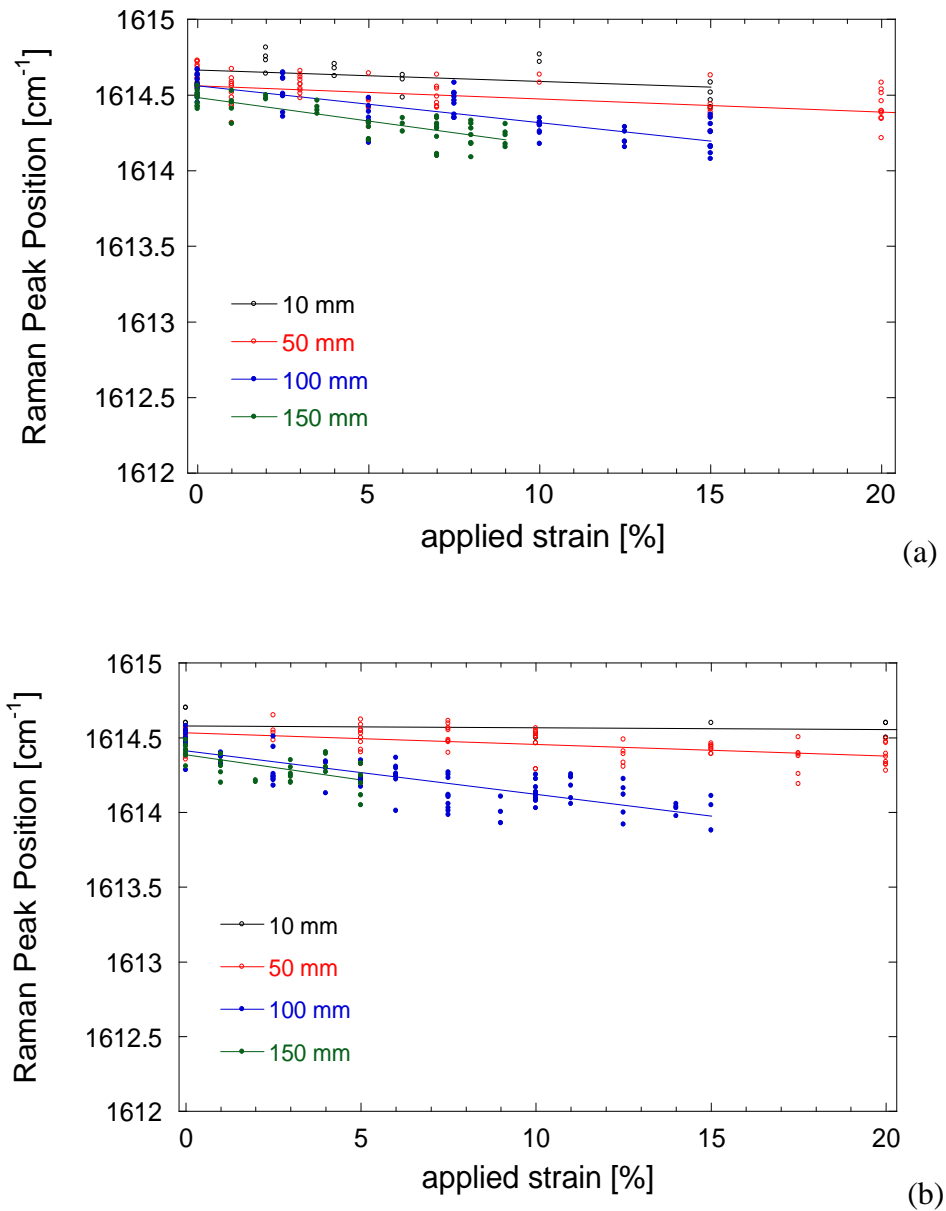
Figure 5. 30 Raman peak position as vs. applied strain for discontinuous composite as a function of gauge length and of cord volume fractions: a) V_c= 1.6%; b) V_c = 3%
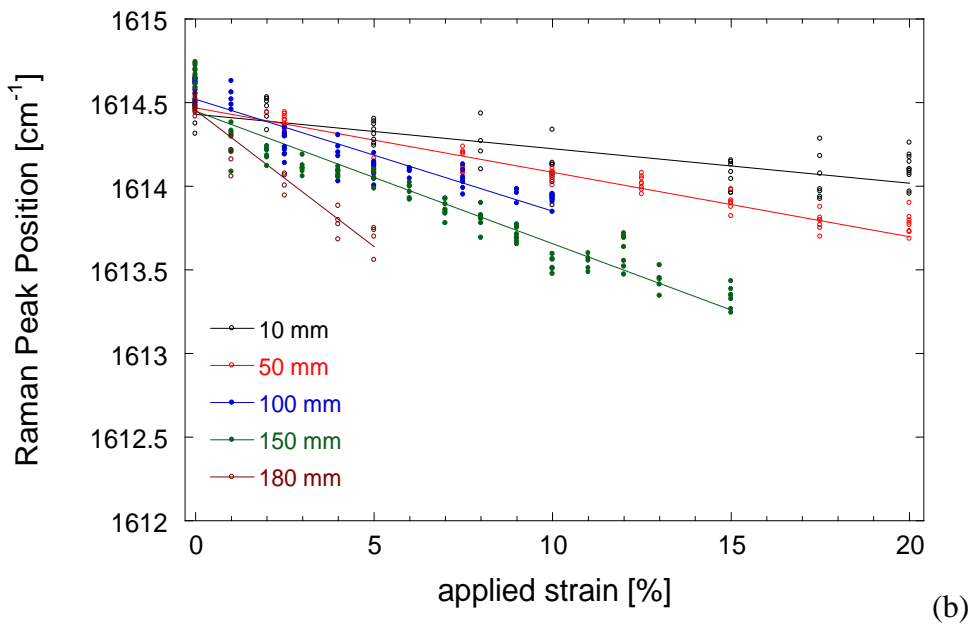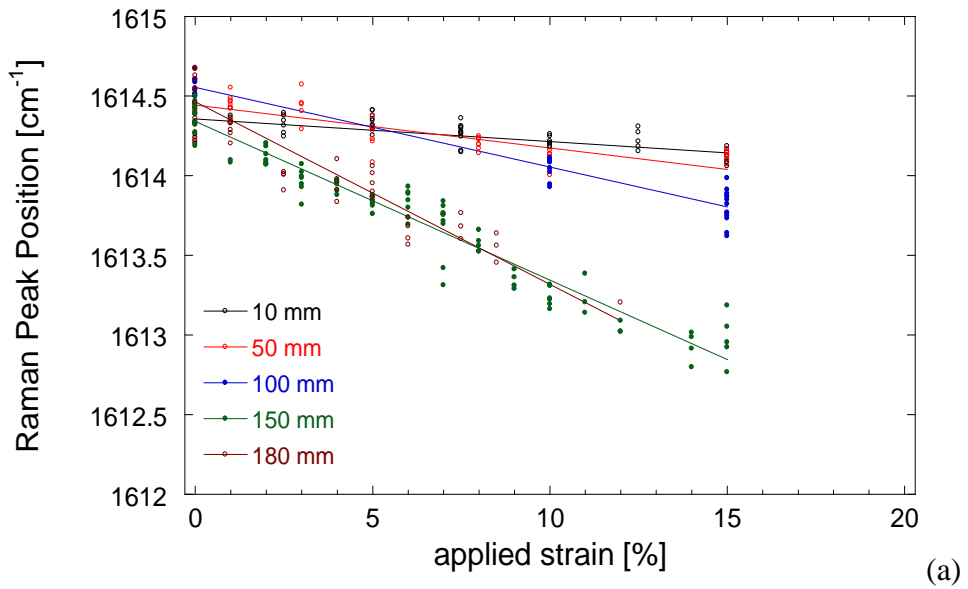
Figure 5. 31 Raman peak position vs. of applied strain for continuous composite as a function of gauge length and of cord volume fractions: a) $V_c = 1.6\%$; b) $V_c = 3\%$

This parameter can be adopted to quantify the efficiency of strain transmission to the embedded cord in the composite. In fact, since the cord is used as a strain sensor into the composite, η^ε simply represents, in percentage, the strain that the rubber-embedded cord experiences compared to the strain applied to the overall composite. For instance, the increasing of the ratio of transmitted strain that can be noticed with the increasing of sample length implies that the behavior of the rubber-embedded cord approaches the behavior of the single cord. In particular, the cord embedded into the 180 mm-long continuous composite with higher cord content experiences the total applied strain, while composite with lower V_c reaches the 78% of applied strain at 180 mm.

The significant difference between continuous and discontinuous composites in terms of ratio of transmitted strain can be straightforwardly attributed to different boundary condition treatments. For discontinuous composites, strain is applied to the matrix ends and then transmitted to the embedded cord, purely through shear stress at the interface. For continuous composites, indeed, embedded cord are clamped, thus promoting strain transmission. Nevertheless, strain transmission strongly depends on sample length yet.

These results can be interpreted on the basis of shear lag models [96-100]. In fact, it has been found that the strain in the fiber may not build up to the maximum value (i.e. strain applied to the overall composite). In fact relative strain occurs between the fiber and the matrix creating a shear stress at the interface. According to the micromechanical approaches, the high shear stress developed near discontinuities (e.g. the fiber ends) must be accommodated in order to take advantage of the properties of high-strength fibers. Hence, there is a critical value of fiber length required for achieving the reinforcing effectiveness. Basically, if the fiber is long enough for the tensile stress to build up, the isostrain condition is achieved among the two phases. As already discussed in Chapter 3, the build-up of the tensile stress gives rise to the 'positively affected length' (PAL), a region characterized by a constant fiber stress curve and a zero interfacial shear stress.

It is clear that it is necessary to determine cord axial stress within the composite, in order to get a complete description of the micromechanical problem. By using the calibration curve shown in Figure 5.29 (the derived stress-induces Raman band position), it is straightforward to convert peak shift (as evaluated for embedded cord at a certain strain) into stress. Table 5.V reports axial stress for the rubber embedded-cord, derived for 1% applied strain, as a function of gauge length. It is evident that longer cord carries a larger stress into the composite.

(a)

(b)
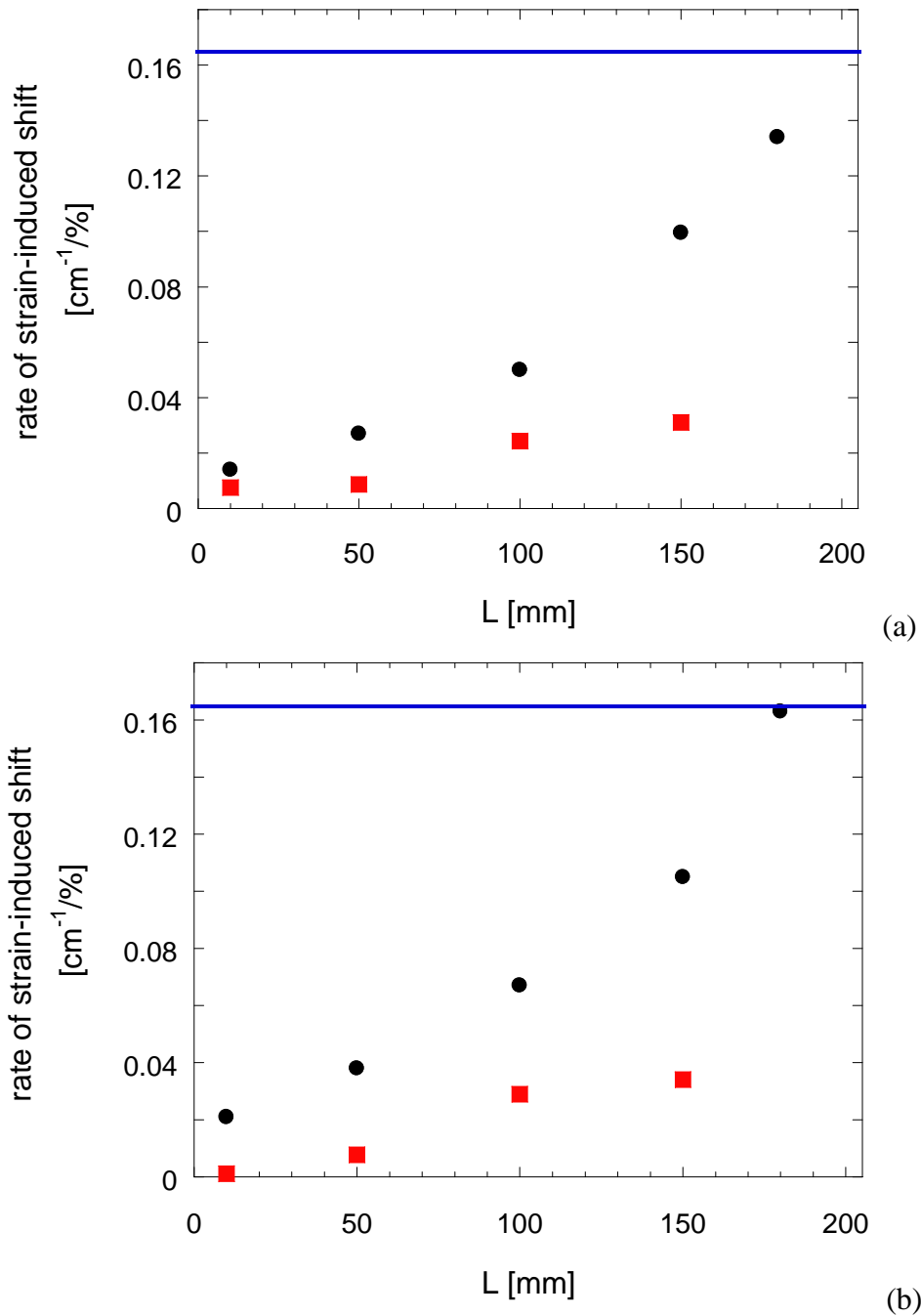
Figure 5.32 Rates of strain-induced peak shift as a function of gauge length, for both continuous (red symbols) and discontinuous (black circles) composites with 1.6% (a) and 3% cord content. Blue line represent the rate of shift for the single PET dipped cord

$\eta^\varepsilon =$		$\dfrac{\text{rate of strain-induced shift for rubber-embedded cord}}{\text{rate of strain-induced shift for PET dipped cord}}$	
		$V_c = 1.7\%$	$V_c = 3\%$
DISCONT.	**10 mm**	0.0464	0.007
	50 mm	0.050	0.042
	100 mm	0.139	0.169
	150 mm	0.180	0.196
CONTINUOUS	**10 mm**	0.081	0.122
	50 mm	0.157	0.221
	100 mm	0.291	0.390
	150 mm	0.58	0.569
	180 mm	0.78	0.957

Table 5.IV Ratio of transmitted strain for investigated composites

		Embedded cord axial stress $\sigma|_{\varepsilon=1\%}$	
		$V_c = 1.7\%$	$V_c = 3\%$
DISCONT.	**10 mm**	1.46	0.23
	50 mm	1.67	1.38
	100 mm	4.6	0.56
	150 mm	5.97	6.48
CONTINUOUS	**10 mm**	2.7	4.04
	50 mm	5.2	7.31
	100 mm	9.61	12.9
	150 mm	19.7	20.2
	180 mm	27.8	31.3

Table 5.V Embedded cord stress evaluated at 1% strain for investigated composites

Figure 5.33 Reinforcing efficiency of discontinuous (red symbols) continuous (black symbols) composites as a function of sample length: a) Vc = 1.7%; b) Vc = 3%.
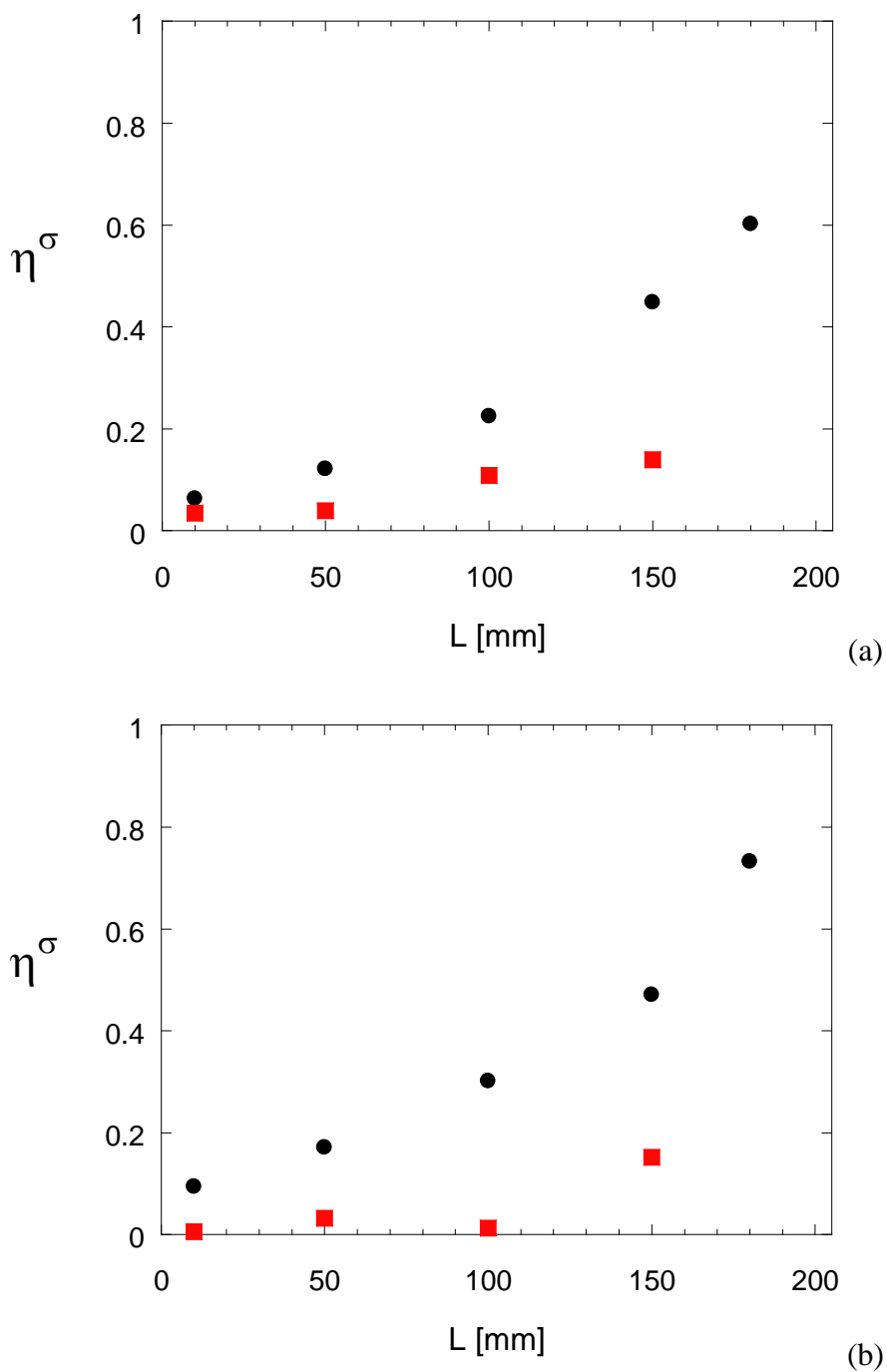
It is thus clear that the efficiency in carrying stress increases with embedded cord length. In particular, it is useful to define a reinforcing efficiency (η^{σ}), as the ratio of axial stress carried by the cord embedded into the composite to the axial stress carried by the single cord. Reinforcing efficiencies evaluated at 1% applied strain are shown as a function of gauge length in Figure 5.33. The significant increase of reinforcing efficiency with length implies that embedded cord provides a more efficient reinforcement as its length increases.

Finally, the calculated ratio of transmitted strain is correlated to the reinforcing efficiency of embedded cord in a master curve (shown in Figure 5.34), confirming that is the longer is the embedded cord, the higher is the strain it experiences (up to the applied strain value) and the stress it carries.
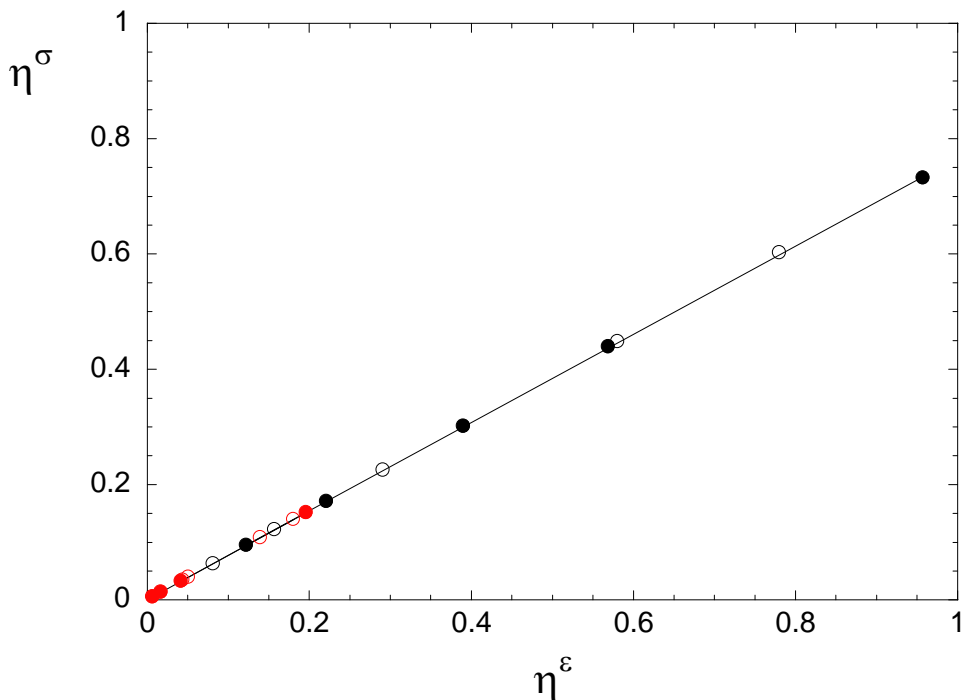
Figure 5.34 Correlation between reinforcing efficiency and ratio of transmitted strain for both discontinuous (red symbols) and continuous (black) composites at 1.7% (open) and 3% (full) cord content

Correlation between macromechanical and micromechanical response of cord-rubber continuous composites. In the light of the micromechanical investigation of the efficiency provided by reinforcement, it is finally possible to discuss the 'finite fiber length effect' observed in the macroscopic investigation of

mechanical behavior of continuous cord-rubber composites. In fact it has been found that elastic modulus increases with sample length (Figure 5.16). It is thus useful to correlate elastic modulus determined at a certain gauge length to the corresponding reinforcing efficiency[4], as shown in Figure 5.35. Modulus has been found to increase with reinforcing efficiency, thus demonstrating that the improvement of mechanical response with sample length is due to finite fiber length effect. The significant increase of reinforcing efficiency with length implies that embedded cord provides a more efficient reinforcement as its length increases and, consequently, the overall macroscopical of composite is finally improved (cf. Figure 5.16). Basically, the longer the embedded cord is, the higher is the stress it carries in the midpoint, the highest is the averaged response as evaluated by tensile test.
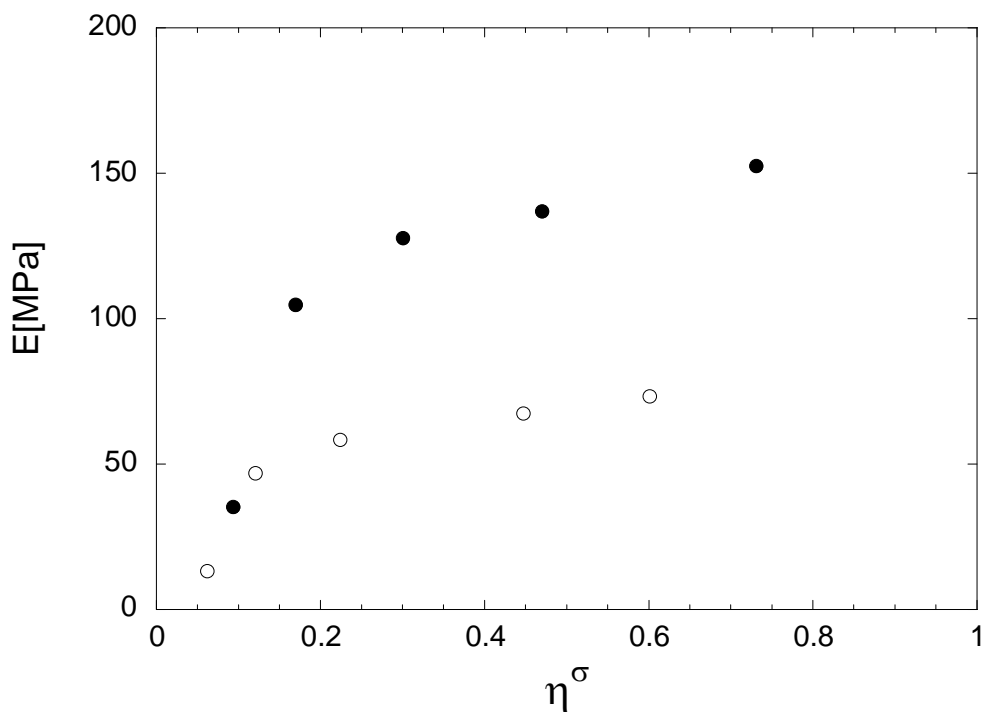

Figure 5.35 Elastic modulus as a function of reinforcing efficiency of the embedded cord

---

[4] It is important to underline that both elastic moduli and reinforcing efficiencies have been determined at 1% applied strain.

Finally, it is interesting to analyze the efficiency of the composite, as evaluated on a microscopic and a macroscopic scales. The reinforcing efficiency can be adopted to define the efficiency of the composite on a microscopic scale because it represents the comparison between the stress carried by the embedded cord with the stress carried by the single cord (strain being equal). The macroscopic efficiency of continuous cord-rubber composites has been defined in Chapter 4 as the ratio of the measured Young modulus to the theoretical modulus as calculated by using the rule of mixtures (Eq. 3.44c), and quantifies the comparison between the actual response of the composite and the ideal behavior of an infinitely long one. It is clear that this parameter increases with sample length, that is composite response reaches the ideal behavior for long samples. Both the efficiencies are found to increase with sample length, although with different trends. However, a direct correlation between the two efficiencies is not straightforward since they have been derived from averaged (macroscopic) and maximum stress (renforcing). Reinforcing efficiency has been in effects derived in the midpoint of the sample whereas axial stress is maximum while micromechanics reveal that stress is not constant all over the cord axis. Actually, as also confirmed by μRE [123], the region of the fiber near the ends (the 'transfer' or 'ineffective' length) - that is out of the PAL - is less heavily stressed than this central plateau region, so that the average fiber stress is lower than in long-fiber composite subjected to the same external solicitation. Accordingly, the macroscopic measurement of stress carried by the composite (as the tensile test) accounts for an average reinforcing efficiency that decreases as the fiber length is reduced, for the proportion of the not fully-loaded fiber length increases.

It is important to underline that the increase of sample length results into the improvement of composite response, as highlighted by both macroscopic and microscopic investigations.

The result of this investigation has thus confirmed the predictions of micromechanical models, in terms of the strong dependence of the response of such composites on embedded cord length. The considerable mismatch between the elastic properties of the phases, along with the very low reinforcement content, makes this dependence particularly pronounced because the ideal conditions for stress transfer are hardly achieved. In such conditions, the application of the rule of the mixtures may induce an error in the prediction of the behavior of the composite, for it does not account for the aforementioned dependence. Hence the rule of mixture represents a valid prediction for composite modulus provided that the isostrain condition is achieved. According
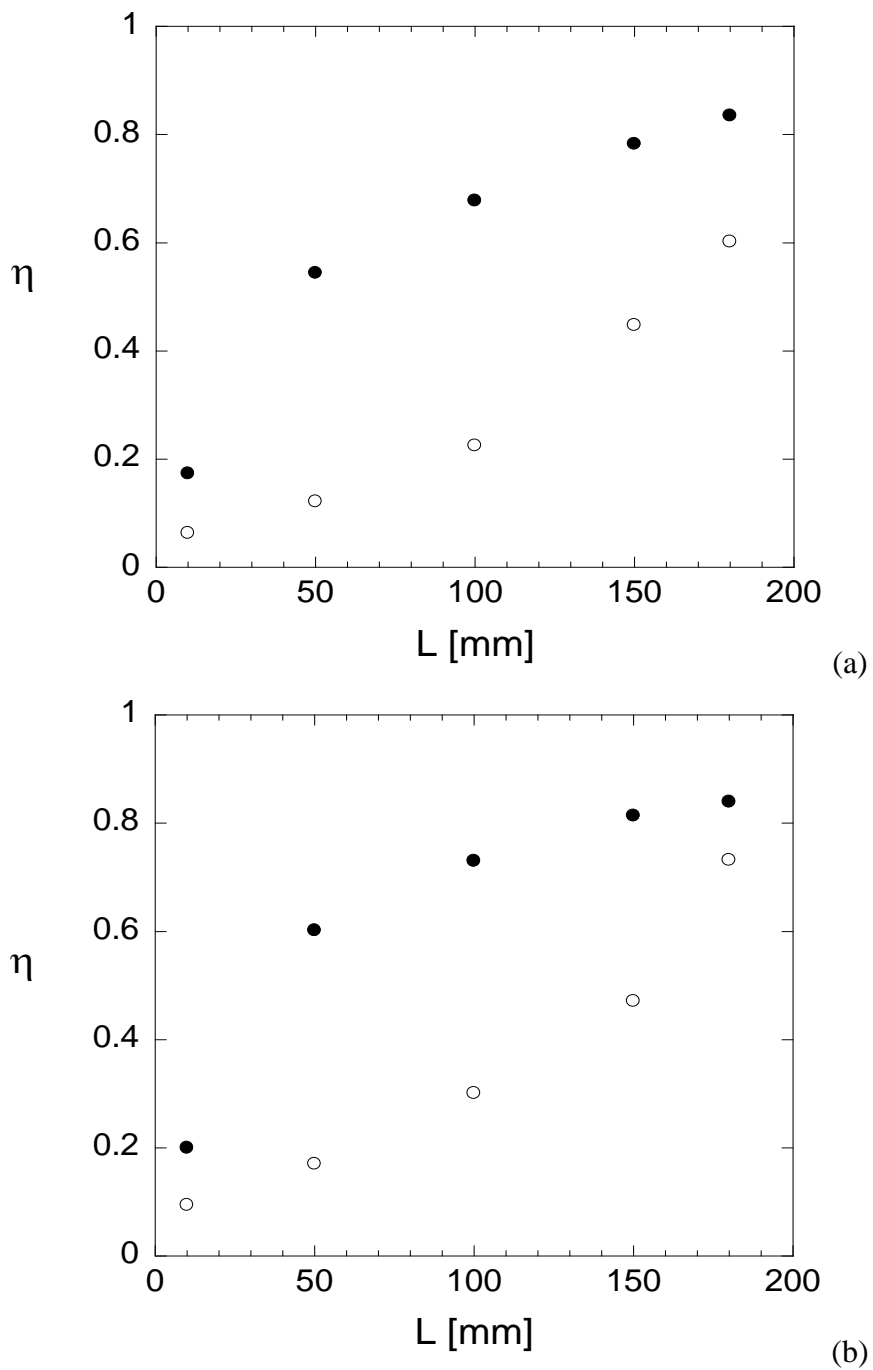
(a)

(b)

Figure 5.36 Macroscopic (full circles) and reinforcing (open circles) efficiencies as a function of sample length

to results shown in Table 5.IV, only 180 mm-long sample with the highest cord content achieves the isostrain condition at least in the observed point (midpoint). Hence, along with the important information on the fiber length effect that have been useful to assess the macromechanical response, the investigation of strain transmission performed by µRE measurements has provided important information on the validity and the applicability of the rule of mixtures. For the prediction of response of short sample, in fact, it should be useful to introduce the dependence of response on embedded cord length, as provided by detailed micromechanical models [100,105] (cf. Figure 3.14).

Investigation of cord interaction. As stated in Chapter. 4, aside from the stiffening due to the increasing of reinforcement content, the variation of cord end count may induce a modification in composite response due to a different level of 'interaction' between adjacent cords. Actually, this effect could be induced by to a sort of matrix hardening, due to a confinement of the matrix itself in the interphase region between two consecutive cords. Tensile test cannot provide a precise information on this phenomenon, hence, µRS has been adopted to investigate any variation in reinforcing efficiency of rubber-embedded cords as a function of cord spacing.

Measurement has been carried out on a 100mm-long composite characterize by three cords (as shown in Figure 5.9), for a cord volume fraction equal to 4.7%. During stretching, each embedded cord has been investigated by acquiring spectrum in the midpoint. Results of this investigation are shown in Figure 5.37 as Raman peak position of the p-phenylene band as function of applied strain. By adopting cord calibration curve for stress, it is possible to evaluate the stress that embedded cords carry at 1% strain and, consequently, the reinforcing efficiency. Data are reported in Table 5.VI showing that the central cord seems to carry a higher stress than the external ones. The increased reinforcing efficiency of the central cord could be thus ascribed to the confinement effect of the matrix leading to the stiffening of the interphase and, consequently, to better stress transfer conditions. However, it is important to underline that measurement cannot be verified since curves are found to lie within the error bar.

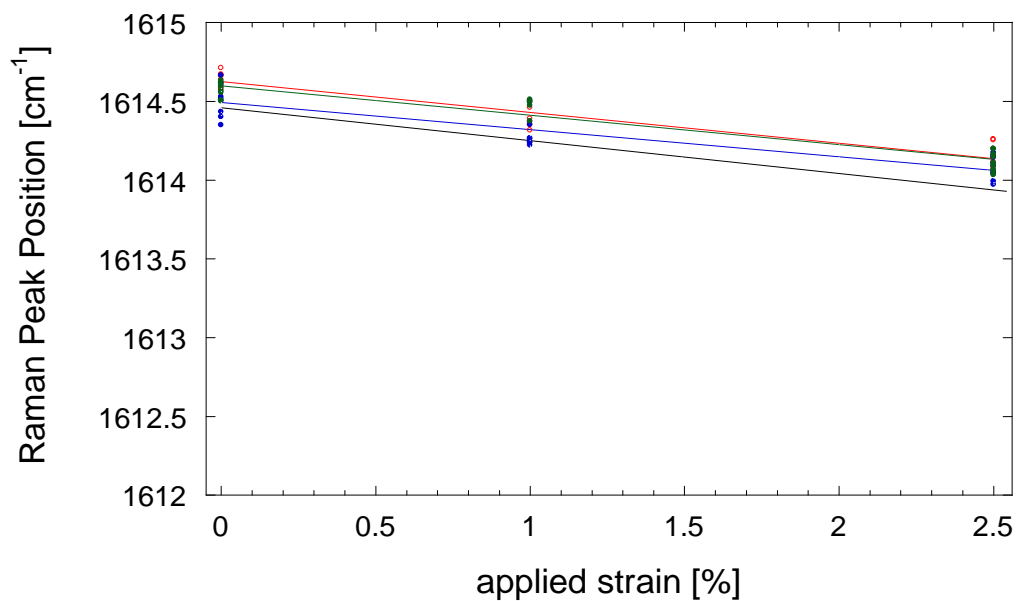Figure 5.37 Raman peak position as a function of applied strain for the three cords: central (red), lower (blue) and upper (green). Cord curve is depicted in black.

CORD	η^ε	Calculated stress [MPa]	η^σ
central	0.93	28.9	0.67
lower	0.82	25.5	0.59
upper	0.89	27.7	0.64

Table 5.VI Characteristic parameters for three-cord composite

Chapter 6

Modeling of mechanical behavior of cord-rubber composites

6.1 Introduction

The analysis of pneumatic tires represents a very complex question because it includes almost all problems related to deformable solid mechanics. This results from the following reasons:
- complex geometry;
- heterogeneous structure consisting of rubber, cords and bead wires;
- rubber is an incompressible material;
- cord content and orientation vary;
- large displacements and strains;
- contact with the rim and road alters the stiffness behavior;
- the initial stiffness of an uninflated tire is very low [1,2,17].

These reasons make analytical methods of tire modeling not accurate enough and too many simplifying assumptions must be made. For this reason, the commonly applied technique for modeling of pneumatic tires is based on numerical method, namely the Finite Element Method (FEM). However, the implementation of a FEM tire model also shows several difficulties. From

1970s, the progress observed in FEM formulations, as well as increased computer processing power, allowed to obtain more and more perfect tire models. Ghoreishy [16] made a wide review of professional literature on the topic. Three-dimensional tire models based on overlaying the orthotropic cord-rubber elements have been proposed in literature [16], however, they do not provide for a complete description of the layers because an important aspect of constitutive behavior is neglected: tension-twisting coupling. The problem has been presented and discussed in Chapter 3, with an overview on the several theoretical approaches adopted to simulate the actual response of cord-rubber composites.

In this chapter, a novel approach for modeling of cord-rubber composites will be discussed. This model has been developed in collaboration with Prof. Massimiliano Fraldi of Department of Structural Engineering of University of Napoli Federico II and represents a step forward in the literature survey of analytical and FEM models, for the introduction of a new hybrid analytical-FEM approach. Unlike the aforementioned orthotropic approach that are commonly adopted in modeling unidirectional laminae, the capability of this model relies on the possibility of simulating the tension-twisting coupling of the cord and, in turn, of the overall composite, by embedding a trigonal cylinder into the pad, whose constitutive behavior was been previously determined on the basis of the analytical model.

6.2 Model implementation

Three-dimensional model of cord-rubber pad has been implemented in ANSYS™. It consists of an homogenized cylinder embedded into a non-linear hyperelastic matrix (as shown in the schematic depicted in Figure 6.1). Details on the constitutive behavior of both the matrix and cylinder are described in the following. Mesh of both cord and rubber have been performed by using three-dimensional, 8-node, brick elements (SOLID185). This element type has been chosen for its capability in simulating deformations of nearly incompressible and fully incompressible hyperelastic materials, such as rubber.
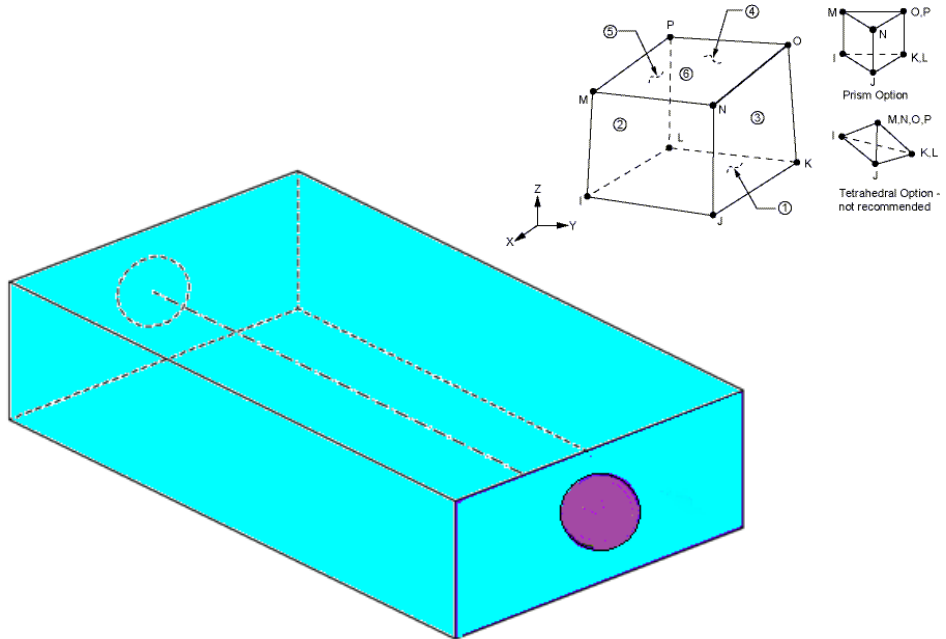
Figure 6.1 Schematic of FEM model. Inset: SOLID185

6.2.1 Matrix modeling

Hyperelastic constitutive relations described in Par. 2.2.3 are appropriate to model this incompressible material under quasi-static loading where deformations are not infinitesimal. Among the several formulations of constitutive equations for hyperelastic behavior, ANSYS™ provides the well-established Mooney-Rivlin formulation (Eq. 2.13).

ANSYS™ provides curve fitting tools to obtain material constants for hyperelastic models from the experimental data and stress-strain data can be directly fed to the FEM software that computes the fitting. Comparison between

experimental data and the fitting based on eq. 2.13 is shown in Figure 6.2. Mooney-Rivlin parameters are reported in Table 6.I.
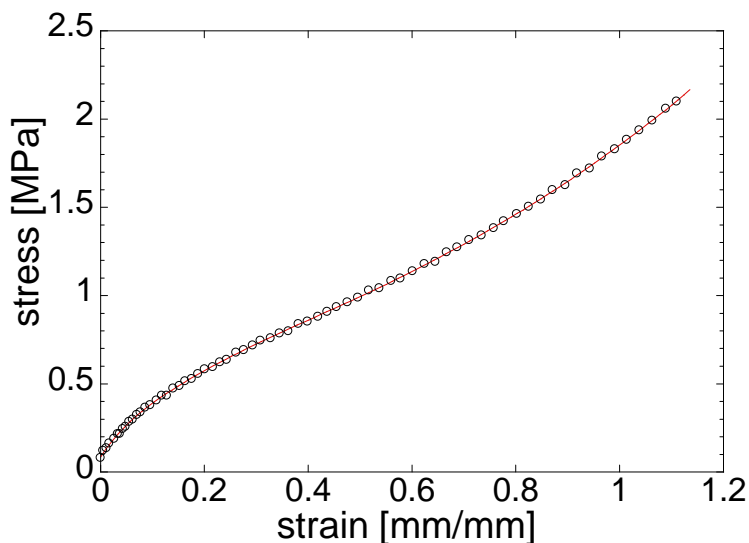
Figure 6.2 Stress-strain curve for rubber: comparison between experimental data (open circles) and polynomial model (red line)

C_1	0.448
C_2	0.398

Table 6.I Mooney-Rivlin parameters

6.2.3 Cord modeling

Cord is a not a continuum but a hierarchical structure, made of hundreds twisted filaments (cf. Par. 2.3). Modeling such a structure is made difficult by the huge amount of the elements and by the peculiar tension-twisting coupling. As stated in Chapters 2 and 3, several analytical and numerical approaches have been adopted to model such a structure and the works of Hruska [61], Leech [147] Machida at al. [62], McConnell et al. [63], Knapp [64], Lanteigne [148], Zimliki [149], Costello [27], Nawrocki et al. [150], Pidaparti [89] and Beltran [151] are worthy of note. However, most of these models often adopt extremely complex formulations. Among the aforementioned woks, Costello's model represents the most well-balanced approach, because of the simple formulation and completeness in phenomena description.

172

The presented model is based on a hybrid analytical-FEM formulation that allows simulating the tension-twisting coupling of cords. It consists of two main steps: the implementation of Costello's analytical model [27] and the homogenization of a FEM cylinder that is equivalent to the analytically simulated cord (Figure 6.3). In the first step, Costello's analytical model is implemented thus, starting from the features of the single monofilaments and provided that the final geometry of the cord is known (yarn and cord radii, twist angle), it provides the constitutive equation of the cord (cf. eq. 3.33), relating both axial and twisting response, as described in Chapter 3. The constitutive equation obtained by the analytical step is then fed to ANSYS™ for the creation of a customized finite element. In fact, ANSYS™ offers the possibility to use external routine in order to get user-programmable features. Accordingly, the second step is the implementation of a homogenized cylindrical model that is made up of finite elements characterized by the previously derived constitutive behavior.

In this way, the homogenized cylinder incorporates the relevant mechanical features of the aforementioned Costello's model. Furthermore the efforts spent to develop the analytical procedure, permit to simplify the geometry of model and bring numerical difficulties down, avoiding the use of advanced features of 3D CAD modeling [152]. In particular, since the analytical model is non-linear, it is necessary to refresh the constitutive equation with the new parameters concerning the new configuration. An automatic system update is performed by recalling the analytical external routine from ANSYS™ model.
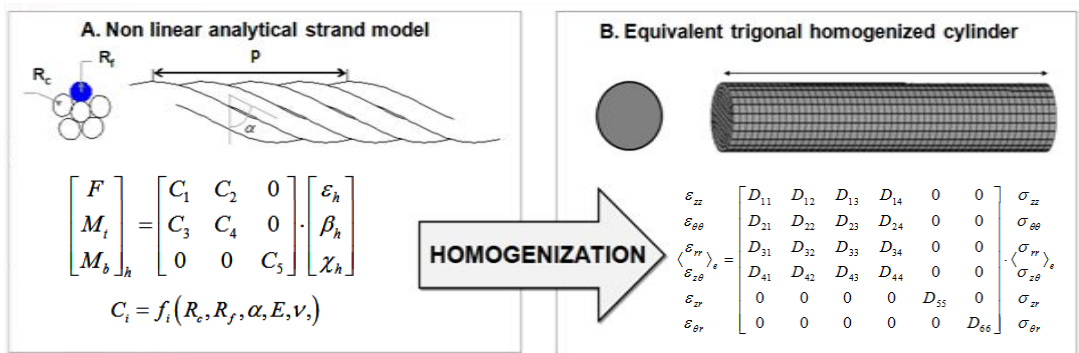

Figure 6.3 Schematic of hybrid analytic-FEM approach

In order to simulate cord performances under large solicitations, a non-linear quasi-static numerical approach has been implemented starting from the fundamentals of Costello's analytical model described in Par. 3.1.3. In

particular, non linearity implies that the elements of stiffness matrix depend on strain level and requires a step-wise analysis.

A classical example of results of analysis based on Costello's model is depicted in Figure 6.4, exhibiting the comparison between the undeformed structure of a six-filament strand and the deformed configuration. It is evident that elongation arises along with change in twist angle and in cross-sectional area of filaments.

The peculiar behavior of twisted structures that is represented in Figure 6.4 can be thus reproduced in a FEM model through the creation of an homogenized trigonal cylinder process. ANSYS™ in fact offers the possibility to create a customized finite element. This feature requires, as input information, the definition of a stiffness matrix. Using this facility, the analytical model discussed in the previous section can be used to implement an hybrid analytical-FEM model. Since results of Costello's model, it is possible to calculate the cord elastic constants and to define a homogenized cylinder characterized by the aforementioned tension-twisting coupling.

Such a customized finite element is characterized by a compliance matrix given by trigonal constitutive law (expressed in cylindrical coordinates):

$$
\left\langle \begin{matrix} \varepsilon_{zz} \\ \varepsilon_{\theta\theta} \\ \varepsilon_{rr} \\ \varepsilon_{z\theta} \\ \varepsilon_{zr} \\ \varepsilon_{\theta r} \end{matrix} \right\rangle_e =
\begin{bmatrix}
D_{11} & D_{12} & D_{13} & D_{14} & 0 & 0 \\
D_{21} & D_{22} & D_{23} & D_{24} & 0 & 0 \\
D_{31} & D_{32} & D_{33} & D_{34} & 0 & 0 \\
D_{41} & D_{42} & D_{43} & D_{44} & 0 & 0 \\
0 & 0 & 0 & 0 & D_{55} & 0 \\
0 & 0 & 0 & 0 & 0 & D_{66}
\end{bmatrix}
\cdot
\left\langle \begin{matrix} \sigma_{zz} \\ \sigma_{\theta\theta} \\ \sigma_{rr} \\ \sigma_{z\theta} \\ \sigma_{zr} \\ \sigma_{\theta r} \end{matrix} \right\rangle_e
\tag{6.1}
$$

where D_{ij} are expressed as a function of cord elastic constants (from Costello's model).
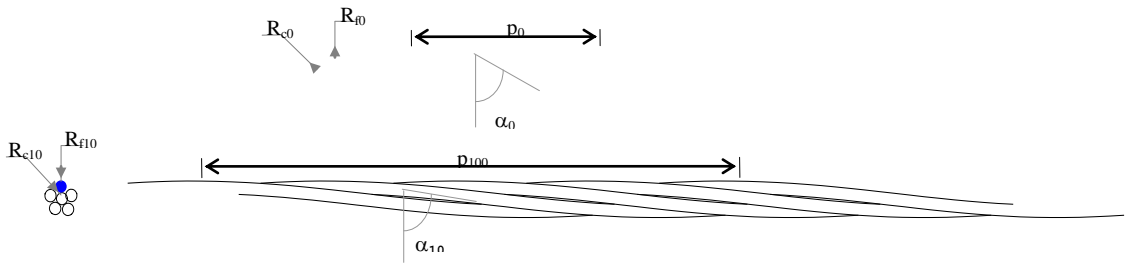
Figure 6.4 Effect of axial stretching on the structure of a six-filament strand
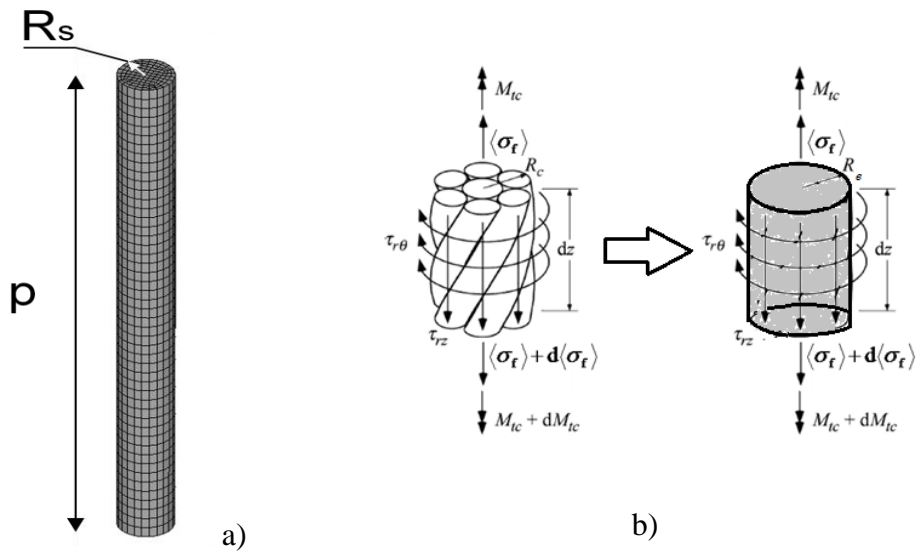
Figure 6.5 Homogenized FEM cylinder (a) and stress components acting on cord element (b)

6.2.3 Model results: composite tension-twisting coupling

Analyses have been performed by applying axial load to the pad. Figure 6.6 shows the deformed configuration of the composite highlighting the presence of tension-twisting coupling. The anisotropic behavior of cord reinforcement thus significantly affects the response of composite and models that do not take into account this important feature provide a very approximate simulation of the cord-rubber layer.
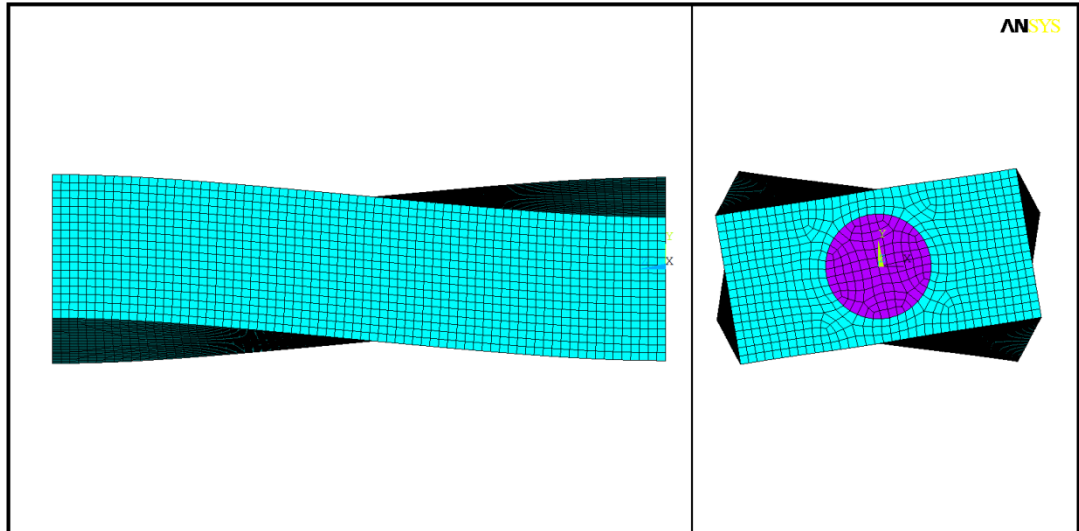
Figure 6.6 Tensile-torsion coupling effect with the trigonal cord

In order to get a complete description of the problem, shear stress $\tau_{r\theta}$ have been evaluated within the cord and the matrix, providing for further information on the raising of tension-twisting coupling in the composite. Figure 6.7 shows the distribution of shear stress $\tau_{r\theta}$ within the cord and on its external surface, highlighting the non-zero value of such shearing stress (unlike the case of an isotropic cylinder, as shown in the inset).

In particular, the non-zero shear stress $\tau_{r\theta}$ at the cord-rubber interface induces also tension-twisting coupling in the matrix (as shown in Figure 6.8).

Figure 6.7 **S**hear stress into the reinforcement and on the cord-rubber interface (black line)

Figure 6.8 Isosurface tension distribution into the rubber matrix

Chapter 7

Conclusions and future work

7.1 Conclusions

A novel investigation of mechanical behavior of cord-rubber composites has been proposed. Both experimental characterization and theoretical modeling have been carried out by using a multi-scale approach.

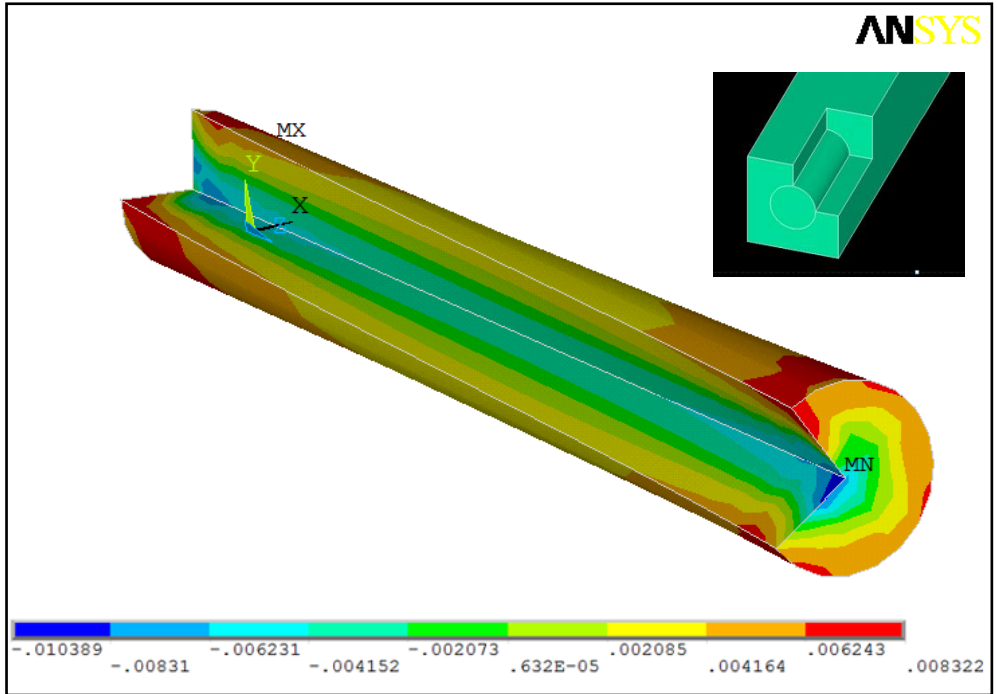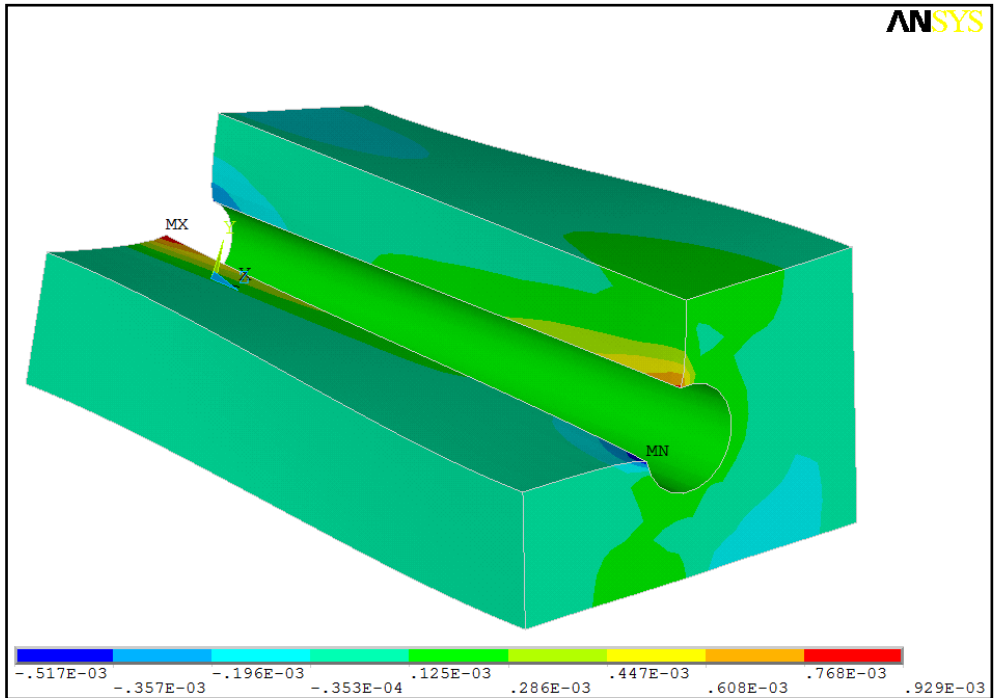Experimental characterization has been performed in order to analyze both the macromechanical and the micromechanical behavior of this composite material.

Preliminary tests have been performed on rubber and on polymeric cord to obtain a theoretical reference frame. In particular, information on glassy transition and on relaxation times of both phases were provided through dynamic-mechanical analysis and stress relaxation test; tensile tests also provided information on elastic behavior and failure of the two constituents. Finally dilatometric measurements were conducted in order to gain information on the volumetric behavior (and, consequently, on the bulk modulus) of both rubber and cord material.

Dynamic-mechanical analysis has revealed that composite shows both glassy transitions of rubber and cords and that response strongly depends on cord orientation. The effect of clamping conditions has also been investigated by comparing the response of uniaxial composite as determined by using the standard clamp of the DMA, held at several levels of clamping pressure, with the response obtained by testing the sample with a custom-made clamping

device. However, dynamic tests have revealed that, for 20 mm-long samples, the behavior of uniaxial composite strongly depends on clamping conditions and that it is significantly worse than predicted response, as calculated by the rule of mixtures.

Elastic response has been investigated on two typologies of cord-rubber composites, namely model and real composites. Model composites are characterized by a very low cord content and a large cord spacing: they response is quite poor and they are not actually used in carcass construction. Real composites show indeed high cord content and small cord spacing: the very good response in cord direction combined with high flexibility makes them the skeleton of tire carcass. Elastic response of both model and real composite has found to significantly depend on sample length. In fact, the elastic modulus evaluated at small strain has been found to increase with sample length until it approaches the predicted values according to the rule of mixtures. This 'finite fiber length effect' has thus been ascribed to stress transfer conditions that, according to micromechanical models, have been found to be quite weak in cord rubber composites. In particular, a macroscopic efficiency has been defined as the ratio of measured elastic modulus to the predicted one. Effects of cord volume fraction and of cord spacing have also been investigated.

Beyond the characterization of macromechanical response, a very detailed investigation has been performed on a microscopic scale by micro Raman spectroscopy. Firstly, a preliminary investigation of deformational processes of PET cord has been performed. In fact, it is well established [11,27] that, when the cord undergoes an axial solicitation, all the filaments are both stretched and rotated transversally to cord axis, resulting into a final rearrangement of the structure at a micrometrical scale. Raman spectrum of PET has found to show peak shift as a consequence of the application of external solicitation and, in particular, p-phenylene Raman band position can be straightforwardly correlated to the applied strain (or stress). Tests have been performed on both PET monofilament and cord (with and without dip) but the experimental set-up has not highlighted any differences between material behavior (from investigation on monofilament) and structure behavior (morphological investigation on cord). Nevertheless, the information about cord behavior represents a very important step for the investigation of composite micromechanics. Actually, the embedded cords have been adopted as internal strain (and stress) sensors into the composite, thanks to the dependence of Raman peak position on strain (or stress) that has been adopted as calibration curve. Measurement has highlighted that strain transmission strongly depends on sample length and that the isostrain

condition between the embedded cord and the matrix is achieved only for long samples. Also, reinforcing efficiency has been found to increase with sample length, according to micromechanical models. Finally, reinforcing efficiency has been correlated to the macroscopic efficiency, providing a valid interpretation of the aforementioned 'finite fiber length effect'.

A three-dimensional finite element model of the cord-rubber lamina has also been developed by adopting a multi-scale hybrid analytical/numerical approach. Costello's analytical model has been implemented to obtain the constitutive equation of the cord, which takes into account the tension-twisting coupling. Then, starting from this analytical model, a homogenized cylindrical model of the cords has been implemented in the FEM code. Finally, the overall mechanical model for the composite has thus been implemented by embedding the hybrid cord model into a FEM non-linear hyperelastic matrix. Simulation results have revealed that composite shows a significant tension-twisting coupling. The stress field in the interfacial region has been found to strongly differ from the stress field derived for an isotropic cylinder embedded in the same matrix.

7.2 Future work

Micro Raman spectroscopy has been found to be a very powerful tool for the investigation of deformational processes in polymer fibers and of micromechanics of composite materials.

The investigation of deformational processes into the cord by following deformation of single monofilaments still represents a very interesting challenge, despite no significant result has been highlighted in the investigation of PET cord morphology. In this respect, it is important to consider that PET shows a small peak shift and that measurements were affected by a quite large relative error. Hence, small variations among the calibration curves could not be ascribed to different behaviors of monofilament and cord. However, several fibers have been found to show strain-induced Raman peak shift and, among them, aramid could represent the best candidate for this very meticulous investigation. Aramid reinforcement is already adopted in cord-rubber composites and is characterized by very high strength, high modulus and low elongation. It is an excellent Raman scatterer and exhibits a very large rate of Raman peak shift, leading to a very precise measurement. Experiments concerning the separation of material and structure behavior could thus lead to

successful results. Furthermore, the reduction of acquisition time along with the improved signal quality could render composite investigation easier and more precise and detailed. In particular, axial stress distribution could be evaluated by a point-to-point mapping of the embedded cord and results could be interpreted in the light of micromechanics models. Also eventual interaction between adjacent cords could be analyzed in detail.

Regarding modeling activity, hybrid model needs validation with an *ad-hoc* experimental set-up able to verify tension twisting coupling of the composite.

Having validated the reliability of the model, the results of the macromechanical characterization, along with those of a more precise micromechanical investigation, could hence be simulated. Finally, providing a very detailed information on the phenomena arising on macroscopic and microsopic scales, model will be a very powerful tool for design and optimization of cord-rubber composites.

Bibliography

[1]   Clark SK (Ed.), *Mechanics of Pneumatic Tires*, US Government Printing Office, Washington, 1981.

[2]   Gent AN, JD Walter (Eds.), *The Pneumatic Tires*, National Highway Traffic Safety Administration, Washington, 2006.

[3]   Wong JY, *Theory of ground vehicles*, 3rd Ed., John Wiley & Sons, New York, 2001.

[4]   Gough VE, *Rubber Chem Technol* **41**, 988, 1968.

[5]   Guan Y, Zhao G and Cheng G, *J Reinf Plast Comp* **26**, 1921, 2007.

[6]   Chou TW, *J Mater Sci* **24**, 761, 1989.

[7]   Noritsugu, T, *Int J Jpn S Prec Eng* **31**, 92, 1997.

[8]   Krey J and Friedrich K, *Plast Rub Proc Appl* **11**, 83, 1989.

[9]   Kuo CM, Takahashi K and Chou TW, *J Compos Mater* **22**, 1004, 1988.

[10]   Walter JD, *Rubb Chem Technol* **51**, 524, 1978.

[11]   Clark SK, *Composite Theory Applied to Elastomers*, Technical Report, NASA CR-180322, N87-27035, 1987.

[12]   Akasaka T and Hirano M, *Compos Mater Struct* **1**, 70, 1972.

[13]   Gough VE, *Wear* **2**, 107, 1958.

[14]   Biderman VL, Drozhzhin PK, Pugin VA and Shchaveleva VF, *Trans Tire Rex Inst (NIIShP)* **3**, 5, 1957.

[15]   Mackerle J, *Model Simul Mater Sci* **6**, 171, 1998.

[16]   Ghoreishy MHR, *Iran Polym J* **17**, 571, 2008.

[17] Pelc J, *Appl Math Model* **31**, 530, 2007.

[18] Noor AK and Tanner JA, *Comput Struct* **20**, 517, 1985.

[19] Mc Allen J, Cuitifio AM and Sernas V, *Finite Elem Anal Des* **23**, 241, 1996.

[20] Mc Allen J, Cuitifio AM and Sernas V, *Finite Elem Anal Des* **23**, 265, 1996.

[21] Shiguo R, Isaac MD and Gdoutos E, *Appl Compos Mater* **11**, 353, 2004.

[22] Guan Y Zhao G and Cheng G, *J Reinf Plast Comp* **25**, 1059, 2006.

[23] Kocak S and Pidaparti RMV, *Mech Compos Mater St* **7**, 19, 2000.

[24] Murayama T and Lawton EL, *J Appl Polym Sci* **17**, 669, 1973.

[25] Galiotis C, Young R J, Yeung PHJ and Batchelder DN, *J Mater Sci* **19**, 3640, 1984.

[26] Young RJ, *J Text I* **86**, 360, 1995.

[27] Costello GA, *Theory of Wire Ropes*, Springer-Verlag, New York, 1990.

[28] *Rubber, Natural and Synthetic – General Test Methods; Carbon Black*, in Annual Book of ASTM Standards, P37, ASTM, Philadelphia, Pa, 1978.

[29] ISO Standard 1382:2002, *'Rubber – Vocabulary',* ISO, Geneva, Switzerland, 20002.

[30] Treloar LRG, *Rep Prog Phys* **36**, 755, 1973.

[31] Mullins L, *J Rubber Res* **16**, 275, 1947.

[32] Mullins L, *Rubber Chem Technol* **42**, 339, 1969.

[33] Mullins L and Tobin NR, *Rubber Chem Technol* **30**, 551, 1957.

[34] Warring JRS, *Trans Inst Rubber Ind* **26**, 4, 1950.

[35] Payne, AR, *J Appl Polym Sci* **3**, 12, 1960.

[36] Payne AR, *Rubber Plast Age*, Aug 963, 1961.

[37] Payne AR and Whittaker RE, *Rubber Chem Technol* **44**, 440, 1971.

[38] Alliger G and Sjothun IJ, *Vulcanization of Elastomers*, Reinhold Publishing Corp., New York,1964.

[39] ASTM Standard D412-06ae2, *Standard Test Methods for Vulcanized Rubber and Thermoplastic Elastomers - Tension*, ASTM International, West Conshohocken, PA, 2007, DOI: 10.1520/D0412-06AE02 www.astm.org.

[40] Tabor D, *Polymer* **35**, 2759, 1994.

[41] James HM and Guth E, *J Chem Phys* **11**, 455, 1943.

[42] Flory PJ, *Principles of Polymer Chemistry*, Cornell University Press, Ithaca, 1953.

[43] Kuhn W and Kuhn H, *Helv. Chim. Acta* **29**, 1095, 1946.

[44] Mooney M, *J App Phys* **11**, 582, 1940.

[45] Rivlin RS, *Large Elastic Deformations,* in *Rheology: Theory and Application*, Eirich FR (Ed.), p. 351, Academic Press, New York, 1956.

[46] Ogden RW, *Proc R Soc Lond* A **328**, 567, 1972.

[47] Valanis KC and Landel RF, *J App Phys* **38**, 2997, 1967.

[48] Bergström JS and Boyce MC, *J Mech Phys Solids* **46**, 931, 1998.

[49] Yeoh OH, *Rubb Chem Technol* **63**, 792, 1990.

[50] Gent AN, *Rubb Chem Technol* **69**, 59, 1996.

[51] Landel RF and Stedry PJ, *J App Phys* **31**, 1885, 1960.

[52] Konyali H, Menceloglu Y and Erman B, Polymer **49**, 1056, 2008.

[53] Bueche F, *Physical properties of polymers*, Interscience Publishers, New York, 1962.

[54] Leblanc JL, *Prog Polym Sci* **27**, 627, 2002.

[55] Medalia A, *Rubber Chem Technol* **51**, 437, 1978.

[56] Lion A, Kardelky C, *Int J Plasticity* **20** 1313, 2004.

[57] Lion A, *Continuum Mech Therm* **8**, 153, 1996.

[58] Gauthier C, Reynaud E, Vassoille R and Ladouce-Stelandre L, *Polymer* **45**, 2761, 2004.

[59] Lorenz H and M Kluppel, *A Microstructure-based Model of the stress-strain behavior of filled elastomers*, Proceedings of European Conference on Constitutive Models for Rubber IV, Dresden, 2009.

[60] Ning P, Brookstein D, *J Appl Polym Sci* **83**, 610, 2002.

[61] Hruska FH, *Wire and Wire Products* **26**, 766, 1951.

[62] Machida S and Durelli AJ, J Mech Eng Sci **15**, 241, 1973.

[63] McConnell KG and Zemke WP, *Exp Mech* **22**, 237, 1982.

[64] Knapp RH, *Int J Numer Meth Eng* **14**, 515, 1979.

[65] Lewin M and Preston J (Eds.), *Handbook of Fiber Science and Technology III*, Marcel Dekker Inc., New York: 1989.

[66]   Frisch JF, *Technical and Cost Optimization of Textile Constructions for Advanced Reinforcement of Passenger and Van Tyres*, IRC 2000 Rubber Conference, Helsinki, 2000.

[67]   Hockenberger AS and Koral S, *Ind J Fibre Text Res* **29**, 19, 2004.

[68]   Aytaç A, Yilmaz and B Deniz V, *Fiber Polym* **11,** 309, 2010.

[69]   Bhakuni RS, Rye GW and Domchick SJ, *Adhesive and Processing Concepts for Tire Reinforcing Materials*, ASTM Symposium on Tire Reinforcement and Tire Performance, Ohio, 1978.

[70]   Takeyama J, Matsui J, *Rubber Chem Tech* **42**, 159, 1969.

[71]   Solomon TS, *Rubber Chem Tech* **58**, 561, 1985.

[72]   Skolnik L, *Tire Cords*, in *Kirk-Othmer, Encyclopedia of Chemical Technology*, 2nd ed, 20, p. 328, John Wiley and Sons New York, New York, 1969.

[73]   Gillberg G and Sawyer LC, *J Appl Polym Sci* **28**, 3723, 1983.

[74]   Rahrig DB, *J Adhes* **16**, 179, 1984.

[75]   Rath JP, Chaki TK and Khastgir D, *J Appl Polym Sci* **108**, 3960, 2008.

[76]   Aytac A, Yilmaz B, and Deniz V, *Fiber Polym* **10**, 221, 2009.

[77]   Wootton DB, *The Application of Textiles in Rubber*, Rapra Technology Ltd., Shawbury, 2001.

[78]   Martin F, *Jahrb. Dtsch. Luftfsrt-Frtch* **1**, 470, 1939.

[79]   Tangorra, G, *Simplified Calculations for Multi-Ply and Rubber Sheets as a Combination of Cord-Rubber Laminating*, Proceedings International Conference, Moscow, 1971.

[80]   Clark SK, *The elastic constants of cord-rubber laminates*, Technical Report, The University of Michigan, 1960.

[81]   Clark SK, *The plane elastic characteristics of cord-rubber laminates*, Technical Report, The University of Michigan, 1960.

[82]   Clark SK, *Cord loads in cord-rubber laminates*, Technical Report, The University of Michigan, 1960.

[83]   Clark SK, *Interply stress and load distribution in cord-rubber laminates*, Technical Report, The University of Michigan, 1961.

[84]   Clark SK, *A comparison of net and continuum theory as applied to cord reinforced laminates*, Technical Report, The University of Michigan, 1967.

[85] Shield CA and Costello GA, *J Appl Mech* **60**, 1, 1993.

[86] Shield CA and Costello GA, *J Appl Mech* **61**, 9, 1994.

[87] Pidaparti RMV, Yang HTY and Soedel W, *J Comp Mat* **26**, 152, 1992.

[88] Pidaparti RMV and AW May, *Compos Struct* **34**, 361, 1996.

[89] Pidaparti RMV, *Compos Struct* **24,** 291, 1993.

[90] Jones RM, *Mechanics of Composite Materials,* 2nd Ed., Taylor & Francis: Philadelphia, 1999.

[91] Clark SK and Dodge RN, *Tire Sci Techn* **18**, 191, 1990.

[92] Walter JD and Patel HP, *Rubb Chem Techn* **52**, 710, 1979.

[93] Walter JD, Avgeropoulos GN, Janssen ML and Potts GR, *Tire Sci Techn* **1**, 210, 1973.

[94] Clark SK, *Rubb Chem Techn* **56**, 372, 1983.

[95] Love AEH, *Treatise on the Mathematical Theory of Elasticity*, Courier Dover Publications, New York, 1944.

[96] Cox HL, *J Appl Phys* **3**, 72, 1952.

[97] Dow NF, Rosen BW, *Evaluation of filament reinforced composites for aerospace structural applications*, Technical Report, NASA CR-207, 1965.

[98] McCartney LN, *Proc R Soc Lond A* **425**, 215, 1989.

[99] Nairn JA, *Mech Mater* **26**, 63, 1997.

[100] Hull D and Clyne TW, *An introduction to composite materials*, 2nd Ed., Cambridge Universiy Press, Cambridge, 1996.

[101] Fu SY, Yue CY, Hu X and Mai YW*, Comp Sci Technol* **60**, 569, 2000.

[102] Lacroix Th, Tiimans B, Keunings R, Desaeger M and Verpoest I, *Sci Technol* **43**, 379, 1992.

[103] Biju J. Thuruthimattam, Anthony M. Waas, Alan S. Wineman, *Int J Nonlin Mech* **36**, 69, 2001.

[104] Okabe T, Takeda N*, Compos Part A* **33**, 1327, 2002.

[105] Paris AJ, *J Appl Mech* **76**, 6, 2009.

[106] Sharpe WN (Ed.), *Springer Handbook of Experimental Solid Mechanics*, Springer, New York, 2008.

[107] Li Y, Ma T and Kniss DA, *Biomaterials* **22**, 609, 2001.

[108] Zoller P, Bolli P, Pahud V and Ackermann H, *Rev Sci Instrum* **47**, 948, 1976.

[109] Hashin Z, *Int J Solids Struct* **6**, 539, 1970**.**

[110] Peel LD and Jensen DW, *J Compos Mater* **35**, 96, 2001.

[111] Russell WB, *J Appl Math Phys* **24**, 581, 1973.

[112] Giannelis EP, Krishnamoorti R and Manias E, *Adv Polym Sci* **138**, 107, 1999.

[113] Vaia RA and Giannelis EP, *Macromolecules* **30**, 8000, 1997.

[114] Galiotis C, Robinson IM, Young RJ, Smith BJE and Batchelder DN, *Polym Commun* **26**, 354, 1985.

[115] Robinson IM, Zakikhani M, Day RJ, Young RJ and Galiotis C, *J Mater Sci Lett* **6**, 1212, 1987.

[116] Galiotis C and Batchelder DN, *J Mater Sci Lett* **7**, 545, 1988.

[117] Schadler LS and Galiotis C, *Int Mater Rev* **40**, 116, 1995.

[118] Mitra VK, Risen WM and Baughman RH, *J Chem Phys* **66**, 2731, 1977.

[119] Batchelder DN and Bloor D. J, *J Polym Sci Pol Phys* **17**, 569, 1979.

[120] Galiotis C, Young RJ and Batchelder DN, *J Polym Sci Pol Phys* **21**, 2483, 1983.

[121] Young RJ, *Polymer Single Crystals Fibres*, in *Developments in Oriented Polymers 2*, Ward IM (Ed.), p.1, Elsevier Applied Science, London, 1987.

[122] Wu O, Tashiro K and Kobayashi M, *Macromolecules* **22**, 188, 1989.

[123] Galiotis C, *Compos Sci Technol* **42**, 125, 1991.

[124] Kittel C*, Introduction to Solid State Physics,* 7th Ed., John Wiley and Sons: New York, 1996.

[125] Raman CV and Krishnan KS, *Nature* **121**, 501, 1928.

[126] Lewis IR and Edwards HGM (Eds.), *Handbook of Raman Spectroscopy - From the Research Laboratory to the Process Line*, Marcel Dekker Inc., New York, 2001.

[127] Long DA, Raman Spectroscopy, McGraw-Hill, New York, 1977.

[128] Anastassakis E, Pinczuk A, Burnstein E, Pollak FH and Cardona M, *Solid State Commun* **8**, 133, 1970.

[129] Englert T, Abstreiter G and Pontcharra J, *Solid State Electron* **23**, 31, 1980.

[130] Tashiro K, *Prog Polym Sci* **18**, 377, 1993.

[131] Gouadec G and Colomban Ph, *Progr Cryst Growth* **53**, 1, 2007.

[132] Galiotis C, Paipetis A and Marston C, *J Raman Spectrosc* **30**, 899, 1999.

[133] Amer MS and Schadler LS, *J Raman Spectrosc* **30**, 919, 1999.

[134] Lévêque D and Auvray MH, *Compos Sci Technol* **56**, 749, 1996.

[135] van den Heuvel CJM, Heuvel HM, Fassen WA, Veurink J and Lucas LJ, *J Appl Polym Sci* **49**, 925, 1993.

[136] Heuvel HM and Huisman R, *J App. Polym Sci,* **30**, 3069, 1985.

[137] RM Christensen, *Mechanics of Composite Materials,* Dover Publications: New York, 2005.

[138] Bahl SK, Cornell DD and Boerio FJ, *Polym Lett Ed* **12**, 13, 1974.

[139] Boerio FJ, Bahl SK and McGraw GE, *J Polym Sci Pol Phys* **14**, 1029, 1976.

[140] Fina LJ, Bower DI and Ward IM, *Polymer* **29**, 2146, 1988.

[141] Young RJ and Yeh W-Y, *Polymer* **35**, 3844, 1994.

[142] Yeh W-Y and Young RJ, *J Macromol Sci B* **37**, 83, 1998.

[143] Rasband WS, ImageJ, U. S. National Institutes of Health, Bethesda, Maryland, USA, http://imagej.nih.gov/ij/, 1997-2011.

[144] Northolt MG and van der Hout R, *Polymer* **26**, 310, 1985.

[145] Northolt MG and Sikkema DJ, *Adv Polym Sci* **98**, 119, 1990.

[146] Baltussen JJM, *Tensile Deformation of Polymer Fibres*, Ph.D. Thesis, Technical University of Delft, 1996.

[147] Leech CM, *Comm Appl Numer C* **3**, 407, 1987.

[148] Lanteigne J , *J Appl Mech* **52**, 423, 1985.

[149] Zimliki DA, Kennedy JM, Hirt DE and Reese GP, *Text Res J* **70**, 991, 2000.

[150] Nawrocki A and Labrosse M , Computers and Structures 77 (2000) 345-359.

[151] Beltran JPH, *Computational Modeling of Synthetic-Fiber Ropes*, PhD Thesis, The University of Texas at Austin, 2006.

[152] Pidaparti RM, Jayanti S, Henkle J and El-Mounayri H, *Compos Struct* **52,** 287, 2001.